

OPTICAL VELOCIMETERS

OPTICAL VELOCIMETERS

by

JOHN HOU-CHEONG CHAN, B.Sc., M.Sc.

A Thesis

Submitted to the Faculty of Graduate Studies
in Partial Fulfilment of the Requirements

for the Degree
Doctor of Philosophy

McMaster University

February 1976

©

JOHN HOU-CHEONG CHAN

1977

DOCTOR OF PHILOSOPHY (1976)
Department of Physics

McMASTER UNIVERSITY
Hamilton, Ontario

TITLE: OPTICAL VELOCIMETERS

AUTHOR: JOHN HOU-CHEONG CHAN B.Sc. (National Taiwan University)
M.Sc. (University of Saskatchewan)

SUPERVISOR: Professor E.A. Ballik

NUMBER OF
PAGES: xvi, 242

ABSTRACT

Three types of optical velocimeters are investigated in this thesis. The first, which employs a laser source, is the differential heterodyne laser Doppler velocimeter (DLDV). The second, which employs a conventional light source, is what we refer to as the white light fringe image velocimeter (WFIV). The third, which employs a laser source, we refer to as Fourier image velocimeter (FIV). The latter two techniques are new and were developed during the course of this work.

The system parameters for all three velocimeters are investigated both theoretically and experimentally. The main objective was to determine optimum operating conditions for achieving a high signal-to-noise ratio (SNR) and good spectral quality.

In the cases of the DLDV and WFIV the research included extensive investigations of the effects of receiver aperture size, particle number density (n), and detection angle, on the SNR. Theoretical derivations of the SNR, based on optical heterodyning and Mie scattering theory for the DLDV and on fringe crossing and Mie scattering theory for the WFIV, are found to have good agreement with carefully conducted experiments.

In particular it was observed that with the WFIV the SNR is proportional to n for n values corresponding to less than one particle in the probe volume. The SNR remains constant for large n values. In the case of the DLDV, the SNR was always found to be proportional to n when the coherent condition was satisfied. Consequently, it is concluded

that the DLDV signal results almost entirely from coherent scattering, even when the number of particles in the probe volume is as low as 0.02 (the lower limit of the measurements).

The FIV is designed to provide a large probe depth. A derivation of the self-imaging property of Fourier images is presented in Chapter 8. Fourier images are a result of Fresnel diffraction from a periodic object, and have the properties of reproducing the intensity distribution of the object. There is excellent agreement between theory and experiment on the functional form of the diffraction patterns at and near the Fourier image. The phenomenon of repair of errors in the object is also observed.

Preliminary applications of the two new techniques (WFIV and FIV) to the measurement of particle velocities have been carried out using a range of particle sizes, both on rotating disks and in fluid flow. In addition, velocity profile measurements of water flow in a square duct were carried out employing the WFIV. In all cases, comparable measurements were carried out employing a DLDV. It is found that under certain conditions the techniques are comparable both in accuracy and sensitivity.

ACKNOWLEDGEMENTS

The author would like to thank his supervisor, Dr. E.A. Ballik, for his guidance and generous support in this work.

Members of his supervisory committee, Dr. B.K. Garside, and Dr. C.J.L. Lock, for their interest and helpful discussions.

Dr. P.C.Y. Yip for helpful discussions.

A.J. Whorwood, D.S. Hodgson, and E.H. Chan for photography and associated services.

This work was supported, in part, by the National Research Council and the Defence Research Board of Canada.

CONTENTS

	<u>PAGE</u>
CHAPTER 1 INTRODUCTION	1
CHAPTER 2 PRINCIPLES OF THE LASER DOPPLER VELOCIMETER	8
2.1 Optical Doppler Shift	8
2.2 Optical Heterodyning and SNR	11
2.3 Light Sources and Coherence Requirements	15
2.4 Basic Systems for Laser Doppler Velocimeters	22
CHAPTER 3 DESIGN OF A DIFFERENTIAL LASER DOPPLER VELOCIMETER	29
3.1 The Doppler-Shift and Fringe-Crossing Phenomena of a DLDV	29
3.2 Characteristics of the Probe Volume	37
3.3 Analysis of the Heterodyning Processes in a Dual-Beam System	43
3.4 Signal Conditioning and Instrumentation	46
3.5 Experimental Configuration for the DLDV	54
3.6 Optimum Detection Conditions for DLDV	63
3.7 Summary	72
CHAPTER 4 DESIGN OF A WHITE LIGHT FRINGE IMAGE VELOCIMETER	73
4.1 Experimental Arrangement of a WFIV	73
4.2 Simple Technique for Visibility Measurement	76
4.3 Longitudinal Extent of the Fringe Image	80
4.4 Variation of d with Δq	90
4.5 Lateral Extent of Fringe Image	93

	<u>PAGE</u>
4.6 Comparison between WFIV and DLDV Measurements	
Employing a Rotating Disk	97
4.7 Summary	103
CHAPTER 5 LAMINAR FLOW MEASUREMENTS	105
5.1 Constant-Head Flow System	105
5.2 Gravitational-Feed Flow System	108
5.3 Flow Particles	109
5.4 Design of a Compact WFIV	110
5.5 SNR	116
5.6 Laminar Flow Measurements with a DLDV and a WFIV	118
5.7 Analysis of Laminar Flow in a Square Duct	120
5.8 Investigations of Frequency Broadening	124
5.9 Summary	129
CHAPTER 6 SNR INVESTIGATIONS OF A DLDV	130
6.1 Derivation of the SNR (Coherent Detection)	130
6.2 Effects of Aperture Size and Number Density on SNR	136
6.3 Angular Scattering Function	143
6.4 Effect of Detection Angle on SNR	149
6.5 Effects of Light Intensity and Velocity on SNR	155
6.6 Summary	156
CHAPTER 7 SNR INVESTIGATIONS OF A WFIV	160
7.1 Derivation of the SNR (Incoherent Detection)	160
7.2 Effect of Aperture Size on SNR	165
7.3 Effect of Number Density on SNR	167

	<u>PAGE</u>
7.4 Effect of Detection Angle on SNR	172
7.5 Summary	174
CHAPTER 8 FOURIER IMAGE VELOCIMETER	177
8.1 History of Fourier Images	177
8.2 Theory of Fourier Images	178
8.3 Computation of Fresnel Integrals	186
8.4 Photographic and Microphotometry Techniques for Diffraction Pattern Measurements	188
8.5 Diffraction Patterns	194
8.6 Application of Fourier Images to the Measurement of Velocities	207
8.7 Summary	222
CHAPTER 9 CONCLUSION	223
APPENDIX A ANGULAR MIE SCATTERING	230
REFERENCES	238

NOMENCLATURE

Only the more commonly used symbols are given below (Greek letters are given last). Several of these symbols also may be used for other less important quantities in the thesis, and this is indicated by †. In all such cases the meaning should be clear from the context.

- a cross-section area of the incident beam at location x .
- A^+ photocathode area radiated.
- B electronic noise bandwidth.
- d periodicity of a grating, fringe spacing.
- e charge of an electron.
- E amplitude of electric field (also E_1, E_2 , etc.).
- f optical frequency (also f_0, f_s , etc.).
- f_D Doppler shift frequency.
- Δf_D bandwidth of Doppler shift frequency.
- h Plank's constant.
- $i_1(\theta, \alpha, m)$ scattering function per particle for light polarized perpendicular to the plane of scattering (defined by the direction of observation and the direction of the incident beam).
- $i_2(\theta, \alpha, m)$ scattering function per particle for light parallel to the plane of scattering.
- $i(\theta, \alpha, m)$ equal to $[i_1(\theta, \alpha, m) + i_2(\theta, \alpha, m)]/2$.
- I_{ac} ac current of a single scatterer.
- I_{AC} total ac current.

I_{dc}	dc current of a single scatterer.
I_{DC}	total dc current.
I_0	intensity of light source.
$I(x)$	light intensity at location x .
$J(\theta)$	radiance ($w\text{-sr}^{-1}$) in the observation angle θ .
L^\dagger	pipe width.
m^\dagger	index of refraction of the particle relative to the surrounding medium.
M	shape and visibility parameter of the fringe pattern.
n^\dagger	particle number density.
$\frac{dn}{d\alpha}$	particle number density having radii between α and $\alpha + d\alpha$.
N^\dagger	total number of particles in the probe volume.
P_0	power of light source ($P_0 = I_0 a$).
P_1, P_2	power of scattered light (also $P(\theta)$, $P_1(\theta_1)$, $P_2(\theta_2)$, etc.).
Q_s	efficiency factor for scattering.
r^\dagger	radius of a particle.
$t(x_1, y_1)$	transmission factor of a two-dimensional object.
$T(u, v)$	Fourier transform of $t(x_1, y_1)$.
$U(x_1, y_1)$	field distribution of a two-dimensional object.
$U(x_0, y_0)$	field distribution of a diffracted field.
\vec{v}	velocity (magnitude v).
V	volume of probe volume
$\Delta x, \Delta y, \Delta z$	dimension of probe volume in the x, y, z direction, respectively.

- z^+ distance between two planes.
- α^+ size parameter, $\alpha = 2\pi r/\lambda$, where r is the particle radius and λ is the wavelength in the medium.
- $\beta(\theta)$ angular volume-scattering function ($\text{cm}^{-1} \text{sr}^{-1}$).
- η quantum efficiency.
- λ optical wavelength (also λ_0 , λ_s , etc.).
- σ total scattering cross-section ($\sigma = \pi r^2 Q_s$)
- ϕ phase factor (also ϕ_j).
- ω angular frequency (also ω_j).
- Ω solid angle seen by the detector (receiver).

FIGURES

	<u>PAGE</u>
2.1	Behaviour of the heterodyne signal amplitude. 18
2.2	Yeh and Cummins reference heterodyne system. 23
2.3	Goldstein and Kreid reference heterodyne system. 24
2.4	Differential heterodyne system. 26
2.5	Symmetric heterodyne system. 28
3.1	Basic system for the DLDV. 31
3.2	Interference pattern of two planar phase fronts. 34
3.3	Ideal probe volume. 39
3.4	Properties of Gaussian beam. 41
3.5	Heterodyning processes in a DLDV. 44
3.6	Schematic representation of a PMT. 48
3.7	DLDV signals as observed on an oscilloscope. 50
3.8	Basic circuit for impedance matching amplifier. 52
3.9	Photomultiplier output of a scanned DLDV fringe pattern. 59
3.10	Doppler spectra from a DLDV. 67
3.11	Effect of pinhole diameter on spectral broadening. 69
3.12	Measurements of the various heterodyning processes. 71
4.1	Experimental arrangement for the WFIV. 74
4.2	Experimental arrangement for visibility measurements. 78
4.3	Fringe image pattern and visibility of a lens system. 79
4.4	Parameters used for the analysis of the fringe image system. 81
4.5	Relative intensity at $ \beta $ as a function of the relative distance $ \alpha $. 83

<u>FIGURES(cont.)</u>	<u>PAGE</u>
4.6 Parameters used for the analysis of a trapezoidal waveform.	85
4.7 Ronchi grating fringe visibility as a function of the parameter $ \beta $.	88
4.8 Scattered signal amplitude as a function of the parameter $ \beta $.	89
4.9 Visibility measurements along the longitudinal extent of the fringe image for an f/8 aperture.	91
4.10 Visibility measurements along the longitudinal extent of the fringe image for an f/4 aperture.	92
4.11 Parameters used for the analysis of signal sidebands.	94
4.12 Signal and sidebands for the fringe intensity distribution shown in Fig. 4.11.	96
4.13 Comparison between the differential Doppler laser and fringe image techniques using particles on a rotating disk.	99
4.14 Observation of signal sidebands.	102
5.1 Schematic of constant-head flow system.	106
5.2 Experimental arrangement of a compact WFIV.	112
5.3 Selective effect of field stop and lens aperture.	114
5.4 Fully-developed velocity profile of laminar water flow through a square duct.	121
5.5 Frequency spectra of the DLDV.	126
5.6 Frequency spectra of the WFIV.	127
6.1 Optical parameters for the flow tube.	133
6.2 DLDV SNR measurements employing 0.62 μm polystyrene particles.	138
6.3 DLDV SNR measurements employing 0.62 μm polystyrene particles.	140
6.4 DLDV SNR measurements employing homogenized milk.	141

FIGURES (cont.)

PAGE

6.5	The geometry for light scattering measurements.	145
6.6	DLDV angular scattering function measurements employing 0.481 μm polystyrene spheres ($\alpha = 3.18$, $m = 1.20$).	147
6.7	DLDV SNR(θ) measurements employing a small receiver aperture ($f/22$).	151
6.8	DLDV SNR(θ) measurements employing a higher number density than in Fig. 6.7.	152
6.9	DLDV SNR(θ) measurements employing a large receiver aperture ($f/2.6$).	154
7.1	Typical WFIV spectrum.	166
7.2	SNR as a function of receiver aperture.	168
7.3	WFIV SNR measurements employing 5.7 μm styrene divinylbenzene and 0.62 μm polystyrene particles.	170
7.4	WFIV angular scattering function.	173
7.5	WFIV SNR(θ) measurements employing an $f/2.6$ receiver aperture.	175
8.1	Diffraction geometry.	179
8.2	Experimental arrangement for photographing diffraction patterns.	189
8.3	Basic components of a microphotometer.	191
8.4	Microphotometer tracings.	193
8.5	Microphotometer traces of measured diffraction patterns together with their corresponding calculated patterns.	195
8.6	Microphotometer traces and theoretical curves of the diffraction pattern near the first Fourier image ($z = 20.4$ cm).	200

<u>FIGURES (cont.)</u>	<u>PAGE</u>
8.7 Microphotometer traces and theoretical curves for the diffraction pattern near the first Fourier image ($z = 20.4$ cm).	203
8.8 Theoretical curves for the diffraction pattern at and near the fifth order Fourier image.	206
8.9 Experimental set-up for the Fourier image velocimeter.	208
8.10 Harmonic content of scattering at $z = 21.4$ cm.	210
8.11 Relative fundamental frequency amplitudes, at and near the first Fourier image, taken with an incident beam diameter of 2 cm.	211
8.12(a) Calculated fundamental frequency amplitudes for an incident beam diameter of 2 cm.	213
8.12(b) Calculated fundamental frequency amplitudes for an incident beam diameter of 2 cm.	214
8.13 Relative fundamental frequency amplitudes at and near the first Fourier image taken with an incident beam diameter of 0.7 cm.	216
8.14(a) Calculated fundamental frequency amplitudes for an incident beam diameter of 0.7 cm.	217
8.14(b) Calculated fundamental frequency amplitudes for an incident beam diameter of 0.7 cm.	218
8.15 Relative fundamental frequency amplitudes, at and near the fifth Fourier image, taken with an incident beam diameter of 2 cm.	220

TABLES

	<u>PAGE</u>
3.1 Some Commercial Instruments Used for the Optical Velocimeters	55
3.2 The Optical and Geometrical Parameters for the DLDV	61
3.3 The Effects of Pinhole Diameter and Receiver Aperture on the Power SNR of a DLDV	65
5.1 Number of Particles in the Probe Volume	111
5.2 Optical and Geometrical Parameters for Various WFIV	115
5.3 Power SNR's for Various WFIV	117
5.4 The Optical and Geometrical Parameters for the DLDV and the WFIV Employed in the Laminar Flow Measurements	119
5.5 Fully-Developed Velocity Profile, u/u_{avg} , for a Square Duct	123
5.6 Frequency Broadening for DLDV and WFIV	128
6.1 Effect of Particle Velocity on DLDV SNR Measurements	157
6.2 Effect of IF Bandwidth on DLDV SNR Measurements	158
8.1 Comparison Between Relative Peak Intensities of Measured and Calculated Diffraction Patterns	204
A.1 Mie Scattering for Three Diameters of Transparent Spheres	235
A.2 The Efficiency Factor, Q_s , and the Total Scattering Cross-Section, σ , for Three Transparent Spheres	237

CHAPTER 1

INTRODUCTION

In 1964, Yeh and Cummins [1] reported the first application of a laser Doppler velocimeter (LDV) to the measurement of fully developed laminar water flow. Since then, progress has been made on many aspects of the subject. This includes the analysis and design of new and improved optical geometries for one component and multi-component velocity measurement, and the design of signal-processing equipment specifically suited to handling laser Doppler signals. Application of the LDV has been extended to measurement of turbulent water flow [2,3], and turbulent air flow [4,5]. More recently, the LDV has been applied to a wider range of flow configurations. These include the measurement of oscillatory water flow [6], the detection of aircraft trailing vortices [7], the study of shock waves through water [8], remote wind sensing [9,10], the measurement of combustion flames [11], the measurement of electrohydrodynamic motion [12], the investigation of supersonic flow [13,14], and particle sizing [15,16].

The primary purpose of this research program was to seek a better understanding of the operating principles of optical velocimeters. As part of the program two new optical velocimeter techniques have been developed. These techniques have assisted in the understanding of the LDV and in addition should broaden the area of application of optical velocimeters. The basic principles of the LDV, and related topics such

as optical heterodyning and coherent conditions, are presented in Chapter 2.

One of the commonly used configuration for the LDV is the differential laser Doppler velocimeter (DLDV). Ideally, this system employs two intersecting beams of equal intensity. The two beams are derived from the same laser source. A photodetector, which collects the light scattered from particles traversing through the intersecting region, produces an output signal whose frequency can be related to the particle velocities. Two interpretations of the system prevail. One is the Doppler-shift interpretation. In this case, the scattered radiation is regarded as being composed of two Doppler-shifted components, each corresponding to one of the incident beams. Optical heterodyning of the scattered radiation results in a difference frequency which is proportional to the velocity. The other is the fringe-crossing interpretation. Here a real fringe system is present at the beam crossover region. As particles cross the fringes, the intensity of the scattered light is modulated at a rate directly proportional to the velocity. It should be noted that both interpretations give the same detector output [17].

Drain [18], in his theoretical investigations of the DLDV, showed that there are two different contributions to the mean-square signal. He referred to these as the coherent and incoherent contributions. This terminology is now used for classifying optical velocimeters. The Doppler-shift and fringe-crossing interpretations are thus classified (in this thesis) as coherent and incoherent modes, respectively. Miller [19] suggested that the coherent and incoherent contributions are

inseparable and occur simultaneously. He showed qualitatively that the incoherent contribution dominates at a low particle concentration of large particles ($\approx 5 \mu\text{m}$), while the coherent contribution dominates at a high particle concentration of small particles ($\approx 0.4 \mu\text{m}$). Several workers have treated the DLDV exclusively as either a fringe-crossing phenomenon [20,21] or as a Doppler-shift phenomenon [22,23].

The problem as to whether a DLDV is best represented by the fringe-crossing interpretation or by the Doppler-shift interpretation is one of the subjects investigated in this thesis. Previous to our work, no carefully controlled quantitative experimental results have ever been reported. This resulted, to a large extent, from the difficulty of performing reliable experiments. Moreover, the interpretation of experimental results depends on many interrelated parameters. These include the receiver aperture size, the particle number density, the detection angle and the particle size distribution. This thesis presents the results of a wide range of careful experimental measurements which indicate that the DLDV operates primarily in the coherent mode, even at low particle concentrations. This is contrary to the conclusion reached by earlier workers that the incoherent mode is dominant at very low particle concentrations [18,19,20,21].

Much effort was devoted to the design and optimization of the DLDV system prior to performing the experiments. An important objective (which was achieved) was to obtain consistent and reliable measurements of the signal-to-noise ratio (SNR), and of the spectral characteristics

of the signal. All the measurements are strongly affected by the optical arrangement as well as by the flow conditions. Chapter 3 describes in detail the experimental arrangement used together with a critical evaluation of its operating characteristics.

The fringe-crossing interpretation of the DLDV led us to develop a new technique based on projected real fringes in the flow region. Since it can employ a conventional incandescent light source, we call this system the white light fringe image velocimeter (WFIV). Briefly, the fringe pattern is an optically produced image of a Ronchi grating. Particles traversing the fringe image produce a modulation of the scattered radiation, whose frequency is proportional to the velocity. Note that the WFIV makes it possible to investigate unambiguously the incoherent mode, which is not possible with the DLDV. A theoretical analysis of the fringe image system, together with the result of investigations employing a rotating disk scatterer, is presented in Chapter 4. The experimental results are compared with similar data obtained from a DLDV.

Since the WFIV possesses a highly localized probe volume it can be used to measure laminar water flow. Experimental results for a 1 cm^2 square duct are presented in Chapter 5 and compared with similar data for the DLDV. It is found that under certain conditions the ultimate sensitivity and accuracy of the two techniques are comparable over a wide range of particle sizes and velocities. Chapter 5 also describes the flow system and the properties of the particle seedings.

The development of optical velocimeters resulted primarily from

the great interest in finding useful applications for lasers. However, the WFIV does illustrate that a suitable system can be developed without the use of coherent sources. However, further research is required to establish practical applications for which the WFIV is clearly superior to the DLDV.

It should be noted that, in the same year that Yeh and Cummins produced the LDV, a fringe-crossing technique was reported by Gaster [24] which makes use of a transmission grating placed in front of a photodetector. The image (at the grating) of an illuminated moving particle produces a detector output frequency which is proportional to the particle velocity. This technique, although optically reciprocal to the WFIV, is probably more difficult to apply. One disadvantage is the relative difficulty of locating the probe volume. A carefully calibrated optical system is required. In the case of the WFIV, a fringe pattern is actually projected into the flow region. Thus only particles passing through the fringe pattern produce modulated signal; other particles, even if detected, can only produce a dc signal. One reason why Gaster's technique was not further developed may be that the study of lasers and their application were (and still are) popular topics. Consequently, less attention was given to conventional light source techniques.

SNR is one of the most important aspects to be studied in optical velocimeters. Many parameters, such as the particle number density, the receiver aperture size, the detection angle, the source power, and the particle size distribution, all affect the SNR. In

Chapter 6, equations derived on the basis of optical heterodyning and Mie scattering theory, are compared with experimental SNR data from a DLDV. Apart from the effect of detection angle, which requires further consideration, all other parameters show excellent agreement with theory. In Chapter 7, similar comparisons between theory and experiment are made for the WFIV. In this case, the theory is based on fringe crossing and Mie scattering theory. Whether a DLDV is governed by fringe-crossing phenomenon, or by Doppler-shift phenomenon is discussed in Chapters 6 and 7.

Both the DLDV and the WFIV possess a highly localized probe volume ($< 1 \times 10^{-3} \text{ cm}^3$). These techniques have been proven to be useful for measuring particle velocities either on a plane rotating disk or in fluid flow. But for other applications, such as determining the velocity of a solid body with a rough surface, these techniques are not very suitable. A standard optical system only focuses to a small region in space. Very rough surfaces, however, will not always pass through this region, and consequently, a very erratic signal will result. An ideal technique would have a fringe pattern continuously distributed along its projected optical path. Thus modulated signals will be emitted from all regions of the rough surface which intercept the fringe pattern. Fourier images provide a reasonable approximation to the ideal. Their application to velocity measurements, first developed by us [25], is called the Fourier image velocimeter (FIV).

Fourier images result from Fresnel diffraction of a periodic object [26]. Briefly, a series of images is formed when the periodic

object (e.g., a Ronchi grating) is illuminated by a collimated monochromatic source. Each image has the same periodicity as the object. The Fourier image reappears at intervals of $2d^2/\lambda$, where d is the periodical spacing of the object and λ is the wavelength. Between Fourier images the diffraction pattern reflects the periodic nature of the object but has a functional form that depends on the distance from the object [26]. The usable image depth for velocity measurement depends on the fringe spacing and the diameter of the collimated beam. Normally, the depth is about 20% of the basic distance, $2d^2/\lambda$. This depth is much larger than that for a DLDV or a WFIV. The theoretical and experimental investigations of the FIV are presented in Chapter 8.

CHAPTER 2

PRINCIPLES OF THE LASER DOPPLER VELOCIMETER

This chapter describes the basic principles of the Doppler shift of optical frequencies, and of optical heterodyning. Both topics are essential for the development of the LDV. Other concepts often used in this field are also explained. These include the basic operating principles of a gas laser, the problems of optical path length equalization, the chromatic coherence requirement, and the SNR of a LDV system. The distinction between coherent and incoherent detection is also discussed.

- A LDV system can always be classified into one of three basic systems. These basic systems are described in order of their development. In addition, brief assessments of the SNR and the operating ease of each of the three systems are provided.

2.1 Optical Doppler Shift

The principle of the Doppler heterodyne technique is based on the frequency shift that a laser beam undergoes when it is scattered from a moving particle. The basic equations for the frequency difference between an incident light beam and the light scattered by a moving particle, as measured by a stationary observer, has been presented in detail by Goldstein and Kreid [29]. They

state that a non-relativistic derivation of Doppler shift leads to the same expressions as those derived from a relativistic point of view. For this reason, and also because we are mainly concerned with velocities much less than c , the following derivations are based on classic non-relativistic considerations.

Consider that a stationary monochromatic light source, of frequency f_0 and wavelength λ_0 , illuminates a particle moving at a velocity \vec{v} in a vacuum. The relative speed between the particle and an incident wavefront having propagation direction \hat{e}_i (unit vector) is $c - \vec{v} \cdot \hat{e}_i$, where $c = f_0 \lambda_0$ is the speed of light in the vacuum. The rate at which wavefronts are intercepted and scattered by the moving particle is [30]

$$\begin{aligned} f' &= (c - \vec{v} \cdot \hat{e}_i) / \lambda_0 \\ &= f_0 - \vec{v} \cdot \hat{e}_i / \lambda_0 \end{aligned} \quad (2.1)$$

The wavelength corresponding to the scattered frequency is

$$\lambda_s = c / f' \quad (2.2)$$

Assume now that a stationary observer views only these secondary wavefronts scattered in a direction \hat{e}_s . The relative motion between the observer and the particle is not changed if the particle is assumed stationary and the observer is assumed to be moving at a velocity $-\vec{v}$. Thus, in a manner analogous to Eq. (2.1), it can be seen that the observer intercepts scattered wavefronts at a rate

$$\begin{aligned}
 f_s &= (c + \vec{v} \cdot \hat{e}_s) / \lambda_s \\
 &= f' + \vec{v} \cdot \hat{e}_s / \lambda_s \\
 &= f_0 + \vec{v} \cdot (\hat{e}_s / \lambda_s - \hat{e}_i / \lambda_0) \quad (2.3)
 \end{aligned}$$

When the velocity of the particle is much less than c , $\lambda_s = \lambda_0$, and Eq. (2.3) can be expressed as

$$f_s = f_0 + \vec{v} \cdot (\hat{e}_s - \hat{e}_i) / \lambda_0 \quad (2.4)$$

Consequently the Doppler shift is

$$f_D = f_s - f_0 = \vec{v} \cdot (\hat{e}_s - \hat{e}_i) / \lambda_0 \quad (2.5)$$

When the particle is in an environment of refractive index n , an identical result is obtained provided that the wavelength λ_0 is replaced by λ_0/n . In such cases, \hat{e}_s and \hat{e}_i are also defined in the refractive medium. They can be determined by the in-vacuo values by use of Snell's law. Thus,

$$f_D = \frac{n\vec{v} \cdot (\hat{e}_s - \hat{e}_i)}{\lambda_0} \quad (2.6)$$

Although light scattered from a moving particle has been assumed, the equations are also applicable to light reflected from a moving surface. The basic requirement is that the moving object must re-emit (scatter or reflect) wavefronts instantaneously.

In an actual laser velocimeter, the frequency shift is measured by optical heterodyning of the scattered laser radiation with a reference beam derived from the same laser. Depending on the velocimeter configuration employed the reference can be either scattered or unscattered. The component of velocity in the direction $(\hat{e}_s - \hat{e}_i)$ can be determined from the measured difference frequency and system geometry by appropriate formulae. These are provided for the basic LDV systems in Figures 2-2, 2-3, 2-4, and 2-5.

2.2 Optical Heterodyning and SNR

Here we present the basic concepts of optical heterodyning. Detailed information on the subject can be found elsewhere [31].

Photomixing (heterodyning) of optical frequencies is commonly achieved by means of a photomultiplier. To simplify the derivation consider that the scattered and reference beams are made coincident on the photocathode, and that their wavefronts are parallel. In addition, assume that both electric fields have the same polarization. Then the total electric field is given by

$$E_t = E_1 \cos 2\pi f_1 t + E_2 \cos 2\pi f_2 t, \quad (2.7)$$

where E_1 and E_2 are the amplitudes of the individual waves. The photocathode current is directly proportional to the incident power and therefore the photocathode current is

$$I_t' = \alpha A \langle E_t^2 \rangle, \quad (2.8)$$

where A is the photocathode area radiated. The proportionality constant, α , is given by

$$\alpha = \frac{\eta e}{hf} \quad (2.9)$$

where η is the quantum efficiency, e is the charge of a single electron, h is Plank's constant and f is the average frequency of the incident light. After substitution of Eq. (2.7) into Eq. (2.8), one obtains

$$\begin{aligned} I'_t &= \alpha A \left[E_1^2 \cos^2 2\pi f_1 t + E_2^2 \cos^2 2\pi f_2 t + E_1 E_2 \cos 2\pi(f_1 + f_2)t \right. \\ &\quad \left. + E_1 E_2 \cos 2\pi(f_1 - f_2)t \right] \\ &= \alpha A \left[\frac{E_1^2}{2} + \frac{E_2^2}{2} + E_1 E_2 \cos 2\pi(f_1 - f_2)t \right] \end{aligned} \quad (2.10)$$

In Eq. (2.10) it is assumed that the time average is over periods much shorter than the difference frequency period. Thus, the current can be split into two parts, a dc current carrying no information (but generating shot noise),

$$I'_{dc} = \frac{\alpha A}{2} (E_1^2 + E_2^2) \quad (2.11)$$

and a signal term carrying information,

$$I'_s = \alpha A E_1 E_2 \cos 2\pi(f_1 - f_2)t \quad (2.12)$$

The mean-square value of the shot noise, measured at the anode of the photomultiplier, is given by [31]

$$\begin{aligned} I_n^2 &= 2Ge I_{dc}^2 B \\ &= Ge \alpha A B (E_1^2 + E_2^2) \end{aligned} \quad (2.13)$$

where B is the noise bandwidth of the signal processing electronics, and G is the cathode-anode power gain given by [32]

$$G = \delta^{2n} \quad (2.14)$$

where δ is the mean-secondary-emission coefficient of the n dynodes. The mean-square value of the signal current is therefore

$$I_s^2 = \frac{1}{2} G \alpha^2 A^2 E_1^2 E_2^2 \quad (2.15)$$

Other sources of photomultiplier noise includes background light noise (amplitude E_p), dark current shot noise, and the thermal noise in the output resistance (R). With adequate signal the dark current shot noise can be made much smaller than the signal shot noise. In most cases it can be neglected, and is done so here. The thermal noise, however, is different. The value of the thermal noise power is given [31] by $(4kTB)$, which is independent of R . But any reduction in the output resistance will reduce the output signal power. On the other hand, due to the gain of a photomultiplier tube (PMT), only the shot noise is amplified; the thermal noise is not affected. Therefore, the SNR (signal power/noise power) at the output of a PMT is

$$\text{SNR} = \frac{I_S^2 R}{I_n^2 R + 4kTB}$$

or

$$\text{SNR} = \frac{G\alpha^2 A^2 E_1^2 E_2^2 R}{2e\alpha GRB(E_1^2 + E_2^2 + E_B^2)A + 8kTB} \quad (2.16)$$

where I_n^2 now includes the background light noise and where Eqs. (2.13) and (2.15) have been substituted. It can be shown that if

$$(E_1^2 + E_2^2 + E_B^2)A \gg \frac{4kThf}{ne^2 GR} \quad (2.17)$$

then Eq. (2.16) reduces to

$$\text{SNR} = \frac{nA}{2hfB} \cdot \frac{E_1^2 E_2^2}{E_1^2 + E_2^2 + E_B^2} \quad (2.18)$$

For a typical value of $G = 10^{12}$ ($\delta = 4$, $n = 10$), $T = 300^\circ\text{K}$, $R = 50 \Omega$, and $\eta = 0.05$ (for $\lambda = 6328 \text{ \AA}$), the right-hand side of Eq. (2.17) is approximately equal to 8×10^{-13} watts. It is therefore very easy to establish experimental conditions such that Eq. (2.18) is valid. Obviously an increase in η and/or a decrease in B will increase the SNR.

Equation (2.18) can be further simplified if it is assumed that $E_1 + E_2 \gg E_B$. This is always true if reference-beam configurations are employed. It is also true for other systems (e.g., DLDV) if adequate precautions are taken to reduce the amount of background radiation reaching the PMT. One technique for this is the use of a lens-spatial filter combination to collect only the radiation scattered from the

beam-crossover region. Consequently, the basic SNR equation can be reduced to

$$\text{SNR} = \frac{nA}{2h\nu B} \cdot \frac{E_1^2 E_2^2}{E_1^2 + E_2^2} = \frac{P_1 P_2}{P_1 + P_2} \quad (2.19)$$

where P_1 and P_2 are the powers of the two electric fields, respectively.

2.3 Light Sources and Coherence Requirements

In this section we discuss the properties of light sources for use in Doppler velocimeters. In an important paper Rudd [17] investigated the possibility of employing conventional incandescent light sources for Doppler velocimeters. His analysis was based on consideration of the coherence requirements. Rudd concluded that while the use of incandescent sources was theoretically feasible, it was very difficult to apply in practice. The main reason is that little power is left after the coherence requirements are fulfilled. Since lasers can provide both power and coherence, therefore they remain the only light sources of practical importance for Doppler velocimeters. In particular, cw gas lasers are the most suitable at present; only they will be considered in the following.

2.3.1 Lasers and Temporal Coherence

Temporal coherence can be related to the optical path length difference between two heterodyning beams from the same source. Foreman [33] observed that the heterodyne signal amplitude depends on the

optical path length difference as well as on the number of axial modes in the laser. However, for most applications, detailed knowledge of the physics of laser action is not necessary to fully assess the required properties of laser sources.

Basically, a cw gas laser consists of an amplifier within a resonant cavity. Usually a discharge tube containing atomic or molecular gas at low pressure is employed as the amplifying medium. An electric discharge is employed, either at radio frequencies, or dc, to excite the gas. The amplifier is normally situated between two high reflectance mirrors which form the resonant cavity. In many lasers, the gain bandwidth is sufficiently large that several cavity resonant frequencies can be made to oscillate.

The number of excited axial modes can be measured by employing a high resolution scanning Fabry-Perot interferometer or can be estimated from the following considerations.

The axial mode frequency spacing is given by

$$\Delta f_M = \frac{c}{2L} \quad (2.20)$$

Since most lasers operate well above threshold for high light power output, the gain bandwidth can approach the line width, Δf_D , of the laser transition. For example, the full width at half maximum (FWHM) of the neon transition at 6328 Å is [34]

$$\Delta f_D = 1700 \text{ MHz} \quad (2.21)$$

Thus the number of excited axial modes can be calculated from

$$N = \frac{\Delta f_D}{\Delta f_M},$$

or

$$N = \frac{2\Delta f_D L}{c}. \quad (2.22)$$

The total electric field from a laser can be represented by

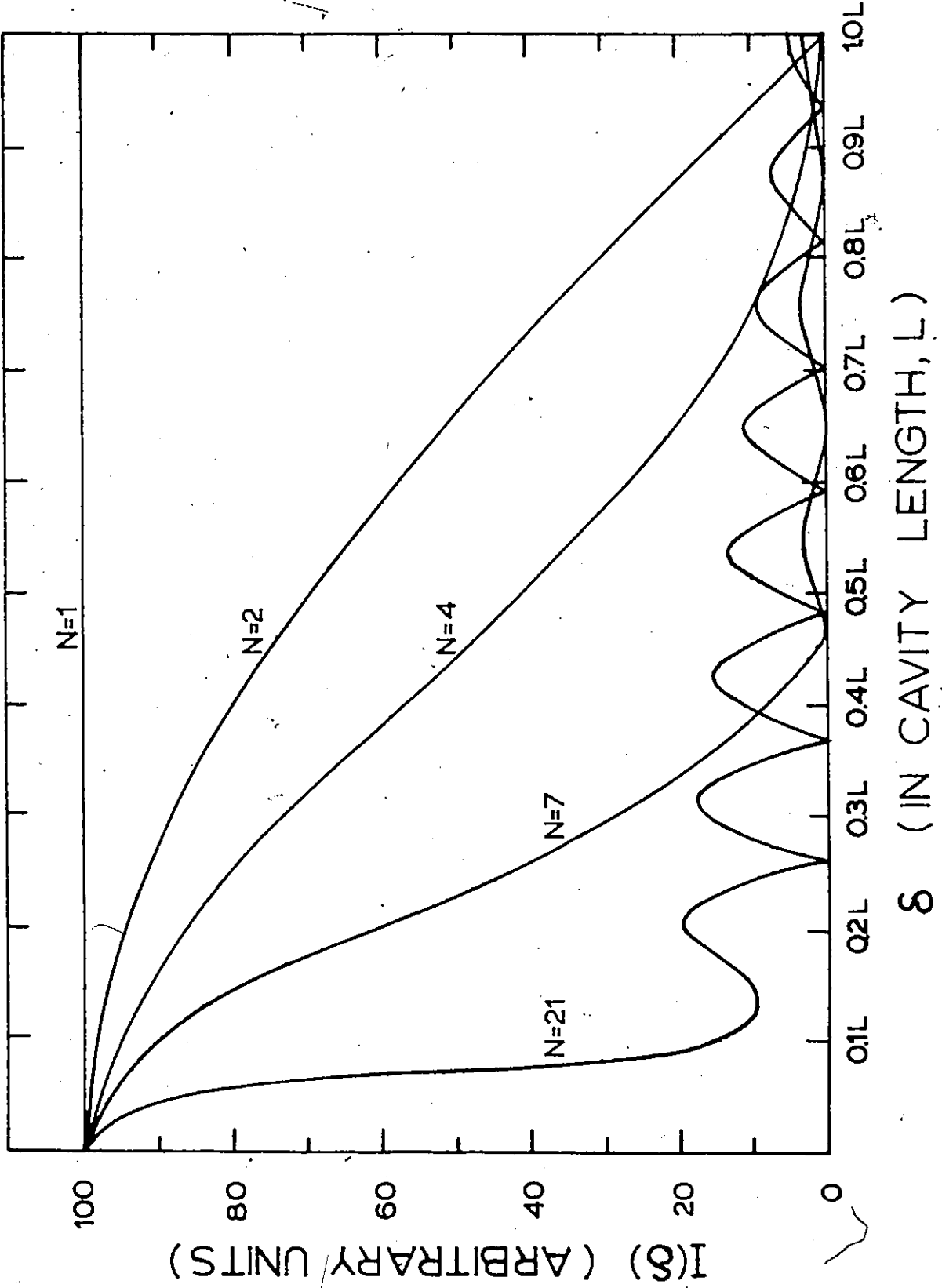
$$E(z,t) = \sum_{j=1}^N [E_0(t)]_j \exp\{-i[k_j z - \omega_j t + \phi_j(t)]\}, \quad (2.23)$$

where j denotes the mode number and N is the total number of excited axial modes. The time dependence of the phase, $\phi_j(t)$, is caused by small thermal and mechanical variations in the cavity length. Discharge fluctuation, mode competition, etc., can produce time variation in $[E_0(t)]_j$. A scattering particle generally spends a relatively small time interval within the probe volume. Therefore for most Doppler velocimeters, the time variations of both $\phi_j(t)$ and $[E_0(t)]_j$ can be neglected. On this basis, Foreman [33] calculated the behaviour of heterodyne signal amplitude as a function of path length difference and number of excited axial modes. Some of his results are reproduced in Fig. 2.1. Note that the functional form of $I(\delta)$ in Fig. 2.1 is symmetric about $\delta = L$, and has a periodicity of $2L$.

Equation (2.22) shows that an increase in L , which usually results in higher power output with the same lasing medium, will increase the number of axial modes. It can be seen from Fig. 2.1 that this

Fig. 2.1: Behaviour of the heterodyne signal amplitude, $I(\delta)$, as a function of the optical path length difference, δ , where δ is in units of the laser cavity length L . The parameter N is the number of excited axial modes.

Fig. 2-2



increased laser power can be fully utilized only for zero path length differences. For finite path length differences, the effective temporal coherence of the laser light is decreased as the number of axial modes is increased. Fortunately, optical path length equalization can be easily achieved in most of the LDV systems; examples will be discussed in the next section. For other systems, path length differences of integer multiples of $2L$ will provide comparable performance.

2.3.2 Chromatic Coherence

Chromatic coherence is concerned with the finite spectral width of a light source. It has been stated [29] that the spectral width of the light source for a LDV must be considerably less than the Doppler shift to be measured. However this is not necessary, although it is desirable. According to Rudd [17], the chromatic coherence requirement is

$$\frac{\Delta\lambda}{\lambda} \leq \frac{\Delta f_D}{f_D} \quad (2.24)$$

where $\Delta\lambda$ is the spectral width of the radiation employed and Δf_D is the bandwidth of the Doppler shift. Thus, a highly coherent laser is not essential for a Doppler velocimeter. Although rather surprising, this conclusion is easy to deduce. From Eq. (2.5) the Doppler shift is

$$f_D = \frac{\vec{v} \cdot (\hat{e}_s - \hat{e}_i)}{\lambda} \quad (2.25)$$

By differentiation,

$$\frac{\delta f_D}{f_D} = - \frac{\delta \lambda}{\lambda} \quad (2.26)$$

If we employ the criterion that $\Delta f_D \geq \delta f_D$, and let the source spectral width $\Delta \lambda = \delta \lambda$, then Eq. (2.24) follows. The negative sign in Eq. (2.26) is omitted because we have converted from frequency change to spectral width.

2.3.3 Coherent and Incoherent Detection

There are generally two extremes representing the response of a photodetector to a superposition of electric fields. One extreme is coherent detection (heterodyne detection) where the photocurrent is proportional to $|\Sigma E_i|^2$. The other extreme is incoherent detection (direct detection), where the photocurrent is proportional to $\Sigma |E_i|^2$. In the first case, the summation of the fields is performed before squaring, while in the second case, after squaring. Review articles on this subject can be found elsewhere [31,35]. Here only detection properties with significant importance to optical velocimeters are discussed.

Consider that a group of particles is illuminated in a LDV, and let these particles be the sources of E_i 's. Lading [36] has pointed out that there will be either coherent or incoherent detection depending on the configuration of the light collecting system. This conclusion can be reached either from the van Cittert-Zernike theorem [37] or from the antenna theorem [38] for optical heterodyning. According to the antenna theorem, one can calculate an area in the "transmitter" plane

(in the probe volume) from which scattered light will contribute to the heterodyne signal. The heterodyne constraint (or coherent criterion) is generally given by

$$A_R \Omega_R \leq \lambda^2, \quad (2.27)$$

where A_R is the receiver (detector) area and Ω_R is the solid angle seen by the detector. The latter can be expressed as

$$\Omega_R = \frac{A_T}{Z^2}, \quad (2.28)$$

where A_T is the transmitter area and Z is the distance between the transmitter and receiver planes. Hence, Eq. (2.27) can be rewritten as

$$\frac{A_R A_T}{Z^2} \leq \lambda^2. \quad (2.29)$$

If A_R is given, then A_T can be determined from Eq. (2.29). If A_T is larger than the area of the illuminating beams at the particles, then one would call the detection system "coherent"; if much smaller, then "incoherent".

A coherent arrangement can provide information about the absolute motion of individual particles together with information about the relative motion between the particles. An incoherent arrangement can only give information about the absolute motion of the individual particles.

As was mentioned in Chapter 1, the terminology of "coherent" and "incoherent" is also used for our classification of optical velocimeters.

This is based on the following definitions: An optical velocimeter which is governed by Doppler-shift phenomenon is classified as being in the coherent mode because its receiving aperture must satisfy the antenna theorem for cases when there are more than one particle in the probe volume. On the other hand, an optical velocimeter which is governed by fringe-crossing phenomenon is classified as being in the incoherent mode because its receiving aperture does not have to satisfy the antenna theorem. Whether or not its receiving aperture meets the antenna theorem (e.g., in the form given by Eq. (2.27)) is immaterial. It should be noted that Eq. (2.27) is applicable to monochromatic (or quasi-monochromatic) sources only. Thus, to achieve meaningful coherent detection employing conventional light sources, the temporal and chromatic coherence requirements must be also be obeyed, as discussed in Sections 2.3.1 and 2.3.2.

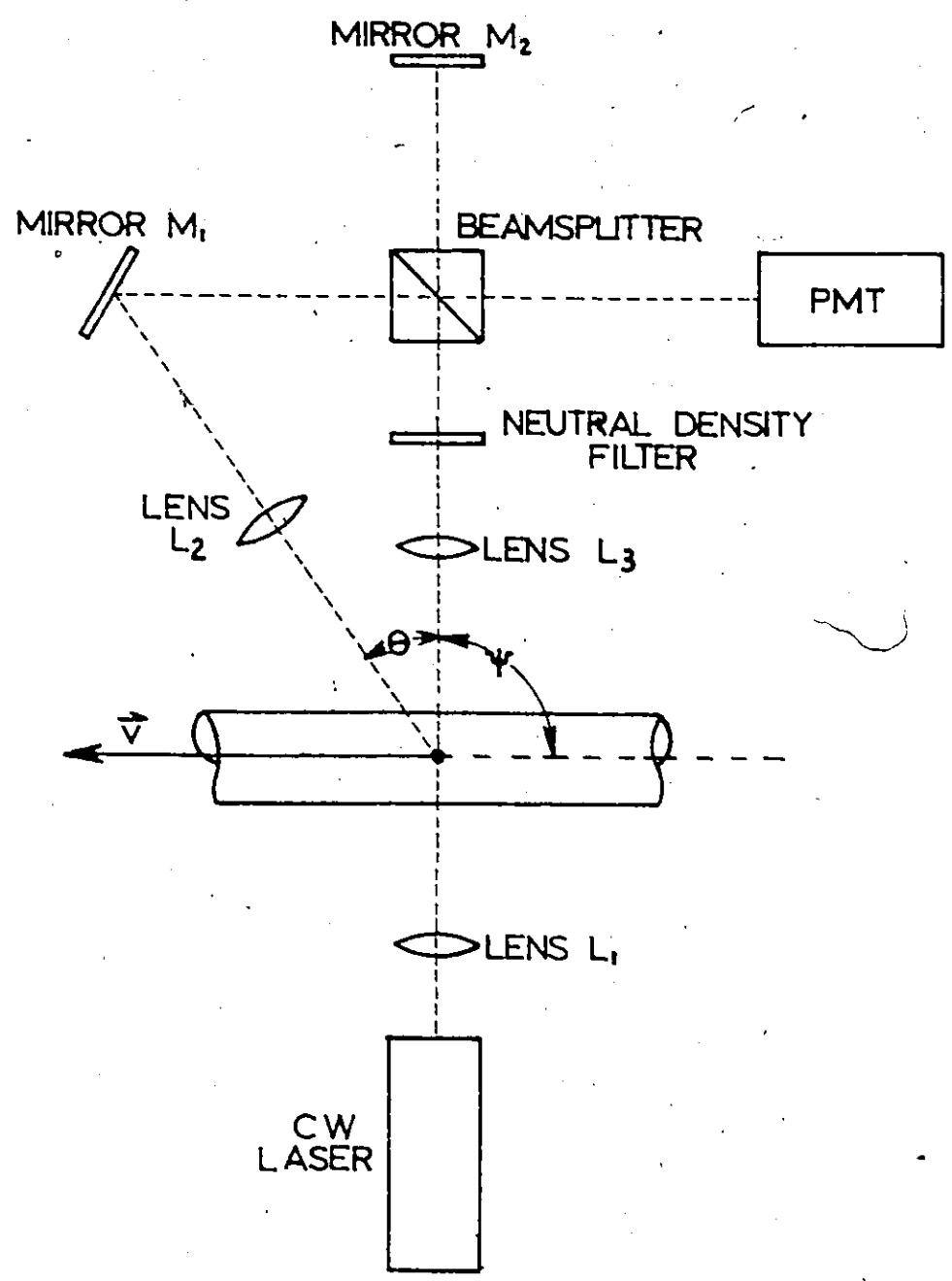
2.4 Basic Systems for Laser Doppler Velocimeters

In this section, a brief description of the LDV systems is given. Detail analyses of the systems which have been used for our experiments are described in Chapter 3. The various optical arrangements for the LDV can be classified into three general categories, as follows:

(1) Reference Beam Heterodyne System

This basic category can be subdivided into two systems - that of Yeh and Cummins, [1] (Fig. 2.2) and that of Goldstein and Kreid [29] (Fig. 2.3). The former was the first LDV technique to be developed. The biggest difference between these two systems concerns their beam

Fig 2-2



$$v = \frac{\lambda \cdot f}{2n} \left[\sin \frac{\theta}{2} \sin \left(\psi + \frac{\theta}{2} \right) \right]^{-1}$$

Fig. 2.2: Yeh and Cummins reference heterodyne system.

Fig. 2-3

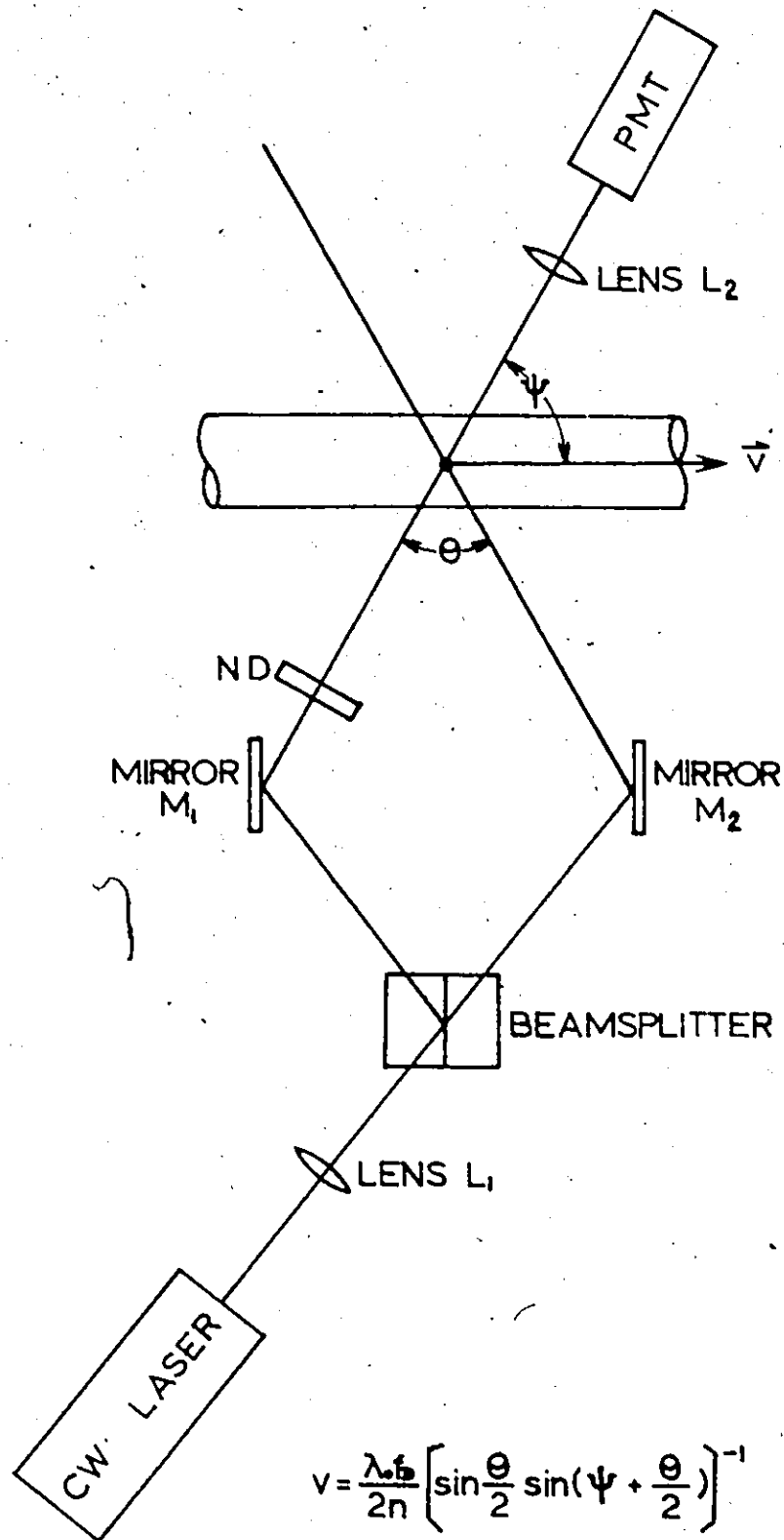


Fig. 2.3: Goldstein and Kreid reference heterodyne system.

geometry. One system has crossed beams (Goldstein and Kreid), and the other system does not (Yeh and Cummins).

In the Yeh and Cummins arrangement, the optical system demands very precise alignment, requires extreme mechanical stability, and is somewhat difficult to operate. Furthermore, it requires path length equalization for multimode beam operation.

The Goldstein and Kreid system offers considerable improvement over the former arrangement. In this system the alignment of the reference and scatter wavefronts is accomplished simply by causing two beams of coherent radiation to be brought to a common focal point in the probe volume. With this technique, the reference and scatter beams are in "perfect" alignment as both radiations are spherical waves concentric about a common focal point, and path length differences are easily minimized.

The receiver configurations of both systems are required to satisfy the antenna theorem. In addition, both systems show an inherent broadening of the frequency spectrum due to the finite apertures of the detection optics. This follows because for practical aperture sizes, a range of velocity components are being observed.

(2) Differential Heterodyne System

The optical arrangement is similar to that of Fig. 2.3 except that no reference beam is allowed to enter the photocathode (Fig. 2.4). A beat signal can be detected by heterodyning the scattered radiation from a common scatter center, which is illuminated simultaneously by two intersecting beams. These beams usually have approximately the same intensity. Since both scattered radiations originated from a

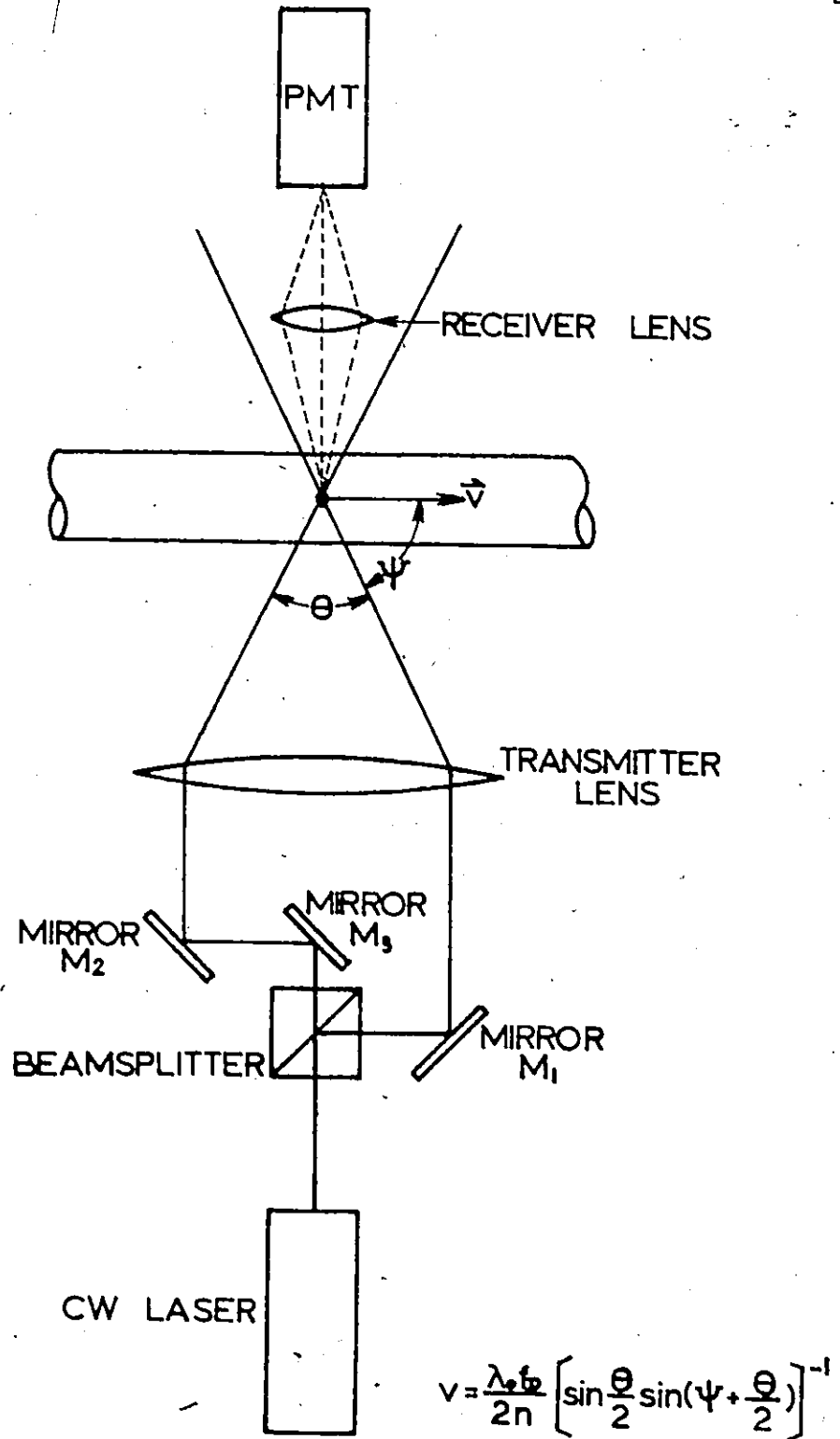


Fig. 2.4: Differential heterodyne system.

common scatter center, they are precisely aligned. Because of the differential heterodyne characteristic, the Doppler frequency is independent of the detection angle. Consequently, a large solid angle of mixed scattered radiations can be collected without introducing signal frequency broadening. This provides an enhanced SNR compared to the previous system [22,23,39].

(3) Symmetric Heterodyne System

This system is characterized by a single incident light beam at the measuring point (Fig. 2.5). The light scattered from the same scattering region, but collected in two different directions, is combined through a beam splitter before entering the photocathode [39, 40]. This one-beam, dual scatter system performs similarly to the difference heterodyne system, and can be regarded as an inverse to it. However, it can not utilize a large receiver collection angle, which may result in lower SNR compared to the differential heterodyne system.

For most applications the differential Doppler configuration is the most satisfactory form of laser velocimeter. For this reason our research on LDV's has been primarily on the DLDV, and only that LDV work is reported in this thesis.

Fig. 2-5

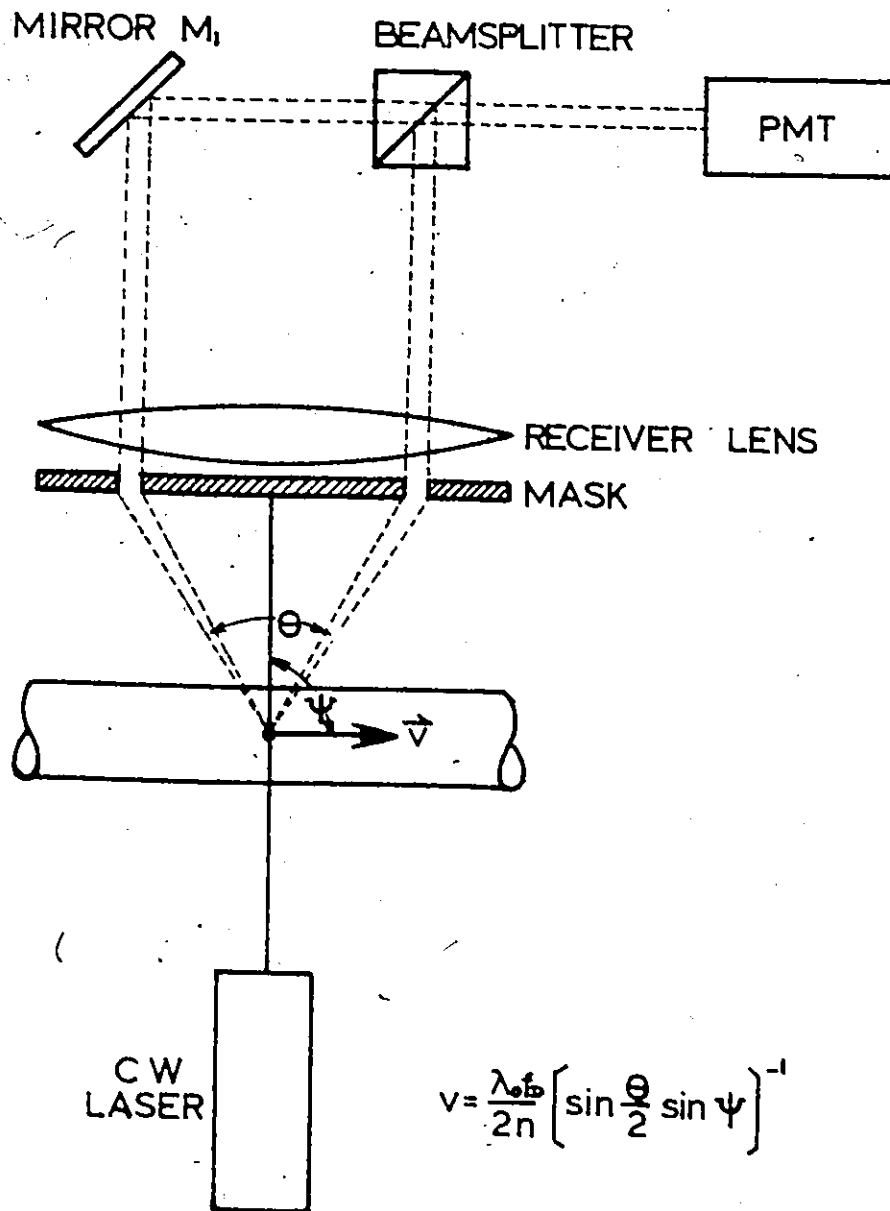


Fig. 2.5: Symmetric heterodyne system.

CHAPTER 3

DESIGN OF A DIFFERENTIAL LASER DOPPLER VELOCIMETER

This chapter describes in detail the design and operation of a differential laser Doppler velocimeter (DLDV). Considerable effort was devoted to the analysis of the system with the objective of obtaining optimum DLDV performance. The analysis covers differential heterodyning, the intensity distribution of the fringe system, the characteristics of the probe volume and its effect on frequency broadening, and the basic signal conditioning and instrumentation techniques employed.

The optical and geometrical requirement for optimum detection are analysed on the basis of the heterodyning processes. Experimental observations of the Doppler signal, its SNR, and its spectral properties are also qualitatively analysed. In addition, experimental results are presented to illustrate the importance of placing a pinhole in front of a detector.

Many of the techniques described here can also be applied to other types of optical velocimeters. This chapter, therefore, should assist in the understanding of optical velocimeter techniques in general.

3.1 The Doppler-Shift and Fringe-Crossing Phenomena of a DLDV

This section is mainly in two parts. The first describes differential heterodyning of a DLDV and its relative merits over conventional

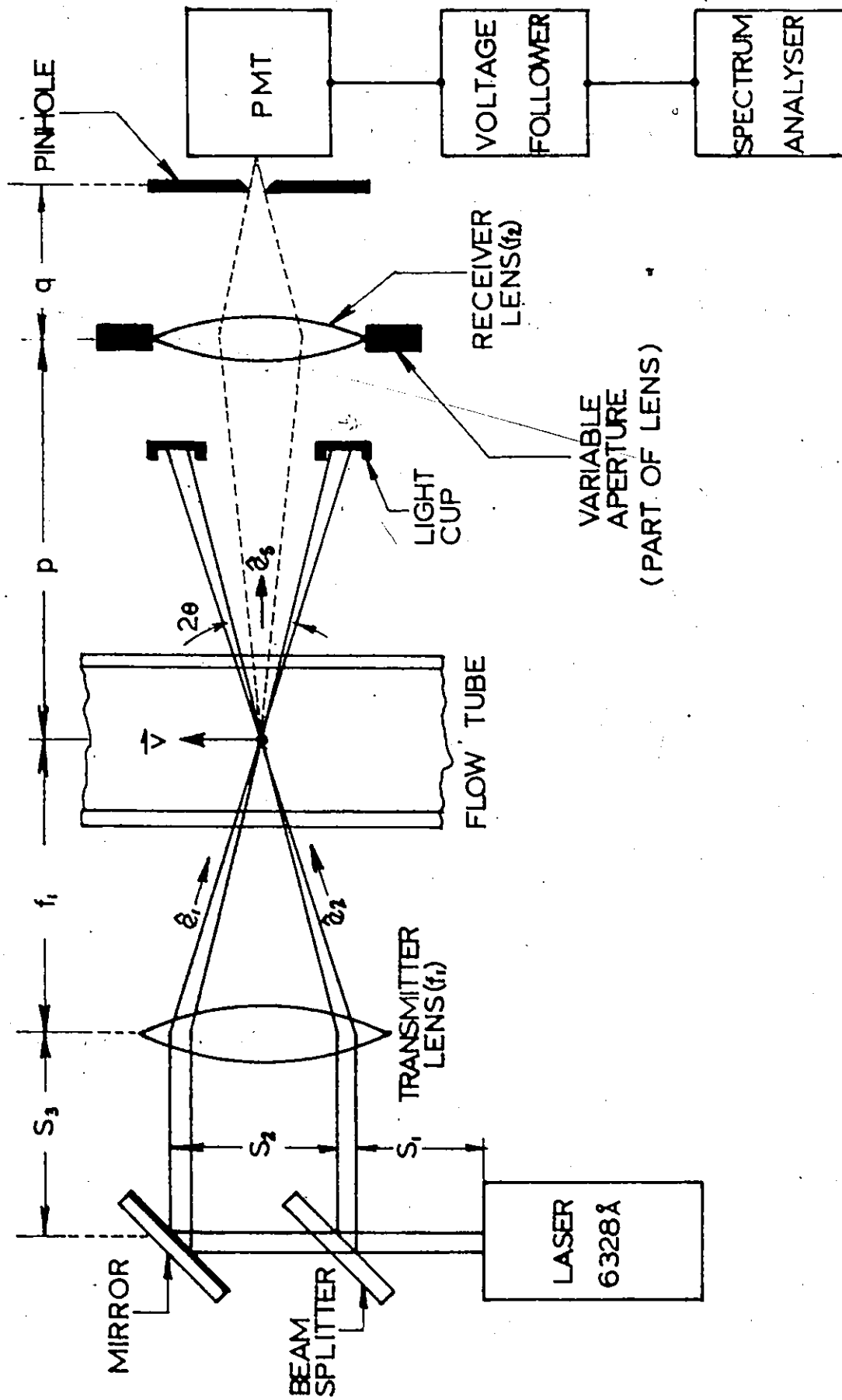
reference-beam techniques. Optical heterodyning is considered as a Doppler-shift phenomenon. The second part of this section gives a derivation of the fringe pattern formed by two intersecting beams. A particle crossing the fringes produces modulation of the scattered radiation. This we call the fringe-crossing phenomenon. The two phenomena are described independently in this section. Further studies and comparisons of their role in optical velocimeters, and their effect on SNR, are discussed in Chapters 6 and 7.

Figure 3.1 illustrates the basic system for our DLDV. A collimated beam from a He-Ne laser is split into two parallel beams of equal intensity (to within 0.5%). They are then made to intersect at an angle 2θ by means of a focusing lens. The unit vectors \hat{e}_1 and \hat{e}_2 designate the direction of beam 1 and beam 2 respectively. Consider that a particle, of velocity \vec{v} , travels across the beam-crossover region (probe volume). The light scattered by the particle generally contains components that have experienced two different Doppler shifts as a result of the different angles of scatter from beams 1 and 2. Because of the overlap, wavefronts of scattered light at the two different frequencies emanate from a common source point. Consequently, they are aligned sufficiently well to yield a useful heterodyne signal. Thus the precise alignment requirement often encountered in optical heterodyning [38] is relaxed to the easily achieved overlap requirement.

From Eq. (2.5) the Doppler shift of the radiation scattered into any particular direction \hat{e}_s from beam 1 is given by

$$(\Delta f)_1 = (n/\lambda_0)(\hat{e}_s - \hat{e}_1) \cdot \vec{v} \quad (3.1)$$

Fig. 3.1: Basic system for the DLDV. Typical values for the parameters are listed in Tables 3.1 and 3.2. Both transmitter and receiver lenses are standard 35 mm Miranda lens ($f = 50$ mm). The pinhole is placed at the image plane of the receiver lens.



Similarly, the Doppler shift of the radiation scattered from beam 2 into the direction \hat{e}_s is given by

$$(\Delta f)_2 = (n/\lambda_0)(\hat{e}_s - \hat{e}_2) \cdot \vec{v} \quad (3.2)$$

The heterodyne process that occurs during detection provides a signal that oscillates at a frequency f_D equal to the difference between these two Doppler shifts, i.e.,

$$f_D = (\Delta f)_2 - (\Delta f)_1 = (n/\lambda_0)(\hat{e}_1 - \hat{e}_2) \cdot \vec{v} \quad (3.3)$$

This frequency is independent of scattering direction. Consequently, light scattered over a wide range of directions can be collected without broadening the spectral distribution of the heterodyne signal, and therefore the detector position and aperture size can be chosen for a particular application. For example, an increase in aperture size increases the amount of scattered light collected which results in an improved SNR.

Equation (3.3) shows that the signal frequency is proportional to the velocity component in the direction of the vector $(\hat{e}_1 - \hat{e}_2)$. This direction is perpendicular to the bisector of the two intersecting beams, and lies in the plane defined by the beams. For a particle moving in the direction of $(\hat{e}_1 - \hat{e}_2)$, the signal frequency is given by

$$f_D = \frac{2nvs \sin \theta}{\lambda_0} \quad (3.4)$$

where θ is defined in the medium of refractive index n .

Doppler shifts were used to derive Eq. (3.4). However, Eq. (3.4)

can also be obtained on the basis of fringe crossings. Each laser beam forms a narrow beam in the focal region. For the ideal case, they will have a diffraction limited diameter together with a Gaussian intensity distribution. In addition, the phase fronts are essentially plane [41], as shown in Fig. 3.2. For most applications, the two radiations are mutually coherent and simultaneously polarized (or can be made so). They will interfere constructively and destructively to establish a set of closely spaced, interference planes (fringes) in the beam-cross-over region. According to Huygen's principle, the distance between the interference fringes is given by

$$d = \frac{\lambda}{2\sin\theta} \quad (3.5)$$

A particle moving with a velocity v perpendicular to the fringes will scatter radiation modulated at a frequency

$$f = \frac{v}{d} ,$$

or

$$f = \frac{2nvs\sin\theta}{\lambda_0} \quad (3.6)$$

This is identical to Eq. (3.4).

A first principle derivation of the intensity distribution of the interference pattern can be obtained in the following manner. Assume that the two illuminating beams have identical intensity and intersect in their planar phase fronts, and that the relative phase difference at the probe volume is zero. The electric field amplitudes of the Gaussian

beams are then given by [41]

$$E_1 = E_0 \exp\left(-\frac{r_1^2}{w_0^2} - i\vec{k}_1 \cdot \vec{r}\right), \quad (3.7)$$

$$E_2 = E_0 \exp\left(-\frac{r_2^2}{w_0^2} - i\vec{k}_2 \cdot \vec{r}\right), \quad (3.8)$$

where w_0 is the beam radius at $1/e^2$ intensity, \vec{k}_1 , \vec{k}_2 are the wave vectors, and \vec{r}_1 , \vec{r}_2 are the radial vectors shown in Fig. 3.2. Note that

$$\vec{k}_1 \cdot \vec{r} = kx \cos\theta + ky \sin\theta, \quad (3.9)$$

$$\vec{k}_2 \cdot \vec{r} = kx \cos\theta - ky \sin\theta \quad (3.10)$$

$$\begin{aligned} r_1^2 &= (\vec{r}_1)^2 = [\vec{r} - (\vec{r} \cdot \hat{k}_1)\hat{k}_1]^2 = r^2 - (\vec{r} \cdot \hat{k}_1)^2 \\ &= x^2 + y^2 + z^2 - (x \cos\theta + y \sin\theta)^2 \\ &= x^2 \sin^2\theta + y^2 \cos^2\theta + z^2 - xy \sin 2\theta, \end{aligned} \quad (3.11)$$

similarly,

$$r_2^2 = x^2 \sin^2\theta + y^2 \cos^2\theta + z^2 + xy \sin 2\theta, \quad (3.12)$$

where \hat{k}_1 and \hat{k}_2 are the unit vectors of the wave vectors \vec{k}_1 and \vec{k}_2 , respectively. The intensity of the total field ($E_1 + E_2$) is given by.

$$I = E \cdot E^*$$

$$\begin{aligned}
 &= [E_0 \exp(-\frac{r_1^2}{w_0^2} - i\vec{k}_1 \cdot \vec{r}) + E_0 \exp(-\frac{r_2^2}{w_0^2} - i\vec{k}_2 \cdot \vec{r})] \times \\
 & [E_0 \exp(-\frac{r_2^2}{w_0^2} + i\vec{k}_1 \cdot \vec{r}) + E_0 \exp(-\frac{r_2^2}{w_0^2} + i\vec{k}_2 \cdot \vec{r})] \\
 &= E_0^2 (\exp(-\frac{2r_1^2}{w_0^2}) + \exp(-\frac{2r_2^2}{w_0^2}) \\
 & + \exp[-\frac{(r_1^2 + r_2^2)}{w_0^2}] [2\cos(\vec{k}_1 \cdot \vec{r} - \vec{k}_2 \cdot \vec{r})]) \quad (3.13')
 \end{aligned}$$

after substitution of Eq. (3.11) and Eq. (3.12)

$$\begin{aligned}
 I &= E_0^2 \exp[-\frac{2}{w_0^2}(x^2 \sin^2 \theta + y^2 \cos^2 \theta + z^2)] [\exp(\frac{2xysin2\theta}{w_0^2}) \\
 & + \exp(-\frac{2xysin2\theta}{w_0^2}) + 2\cos(2kysin\theta)] \\
 &= 2I_0 \exp[-\frac{2}{w_0^2}(x^2 \sin^2 \theta + y^2 \cos^2 \theta + z^2)] [\cosh(\frac{2xysin2\theta}{w_0^2}) \\
 & + \cos(2kysin\theta)] \quad (3.13)
 \end{aligned}$$

Note that I_0 is the maximum intensity of one Gaussian beam at the focal plane.

The cross-section in the center of the probe volume ($x=0, z=0$) has an intensity distribution along the y -axis which is given by

$$I^* = 2I_0 \exp\left[-\frac{2y^2 \cos^2 \theta}{w_0^2}\right] [1 + \cos(2kysin\theta)] \quad (3.14)$$

Thus the interference pattern, with periodicity $\lambda/2\sin\theta$, is clearly governed by a Gaussian intensity profile. Further consideration of Eq. (3.13) will show that the first factor in square brackets corresponds to surfaces of constant intensity which are in the form of ellipsoids. In the next section, the effective probe volume will be defined in terms of one of these ellipsoids. The second factor in square brackets in Eq. (3.13) corresponds to the formation of fringes.

3.2 Characteristics of the Probe Volume

The probe volume of a DLDV can be approximately defined as the volume in which signals of significant amplitude can be generated by scatter centers located anywhere within the volume [43]. As stated in the last section, the constant intensity surface is in the form of an ellipsoid. For convenience, the probe volume can be defined by either the $1/e$ or $1/e^2$ constant intensity surface relative to the geometric center. Either of these two volumes will provide virtually all of the available signal. Note that the contribution from a volume element to a photomultiplier output is directly proportional to the corresponding elemental intensity.

From Eq. (3.13) the $1/e$ intensity ellipsoid (probe volume) is given by

$$x^2 \sin^2 \theta + y^2 \cos^2 \theta + z^2 = w_0^2 / 2 \quad (3.15)$$

where w_0 is the beam radius at $1/e^2$ intensity. Here

$$w_0 = 2\lambda F/\pi \quad , \quad (3.16)$$

where F is the "f-number" of the beam (focal length/beam diameter).

From Eq. (3.15), the dimensions of the probe volume are

$$\left. \begin{aligned} \Delta x(1/e) &= \sqrt{2} w_0 / \sin\theta \quad , \\ \Delta y(1/e) &= \sqrt{2} w_0 / \cos\theta \quad , \\ \Delta z(1/e) &= \sqrt{2} w_0 \quad , \end{aligned} \right\} \quad (3.17)$$

and the volume is

$$V(1/e) = 2 \sqrt{2} \pi w_0^3 / (3 \sin 2\theta) \quad . \quad (3.18)$$

The geometry of the above probe volume is shown in Fig. 3.3. Similarly, the ellipsoid

$$x^2 \sin^2\theta + y^2 \cos^2\theta + z^2 = w_0^2 \quad , \quad (3.19)$$

represents the $1/e^2$ intensity surface. The dimensions of this ellipsoid are

$$\left. \begin{aligned} \Delta x(1/e^2) &= 2w_0 / \sin\theta \quad , \\ \Delta y(1/e^2) &= 2w_0 / \cos\theta \quad , \\ \Delta z(1/e^2) &= 2w_0 \quad , \end{aligned} \right\} \quad (3.20)$$



Fig. 3.3: Ideal probe volume. Signals of significant amplitude are generated by scatter centers located within the volume. Two ellipsoids are defined. The $1/e^2$ ellipsoid passes through the intersection of the $1/e^2$ intensity profiles of the two beams, while the $1/e$ ellipsoid is tangent to the $1/e^2$ intensity profiles.

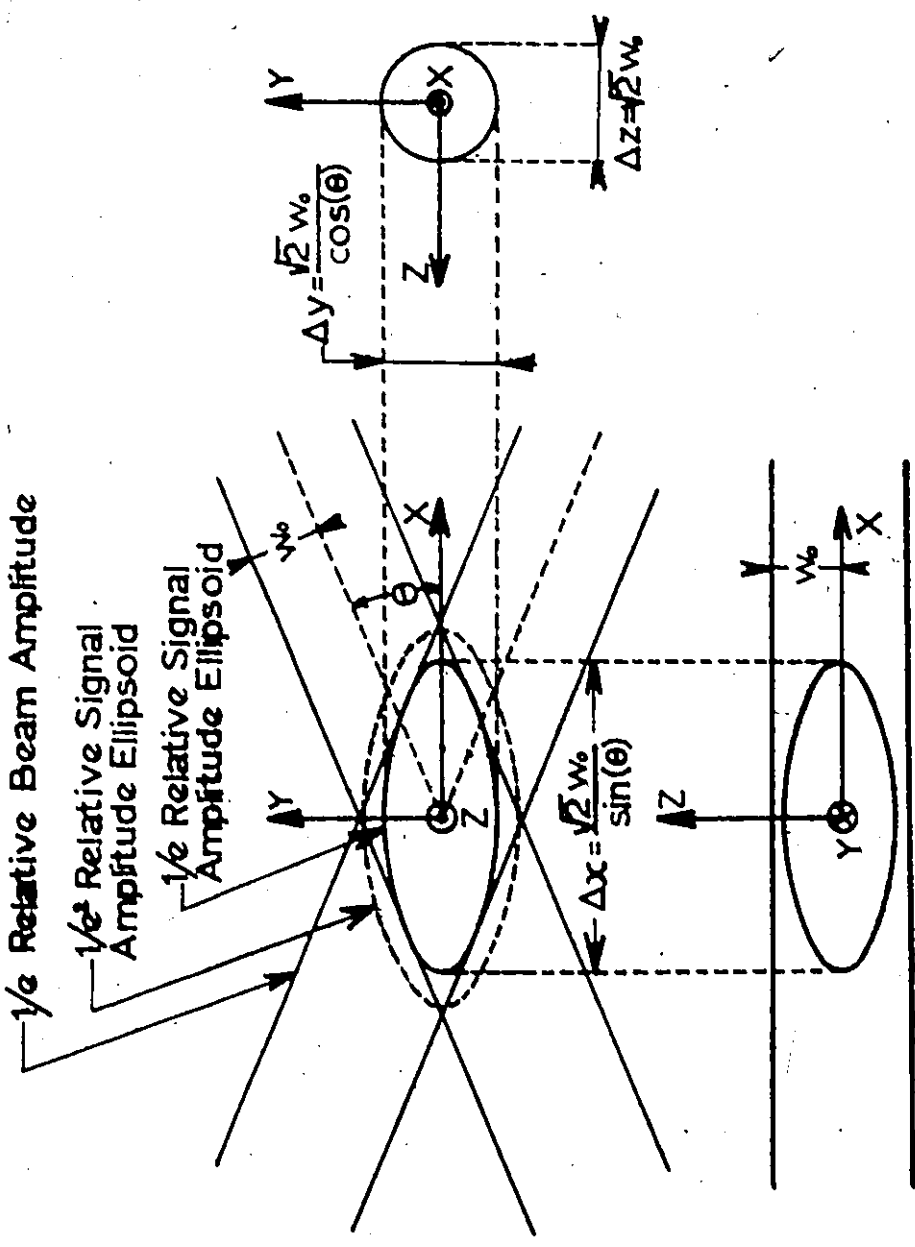


Fig. 3-3

and the volume is

$$V(1/e^2) = 8\pi w_0^3 / (3\sin 2\theta) \quad (3.21)$$

This volume is about three times as large as the one previously defined by Eq. (3.18). Its geometry is shown in Fig. 3.3.

Note that the probe volumes described above are for the ideal case of planar phase fronts. However, the probe volume is not governed solely by planar phase fronts. Kogelnik [41] has shown that when a Gaussian beam passes through a lens, it will be transformed into another Gaussian beam whose minimum beam waist is not generally located at the focal plane of the lens. The position and the radius of the new beam waist are given by [41]

$$z_2 = f + (z_1 - f)f^2 / \{(z_1 - f)^2 + (\pi w_1^2 / \lambda)^2\} \quad (3.22)$$

and

$$1/w_2^2 = (1/w_1^2)(1 - z_1/f)^2 + (1/f^2)(\pi w_1/\lambda)^2 \quad (3.23)$$

where z_1 and w_1 are the input parameters as defined in Fig. 3.4(a), and f is the focal length of the lens. The beam radii w_{1f} and w_{2f} in the two focal planes of the lens are given by

$$w_{1f} = \lambda f / (\pi w_2) \quad (3.24)$$

$$w_{2f} = \lambda f / (\pi w_1) \quad (3.25)$$

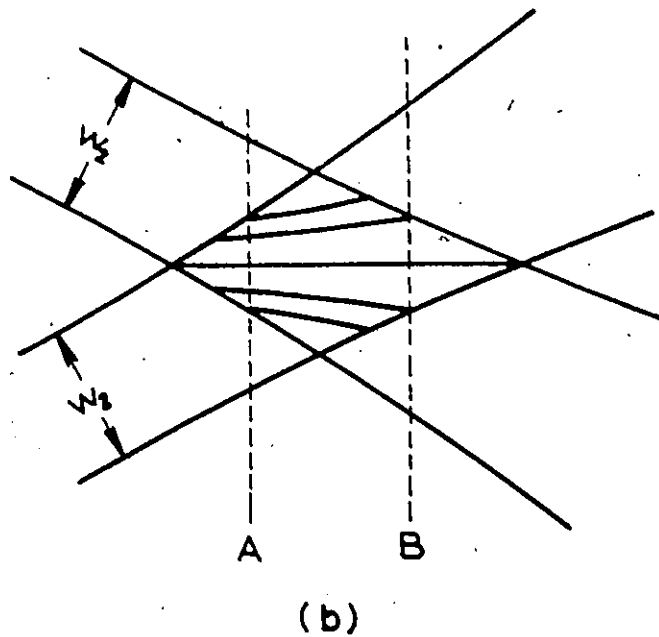
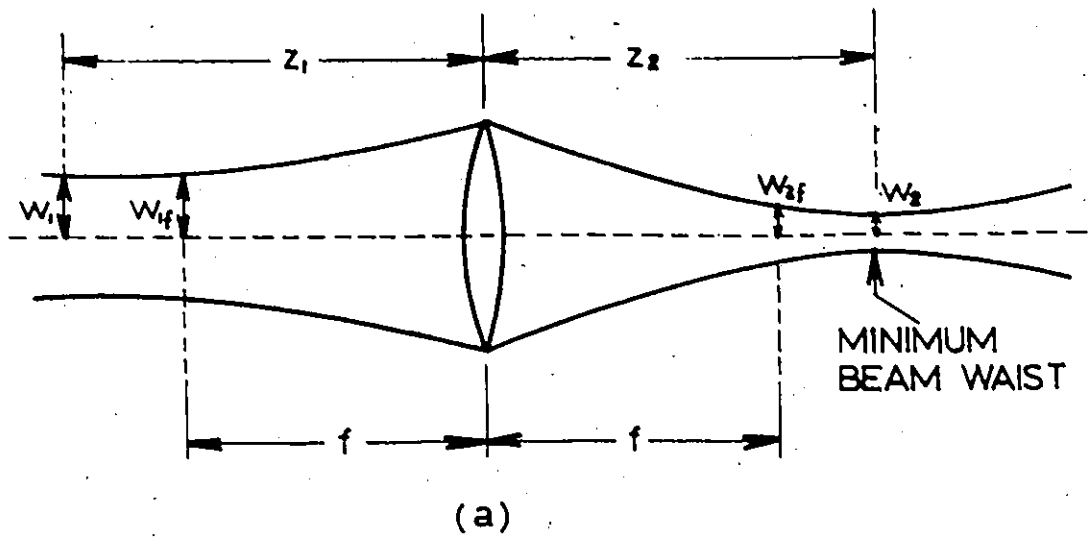


Fig. 3.4: Properties of Gaussian beam. (a) Gaussian beam transformed by a lens; (b) Fringe pattern formed by two intersecting Gaussian beams. Generally, the two beams do not intersect at their minimum beam waists. Note that the fringe spacing at plane A is smaller than that at plane B.

As before, all beam radii are defined at the $1/e^2$ intensity circumference of the Gaussian beam. Consideration of Eq. (3.22) shows that when two parallel beams are brought to focus by a lens, the two beams do not necessarily cross at their minimum beam waists. The wave fronts are only planar at the minimum beam waist. Consequently, a particle traversing the probe volume at plane A in Fig. 3.4(b) will radiate with a higher frequency than a particle traversing at plane B. This results in frequency broadening of the Doppler spectrum.

For a given system it is possible to calculate the frequency shifts due to the fringe spacing gradients [42]. In practical applications, however, they can be minimized by adjusting some of the geometrical parameters. One method is to deviate the collimated beams from parallelism until the two beams cross at their minimum beam waists. In some applications, this can be done with the aid of a microscope. Another method is to make the laser-to-lens distance, z_1 , equal to the focal length, f , of the lens. This is readily seen from examination of Eq. (3.22).

Although the frequency broadening due to the gradients of the interference pattern can be virtually eliminated, that due to the finite time of the scattering particles can not. According to Rudd [17] the inherent Doppler width is approximately given by

$$\frac{\Delta f_D}{f_D} = \frac{1}{N} \quad (3.26)$$

where N is the number of fringes crossed by the particles. (In the terminology of the Doppler-shift phenomenon, the equivalent equation is

given by $\Delta f_D = 1/\tau$, where τ is the transit time of the particle). This frequency broadening is inherent to all optical velocimeters. Its effect on the resolution of optical velocimeters is discussed in Chapter 5.

3.3 Analysis of the Heterodyning Processes in a Dual-Beam System

The various heterodyning processes must be first understood before optimum conditions can be found for a dual-beam system. Figure 3.5 is included to assist in explaining these processes. For convenience, the probe volume is placed in the center axis of a flow tube (the fringe pattern is not shown). The velocity profile is assumed to be symmetrical about the axis. Thus, all particles traversing at an equal distance from the axis possess identical velocities. The heterodyning processes are classified into four categories according to the source of scattered radiation, as follows.

(A) Radiation is scattered from an individual particle which is simultaneously illuminated by the two laser beams. A particle moving through the probe volume, such as A_1 in Fig. 3.5, belongs to this category. This process, often referred to as homodyning, is the ideal process for a differential heterodyne system. Here no size limitation is imposed on the receiver. The detector output signal frequency peaks at, and spreads about, the frequency $f_D = n\vec{v}_0 \cdot (\hat{e}_1 - \hat{e}_2)/\lambda_0$, where \hat{e}_1 , \hat{e}_2 are the unit vectors as defined in Eq. (3.3). Note that there is generally more than one particle in the probe volume. The electric fields may add randomly or coherently depending on how well the coherent


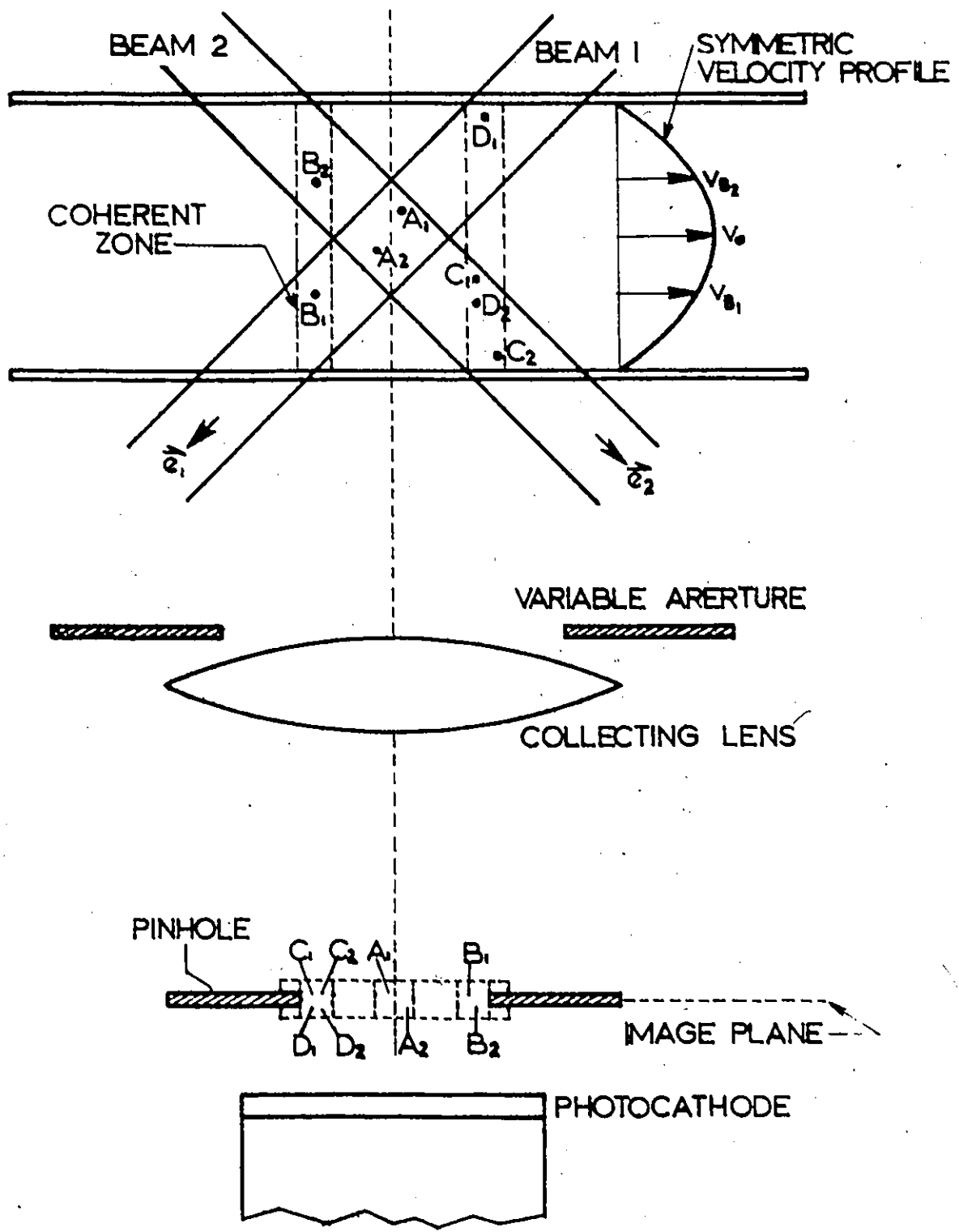


Fig. 3.5: Heterodyning processes in a DLDV. Four heterodyning processes are classified in the text. The processes can be simultaneously detected unless a proper field aperture is placed in front of the detector. In practice the optimum pinhole will only pass radiation scattered from the probe volume.

Fig. 3-5



condition is fulfilled. Heterodyning of signals scattered from two different particles in the probe volume is treated in category (D).

(B) Radiation is scattered from equal-velocity particles (i.e., symmetrically located about the axis). In this case, each particle is illuminated by a different beam, e.g., particles B_1 and B_2 in Fig. 3.5. Note that although both particles are separated by a significant distance, they are still capable of being efficiently heterodyned because the coherent condition is fulfilled. Since particles can be observed with velocities from 0 to v_0 , the signal frequency ranges from $f = 0$ to $f = n\vec{v}_0 \cdot (\hat{e}_1 - \hat{e}_2) / \lambda_0$. Particle pairs such as B_1 and D_2 are less likely to fulfill the coherent condition.

(C) Radiation is scattered from particles of different velocity which are illuminated by a single beam. Particles C_1 and C_2 in Fig. 3.5 are an example. The coherence requirements are the same as those for category (B). In this case, the signal frequency peaks at, and spreads about, $f = 0$.

(D) Radiation is scattered from particles of different velocity which are illuminated by two different beams. Particles D_1 and D_2 in Fig. 3.5 belong to this category. The coherence requirements are the same as those for category (B). The signal frequency can range from $f = 0$ to $f = f_D$. The highest frequencies correspond to particles inside the probe volume, such as particles A_1 and A_2 . For the special case where the velocities of a pair of particles are identical (e.g., A_1 and A_2), the process falls into category (B).

The above are the four heterodyning processes which can generally

take place in a DLDV. However, observed signals are more complicated. All the above processes can occur simultaneously and, in addition, the scattered radiation is influenced by random particle motion and multiple scattering. Theoretical and experimental investigations of categories (A) and (D) are presented in Chapters 6 and 7.

It should be noted that only category (A) produces a homodyne signal frequency. The other categories exhibit broad range of signal frequencies from $f = 0$ to $f = f_D$. Consequently, to obtain a well-defined frequency spectrum requires that any processes other than (A) must be rejected. This can be achieved by inserting a field aperture or pinhole in the image plane of the receiver system as shown in Fig. 3.5. The pinhole should be chosen so that only radiation scattered from the probe volume is collected. Theoretically, the diameter of the pinhole is

$$d_{ph} = M\Delta y(1/e^2) \quad , \quad (3.27)$$

where M is the magnification (or reduction) factor of the receiver system and $\Delta y(1/e^2)$ is the diameter of the probe volume as given by Eq. (3.20). It is shown experimentally in section 3.6 that the optimum pinhole diameter is usually larger than that given by Eq. (3.27) because of lens aberrations.

3.4 Signal Conditioning and Instrumentation

Since the main purpose of this research was to study the basic property of the optical heterodyning and of the fringe-crossing phenomena,

relatively sophisticated signal conditioning techniques were neither employed or required. The frequency spectrum of interest ranges from dc to above the Doppler shift frequency. In the range of interest, signal conditioning which could in any way alter the power spectrum was carefully avoided.

Basically, for the measurements, one requires a PMT, a broadband voltage follower (or preamplifier) and a spectrum analyser, as illustrated schematically in Fig. 3.1. The functions and characteristics of these components are briefly described in the following.

3.4.1 Photomultiplier Tube (PMT)

The conventional PMT generally consists of three main sections: a photoemissive cathode, a photoelectron focusing assembly, and a series of dynodes as shown schematically in Fig. 3.6. The ultimate frequency response of a PMT is limited by transit time spread [31]. This limit is well above any frequencies used in our experiments. However, the practical limit is governed by the time constant of the load resistor, R_L , and capacitance, C_p , associated with the anode lead. The 3-dB attenuation frequency is given by

$$f_c = \frac{1}{2\pi R_L C_p} \quad (3.28)$$

Note for our work, f_c was always less than 200 kHz; an R_L of 50 k Ω was found to be satisfactory.

It was shown in section 2.2 that the output of a PMT consisted of a dc component proportional to $(E_1^2 + E_2^2)/2$, and a cosinusoidally

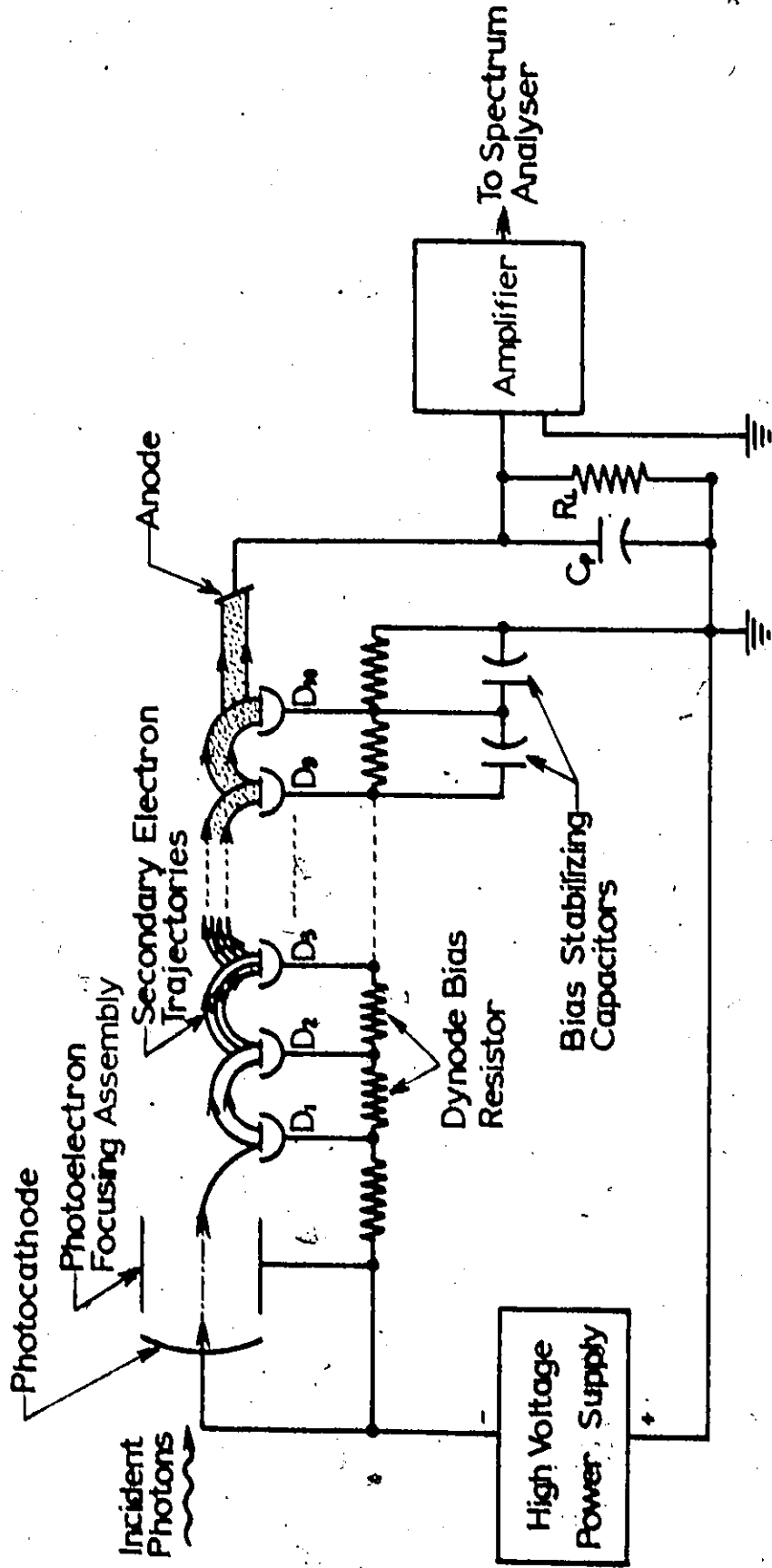


Fig: 3.6: Schematic representation of a PMT.

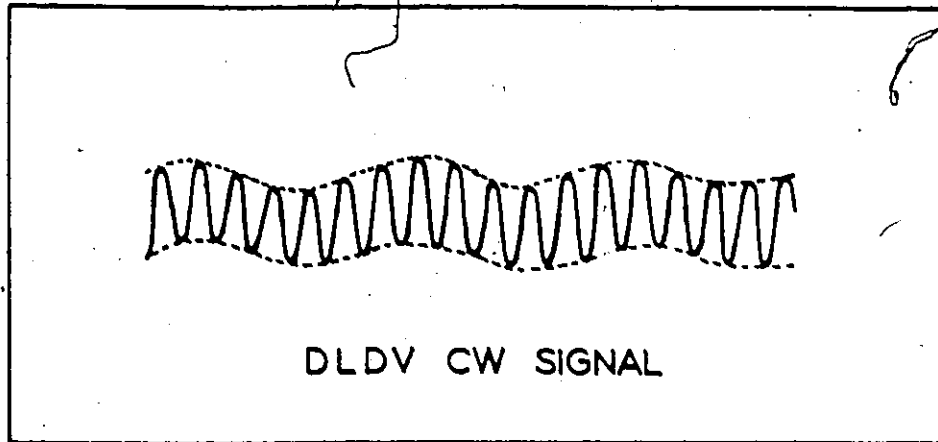
varying current proportional to $E_1 E_2 \cos 2\pi(f_1 - f_2)t$. The latter is associated with the Doppler shift frequency. Gain saturation of the PMT can be avoided if the dc component is checked during measurements.

If a large number of scattering particles are always present in the probe volume, then a continuous wave (cw) signal will be produced at the PMT output, as shown in Fig. 3.7(a). When the scattering particle density is very small, the DLDV signal is characterized by bursts of Doppler frequency information superimposed upon a pedestal voltage, as shown in Fig. 3.7(b). The Gaussian shape of the signal follows the Gaussian intensity variation across the incident laser beam. The pedestal voltage arises from the dc component of the PMT current and represents a severe signal-conditioning problem. The ratio of Doppler signal (volts peak-to-peak) to pedestal voltage level (volts) approaches unity for scatter particles passing through the center of the probe volume, but rapidly decreases for scattering particles near the edges of the probe volume. This is explained by the fact that the two illuminating beam intensities are equal at the geometric center of the probe volume, but are quite disproportionate at the edges of the probe volume.

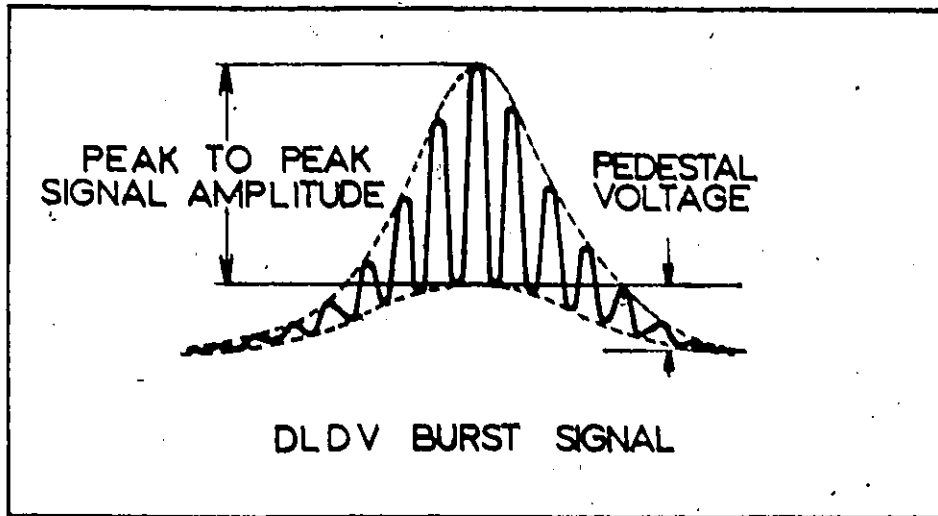
Two PMT's were employed; an EMI 6256S and a RCA 6199. Both have approximately equal quantum efficiencies at 6328 \AA ($\approx 0.5\%$). The former, however, has much higher gain and much lower dark current.

3.4.2 Impedance Matching Amplifier

Since the frequency bandwidth required is not too great, a gain in PMT output signal amplitude can be obtained by the use of a



(a)



(b)

Fig. 3.7: DLDV signals as observed on an oscilloscope. (a) CW signal for a large number of particles passing through the probe volume; (b) Burst signal for a single particle passing through the center of the probe volume.

relatively high load resistance. However, the spectrum analyser employed has an input impedance of 50 ohms. Therefore a voltage follower (Fairchild IC 310) having approximately a 3 MHz bandwidth was used for impedance matching. With reference to Fig. 3.8, the voltage follower has an input impedance which is essentially resistive, and close to R_1 , and an output impedance which is essentially zero.

3.4.3 Spectrum Analyser

Two spectrum analysers were used; a Hewlett-Packard 8553B/8552B and a Hewlett-Packard 3580 A. The former has a frequency range of 1 kHz to 110 MHz, and a resolution of 20 Hz. The latter has a frequency range of 50 Hz to 50 kHz, and a resolution of 1 Hz.

3.4.4 Noise Sources

For our studies, noise can be classified into three basic types: 1-shot noise, 2-thermal noise, and 3-any other unwanted noise levels which are significant compared to the desired signal. Type 3 noise includes laser intermode beat signals and extraneous radiation sources. Type 3 noise, however, will not be treated here.

1(a) - PMT dark current shot noise establishes the lower limit for detection. Thermionic electron emission from the photocathode is the principal source of the dark current. This current (per unit area of the photocathode) is given by the Richardson equation [44]

$$i_d = AT^2 \exp\left(-\frac{e\phi_{th}}{kT}\right) \quad (3.29)$$

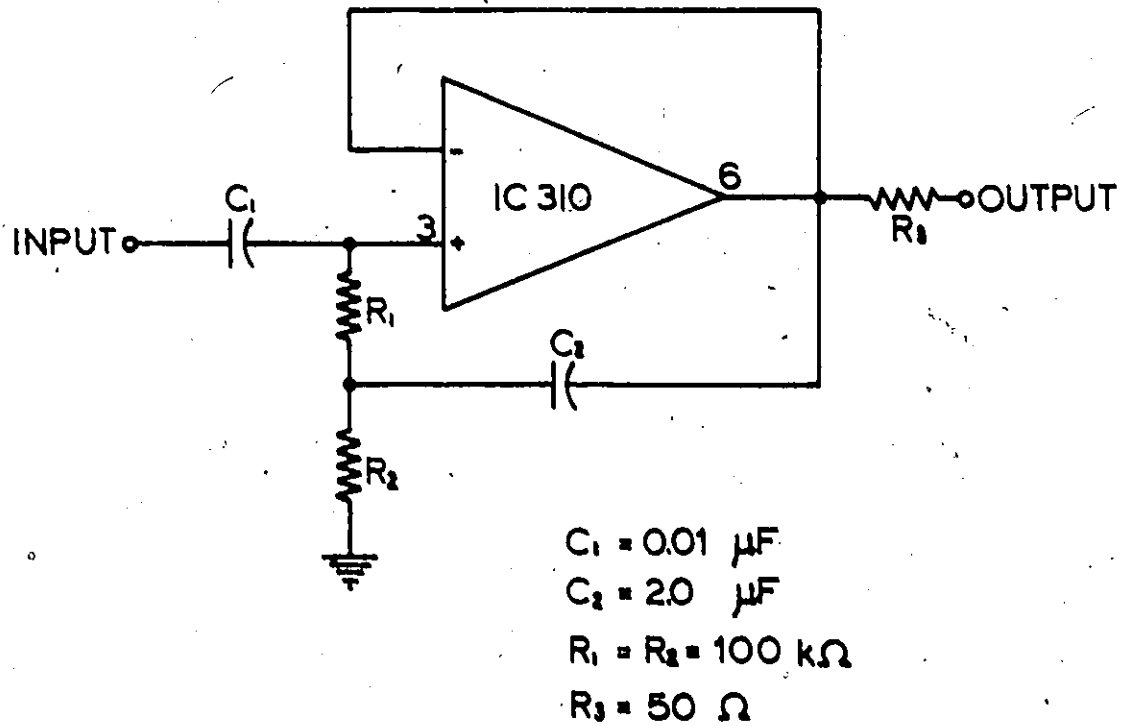


Fig. 3.8: Basic circuit for impedance matching amplifier. The input impedance is $\approx 100 \text{ k}\Omega$ while output impedance is $\approx 50 \Omega$.

where T is the absolute temperature in $^{\circ}\text{K}$ and ϕ_{th} is the thermionic work function of the photocathode material. The rms anode current due to dark current shot noise is given by [45]

$$i_D = \mu [2ei_d (1 + \frac{\beta}{\delta - T}) B]^{1/2}, \quad (3.30)$$

where μ is the PMT amplification factor, β is an empirical statistical factor (≈ 1.5), δ is the dynode secondary emission ratio, and B is the measurement bandwidth.

1(b) - Signal shot noise is caused by the random nature of the photoemission and secondary emission processes. These produce a rms noise current at the PMT anode of

$$i_S = \mu [2ei_s (1 + \frac{\beta}{\delta - T}) B]^{1/2}, \quad (3.31)$$

where i_s is the rms signal current.

2 - Thermal noise (Johnson noise) occurs in the PMT load resistor, R_L . The rms voltage produced across R_L by the Johnson noise is given by the Nyquist formula

$$V_T = [4kTR_L B]^{1/2}. \quad (3.32)$$

Note that the thermal noise power is independent of R_L .

Under normal operating conditions the signal shot noise is significantly greater than the other sources of noise. However, the latter determines the minimum useful scattering power for velocity measurements. A general discussion of SNR is provided in section 2.2.

3.5 Experimental Configuration for the DLDV

The basic parameters of the DLDV have been described in the last few sections. These parameters include the characteristics of the probe volume, the classification of the heterodyning processes, and the techniques of signal conditioning and instrumentation. In this section we consider the complete experimental configuration of the system. Its performance is assessed in the next section.

The major commercial instruments employed for the DLDV are listed in Table 3.1. Most of the equipment is also used for the other types of optical velocimeters discussed in later chapters of this thesis. Details of the optical alignment and determination of some of the beam parameters for a DLDV are presented in three parts. These are (a) the transmitting system, (b) the flow system, and (c) the receiving system. Unless otherwise stated, the following discussion refers to the arrangement in Fig. 3.1.

(a) The transmitting system consists of a laser source, a beam divider, and a focusing lens. The He-Ne laser, providing 2.5 mW at 6328 \AA , was operated in the TEM_{00} mode. The beam was non-polarized and its intensity had a Gaussian cross-section. In addition, it was determined by means of a Fabry-Perot interferometer that four axial modes were operating. Because of this small number, and because the optical path length difference ($\approx 2 \text{ cm}$) is small compared to the length of the optical cavity ($\approx 40 \text{ cm}$), the loss in the heterodyning is small (as evaluated from Fig. 2.1). Consequently, no further effort was made to equalize the two path lengths.

Table 3.1: Some Commercial Instruments Used for the Optical Velocimeters.

Instrument	Manufacturer
Optical table (4' x 10')	Newport Research Corp., Model RS-410
He-Ne Laser (2.5 mW)	Metrologic Model 920
3-dimensional translators	Metrologic
Beamsplitter ($\lambda/20$, R=T)	Oriel
Mirror ($\lambda/20$)	Oriel
Pinholes	Oriel
Interference filter ($\lambda=6328\text{\AA}\pm 5\text{\AA}$)	Oriel
35 mm camera lenses	Miranda, f = 50 mm Soligor, f = 135 mm
Photomultiplier Tubes (S-11 response)	EMI 6256S, RCA 6199
Photomultiplier H.T. Supplies	Fluke 415B
Voltage Follower	Fairchild IC 310
Oscilloscope	Tektronix Type 547
Electronic Counter	Hewlett Packard Model 5245
Signal Generator (0-600 kHz)	Hewlett Packard Model 200 cd
Oscilloscope Camera	Hewlett Packard Model 197A
Spectrum Analyser (1 kHz - 110 MHz)	(i) Hewlett Packard 141T Display section 8553B RF section 8552B IF section
Spectrum Analyser (5 Hz - 50 kHz)	(ii) Hewlett Packard 3580A

An important parameter of a DLDV is the laser beam diameter. Approximate values only are found in the laser specification; accurate values can only be obtained from measurements. For practical reasons, the diameter was measured indirectly employing the following technique.

Neglecting the time variation, the intensity of a Gaussian beam at a radius r is

$$I = I_0 e^{-\frac{2r^2}{w^2}} \quad (3.33)$$

where w is the beam radius at $1/e^2$ intensity. The total power of the beam, integrated over the infinite radius, is

$$\begin{aligned} P_0 &= \int_0^{\infty} 2\pi I r dr \\ &= \int_0^{\infty} 2\pi I_0 e^{-\frac{2r^2}{w^2}} r dr \\ &= \pi w^2 I_0 / 2 \end{aligned} \quad (3.34)$$

If now the beam is passed concentrically through a circular aperture of radius R , then the transmitted power is

$$\begin{aligned} P(R) &= \int_0^R 2\pi I_0 e^{-\frac{2r^2}{w^2}} r dr \\ &= \frac{\pi w^2 I_0}{2} \left[1 - e^{-\frac{2R^2}{w^2}} \right] \\ &= P_0 \left[1 - e^{-\frac{2R^2}{w^2}} \right] \end{aligned} \quad (3.35)$$

Experimental measurement of P_0 and $P(R)$ allows determination of w by use of the equation

$$w = \frac{\sqrt{2R}}{\sqrt{\ln\left(\frac{1}{1-t}\right)}} \quad (3.36)$$

where $t = P(R)/P_0$. Thus the problem of measuring the beam radius becomes that of measuring the power ratio t , and the radius R . For our measurement a 1 mm diameter pinhole was employed. The pinhole was aligned concentrically with the laser beam by displacing it to give maximum detector output. Subsequently, the pinhole was removed, and the beam power measured. From the ratio t and Eq. (3.36) yielded an average beam radius $w = 0.06 \pm 0.005$ cm.

The beam divider consists of a high quality beamsplitter and front surface mirror (both 50.8 mm diameter and better than $\lambda/20$). Measurements indicated that the two resultant beams were of equal intensity to within 0.5%. In other measurements, the short term and long term intensity variations of the laser source were about 1% and 5%, respectively. The measurements were made after the laser had been operated for a minimum of two hours.

The two beams were first made parallel with the aid of a screen located several meters from the beam divider. A standard 35 mm camera lens (Miranda, $f = 50$ mm) was employed for focusing into the probe volume. Such a lens provides relatively high optical quality at a reasonable cost. Considerable care was taken to ensure that the two beams crossed at their minimum beam waists. Firstly, the laser-to-lens

distance ($S_1 + S_3 = 18$ cm, Fig. 3.1) was kept as small as possible as discussed in section 3.2. Secondly, the fringe pattern was projected on a screen by means of a X40 microscope objective lens. In most cases, the two beams were observed to intersect at approximately their minimum beam waists, and no further adjustment was required. Any final adjustment, when necessary, was carried out by means of fine pitch screws on the beam divider.

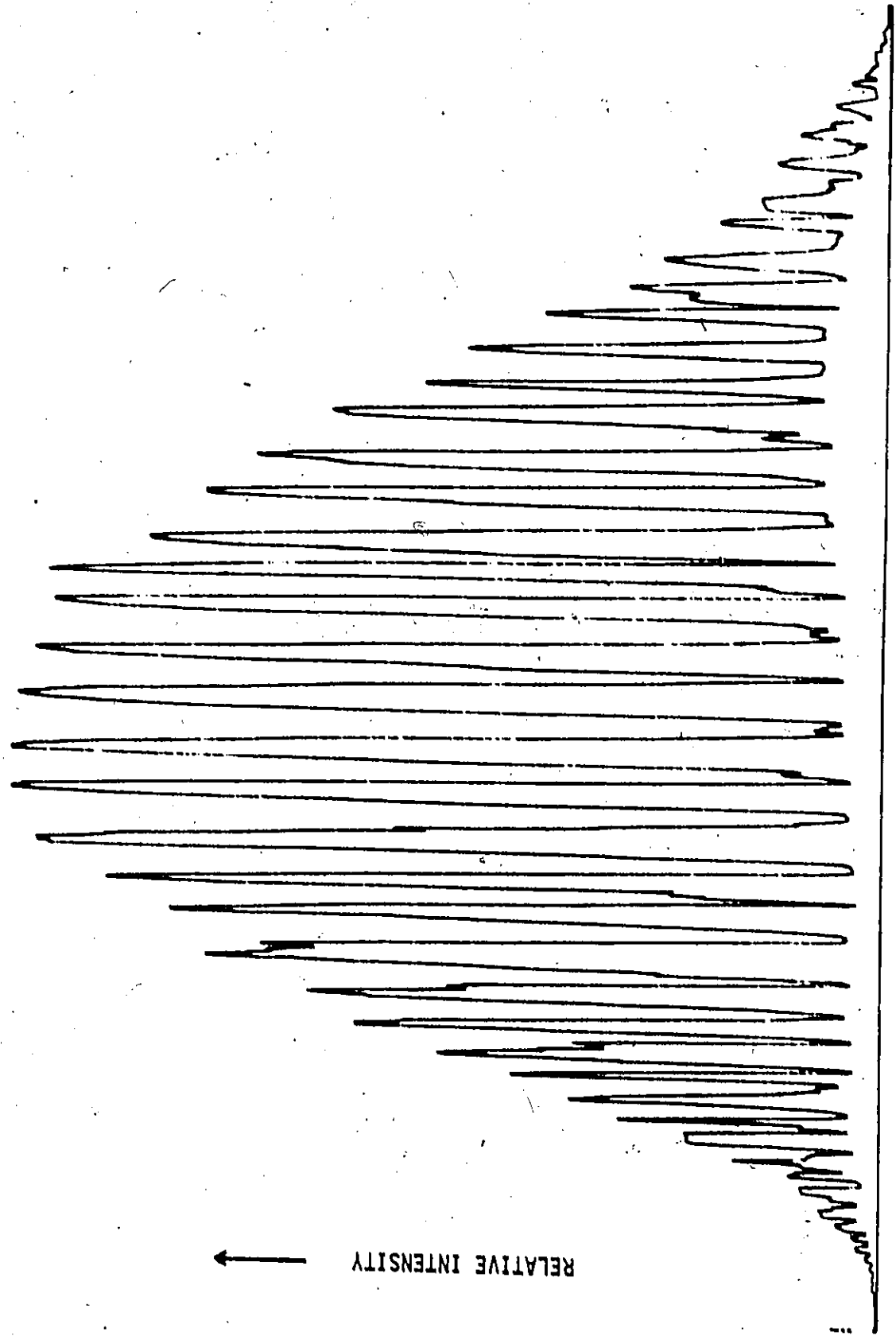
A more accurate method to observe beam intersection is by scanning the pattern with a pinhole. The scanned output should exhibit a Gaussian intensity distribution envelope. A typical scan of a fringe image is shown in Fig. 3.9. Note that the intensity distribution is close to Gaussian, as expected. Because of the manual scanning procedure used, the fringe spacings are somewhat distorted. However, the figure does illustrate that the two beams are indeed intersecting.

(b) A full description of the flow system is presented in Chapter 5. For the present, we need only note that the test section is a 30 cm length of straight, precision-bore square glass tubing, of internal dimension of 1 cm. Depending on the experiment, either a constant-head flow system or a gravitational-feed flow system was employed. The flow fluid consisted of de-ionized water seeded with a controlled quantity of polystyrene particles. Unless otherwise stated, all measurements refer to the center of the flow tube.

(c) The receiving system consists of two light cups, a collection lens, a pinhole (field aperture), and an interference filter. The PMT and its auxiliary equipment can be regarded as part of the receiving

Fig. 3.9: Photomultiplier output of a scanned DLDV fringe pattern.

The image of the beam-crossover region was projected into the image plane by means of a X40 microscope objective. The photocathode illumination was limited by a 50 μm pinhole located on the PMT assembly. The whole assembly was mounted on a x-y-z translation stage. The assembly was scanned manually to move the pinhole along the fringe axis in the image plane. The recorder trace is linear with time. Consequently, any variations in fringe spacing observed in the figure are not present in the crossover region.



system. These were discussed in section 3.4.

The purpose of the light cups is to block the direct beams from entering the detector at all detection angles. This helps prevent photocathode damage.

A second Miranda lens ($f = 50$ mm) was employed for the collection lens. Its effective f -number (lens-to-image) could be adjusted in the range 2.6 to 22. These values were obtained from multiplying the engraved f -number with a close-up correction factor [46]. For an object which is at a distance of S times the focal length, the correction factor is given by $S + (S - 1)$, which in our case was usually 1.37. The lens-to-object (probe volume) distance was primarily established by the antenna theorem. The criterion used was that the $f/22$ collection aperture should satisfy the coherent condition. Other parameters related to the coherent area and the collecting lens are given in Table 3.2.

A pinhole, approximately 35 μm in diameter, was placed at the image point of the receiver lens. This diameter was found experimentally to give the best performance in terms of the observed Doppler spectrum and the power SNR. Radiation passing through the pinhole was filtered by a 10 \AA full-width at half-intensity bandwidth interference filter. It was then made incident on the cathode of the PMT (EMI 6256S).

The collecting lens and the PMT are both mounted on a bar which can be rotated $\pm 65^\circ$ about a vertical axis passing through the probe volume. The zero degree reference corresponds to the bisector of the two intersecting beams. The angles could be determined with an accuracy of $\pm 1/4^\circ$.

Table 3.2: The Optical and Geometrical Parameters for the DLDV

(A) Transmitting System

(1) TEM ₀₀₄ laser beam radius:	$w_1 = 0.06 \pm 0.005$ cm
(2) Laser-to-transmitter lens distance:	$S_1 = 6$ cm, $S_2 = 2$ cm, $S_3 = 12$ cm
(3) Transmitter lens focal length:	$f_1 = 5$ cm
(4) Flow tube diameter:	$w = 1$ cm
(5) Beam crossing half angle:	$\theta_0 = 11^\circ 20' \pm 15'$
(6) Minimum beam waist (radius):	$w_0 = 16.8$ μ m
(7) Probe volume parameters:	(i) $\Delta x(1/e) = 120.9$ μ m $\Delta y(1/e) = 24.2$ μ m $\Delta z(1/e) = 23.7$ μ m $V(1/e) = 3.644 \times 10^{-8}$ cm ³ (ii) $\Delta x(1/e^2) = 171$ μ m $\Delta y(1/e^2) = 34.3$ μ m $\Delta z(1/e^2) = 33.6$ μ m $V(1/e^2) = 1.031 \times 10^{-7}$ cm ³
(8) Fringe spacing:	$d = 1.61$ μ m
(9) Fringe numbers:	(i) Calculated: $N(1/e^2) = 21.3 \pm 2$ (ii) Measured: $N(1/e^2) = 23 \pm 2$

(B) Receiving System

(10) Receiver lens focal length:	$f_2 = 5$ cm
(11) Object-to-lens distance:	$p = 18$ cm
lens-to-image distance:	$q = 7$ cm

(continued)

Table 3.2: The Optical and Geometrical Parameters for the DLDV (continued)

Magnification factor:	M = 0.4		
(12) Pinhole diameter:	35 μm		
(13) Receiver apertures:	as below		
Engraved f-number	Effective f-number	Aperture Diameter	
16	22	0.31cm	
1.9	2.6	2.6 cm	

Note: The f/22 aperture satisfies the coherent condition $An \leq \lambda^2$.
 Here n is calculated from $n = \pi(\Delta y)^2/4p^2$, where Δy and p are defined above by (7) and (11), respectively, and A is the receiver aperture area.

Table 3.2 is a summary of the optical and geometrical parameters, together with typical values. Figure 3.1 or Fig. 3.3 may assist in defining some of the parameters. Both the laser beam radius and the beam crossing angle ($2\theta_0$) are measured quantities. Most other parameters are calculated from these two measured values. The general agreement between theory and experiment on the fringe number indicates that the calculated parameters are reliable to within the experimental error ($\pm 10\%$ of the beam radius).

3.6 Optimum Detection Conditions for DLDV

In section 3.3 we discussed the use of a pinhole to select a desired heterodyning process. Here we will describe in detail how the pinhole size was chosen and aligned, and then describe its effect on SNR, on spectral quality, and on spectral broadening. The optimum detection criteria are described and analysed on the basis of experimental results.

The selection of a pinhole is best achieved experimentally by using a range of pinhole diameter. Because of spherical aberration, for example, the ideal pinhole diameter calculated from Eq. (3.27) can only be regarded as a limiting value. In most cases, the probe volume / image is enlarged from the ideal size. The PMT, together with a pinhole, was mounted on an x-y-z translation stage so as to allow alignment of the pinhole with the image of the probe volume. The photomultiplier output was fed through a voltage follower into a spectrum analyser. Alignment was achieved by obtaining the maximum available

SNR through adjustment of the translation stage. The maximum SNR will always be achieved when the image of the probe volume is located at the pinhole.

The maximum SNR corresponding to each pinhole employed was observed and recorded. Table 3.3 lists the power SNR for different receiver apertures and particle concentrations. A gravitational-feed flow system was employed for the measurements. Each SNR was taken from the ratio of the peak signal to the mean value of the baseline. The latter is obtained when the flow rate is reduced to zero, all other detection parameters remaining constant. For most measurements, unless otherwise stated, the "log display" of the spectrum analyser was employed. Therefore, the SNR can be readily obtained from the vertical scale of the display, which is calibrated for 10 dB/cm. Note that the SNR of a well-aligned DLDV is independent of the total dc current provided the signal shot noise is larger than that of the electronics. This is usually achieved by having sufficient PMT gain. In most of our measurements, the signal shot noise (the base line) was about 35 dB above that of the electronics.

Generally speaking, the SNR improves by about 6 dB in going from a large pinhole to one having a diameter of about 100 μm (Table 3.3). There is no improvement in SNR when the pinhole is made smaller. However, a good SNR is not the only requirement for velocity measurements. Spectral quality also has to be considered. The effect of the pinhole on the spectral quality is quite remarkable. Comparison of the spectra taken with different pinholes are shown in Fig. 3.10. In all cases, the PMT voltage was adjusted to give similar dc anode current.

Table 3.3: The Effects of Pinhole Diameter and Receiver Aperture on the Power SNR of a DLDV.

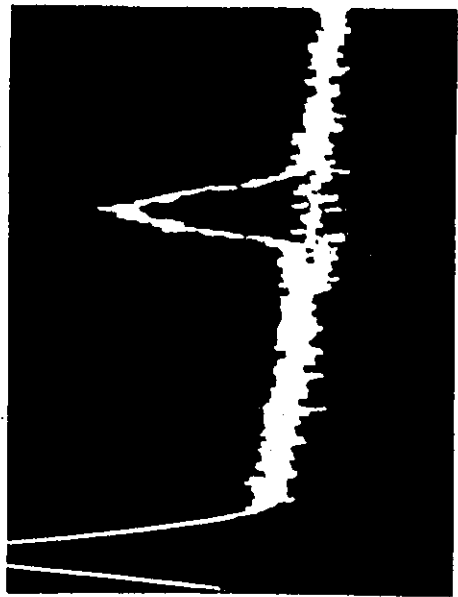
Particle Concentration (wppm)	Pinhole Diameter (μm)	SNR for f/2.6 Receiver Aperture (dB)*	SNR for f/22 Receiver Aperture (dB)*
25	5000	24	25
25	1000	25	26
25	250	27	28
25	100	31	31
25	35	31	31
25	25	31	31
25	10	29	29
0.2	5000	12	7
0.2	100	18	12
0.2	35	18	12

*The accuracy of the SNR is ± 1 dB at a particle concentration of 25 wppm (weight part per million) and ± 2 dB at 0.2 wppm.

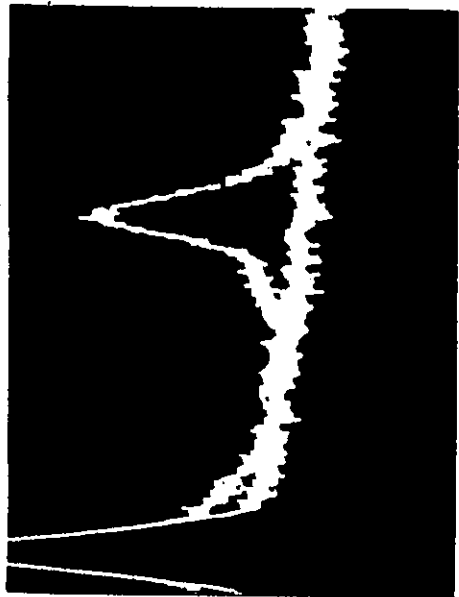
Figures 3.10(a) and 3.10(b) employed a 5000 μm pinhole, and receiver apertures of $f/2.6$ and $f/22$, respectively. Figures 3.10(c) and 3.10(d) employed a 35 μm pinhole, and receiver apertures of $f/2.6$ and $f/22$, respectively. Note that in either (a) or (b), the detected signal ranges from dc up to a peak at the maximum Doppler frequency. In (c) or (d), however, the signal is limited to the Doppler peak, in sharp contrast to (a) and (b). The difference results from the number of heterodyning processes contributing to the signal (see section 3.3).

Careful study of the spectra shows two other effects which are directly or indirectly caused by the size of the receiver aperture. The first concerns the relative power distribution of the frequency spectrum. Except for the Doppler peak, the other signal amplitudes in Fig. 3.10(a) are lower than those of Fig. 3.10(b). Note that the receiver aperture ($f/22$) of (b) satisfies the coherent condition, which results in an over-all higher heterodyne signal. On the other hand, the receiver aperture ($f/2.6$) of (a) does not satisfy the coherent condition. Therefore only the light scattered from the beam crossover region is efficiently heterodyned (heterodyning process category (A), section 3.3). Also note that although the relative power distributions are different, the SNR's at the Doppler peak are approximately equal (at this particular particle concentration). It should be clear that SNR alone does not determine optimum condition for velocity measurements. Spectral distribution, as discussed here, should also be considered. The second effect concerns the residual frequency components presented in a Doppler peak. Comparison between Fig. 3.10(c) and Fig. 3.10(d) shows that although both spectra are similar, they have different

Fig. 3.10: Doppler spectra from a DLDV. (a) and (b) employed a 5000 μm diameter pinhole. (c) and (d) employed a 35 μm diameter pinhole. The receiver aperture for (a) and (c) was $f/2.6$ while that for (b) and (d) was $f/22$. The IF bandwidth of the spectrum analyser (Hewlett-Packard 8553B/8552B) was 0.3 kHz, the scan time was 2 s/cm, the centre frequency was 10 kHz (corresponding to $v = 1.6$ cm/s), and the scan width was 2 kHz/cm. The de-ionized water was seeded with 0.62 μm diameter polystyrene particles at a particle concentration of 25 wppm.

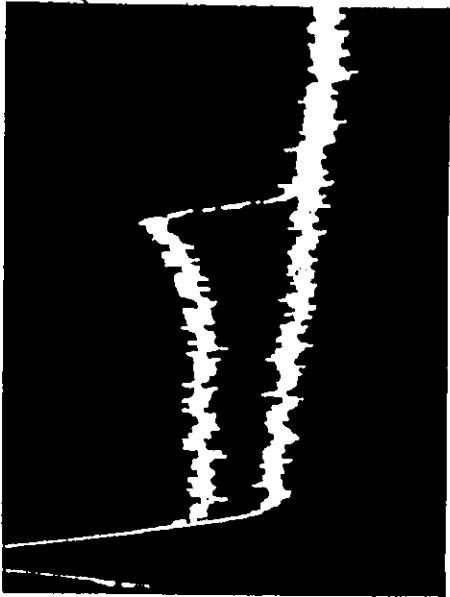


(p)

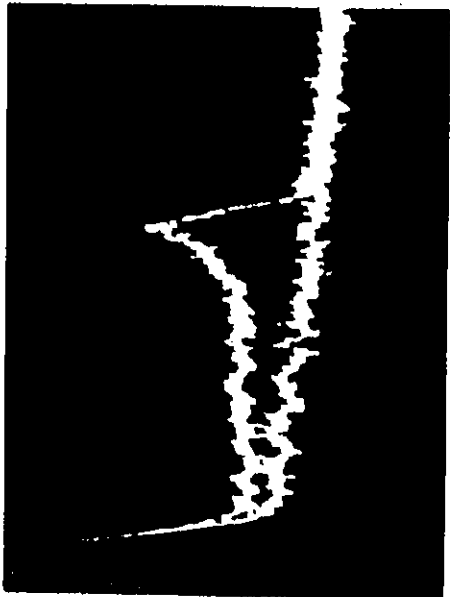


(c)

(q)



(d)

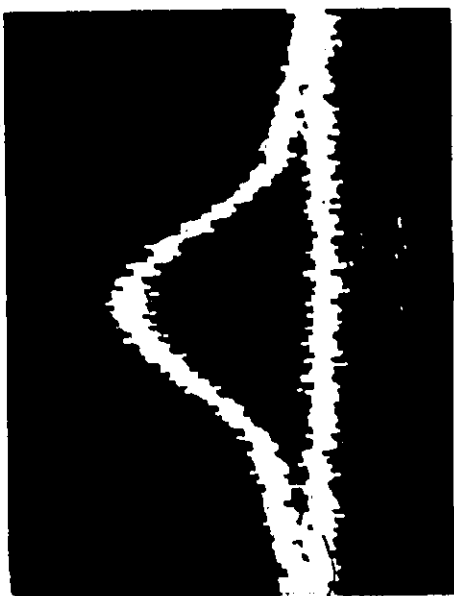


15

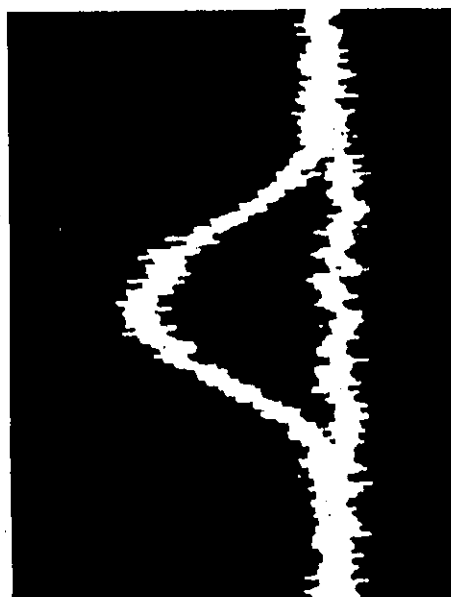
frequency distribution, particularly away from the peak. Attempts to decrease the "sidebands" components by employing a smaller pinhole for Fig. 3.10(c) were not successful. However, the effect was later found to be dependent on particle concentration (n). The "sidebands" diminished at lower n , and completely disappeared for $n \leq 1$ wppm. They are believed to be due to multiple scattering which is a function of particle concentration. Light from regions that should have been blocked by the pinhole are now detected by multiple scattering. However, if the size of the receiver aperture is reduced, as in Fig. 3.11(d), the light collected from the random processes is also reduced. Note that the SNR of the Doppler peak remains constant at high particle concentration, irrespective of the receiver aperture. The signal level, however, is clearly a function of the receiver aperture.

We now consider the effect of pinhole diameter on spectral broadening. Figures 3.11(a) and (b) and Figures 3.11(c) and (d) represent the spectra obtained from a 25 μm and a 35 μm pinhole, respectively. A $f/2.6$ receiver aperture was used for (a) and (c) and a $f/22$ aperture for (b) and (d). Careful study of the figures show that although the SNR's are equal, their bandwidths are not. This can be seen by comparison of (a) with (c), and (b) with (d). For a given receiver aperture, the spectral width obtained using a 25 μm pinhole is about 5% larger than that using a 35 μm pinhole (measured at 1/2 intensity points). The bandwidth obtained employing a 10 μm pinhole was even larger. A smaller pinhole in effect reduces the measured probe volume. Consequently particle transit time is reduced, which results in a larger spectral

Fig. 3.11: Effect of pinhole diameter on spectral broadening. (a) and (b) were obtained with a 25 μm pinhole; (c) and (d) with a 35 μm pinhole. The receiver aperture for (a) and (c) was $f/2.6$; that for (b) and (d) was $f/22$. The scan width was 0.5 kHz/cm. All other caption data in Fig. 3.10 apply.

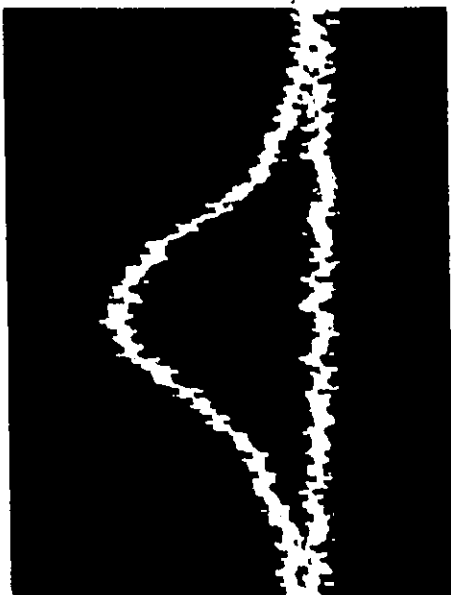


(c)

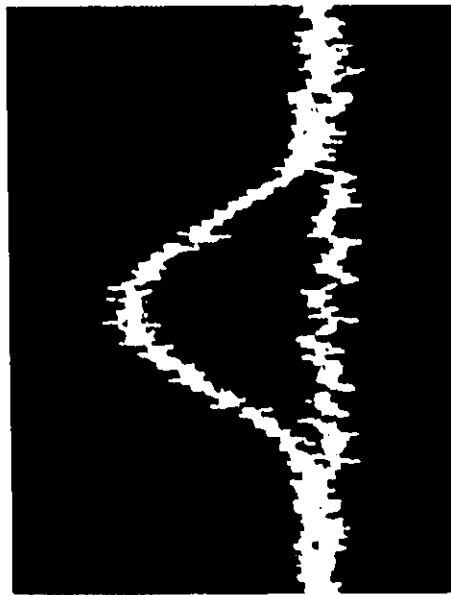


(d)

1cm



(a)



(b)

width. Pinholes larger than 35 μm introduced additional heterodyning processes and consequently spectral asymmetries and broadening of the signal.

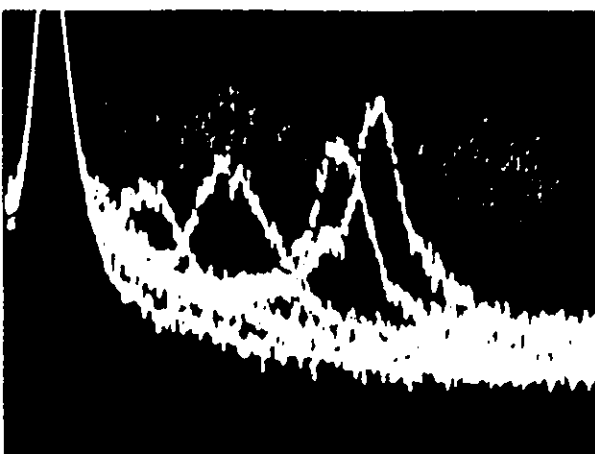
On the basis of the above consideration, it was found that a 35 μm diameter pinhole provided optimum performance in our DLDV configuration. This diameter is about three times larger than calculated. As mentioned before, lens defects such as spherical aberrations can cause enlargement of the image size when observing an object which is an approximation to a point source, as in our case. Furthermore, the resolution of standard camera lens is generally poorer than expected from diffraction considerations. Note that an appropriate pinhole can still perform its function even though the image is enlarged due to lens aberrations. As long as satisfactory results can be obtained, an expensive, high resolution receiver lens is not necessary.

The various categories of heterodyning processes (section 3.3) can be illustrated experimentally by placing a pinhole at different horizontal positions in the image plane. Figure 3.12 shows the results of such measurements employing a 35 μm pinhole. Figure 3.12(a) was obtained using a f/2.6 receiver aperture, while Fig. 3.12(b) employed a f/22 receiver aperture. Note that the probe volume was located in the center of the flow tube. Consequently, each probe corresponds to the differential heterodyning of two symmetrical points which possess identical velocity (see Fig. 3.5). Furthermore, the intensity of each peak is governed by the amplitude envelope of the spectrum observed using a large pinhole. This can be seen by comparing the relative amplitudes of Figures 3.12(a) and 3.12(b) with those of



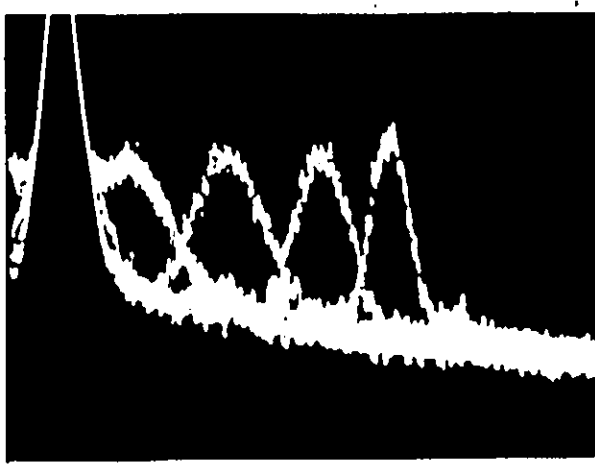
Fig. 3.12: Measurements of the various heterodyning processes. The pinhole location on the image plane determines the position of the region in the flow volume. Each peak corresponds to a particular flow velocity in the flow tube. The lower the frequency, the closer the measuring point approaches the wall. (a) was taken with a receiver aperture of $f/2.6$; (b) with a receiver aperture of $f/22$. Both sets of measurements employed a $35\ \mu\text{m}$ pinhole. All other caption data in Fig. 3.10 apply.

1 cm



(a)

a



(b)

Figures 3.10(a) and 3.10(b), respectively. The function of the pinhole is thus twofold. It determines both the observation region and the SNR. Note that in the particular case of the data in Fig. 3.12, the highest SNR occurs at the highest frequency. This results from the probe volume being at the maximum velocity region of the flow tube. Note also that in general, the highest SNR corresponds to scattering from the crossover region. This property can be used either to locate the pinhole position corresponding to the probe volume, or taken together with frequency measurement, the position of probe volume at a particular velocity.

3.7 Summary

We have analysed the important properties of a DLDV and have shown experimentally how optimum performance can be obtained. In particular, spatial filtering, by means of a suitable pinhole on the image plane of the receiver lens, is necessary. Firstly, it determines the measuring region in the flow tube. Secondly, it is required for optimum SNR. Finally, it provides an improved spectral quality and spectral width. These parameters should be carefully investigated before a DLDV system is used for accurate measurements. Other important parameters which affect the SNR include the receiver aperture, and the particle concentration. Further theoretical and experimental studies of these parameters are described in Chapter 6.

CHAPTER 4

DESIGN OF A WHITE LIGHT FRINGE IMAGE VELOCIMETER

This chapter introduces the experimental arrangement of the white light fringe image velocimeter (WFIV) and the optical and geometrical properties of the fringe image. As mentioned in the introduction, one interpretation of the DLDV is that real fringes are formed in the flow region. Particles crossing alternate bright and dark interference fringes produce a modulation of the scattered radiation whose frequency is proportional to the flow velocity. The new WFIV technique is similar in principle except that it uses localized fringes formed by the optical image of a grating (e.g., a Ronchi grating) illuminated with an incandescent source.

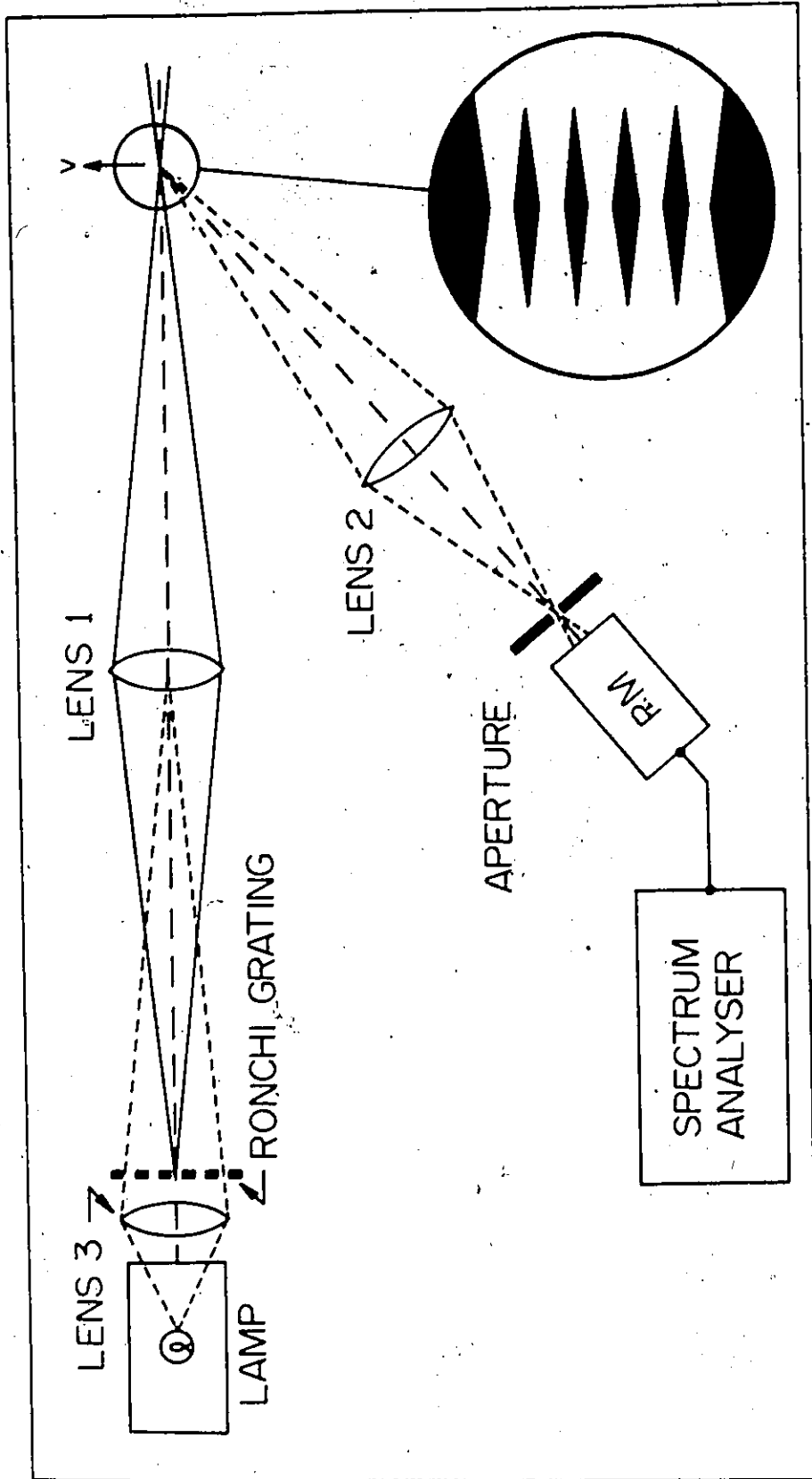
A simple technique is also presented to assess fringe visibility and image depth-of-field.

Finally, comparisons are made between DLDV and WFIV measurements employing a rotating disk.

4.1 Experimental Arrangement of a WFIV

Figure 4.1 illustrates the experimental arrangement for velocity measurements using an image of a Ronchi grating. This type of grating has alternate opaque and clear sections each of uniform width. The image of the grating is formed in the flow region by means of the imaging lens. Best results are obtained when the chromatic aberrations

Fig. 4.1: Experimental arrangement for the WFIV. The imaging lens (lens 1) forms an image of the Ronchi grating in the flow region. An image of the lamp filament is formed in the region of lens 1 by the condenser lens (lens 3). A simplified fringe image pattern is shown in the inset. In this figure, the photomultiplier is shown in the backward scattering position.



and image distortion of the lens are small. Standard lenses for use with a 35 mm camera were generally found to give satisfactory performance, provided that the fringe spacing is not too small. A standard condenser arrangement is used to give a fairly uniform image intensity - i.e., the condensing lens forms an image of the source (incandescent lamp) in the region of the imaging lens. Note that in Fig. 4.1, the detector is shown in a backward scattering position. Forward scattering, however, may be more suitable for many applications.

In this section we consider only a brief analysis of the method; further details are provided in the following sections.

Let D be the spacing of the rulings on the grating, p , the grating-to-lens distance, and q , the lens-to-image distance. Both p and q are referred to the principal (nodal) planes of the lens. The distances p and q are related to the imaging lens focal length F by

$$\frac{1}{p} + \frac{1}{q} = \frac{1}{F} \quad (4.1)$$

The image formed in the flow region is a three-dimensional fringe pattern, with fringe spacing

$$d = \frac{q}{p} D \quad (4.2)$$

Note that d in Eq. (3.5) is proportional to λ but that d in Eq. (4.2) is independent of λ . In the latter case, however, d will be constant only in a small region of the image volume. The main effect of a non-constant d is to increase the spectral width of f ; it has negligible

effect on the value of f . This is discussed in more detail in section 4.3. The mean value of d in the fringe volume (i.e., the value of d at the image plane of the imaging lens) can be used for most calculations.

If a particle of velocity v traverses the fringes at an angle ϕ to the direction perpendicular to the fringe planes, then the scattered light will be modulated at the same frequency that was stated for the differential Doppler technique, i.e.,

$$f = \frac{v \cos \phi}{d} \quad (4.3)$$

where d is given by Eq. (4.2).

The velocity can be readily evaluated from Eq. (4.3) because all the system parameters can be easily measured. These parameters are the focal length of the lens, the lens-to-object distance, and the fringe spacing of the grating. Moreover the system is independent of the coherence properties of the light. This makes the system optically and physically easy to use. The measurements are less affected by mechanical vibrations, and by optical path inhomogeneities, than the various laser velocity measurement techniques.

4.2 Simple Technique for Visibility Measurement

The performance of a WFIV is determined primarily by the lens resolution. A high resolution imaging lens system is not only essential for measuring extremely low velocities, but is also necessary to achieve sensitivity (i.e., high SNR) and accuracy.

Resolution is usually related to the modulation transfer function [47]. Basically, this is a measurement of the fringe image visibility, V , given by

$$V = \frac{I_{\max} - I_{\min}}{I_{\max} + I_{\min}}, \quad (4.4)$$

where I_{\max} and I_{\min} are the maximum and minimum intensities of the fringe image pattern, respectively.

A simple but reliable technique for measuring visibility is shown in Fig. 4.2. A one micron diameter pinhole was mounted on a metal plate. This plate was mounted on an x-y-z translation stage by means of a flexible strip composed of magnetic material. An electromagnet was used to provide a scan of the fringe image pattern. Both an oscilloscope and an x-y recorder (not shown in the figure) were used to observe the PMT output. Optimum signal visibility was obtained by adjusting the translation stage.

A typical fringe image pattern observed with an x-y recorder is shown in Fig. 4.3(a). Note that all of the fringes have approximately equal intensities. This should be compared with the DLDV, where the intensities follow a Gaussian distribution (Fig. 3.10). Note also that a rounding off of the fringes in Fig. 4.3(a) is caused by diffraction and lens aberrations.

The visibility of the image formed by a lens employed for WFIV measurements is presented in Fig. 4.3(b). This data covers a range of f -numbers and image fringe spacings. It can be seen that the visibility is strongly dependent on the f -number. Consequently, visibility

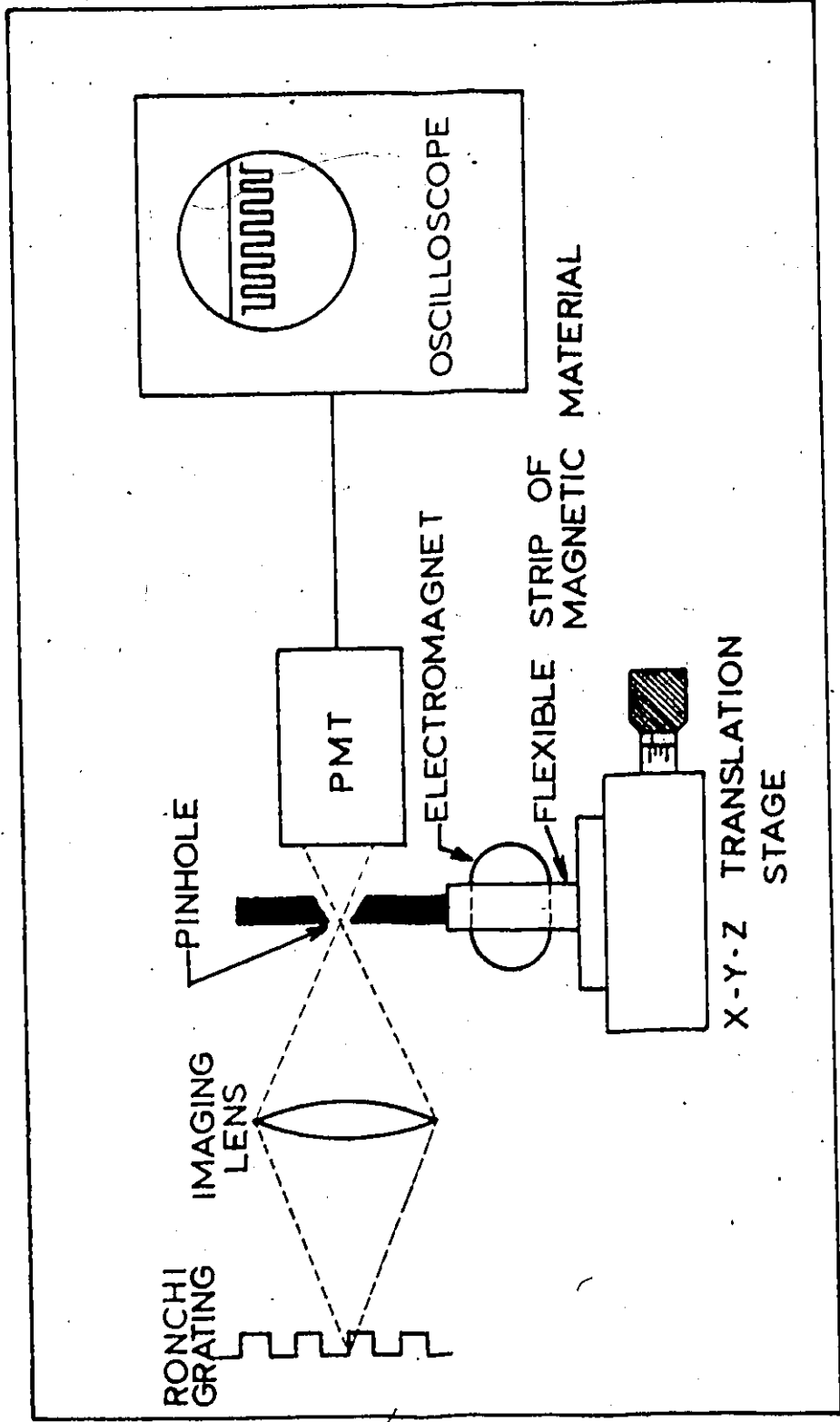
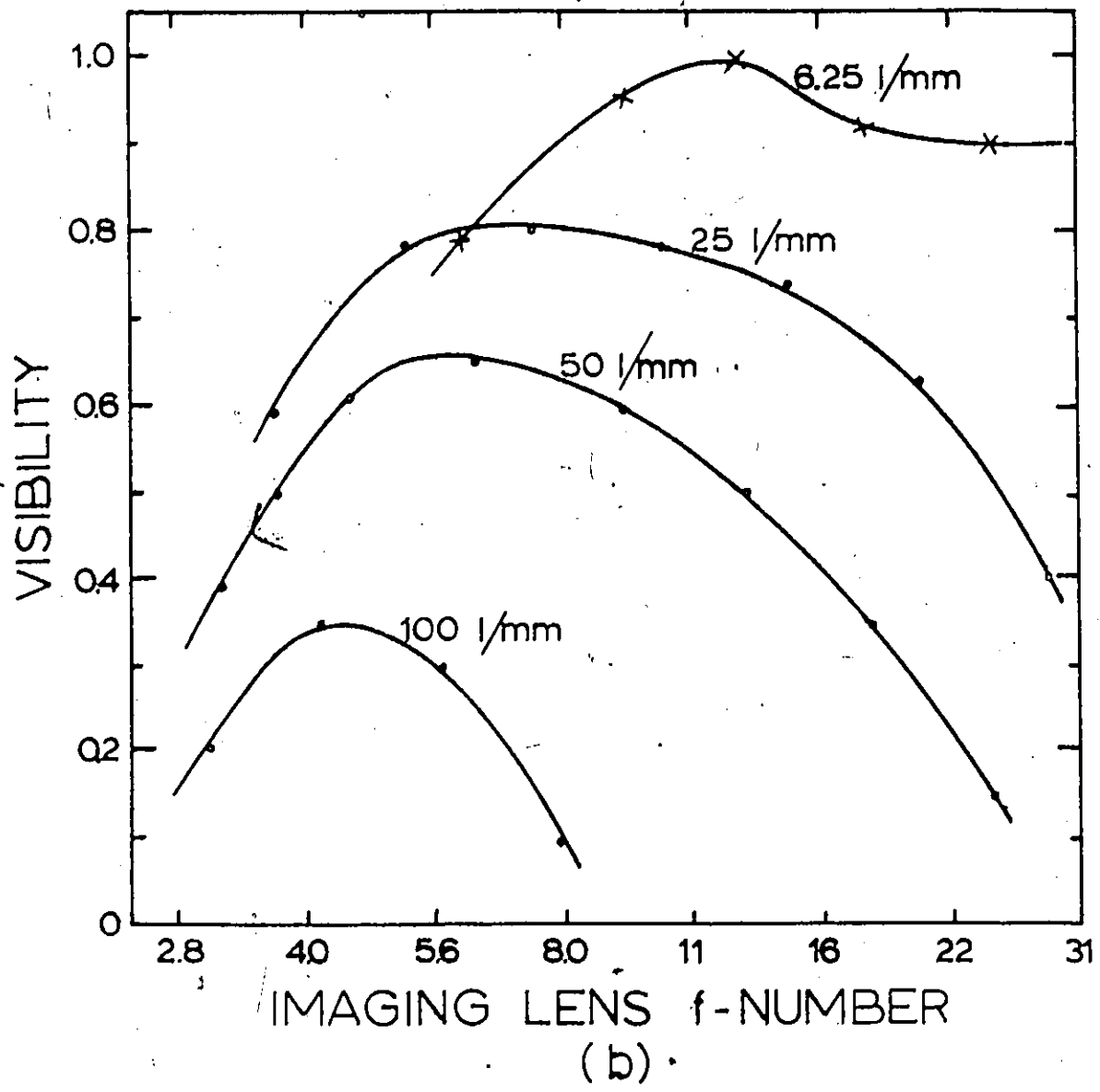
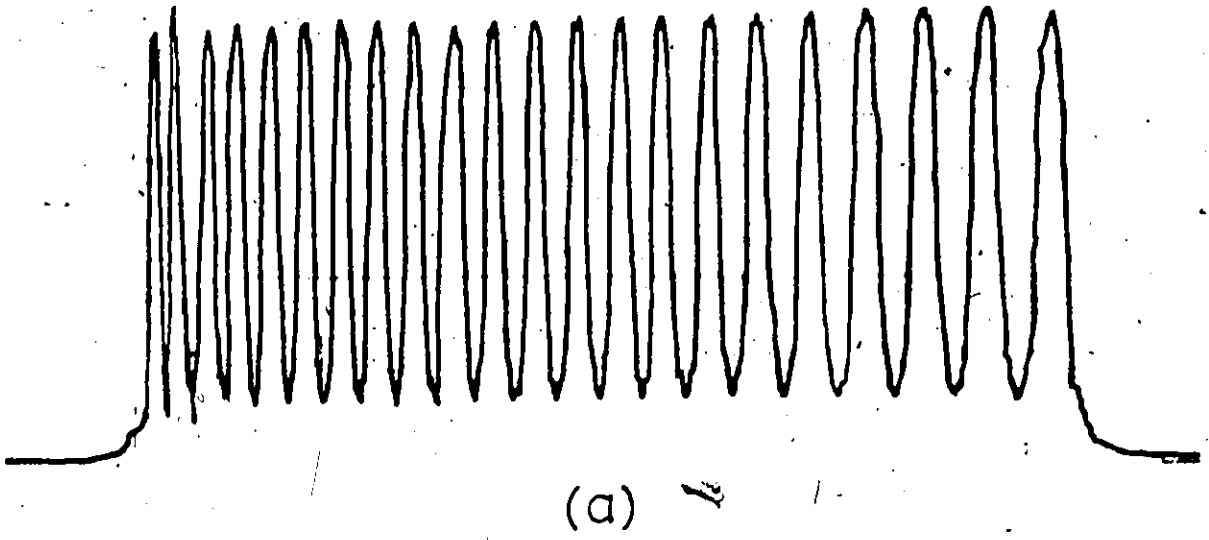


Fig. 4.2: Experimental arrangement for visibility measurements. The fringe image pattern of the Ronchi grating is formed at the image plane by the imaging lens. The electromagnet scans the pinhole along the image plane.

Fig. 4.3: Fringe image pattern and visibility of a lens system.

(a) represents the scanned fringe image pattern of a 35 mm camera lens (Soligor, $f = 135$ mm) at $f/8$. The object was a 200 lpi Ronchi grating, which resulted in a fringe image of spacing $d = 0.004$ cm (25 l/mm). The fringe visibility is about 0.8. Note that the variation of the fringe spacing is due to nonlinearities in the scan.

(b) presents the visibility of the above lens at different f -numbers and fringe spacings. The image fringe spacing was established by adjustment of the grating-to-lens distance. Note that the f -numbers are corrected for lens-to-image distance. It is expected that changing gratings to vary fringe spacings would give somewhat different results.



measurements are necessary to achieve optimum performance of a WFIV. Unless otherwise stated, our WFIV measurements employed an image fringe spacing of 25 μ m ($d = 0.004$ cm) and an effective aperture of $f/8$. This provides a visibility of about 0.8.

4.3 Longitudinal Extent of the Fringe Image

A very simple model will be used to represent the fringe image system. This model can provide good quantitative information on the performance of a system using fringe images for the measurement of particle velocity. At the present time it is felt that a more exact solution would not significantly improve the analysis accuracy because there exist several parameters in any practical system which are not accurately known. These parameters include the size and shape of the flow particles and image aberrations in the flow region.

Consider the image of a Ronchi grating formed at a distance q from the imaging lens, as shown in Fig. 4.4. With an ideal optical system, the intensity of the image at q can be represented by a square wave of visibility $V = 1$. Here it is assumed that diffraction effects can be neglected, that a very large number of fringes are used, and that the ruling length is much greater than the ruling spacing. The fringe image is taken to be an even function which is symmetrical about the optical axis of the lens. Furthermore it is assumed that the fringe spacing $d \ll q$.

Let R be the radius of the active portion of the lens, and y the distance from 0 on the optical axis to a point P_1 on a reference

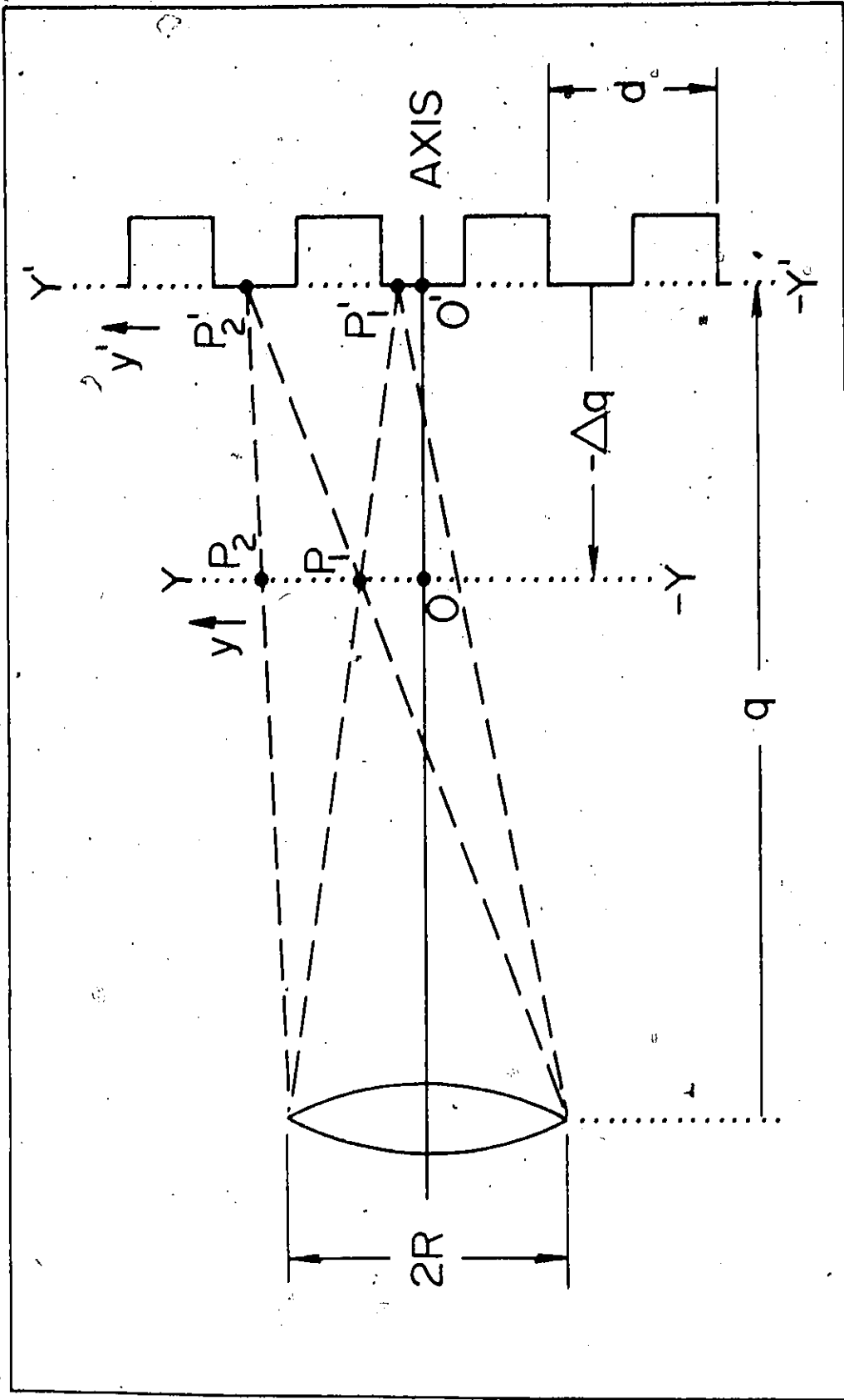


Fig. 4.4: Parameters used for the analysis of the fringe image system. The plane $(Y, -Y)$ can be

located either side of q :

plane $(-Y, Y)$. This reference plane is located a distance Δq from the image plane $(-Y', Y')$. Distances from O' along the $(-Y', Y')$ axis are given by y' . The reference plane $(-Y, Y)$ can be located on either side of the image plane; it is shown at a distance $-\Delta q$ in the figure. The intensity at any point P_1 can be calculated from integration of the incremental intensities at P_1 due to the radiation which produces the image between P_1' and P_2' . Note that the distance between P_2' and P_1' , given by $(y_2' - y_1')$, corresponds to the maximum diameter of the beam converging to a point on $(-Y, Y)$. This diameter is related to the distance between P_2 and P_1 , given by $(y_2 - y_1)$. For $d \ll q$ the distances are related by

$$(y_2 - y_1) = \left(1 + \frac{\Delta q}{q}\right)(y_2' - y_1') \quad (4.5)$$

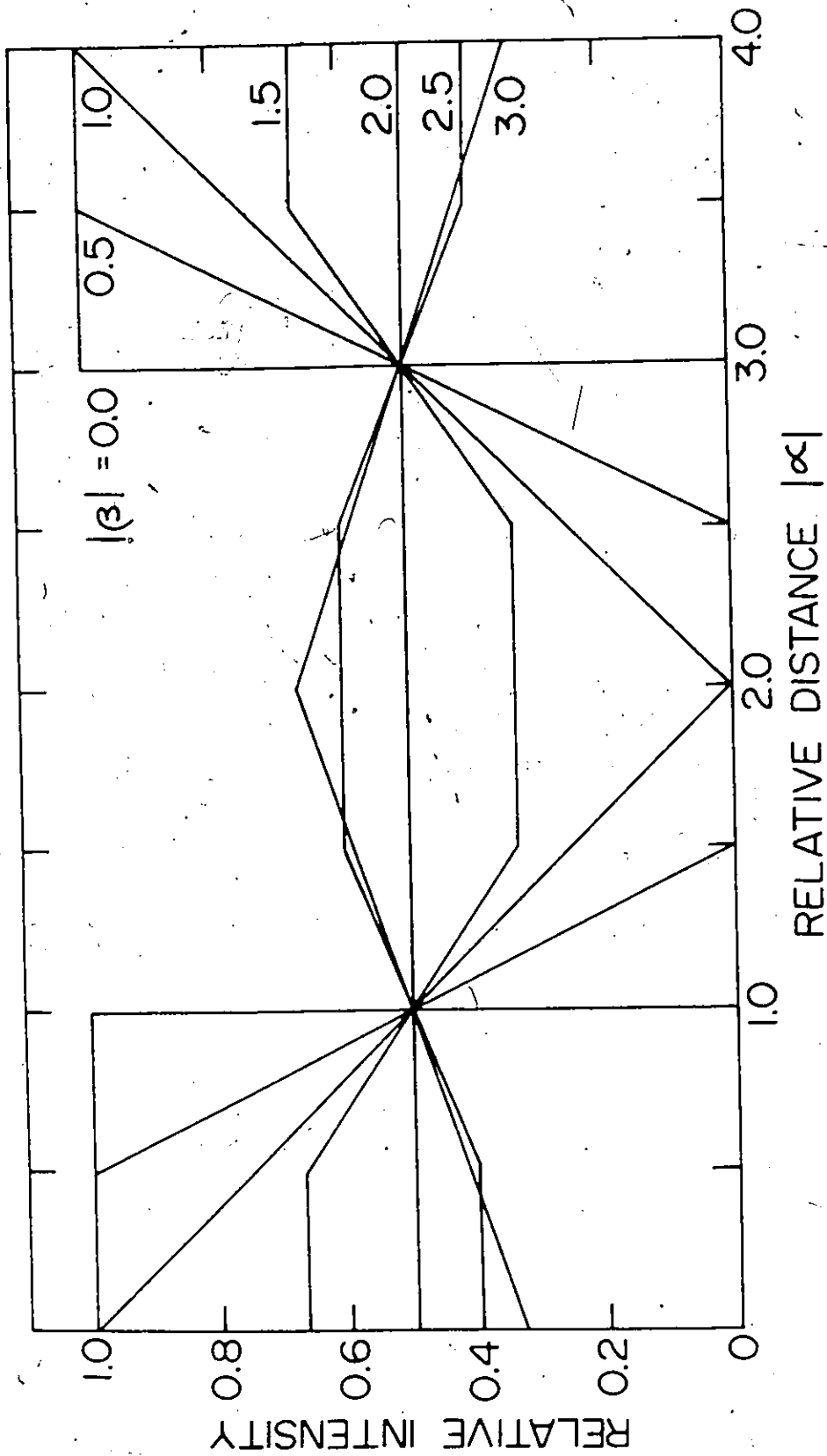
Results of intensity calculations are presented in Fig. 4.5, where the relative intensity is plotted against the relative distance $|\alpha|$ where α is defined by

$$\alpha = \frac{4y}{d} \quad (4.6)$$

Each "curve" corresponds to a β such that $\beta = \pm 1$ represents the value of $\pm \Delta q$ which gives the maximum amplitude triangular intensity distribution. It is also the maximum value of the magnitude of β for which the visibility $V = 1$. With the aid of Fig. 4.4 it can be shown that, for d small, this maximum occurs when

$$\Delta q = \frac{qd}{4R} \quad (4.7)$$

Fig. 4.5: Relative intensity at $|\beta|$ as a function of the relative distance $|\alpha|$. The parameter $|\alpha|$ is defined by $\alpha = 4y/d$ and the parameter $|\beta|$ by $\beta = 4R\Delta q/qd$, where y , d , R , Δq , and q , are given in Fig. 4.4.



Therefore

$$\beta = \frac{4R}{qd} \Delta q \quad (4.8)$$

Note that the intensity distribution is symmetrical about $y = 0$, and therefore about $\alpha = 0$. Similarly, when $d \ll q$, the intensity distribution through the planes β and $-\beta$ are identical.

Consider now that a particle, of dimensions much smaller than d , traverses the fringe at a velocity v . From Eq. (4.3), and assuming $\phi = 0$, the fundamental frequency component in the scattered intensity is given by

$$f = v/d \quad (4.9)$$

The complete frequency spectrum at a plane through Δq , and therefore through β , in Fig. 4.4 is given in general by the Fourier series for a trapezoidal wave, of the type shown in Fig. 4.6. This series can be represented by

$$I(t) = I_m/2 + \sum_{n=1}^{\infty} C_n \cos 2\pi nft \quad (4.10)$$

where f is given by Eq. (4.9), and where

$$C_n = I_m \frac{\sin(\pi n d_1/d)}{\pi n d_1/d} \frac{\sin \pi n/2}{\pi n/2} \quad (4.11)$$

Here we are primarily interested in the fundamental frequency component, for which $n = 1$. Therefore the coefficient of the fundamental frequency

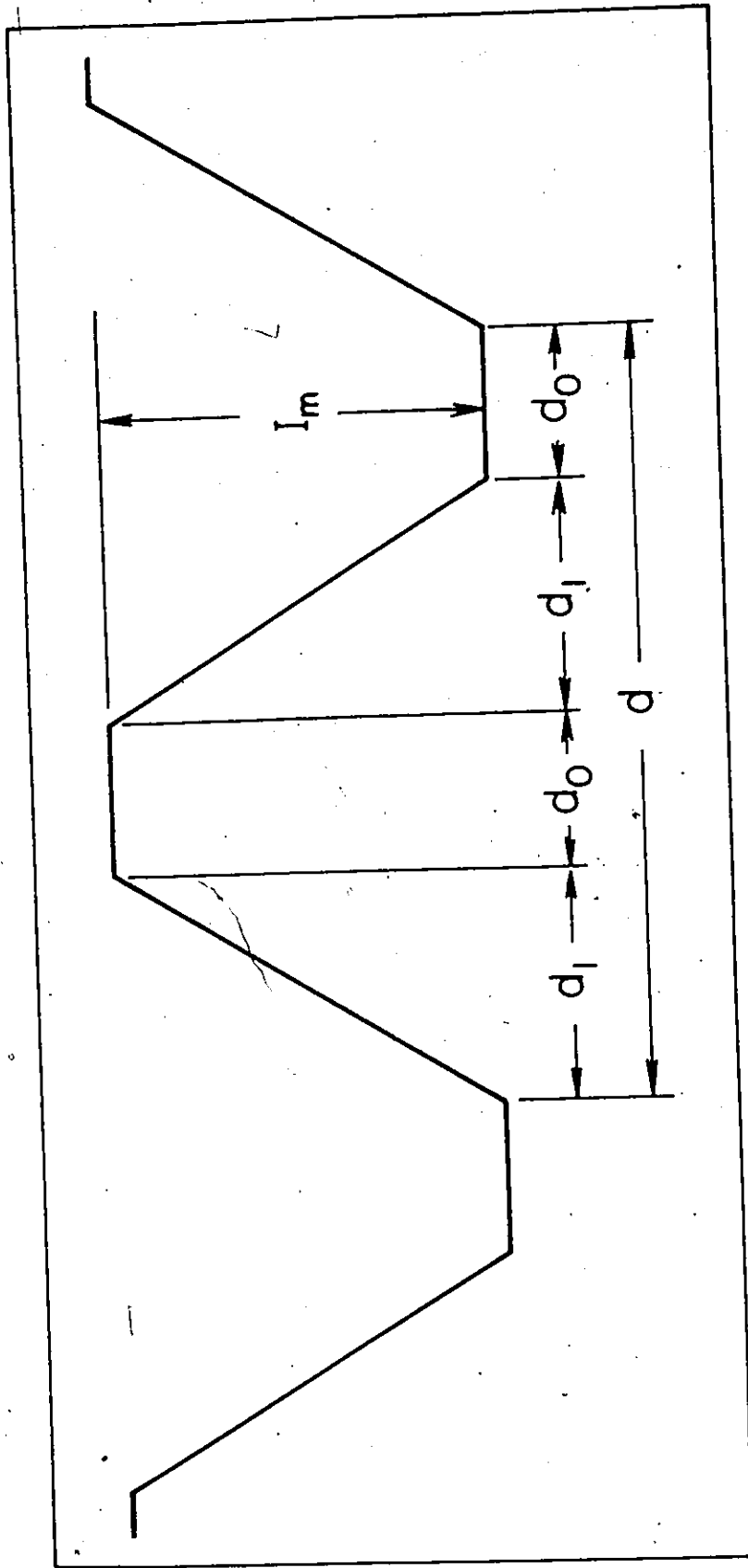


Fig. 4.6: Parameters used for the analysis of a trapezoidal waveform.

component is given by

$$C_1 = \frac{2I_m}{-\pi} \frac{\sin \pi d_1/d}{\pi d_1/d} \quad (4.12)$$

When $d_1 = 0$, the series given by (4.10) represents a square wave and therefore $C_1 = (2/\pi)I_m = 0.637 I_m$. When $d_1 = d/2$ the series represents a triangular wave for which $C_1 = (2/\pi)^2 I_m = 0.406 I_m$. Thus C_1 is always in the range $0.406 I_m$ to $0.637 I_m$.

The total scattered signal at frequency f can be found by integration of all the Fourier series for the intensity which correspond to all values of β . Here it is assumed that a sufficiently large number of scattering particles are involved so that the integration is valid. As an approximation we can consider that the multiplicative factor for I_m in C_1 remains constant at some average value. For convenience this average is taken as 0.5. With the aid of Fig. 4.5, it can be seen that I_m is always proportional to the visibility. Thus the total scattered intensity $I_s(t)$ at frequency f , is related, to a good approximation by

$$I_s(t) \propto \left[\int_{-\beta}^{\beta} d\beta + \cos 2\pi ft \int_{-\beta}^{\beta} V(\beta) d\beta \right], \quad (4.13)$$

where for convenience the integral is taken from $-\beta$ to β . The first integral in (4.13) corresponds to the dc term in the scattered intensity. Note that the incremental contribution to this integral is a constant for all values of y and β which fall within the range of the approximation, as can be seen with the aid of Fig. 4.5.

Figure 4.7 shows the visibility as a function of $|\beta|$ for the intensity distributions shown, in part, in Fig. 4.5. Substitution of this data in Eq. (4.13), and carrying out a numerical integration, results in values for the dc signal amplitude and fundamental frequency amplitude shown in Fig. 4.8. Note that the dc amplitude increases linearly with $|\beta|$. The amplitude of the fundamental frequency increases linearly at first, and then levels off with a slow rate of increase at large values of $|\beta|$. A change in $|\beta|$ from 20 to 40, for example, increases the amplitude from 2.54 to 2.88. A further increase of $|\beta|$ to 100 will increase the amplitude to 3.34. It should be clear that the ratio of fundamental frequency amplitude to dc amplitude remains relatively constant for $|\beta|$ in the range of 0 to 1.5 and decreases rapidly for $|\beta|$ above 1.5. The range of $|\beta|$, and therefore the flow volume, observed experimentally depends on the detection optics. Too large a $|\beta|$ will give a deterioration in detection signal-to-noise ratio, because the amplitude of the fundamental frequency component will be small compared to the dc signal.

For larger values of $|\beta|$ (i.e., $|\beta| > 1.5$) the ac signal amplitude remains relatively constant; the dc amplitude increases linearly with $|\beta|$. The noise amplitude, however, is proportional to the square root of the dc amplitude. Therefore the maximum obtainable signal-to-noise ratio is approximately proportional to the square root of the signal to dc amplitude ratio. Consequently fairly large values of $|\beta|$ can be employed in a practical experimental situation. Note that the field aperture (pinhole) eventually determines the depth of field of

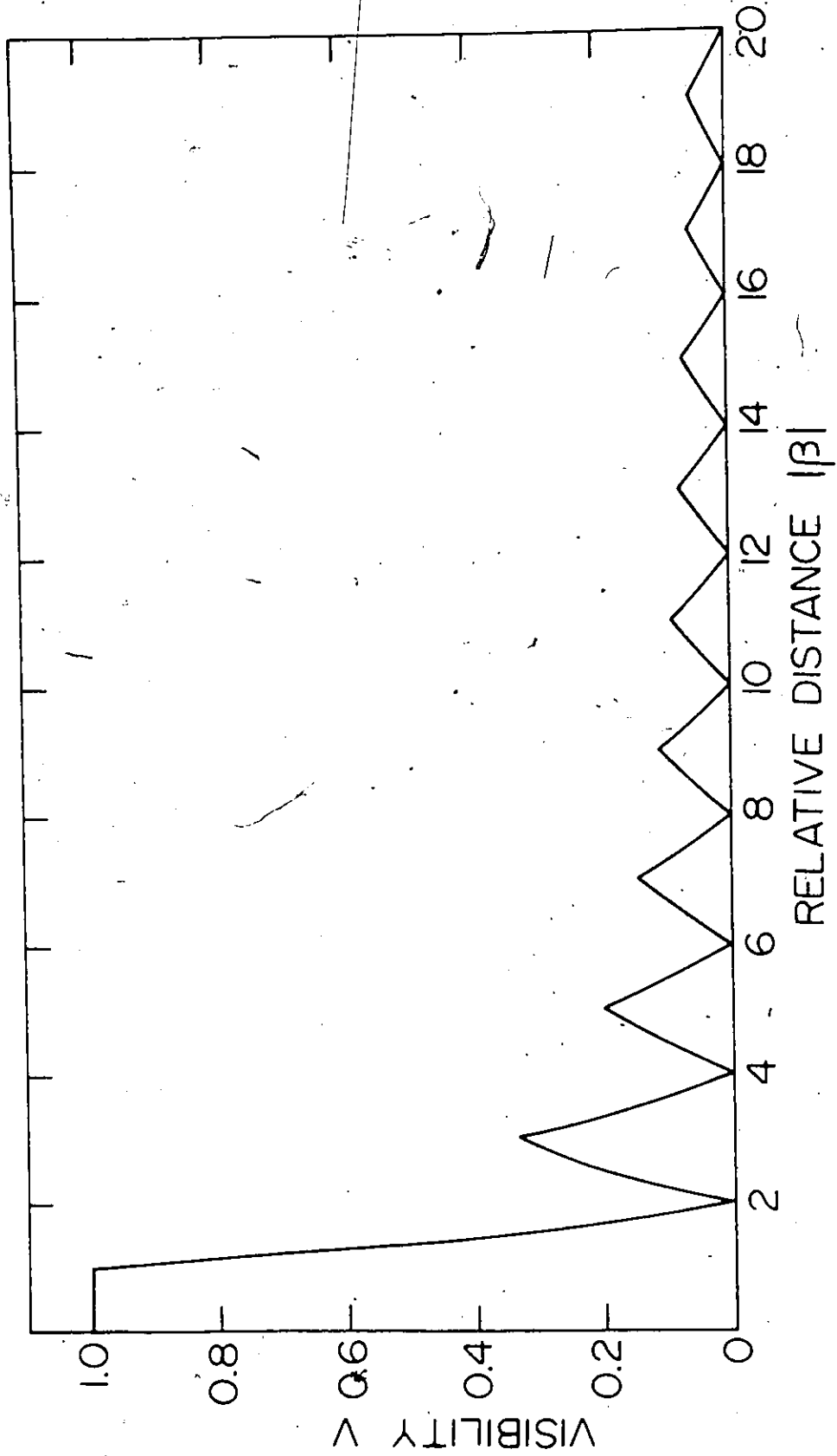
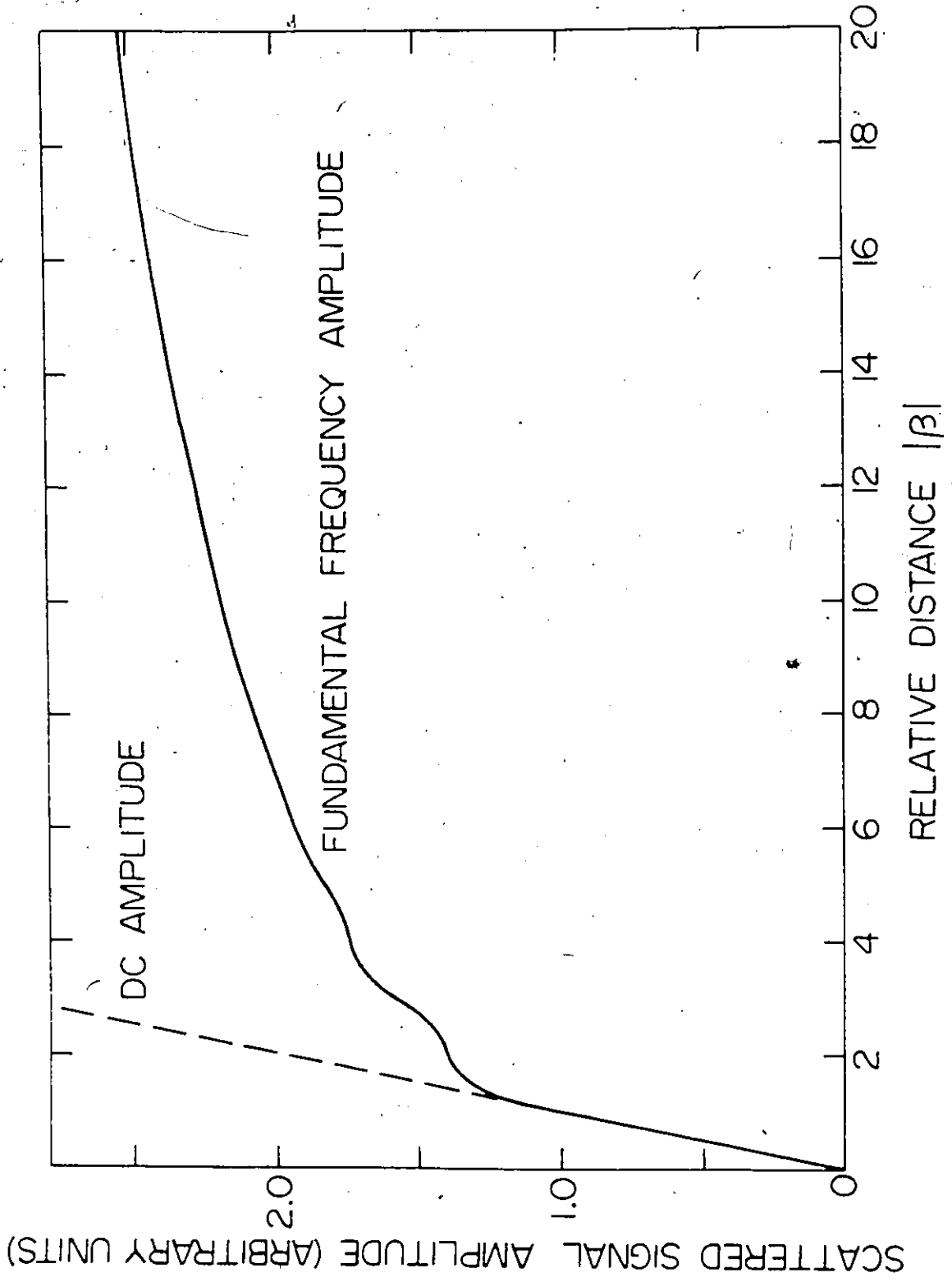


Fig. 4.7: Ronchi grating fringe visibility as a function of the parameter $|\beta|$. This is the same β used for Fig. 4.5.

Fig. 4.8: Scattered signal amplitude as a function of the parameter $|\beta|$. This is the same β used for Fig. 4.5. The dc amplitude and the fundamental frequency amplitude both have the same scale factor.

Fig 4.9



the measured probe volume. This is described in detail in Chapter 5 when the subject of fluid flow measurement is presented.

Experimental measurements of the visibility along the longitudinal extent of the fringe image have been carried out. The measurements techniques are similar to those employed for Fig. 4.3. The same lens was used. Results for $f/8$ and $f/4$ are shown in Figures 4.9 and 4.10, respectively. Each point on the curves represents the visibility of a given β plane. These planes were located at intervals of $100 \mu\text{m}$. Additional observations indicated that no anomalies existed between adjacent measurement planes.

Note that the above experimental results are qualitatively in reasonable agreement with theoretical results shown in Fig. 4.7. However, the first minima occur approximately at $\beta = \pm 4$, compared to the theoretical $\beta = \pm 2$. The difference probably results from lens aberrations because the resolution is significantly lower than the diffraction limit. Note that the overall visibility for the $f/8$ aperture is much better than that for $f/4$.

4.4 Variation of d with Δq

In the above section the assumption has been made that d is a constant for all values of β and consequently for all values of Δq . There is, however, a variation which can be calculated with the aid of Eq. (4.5). If we let $(y_2' - y_1') = d'$, then the d at the plane $(-Y, Y)$ is given by

$$d = \left(1 + \frac{\Delta q}{q}\right) d' \quad (4.14)$$

Fig. 4.9: Visibility measurements along the longitudinal extent of the fringe image for an $f/8$ aperture. The lens employed was identical to that used for Fig. 4.3 ($f = 135$ mm). Note that β was calculated from Eq. (4.8), using $d = 0.004$ cm (25 1/mm), $q = 18$ cm, and $R = 1.2$ cm. This gives $\Delta q = 0.015\beta$ cm. The pinhole diameter was $5 \mu\text{m}$.

Fig. 4-9

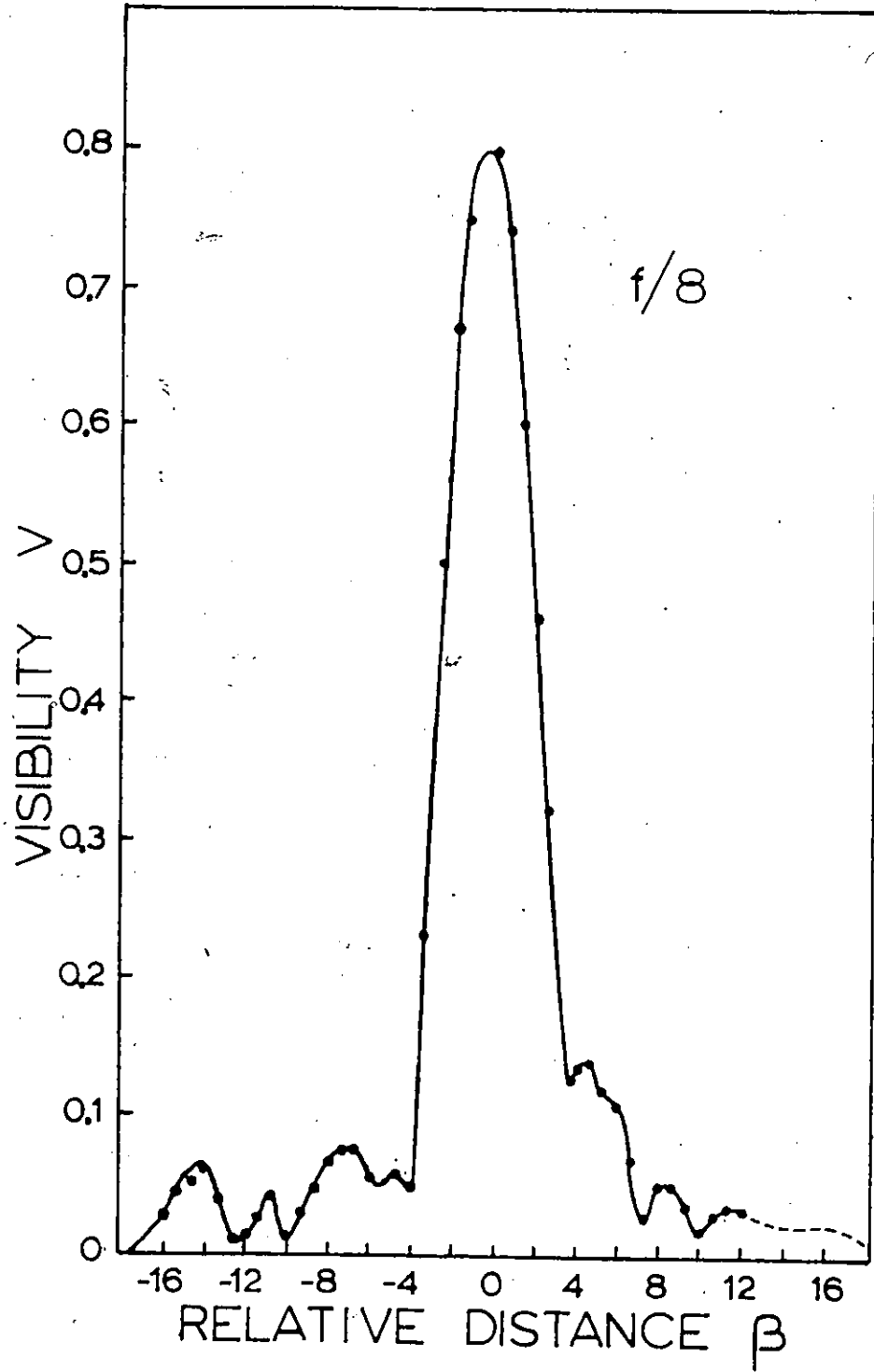
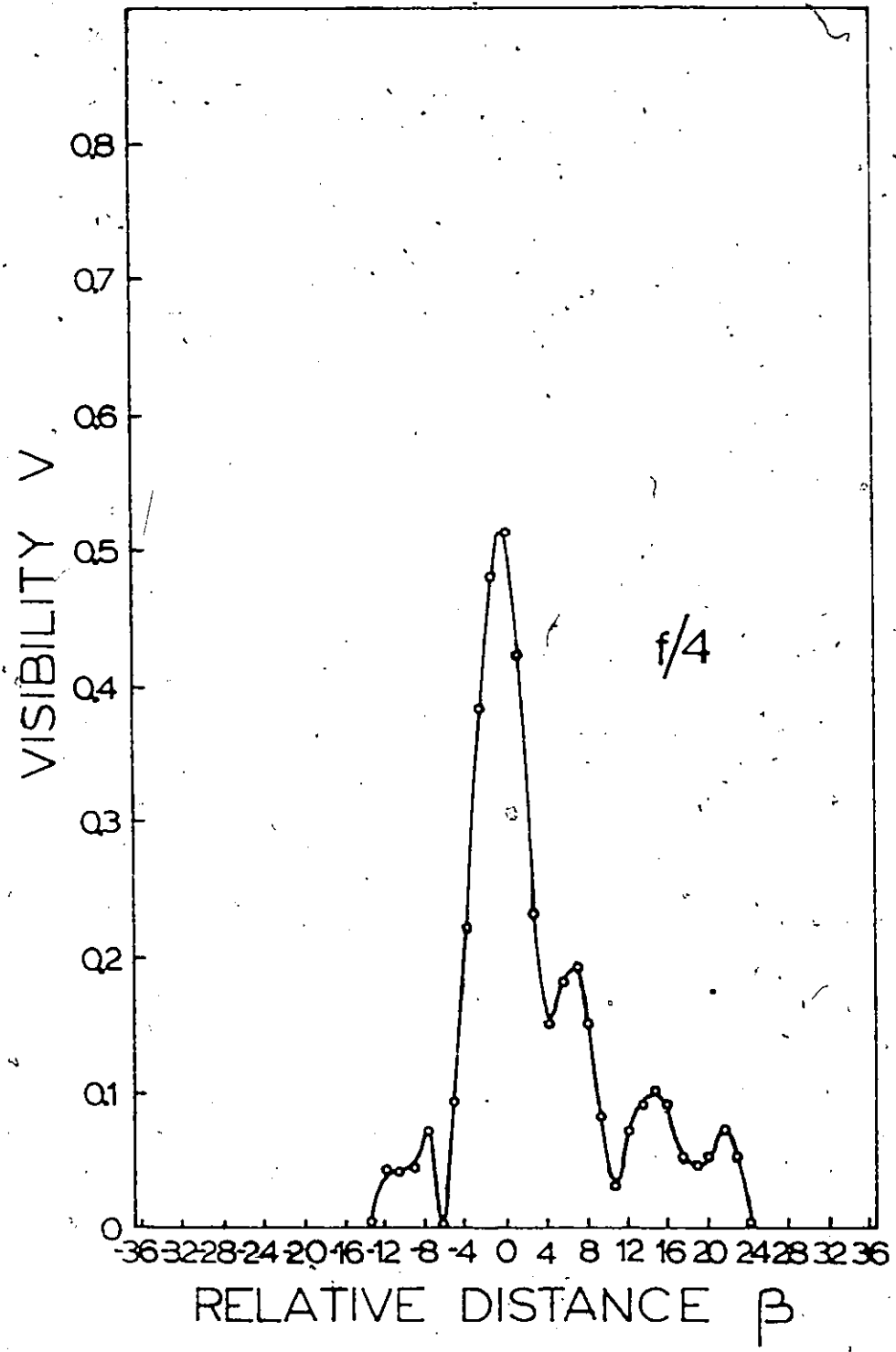


Fig. 4.10: Visibility measurements along the longitudinal extent of the fringe image for an $f/4$ aperture. Here $\Delta q = 0.00758$ cm and the pinhole diameter was $10 \mu\text{m}$. All other caption data in Fig. 4.9 apply.



Note that the change in d is symmetrical about the plane $(-Y', Y')$, for which $\Delta q = 0$ and that the frequency $f \approx 1/d$. The net effect is that contributions to the cosinusoidal term in Eq. (4.13), at larger values of β , will result in a broadening of the spectrum about the frequency f . Thus the center frequency of the scattered signal is not changed. In a practical experimental system the detection optics can be arranged so that $\Delta q/q \ll 1$.

4.5 Lateral Extent of Fringe Image

In general the image at q will have a finite number of fringes. If N is the total number of fringes, then the lateral extent of the image at q is given by

$$l = (N - 1/2)d, \quad (4.15)$$

as shown in Fig. 4.11. For a particle moving with velocity v in the direction of y' , the time t is related by

$$t = \frac{y'}{v} \quad (4.16)$$

and the period is given by

$$T = \frac{d}{v} \quad (4.17)$$

The Fourier transform of the amplitude intensity function in Fig. 4.11 is given, for N odd, by

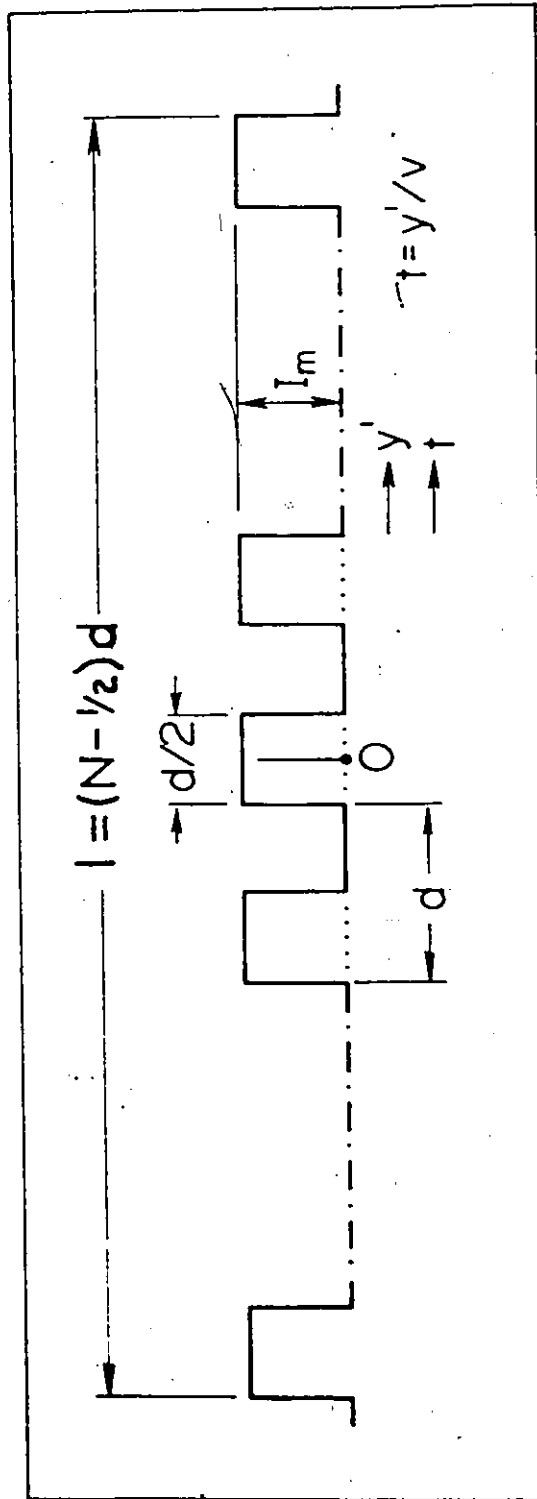


Fig. 4.11: Parameters used for the analysis of signal sidebands.

$$I(f') = 2I_m \frac{\sin 2\pi f' T/4}{2\pi f'} \frac{\sin(N + 1/2)2\pi f' T}{\sin(\pi f' T/2)}, \quad (4.18)$$

the Fourier transform of a square wave. Of primary interest here is the fundamental frequency component at $f = 1/T$. The frequency axis can be shifted and Eq. (4.18) put in the form

$$I(f') = \frac{I_0}{(2N + 1)} \frac{\sin[(2N + 1)\pi(f' - f)T]}{[\sin\pi(f' - f)T]}, \quad (4.19)$$

where I_0 is the peak value of $I(f')$ which occurs when $(f' - f) = 0$.

For N large (4.19) can be expressed in the form

$$\frac{I(z)}{I_0} = \frac{\text{sinc } z}{z} \quad (4.20)$$

where

$$z = (2N + 1)\pi(f' - f)T \quad (4.21)$$

The absolute value of $(\text{sinc } z)/z$ is given in Fig. 4.12 for z in the range -10 to 10 . The first zeros about $z = 0$ are separated by

$$\Delta f = (f' - f) = \frac{f}{(N + 1/2)}, \quad (4.22)$$

which may be expressed by

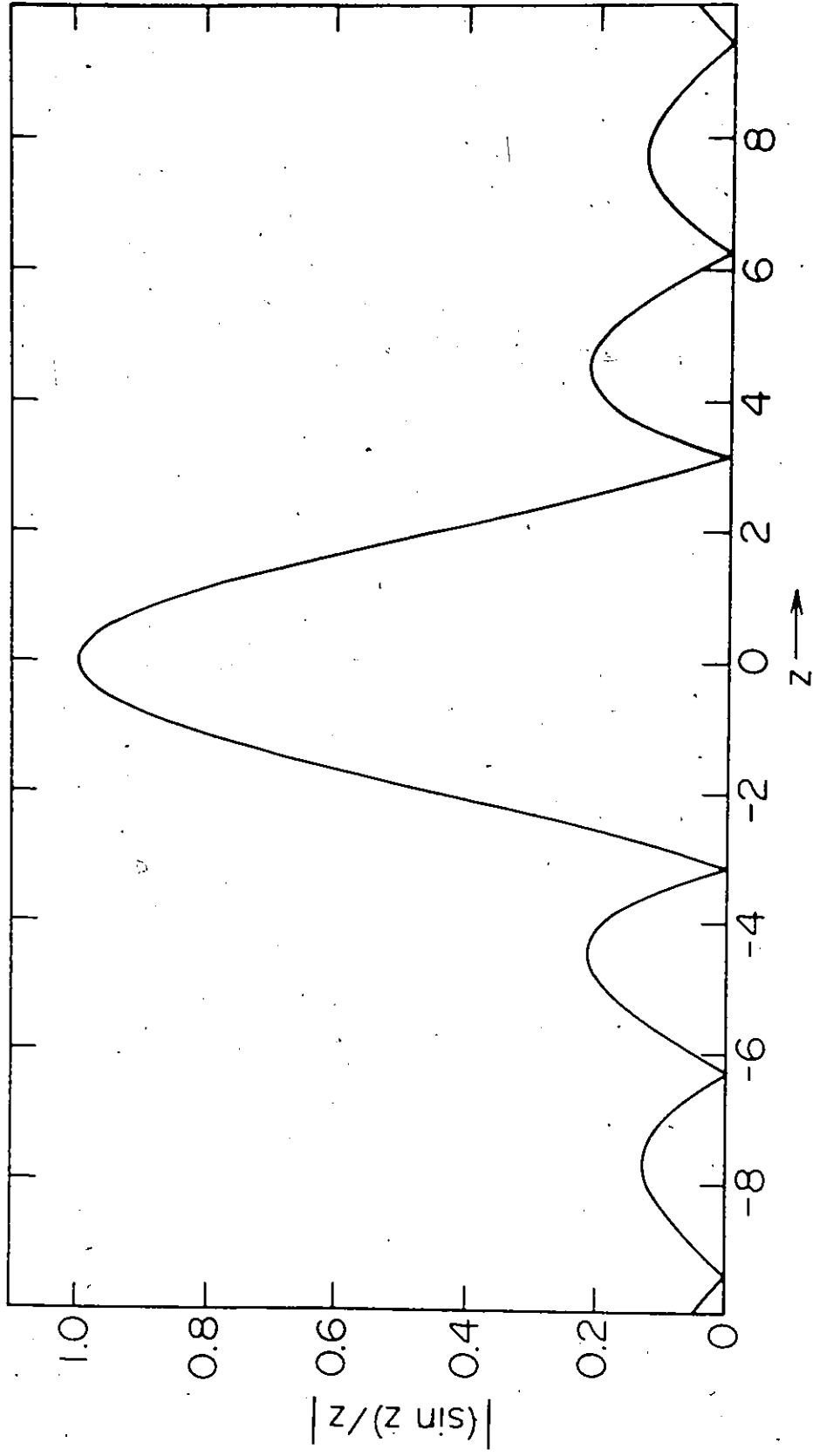


Fig. 4.12: Signal and sidebands for the fringe intensity distribution shown in Fig. 4.11. The parameter z is defined in the text.

$$\left(\frac{\Delta f}{f}\right)_N = \frac{1}{(N + 1/2)} \quad (4.23)$$

It should be clear that the signal arising from the intensity distribution represented by Eq. (4.20) consists of side-bands located symmetrically about the fundamental frequency.

Note that (4.20) will also apply to any symmetrical trapezoidal intensity distribution of the form shown in Fig. 4.6. Therefore the analysis carried out in section 4.3 is valid for N rulings if a signal amplitude with the frequency distribution given by Eq. (4.20) is substituted for the single frequency f.

4.6 Comparison between WFIV and DLDV Measurements Employing a Rotating Disk

Measurements have been carried out to provide direct comparisons between the fringe image and differential Doppler techniques. No attempt was made to find the optimum operating region for either of the techniques. However, care was taken to ensure that all comparisons were made using similar parameters.

As a means of obtaining accurate known velocities the initial investigations employed backward scattering from particles situated on a rotating disk. These particles were the abrasive surface of silicon-

carbide grit paper. An adhesive was used to apply the paper to a flat disk and this provided a reasonably plane particle surface. The grit surface was aluminized to provide "particles" which would give a large scattered signal intensity. This allowed the use of a relatively low power light source.

A rotation of the disk, of angular velocity ω , results in a particle velocity

$$v = r\omega , \quad (4.24)$$

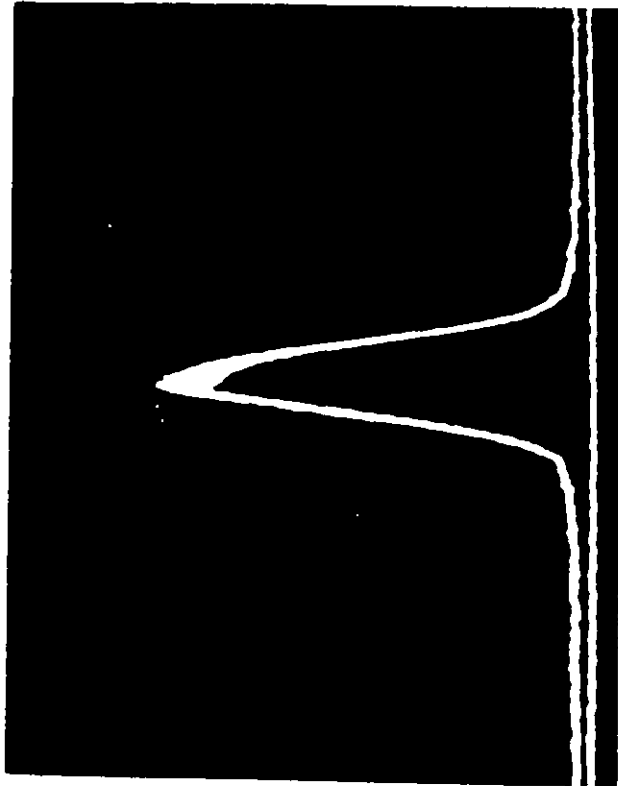
where r is the distance of the particle from the axis of rotation.

Observed spectra from #180 grit (80 μ diameter) silicon-carbide paper are shown in Fig. 4.13. All spectra were taken with a Hewlett-Packard 8553B/8552B spectrum analyser. The baseline in the photographs corresponds to zero incident radiation on the photocathode when all photomultiplier voltages are applied. Figure 4.13(a) represents a measurement using the differential Doppler laser technique similar to that discussed in Chapter 3, except that backward scattering was employed. Figure 4.13(b) represents a measurement using a fringe image method similar to that shown in Fig. 4.1.

Figures 4.13(a) and 4.13(b) give a direct comparison between the two techniques under nearly identical experimental conditions. In both cases, the fringes were approximately perpendicular to the

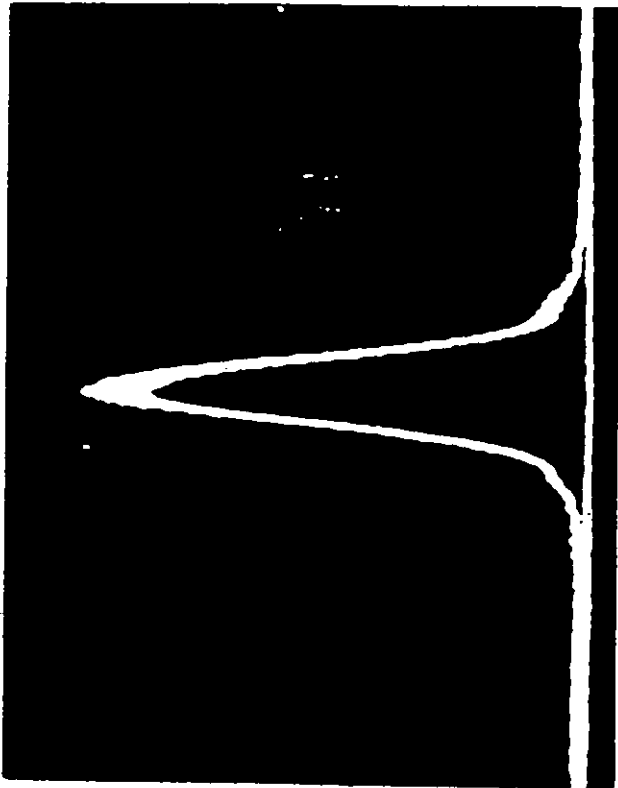
Fig. 4.13: Comparison between the differential Doppler laser and fringe image techniques using particles on a rotating disk. The differential Doppler laser measurement is represented by (a); the fringe image by (b). The center frequency of the signals is $f = 250$ kHz. The vertical scale is linear in amplitude.

20 KHZ



(a)

20 KHZ



(b)

direction of v , the fringe separation $d = 0.004$ cm, and the velocity $v = 1,000$ cm/sec. This results in $f = 250$ kHz. The total number of fringes (50) and the fringe area (2 mm wide by 1 mm high) were kept constant. Note, however, that all the fringes in the fringe image system have approximately equal intensity; those in the laser system have approximately a Gaussian intensity distribution. The spectrum analyser sensitivity, sweepwidth and bandwidth (3 kHz), and the photomultiplier dc current were constant for the two sets of data. The photocathode currents were approximately constant. In all cases, the axis of the incident beam was approximately normal to the plane of the disk. Furthermore the axis of the collected scattered radiation was at an angle of 65° relative to the axis of the incident beam and perpendicular to the direction of the fringes. A detector collection-lens aperture (ratio of lens-image distance to lens diameter) of approximately $f/10$ was employed.

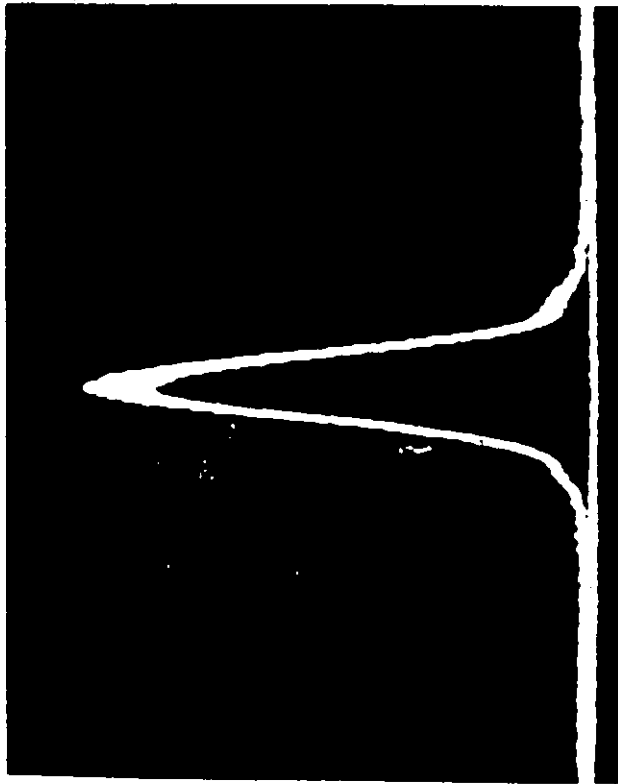
It should be clear from Fig. 4.13 that the fringe image system gave both a larger signal amplitude and a significantly better signal-to-noise ratio than the differential laser Doppler system. In addition, the laser signal has a larger frequency width, as expected from the Gaussian intensity distribution of the laser fringes. It should be noted, however, that particles on a flat rotating disk will generally provide close to optimum conditions for the operation of a fringe image system. The effective longitudinal extent of the fringe image, as described in section 4.3, can be made substantially greater than the particle depth. Therefore all the particles can pass through a

high visibility fringe region with the result that the ratio of fundamental-frequency signal to dc amplitude is close to the maximum possible. This should give, as it does experimentally, a signal-to-noise ratio and accuracy which is at least comparable to that from a differential laser Doppler system.

In section 4.5, it is shown that sidebands should be present in the signal represented by Fig. 4.13(b). Sidebands can be seen, but their amplitudes are much less than expected from inspection of Eq. (4.20). This results from several instrumental problems, such as a small non-uniformity in the illumination of the particular light source employed, and from frequency variations (e.g., resulting from fluctuations in disk speed and flatness) which increase the spectral width of the signal. Careful adjustment of the experimental parameters produced large amplitude sidebands, as shown in Fig. 4.14. For purposes of comparison, Fig. 4.14(a) is a repeat of the measurement shown in Fig. 4.13(b). Figure 4.14(b) is taken with identical experimental parameters as Fig. 4.14(a) (including dc photomultiplier current) except that the total number of fringes is decreased to 25 (1 mm wide by 1 mm high). In the latter case, the use of fewer fringes achieved a more uniform illumination of the fringe pattern because only the central portion of the Ronchi grating was imaged. In section 4.5, it is shown that the spectral width of the signal and the separation of the sideband zeros both vary approximately as $1/N$. A more uniform illumination, and an increased separation of the zeros, both contribute to the increase in the relative sideband amplitude. Comparison between Fig. 4.14(a) and 4.14(b) clearly illustrates the change

Fig. 4.14: Observation of signal sidebands. The measurement represented by (a) is a repeat of that shown in Fig. 4.13(b). For (b) the total number of fringes was reduced by a factor of two; the fringe spacing was unchanged. Both signal center frequencies are at $f = 250$ kHz. The vertical scale is linear in amplitude.

20 KHZ



(a)

20 KHZ



(b)

in the signal spectral width resulting from a decrease in the number of fringes.

Sidebands are not generally expected when the differential laser system is employed because of the Gaussian intensity distribution of the laser output. In a practical system, however, aberrations in the optical components can cause deviations from the Gaussian intensity distribution and result in the formation of sidebands. Such sidebands have been observed, but these usually have considerably lower amplitude than those observed with a fringe image system having an identical fringe separation and an identical number of fringes.

4.7 Summary

The results presented show that under certain circumstances, the fringe image technique can provide data which is comparable, in sensitivity and velocity measurement accuracy, to data obtained using the differential Doppler laser method. Comparison of the two optical techniques in fluid flow measurements are presented in the next chapter.

For many applications, the WFIV may have other advantages. These advantages include the following:

- 1) The system is very easy to set up and use, and capable of a high degree of mechanical stability. It can also be made small by a proper choice of optical components.
- 2) Operation can be in the shorter wavelength region of the spectrum where photomultipliers are the most sensitive. In this region, suitable lasers can be relatively expensive.

- 3) It is easy to obtain localized fringes. The longitudinal extent of the fringe image which contributes to the signal at frequency f is of the order of a few β ; the corresponding value of Δq is directly related to the lens aperture, and can therefore be controlled. The position of the localized fringes can be readily changed by moving either the lens, or the whole lens-grating system; this can be done very accurately. Consequently the position of the localized fringes can be accurately determined.
- 4) A large fringe spacing is easy to achieve. This is important if large flow particles are involved.
- 5) A system can be designed such that a fixed-frequency receiver can be used instead of a spectrum analyzer. Measurements are made by adjusting the fringe spacing to $d=v/f_0$, where f_0 is the receiver frequency. This adjustment may be made, for example, by employing a variable focal length lens or by varying the grating-to-lens distance. In the latter case, the lens position would also have to be changed in order that the fringe region remains in the same location.

In addition to the above advantages, the fringe image technique provides an excellent method of investigating the properties of non-coherent scattering. Such investigations are presented in Chapter 7.

CHAPTER 5

LAMINAR FLOW MEASUREMENTS

This chapter describes the two types of water flow systems employed in our experiments and the application of a DLDV and a WFIV to fluid flow measurements. The properties of the flow particles are also discussed.

A new and compact WFIV employing a microscope objective is described. The previous work on WFIV employed a rotating disk (Chapter 4). Here the system is evaluated from the results of measurements on laminar water flow. The sensitivity and accuracy of the WFIV were found to be comparable to those of a DLDV.

Frequency broadening and velocity resolution are also evaluated for both systems.

5.1 Constant-Head Flow System

The constant-head flow system, shown schematically in Fig. 5.1, was employed for laminar water flow measurements. Such a system provides a very stable water flow velocity. It does have the disadvantage, however, that the fluid can be contaminated by materials from readily available pumps.

The two constant-head reservoirs were kept at a fixed height. From the upper head tank, the fluid passes through the flow tube to a series of capillaries, which serve as flow resistances. The overall

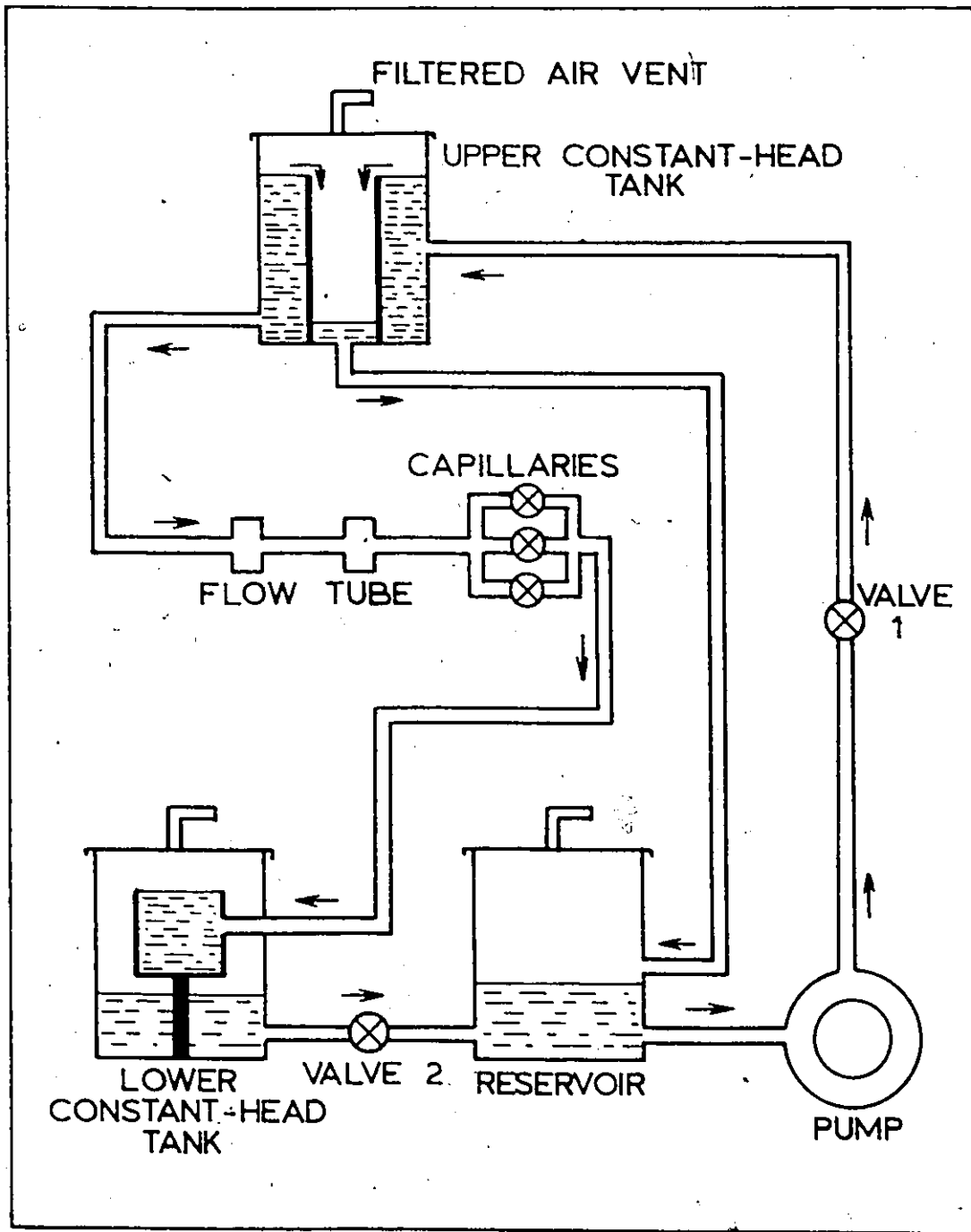


Fig. 5.1: Schematic of constant-head flow system. The arrows indicate the direction of fluid flow.

flow rate can be changed by selecting the capillaries. Next the flow proceeds from these capillaries to the lower constant-head tank. During velocity measurements, Valve 2 is open and the flow proceeds to the reservoir. Finally, a centrifugal pump returns the fluid to the upper constant-head tank. For our measurements, the fluid was water with a suspension of particles whose properties are described in detail in section 5.3.

It was arranged that the lower constant-head tank could be placed on a scale for measuring the volume flow rate. For this measurement, Valve 2 was closed. This measurement, and the dimension of the flow tube, allow calculation of the average flow velocity.

A Reynolds number as high as 10,000 can be achieved with our system. The upper tank level was maintained to within 0.5 mm at a height differential of about 2m. The pump flow rate was controlled by a combination of Valve 1 and an adjustable voltage input to the pump motor. A minimum of 6 liters of fluid could be employed. Excessive fluid is collected by the reservoir.

The test section of the flow tube is a straight, precision-bore glass tube of square cross-section, 1 cm square ID and approximately 30 cm long. It was determined that the walls were of sufficiently high optical quality to allow formation of a good fringe image. A cylindrical glass tube (1.3 cm ID x 5 cm long) is joined to each end of the tube in such a way as to provide a smooth transition from round to square cross-section. The flow tube is mounted on an adjustable platform that can be moved in three orthogonal directions by means of micrometers. This

is found to be more convenient than adjusting the optical paths.

5.2 Gravitational-Feed Flow System

The gravitational-feed flow system is primarily employed for measuring the effects of particle number density. Here, system cleanliness is more important than a very constant flow velocity. This is much easier to achieve if mechanical pumps are not employed.

The flow system consists of two tightly closed 3 liter cylindrical glass jars (each equipped with a filtered air vent), approximately 2 m of 6.5 mm ID Tygon tubing, a 30 cm length of precision bore square glass tubing for the test section (as described in the last section), and a set of capillaries to control flow velocity. The relative height of the jars was adjusted to provide a Reynolds number of 75 for most experiments. This corresponds to a velocity $v = 1.6$ cm/s in the centre of a 1 cm square flow tube. Unless otherwise stated, all particle number density investigations were carried out at the centre of the flow tube (i.e., $v = 1.6$ cm/s). Note that the water flow is essentially constant during the period of detection because the upper tank water level decreases very slowly. Distilled water, processed to remove residual particles, was used for the flow fluid. The processing consisted of prefiltration of the distilled water, followed in order by organic absorption, de-ionization, and final filtration. For the latter, the pore size was $0.45 \mu\text{m}$.

5.3 Flow Particles

Artificial seedings are not required in normal water flow measurements. For some applications, however, such as investigations of the effect of particle number density on SNR, particle seeding becomes necessary.

Measurements have been made employing 0.481 μm and 0.62 μm (all dimensions refer to diameter) polystyrene spheres, 1 μm latex spheres, 5.7 μm styrene divinylbenzene spheres, and homogenized milk. The standard deviation was 0.4%, 1.5%, 50%, and 26% for the 0.481 μm , 0.62 μm , 1 μm , and 5.7 μm , respectively. Microscope examination confirmed that the particles were spherical. No attempt was made to accurately determine the size and shape distribution of the milk particles. Preliminary measurements indicate that they are in the sub-micrometer to micrometer range. All particles for seeding were carefully weighed ($\pm 1\%$) and diluted with a suitable concentration of wetting agent (photo-flo) before being added to the flow system.

Initial experiments indicated that the processed water still contained a minute number of particles. From light scattering data, it was estimated that the residual particle number density, n , was approximately equivalent to 0.0075 wppm of 0.62 μm polystyrene particles. Note that all n values are by weight when stated in wppm. Otherwise n corresponds to the number of particles per unit volume.

All fluid seeding commenced at 0.02 wppm, taking into account the presence of residual particles. At somewhat higher concentrations (e.g., > 0.1 wppm) the scattering contribution from residual particles

can be neglected.

Table 5.1 lists the total number (N) of $0.62 \mu\text{m}$ and $5.7 \mu\text{m}$ particles in the probe volume for two optical systems. N was determined employing the value of n , in wppm, and the calculated weight of a single particle. It will be shown in Chapters 6 and 7 that the number of particles in the probe volume plays an important role in the determination of the power SNR.

5.4 Design of a Compact WFIV

As in the case of the DLDV, the spatial resolution of the WFIV depends on the optical quality of the focusing lens employed. Since very high quality camera or process lenses are expensive, we have used a microscope objective. Although microscope objectives generally have a very high resolution, they have short working distances: The higher the resolution is the shorter the working distance becomes (specially designed objectives are available with a working distance of about 3 cm at $N.A. = 0.28$).

Figure 5.2 illustrates the experimental arrangement for the compact WFIV. A Cooke microscope objective ($\times 10$, $N.A. = 0.28$) is used for the focusing lens. A Ronchi grating (1000 lpi) is placed in front of a 35 mm slide projector (500 watts) whose imaging lens has been removed. The distance between the grating and the image plane is about 8 cm; the working distance is about 0.5 cm. The receiving system is similar to the one previously described in section 3.5, except that a HP10534A balanced mixer is added to upshift the PMT output frequency.

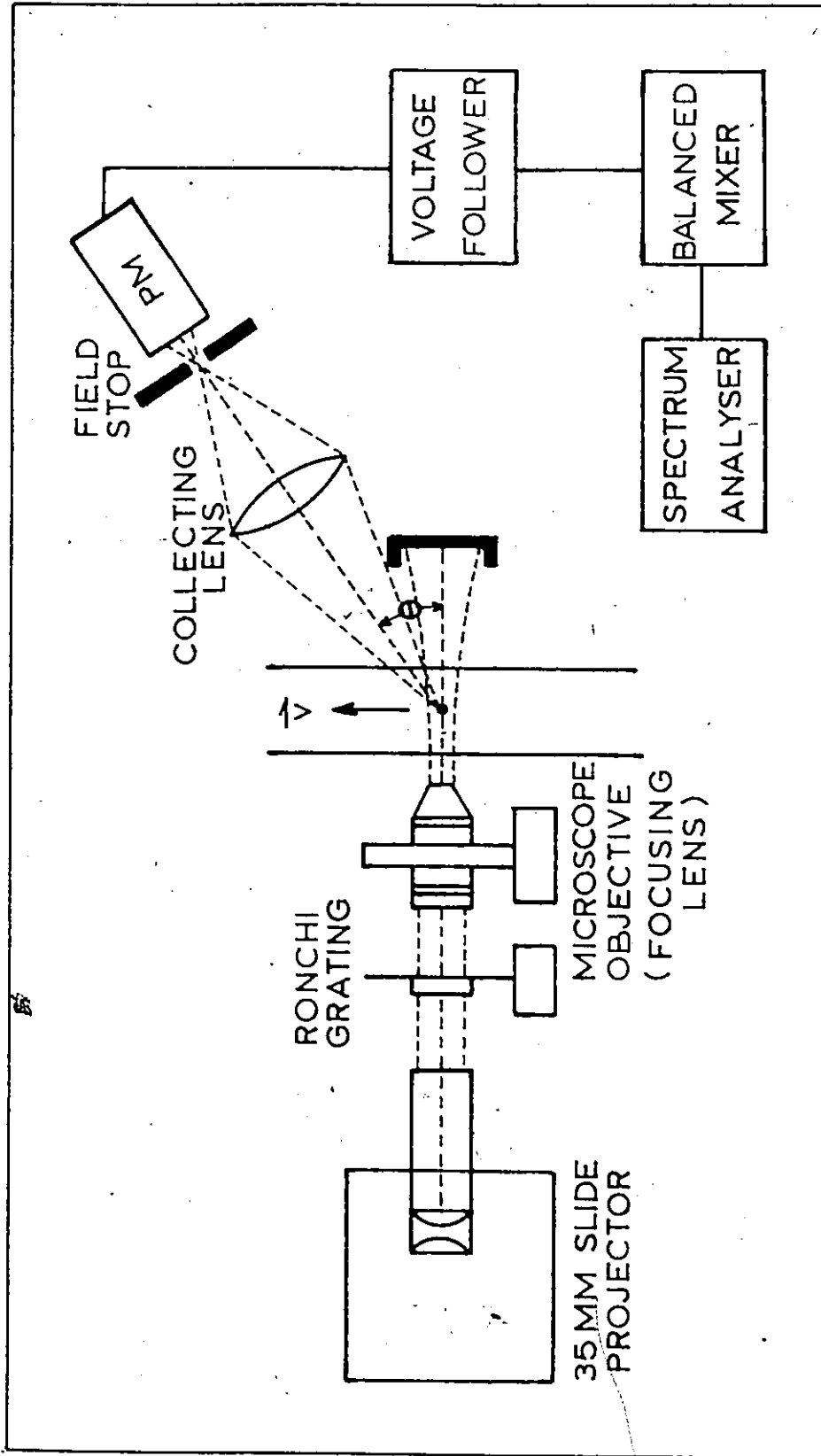
Table 5.1: Number of Particles in the Probe Volume. The diameters refer to 0.62 μm polystyrene and 5.7 μm styrene divinylbenzene particles

Density, n, by weight (wppm)	DLDV(V = $1 \times 10^{-7} \text{ cm}^3$) [†]		Number of particles, N, in the probe volume MFIV(V = $1.25 \times 10^{-4} \text{ cm}^3$)	
	0.62 μm	5.7 μm	0.62 μm	5.7 μm
*0.0075	0.006		7.1	
0.02	0.015	2×10^{-5}	1.9×10^1	0.025
0.1	0.075	1×10^{-4}	9.5×10^1	0.125
0.2	0.15	2×10^{-4}	1.9×10^2	0.25
1	0.75	1×10^{-3}	9.5×10^2	1.25
5	3.75	5×10^{-3}	4.7×10^3	6.25
10	7.5	1×10^{-2}	9.5×10^3	12.5
25	19	2.5×10^{-2}	2.4×10^4	31.25
100	75	0.1	9.6×10^4	125
400	300	0.4	3.8×10^5	500
2000	1500	2	1.9×10^6	2500

*Corresponds to the residual density (assumed approximately equivalent to 0.62 μm particles) in absence of seeding of the fluid.

† Not employed in the measurements. Given for reference only.

Fig. 5.2: Experimental arrangement of a compact WFIV. The focusing lens (microscope objective) forms an image of the Ronchi grating in the flow region. An image of the lamp filament is formed in the region of the microscope objective by the condenser lens. The detection angle θ ranges from 15° to 65° . The light cup is used to block the direct light beam from entering the PMT. The collecting lens is a 35 mm camera lens ($f = 50$ mm).



The collecting lens is identical to the one used for the DLDV. It was found experimentally that the usable detection angle ranges from $\theta = 15^\circ$ to $\theta = 65^\circ$ (measured from the direct light beam).

As in the case of the DLDV, the field stop (pinhole) also plays a very important role in the WFIV, especially in the measurements of fluid flow. It rejects extraneous light and in addition, it selects the location and size of the probe volume. This can be understood with the aid of Fig. 5.3. The proper size of the pinhole (to fully contain the lateral extent of the fringe image) should be determined experimentally and not theoretically since imperfection in the lens generally increases the image size. This necessitates a larger pinhole than calculated theoretically. The position of the field stop is best established by optimizing the SNR, as described in section 3.6.

Several configurations for the compact WFIV have been studied. Table 5.2 presents some of their optical and geometrical parameters. All parameters were measured except for the probe volume, which was calculated. A 25% improvement in visibility was obtained by inserting a filter ($5000 \text{ \AA} \pm 100 \text{ \AA}$) in front of the slide projector. Unfortunately this results in a large decrease in available intensity, together with a corresponding decrease in SNR.

For some applications, filters (on source and/or detector) may be required to minimize extraneous light. For the present studies, however, all WFIV experiments were performed in a dimly lit room. Note that total darkness is not required because the field stop will attenuate much of the extraneous radiation.

Fig. 5.3: Selective effect of field stop and lens aperture. The field stop is usually centered and attached to the PMT window. The whole assembly (field stop and PMT) is mounted on a x-y-z translation stage. Note that the light paths indicated by the "dashed" or "light" lines are blocked by the field stop.

Fig. 5-3

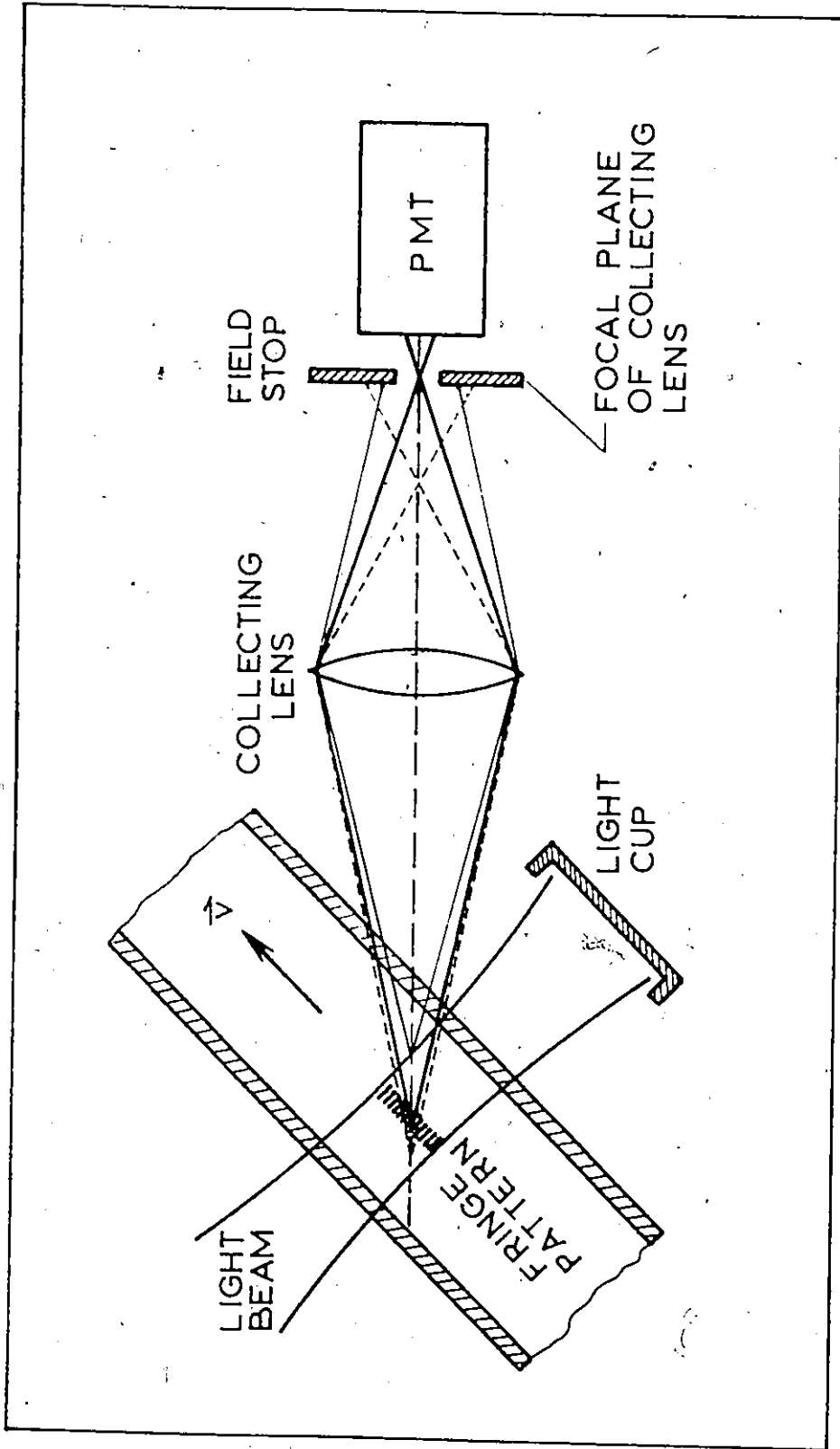


Table 5.2: Optical and Geometrical Parameters for Various WFIV*

System Number	Fringe Spacing (μm)	Aerial Resolution (1/mm)	Visibility A (White Light)	Visibility B ($\lambda=5000 \text{ \AA}$ $\pm 100 \text{ \AA}$)	Longitudinal extent of the probe volume (μm)	Calculated probe volume for $\theta = 30^\circ$ (cm^3)
A	11.7	85	0.61	0.72	700	5.8×10^{-5}
B	6.4	153	0.55	0.63	130	3.3×10^{-6}
C	4.6	218	0.47	0.59	70	9.1×10^{-7}
D	3.4	293	0.42	0.54	60	4.2×10^{-7}
E	2.8	358	0.37	0.45	50	2.4×10^{-7}

* The focusing lens employed for all systems is a Cooke microscope objective (X10, N.A. = 0.28)

For convenience, the longitudinal extent of the probe volume was taken as the distance between the first planes of zero visibility located either side of the peak. Note that the probe volume was calculated using the following parameters: a circular pipe containing approximately 40 fringes with a pipe length equal to half of the longitudinal extent value listed in Table 5.2.

5.5 SNR

The influence of visibility and particle number density on SNR were studied for the various WFIV. All measurements employed the same gravitational-feed flow system which was seeded with 50 wppm of 5.7 μm styrene divinylbenzene particles. Experimental and theoretical results are listed in Table 5.3. The theoretical results were obtained from Eq. (7.15) and Eq. (7.19). For the present, we need only note that the SNR of a WFIV is proportional to the square of the fringe visibility, and is directly proportional to the number of particles in the probe volume, N , if N is less than one. The SNR is independent of N if N is larger than one.

It can be seen from Table 5.3, that the SNR's are nearly identical for systems A and B; here, the N 's are very different but larger than one. However, for systems C, D, and E, the N 's are different and less than one (resulting from changes in the probe volume). In these cases, it is expected that the SNR should be proportional to the product of N and to the square of the visibility. This is confirmed by the excellent agreement between theory and experiment presented in the table. In all cases,

Table 5.3: Power SNR's for Various WFIV. The Optical and Geometrical Parameters are Listed in Table 5.2

System Number	Fringe Visibility V	Particles Number N [*]	Measured SNR (Absolute) (dB)	Measured SNR (Relative) (db)	Calculated ⁺ SNR (Relative) (dB)
A	0.61	29	20 ± 1	0	0
B	0.55	1.6	19 ± 1	- 1	- 0.9
C	0.47	0.4	15 ± 2	- 5	- 6.2
D	0.42	0.2	10 ± 2	-10	-10.1
E	0.37	0.1	6 ± 2	-14	-14.3

* N is the number of particles in the probe volume taken from a particle concentration of 50 wppm of 5.7 μm divinylbenzene particles.

⁺ For A and B, Eq. (7.14) was used. For C, D, and E, Eq. (7.18) was used. The calculated values are relative to that of A.

the fringe intensities were identical, to within experimental error.

Further studies of the influence of particle number density on SNR are presented in Chapter 7. There it is concluded that the WFIV performs best for N approximately equal to 1, and with a fringe pattern of high visibility. For this reason, system configuration B was chosen for the following laminar water flow measurements. In addition, its longitudinal extent was comparable to that of the DLDV used for similar measurements.

5.6 Laminar Flow Measurements with a DLDV and a WFIV

The following measurements were not carried out to obtain results of significance to fluid mechanics, but to evaluate the performance of the optical velocimeters. Our experimental results, as well as those of other researchers [29, 48, 49, 50], contribute to the growing evidence that optical velocimeters have considerable potential. These results also demonstrate some of the difficulties of employing optical velocimeters, and of carrying out the signal analysis.

The DLDV and the WFIV which were used for the laminar water flow measurements are described in sections 3.5 and 5.4, respectively. The optical and geometrical parameters for the two systems are summarized in Table 5.4.

The detected signal ranged from 0 Hz to 10 kHz for the DLDV and 0 Hz to 2.5 kHz for the WFIV. Because of spectrum analyser limitations at low frequencies (high noise, etc.), the PMT output was up-shifted in frequency (600 kHz) by use of a balanced mixer. The shifted PMT output frequency was measured from the spectrum analyser CRT display

Table 5.4: The Optical and Geometrical Parameters for the DLDV and the WFIV Employed in the Laminar Flow Measurements

Parameters*	DLDV	WFIV
Light source	2.5 mW He-Ne Laser	500 W Tungsten filament
Wavelength	6328 Å	White Light
Wavefront	Coherent	Non-Coherent
Fringe spacing	1.6 μm	6.4 μm
Fringe number	23 ± 2	40 ± 2
Fringe visibility	0.93	0.55
Longitudinal extent of the probe volume	171 μm	130 μm
Lateral extent of the probe volume	34.3 μm	252 μm
Probe volume†	$1 \times 10^{-7} \text{ cm}^3$	$3.3 \times 10^{-6} \text{ cm}^3$
Detection angle	0°	30°
Flow seeding	25 wppm (0.62 μm Polystyrene)	50 wppm (5.7 μm Divinylbenzene)
Number of particles in the probe volume	≥ 19	≥ 1.6

*The origins and definitions of the parameters can be found in Table 3.2 for the DLDV, and in Table 5.3 for the WFIV.

†Note that both probe volumes have circular cross-section.

unit with an accuracy of about $\pm 3\%$.

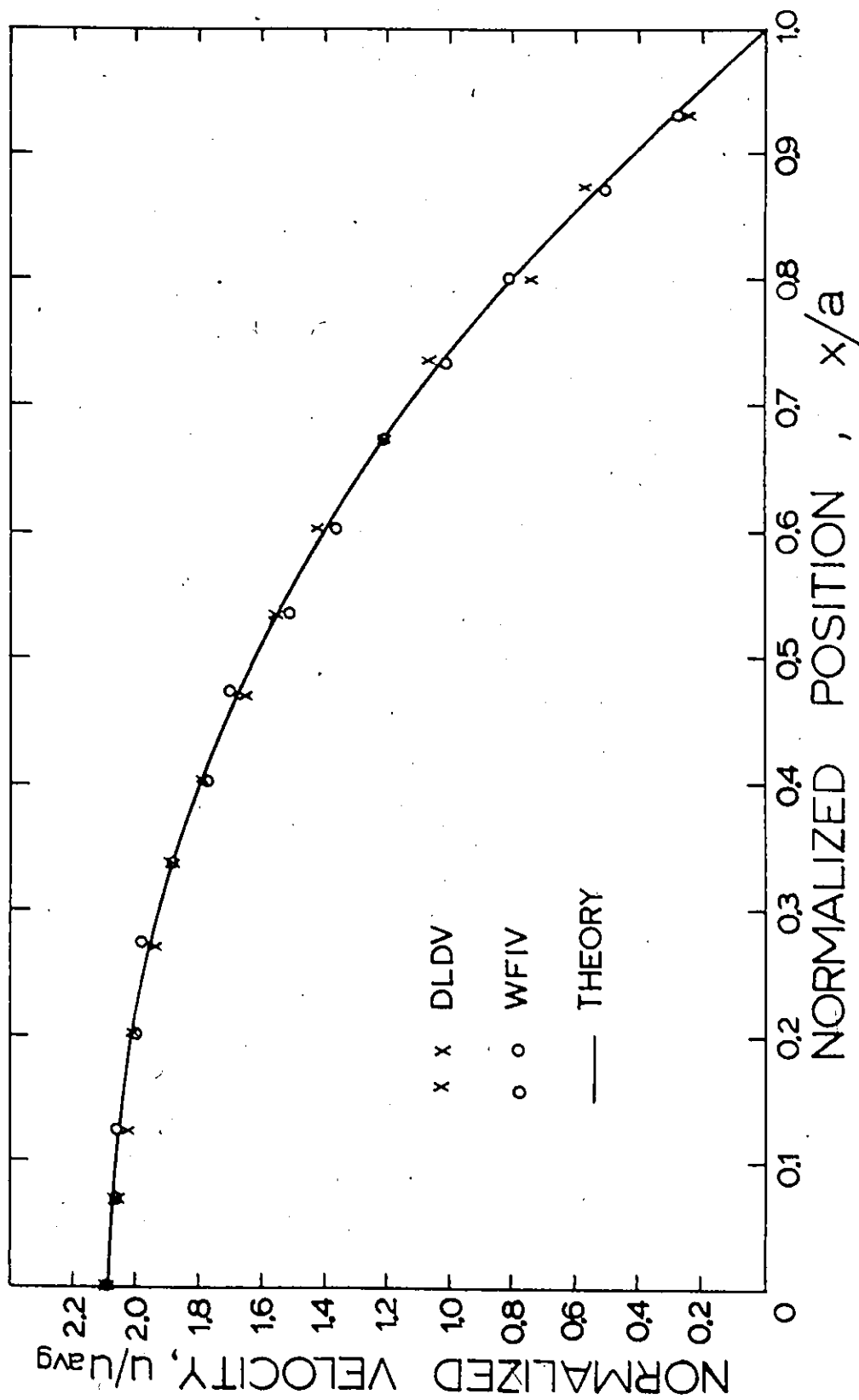
The measurements were made at the fully developed region about 15 diameters downstream of the 1 cm square duct. The constant-head flow system was used to maintain a constant flow velocity of 1.6 cm/s at the center of the tube. This corresponds to a volumetric flow rate of $0.75 \text{ cm}^3/\text{s}$ ($R_e = 75$). The results of measurements for both velocimeters are shown in Fig. 5.4. Excellent agreement is found between the experimental points and the theoretical curve, as calculated in the next section. The agreement between the two sets of experimental data indicates that, for our flow system and instrumentation, the WFIV and the DLDV provided similar sensitivity and accuracy.

5.7 Analysis of Laminar Flow in a Square Duct

This section briefly describes the origin of the theoretical curve presented in Fig. 5.4, and discusses some of the measurement results.

The problem of determining the entrance length in a rectangular channel was treated by the method of linearizing the Navier-Stokes equation [51]. The resulting approximate equation was used to generate a mathematical expression for the axial velocity in the entire region. The approximate solution for the velocity profile at a given cross-section is given by [51].

Fig. 5.4: Fully-developed velocity profile of laminar water flow through a square duct. x is the displacement from the center axis. $2a$ is the width of the square tube ($a=0.5$ cm). The solid line represents the theoretical velocity profile, some points of which are given in Table 5.5.



$$\frac{u}{u_{avg}} = \left(\frac{\pi^2}{4}\right) \left\{ \sum_{m,n=1,3,5,\dots}^{\infty} \frac{(-1)^{\frac{m+n}{2}} - 1}{mn[m^2 + n^2\gamma^2 + (2\beta a/\pi)^2]} \cos(m\pi x/2a) \cos(m\pi y/2b) \right\} / \left\{ \sum_{m,n=1,3,5,\dots}^{\infty} \frac{1}{m^2 n^2 [m^2 + n^2\gamma^2 + (2\beta a/\pi)^2]} \right\} \quad (5.1)$$

where $2a$ is the width and $2b$ is the height of the duct, γ is the aspect ratio (a/b), x, y, z , are the coordinate axes centered at the centerline of the duct, and z is the direction of the flow. β is a parameter such that the equation assumes a uniform velocity profile at $\beta = \infty$ and becomes a fully-developed velocity at $\beta = 0$. Any other value of β is a function of z . For a square duct, the fully-developed velocity profile on the central plane ($y=0, \beta=0, \gamma=1$) is thus given by

$$\frac{u}{u_{avg}} = \left(\frac{\pi^2}{4}\right) \left\{ \sum_{m,n=1,3,5,\dots}^{\infty} \frac{(-1)^{\frac{m+n}{2}} - 1}{mn(m^2 + n^2)} \cos(m\pi x/2a) \right\} / \left\{ \sum_{m,n=1,3,5,\dots}^{\infty} \frac{1}{m^2 n^2 (m^2 + n^2)} \right\} \quad (5.2)$$

It should be noted that Eq. (5.2) gives results nearly identical to those obtained from an analytic solution [52]. Numerical values of Eq. (5.2) for ten normalized positions are listed in Table 5.5. It can be seen that the ratio of center line velocity to average velocity in the fully-developed region is given by

Table 5.5: Fully-Developed Velocity Profile, u/u_{avg} , for a Square Duct

x/a *	u/u_{avg}
0.0	2.096
0.1	2.078
0.2	2.024
0.3	1.933
0.4	1.802
0.5	1.630
0.6	1.412
0.7	1.145
0.8	0.824
0.9	0.442
1.0	0.000

* Fractional position where $x = 0$ refers to the center line point, and a equals to the half-width of the square duct.

$$\frac{U_o}{U_{avg}} = 2.096 \quad (5.3)$$

This is in excellent agreement with our measured value

$$\frac{U_o}{U_{avg}} = 2.1 \quad (5.4)$$

obtained from both the DLDV and the WFIV.

LDV measurements on a square duct have also been conducted by Goldstein and Kreid [29], and on a rectangular duct by Snyder and Goethert [49]. In general, there was excellent agreement between experiment and theory in the fully-developed region, where an analytic solution is available (approximations have to be used in other regions). In the developing region, the velocity distribution is considerably flatter near the axis of the duct than predicted by analysis. It is also suggested in reference [29] that a somewhat greater than the minimum entrance length is required for development of the velocity profile. For this reason, all of our measurements were made at approximately twice the minimum entrance length.

5.8 Investigations of Frequency Broadening

It has been mentioned earlier that the spectra of optical velocimeters possess an inherent broadening which is due to the finite transit time of the particles through the probe volume. A further broadening can occur because of spatial velocity gradients. Complete analyses of spectral broadening in LDV were given by Edwards et al.,

[53, 54]. Here we briefly describe their results, and show that the analysis can also be applied to the WFIV.

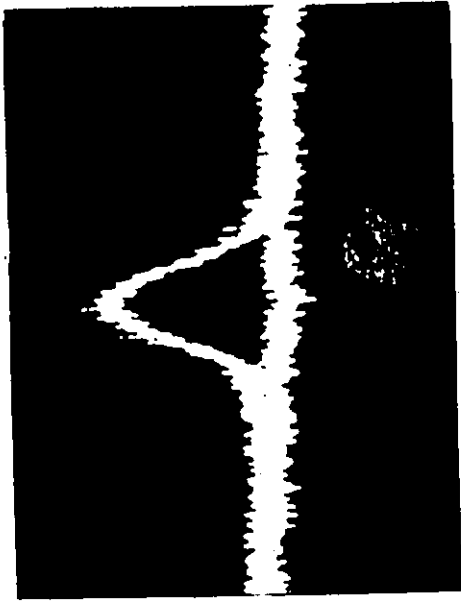
The broadening from the finite transit time is generally symmetrical because of the assumed symmetry of the probe volume. However, the broadening from the spatial velocity gradient is asymmetric, which results in a skewness of the spectrum. Moreover, due to the velocity gradient, the mean frequency of the spectrum is always lower than the Doppler shift computed from the velocity of the fluid at the center of the probe volume. The magnitude of the deviation can be significant, especially when making measurements close to the wall in narrow channels (= 0.1 cm diameter). For our case, the deviation is less than 1% at $x/a = 0.95$, and can be neglected. Figures 5.5 and 5.6 present some typical observed spectra taken during laminar flow measurements employing the DLDV and the WFIV, respectively. In order to achieve satisfactory SNR, the particle seedings and the IF bandwidth for the two systems were different. The normalized bandwidth, $\Delta f_D/f_D$, can be evaluated and used for comparison purposes. Results are presented in Table 5.6. The IF correction was applied according to

$$(\Delta f_D)^2 = (\Delta f')^2 - (IF)^2, \quad (5.5)$$

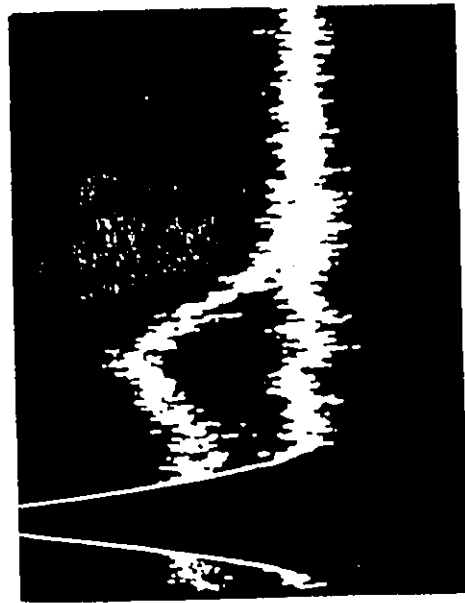
where $\Delta f'$ is the FWHM of the spectrum, and the IF is the IF FWHM of the spectrum analyser.

It can be seen from Table 5.6 that the normalized parameter, $\Delta f_D/f_D$, increases as the magnitude of the velocity gradient increases.

Fig. 5.5: Frequency spectra of the DLDV. The spectra correspond to different probe volume positions in the flow tube, as given in Table 5.6. 0.62 μm polystyrene particles were employed. The power SNR's are approximately 24 dB. The large peaks in (c) and (d) are the drive frequency (600 kHz) of the balanced mixer.

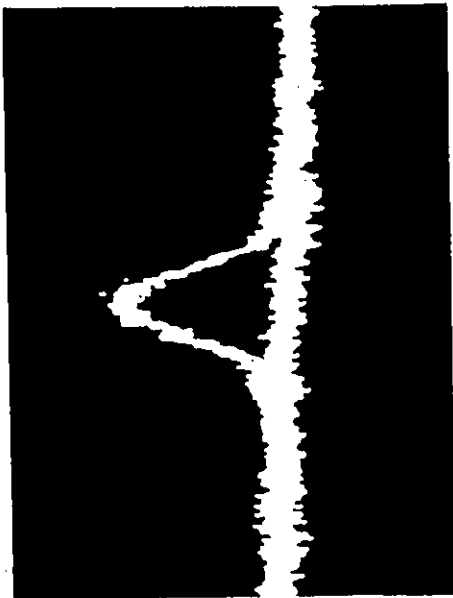


(b)



(d)

10 μ m



(a)



(c)

Fig. 5.6: Frequency spectra of the WFIV. 5.7 μm styrene divinyl-
benzene particles were employed. The power SNR's are approxi-
mately 19 dB. The "spiking" is due to the small number of
particles in the probe volume. Refer to caption data in
Fig. 5.6, and to Table 5.6, for further details.



(b)



(d)

1cm



(a)



(c)



Table 5.6: Frequency Broadening for-DLDV and WFIV

Figure Number	Normalized* Positions (x/a)	Spectrum Analyser I.F. Bandwidth (kHz)	Spectrum Analyser Scan width ^o (kHz/cm)	Linewidth [†] before I.F. Correction Δf (kHz)	Linewidth [†] after I.F. Correction Δf_D (kHz)	Peak Frequency f_D (kHz)	Normalized Broadening Parameter $(\Delta f_D/f_D)^{1/2}$
(a)	0	0.3	1.0	1.1	1.06	10.0	0.11
Fig. 5.5 (b)	0.533	0.3	1.0	1.3	1.26	7.2	0.17
(DLDV) (c)	0.867	0.3	1.0	1.3	1.26	2.4	0.52
(d)	0.933	0.1	0.5	~ 1.1	1.09	1.2	~ 0.9
(a)	0	0.1	0.5	0.18	0.15	2.50	0.06
Fig. 5.6 (b)	0.533	0.1	0.5	0.22	0.20	1.80	0.11
(WFIV) (c)	0.867	0.1	0.2	0.18	0.15	0.60	0.25
(d)	0.933	0.03	0.1	~ 0.11	0.11	0.32	~ 0.33

*The accuracy of determining the positions is about $\pm 1.5\%$

[†]The accuracy of determining the linewidth is about $\pm 15\%$

^oIn all cases, the scan rate was 2 s/cm

Note that the steepest gradients, and hence the greatest broadening, exist near the wall, where x/a approaches unity. This holds for both the DLDV and the WFIV. Note also that the broadening due to the finite volume effect is inversely proportional to the fringe number, N , as expected at $x/a = 0$. For laminar flow and negligible velocity gradient, we find empirically that this broadening is best represented by

$$\left(\frac{\Delta f_D}{f_D}\right)_0 = \frac{2}{N} \quad (5.6)$$

From the above it can be seen that the spectral characteristics of the DLDV and the WFIV are very similar under similar operating conditions.

5.9 Summary

This chapter describes the two fluid flow systems employed in this work and the properties of the flow particles. For reference, Table 5.1 lists the number of particles in the probe volume for most experimental measurements employed in this thesis.

Comparisons are made between laminar water flow measurements employing a DLDV and a WFIV. These measurements were made at the fully developed region. There is excellent agreement between theory and experiment. It is found that, for our flow system and instrumentation, the WFIV and the DLDV provide similar sensitivity and accuracy.

The frequency broadening of the signal due to transit time and velocity gradient effects are investigated for both the DLDV and WFIV. It is found that both velocimeters possess similar broadening characteristics.

CHAPTER 6

SNR INVESTIGATIONS OF A DLDV

Preliminary investigations of the SNR related to the instrumental design, such as the effect of pinholes, are described in Chapter 3. This chapter describes in detail some additional parameters which affect the SNR of a DLDV. Here the SNR is derived on the basis of optical heterodyning and Mie scattering theory. Results of carefully controlled experiments are then compared with this theory.

From consideration of the effect of particle number density on SNR, it is found that a DLDV operates primarily in the coherent mode. However, the results of measurements of the dependence of SNR on detection angle indicate that the theory developed does not completely describe the measurements. Considerable further effort is required to resolve this difference.

It is shown that the SNR is inversely proportional to velocity. Thus, relatively high power laser sources are required in the detection of very high velocities.

6.1 Derivation of the SNR (Coherent Detection)

Optical heterodyning and Mie scattering theory form the basis of the following derivation of the power SNR in a DLDV. In this section we ignore the fringe pattern in the scattering region. It is not our intention to derive highly theoretical formulae, but to find a pheno-

menological equation that can be used to describe the principal effects of particle number density and of several other parameters.

Let E_1 and E_2 be the electric fields scattered from a given particle due to incident laser beams 1 and 2, respectively. This requires that the particle is illuminated simultaneously by the two beams, which are produced from a single laser. The scattered fields E_1 and E_2 are known to be "perfectly" aligned. When made incident on a square law detector they will produce "perfect" heterodyning. No limit is imposed on the size of the receiving aperture. It has been shown (section 2.2) that the power SNR is given by

$$\text{SNR} = \frac{\eta A}{2hfB} \frac{(E_1 E_2)^2}{E_1^2 + E_2^2} = \frac{P_1 P_2}{P_1 + P_2} \quad (6.1)$$

where η is the quantum efficiency, A the photocathode area radiated, h Planck's constant, f the laser frequency, and B the noise bandwidth of the signal processing electronics. P_1 and P_2 are the powers of the two scattered light beams. It has also been shown [55] that the power SNR will be maximum when the detector is placed along the bisector in the forward scattering mode, as shown in Fig. 6.1. If both incident beams have equal intensity, then $P_1 = P_2 = P_s$, where P_s is the power scattered from either beam by a single particle. Therefore

$$\text{SNR} \propto P_s \quad (6.2)$$

It should be noted that use of the configuration which provides maximum SNR does not result in loss of generality. Instead it simplifies derivations because of the symmetry in the Mie scattering lobe. The results

can be readily applied to any other detection angle apart from those which contain a direct laser beam.

Some of the flow system parameters are shown in Fig. 6.1. The probe volume is at a mean distance x from the wall of the flow tube of width L . Photomultipliers PM1 and PM2 allow simultaneous measurement of transmitted beam intensity and Doppler signal, respectively. It is assumed that the fluid is uniformly seeded with monodispersed particles of number density n .

Consider a beam of intensity $I(x)$ incident on particles in the scattering volume V . The radiance in the direction θ , taken with respect to the forward direction of the incident beam, is given by

$$J(\theta) = \beta(\theta)I(x)V \quad (\text{W-sr}^{-1}) \quad (6.3)$$

where $\beta(\theta)$ is the angular volume-scattering function ($\text{cm}^{-1}\text{sr}^{-1}$). The scattered radiant power at the receiving aperture, of solid angle Ω , is given by

$$P'_s(\theta) = I(x)V \int_{\Omega} \beta(\theta)d\Omega \quad (\text{W}) \quad (6.4)$$

where $d\Omega = 2\pi\sin\theta d\theta$. In the case of independent single-particle scattering the angular volume scattering function can be expressed in terms of the scattering function per particle obtained from Mie theory, and the colloidal size distribution [56]. A brief discussion of Mie theory is presented in Appendix A. When the incident radiation is unpolarized

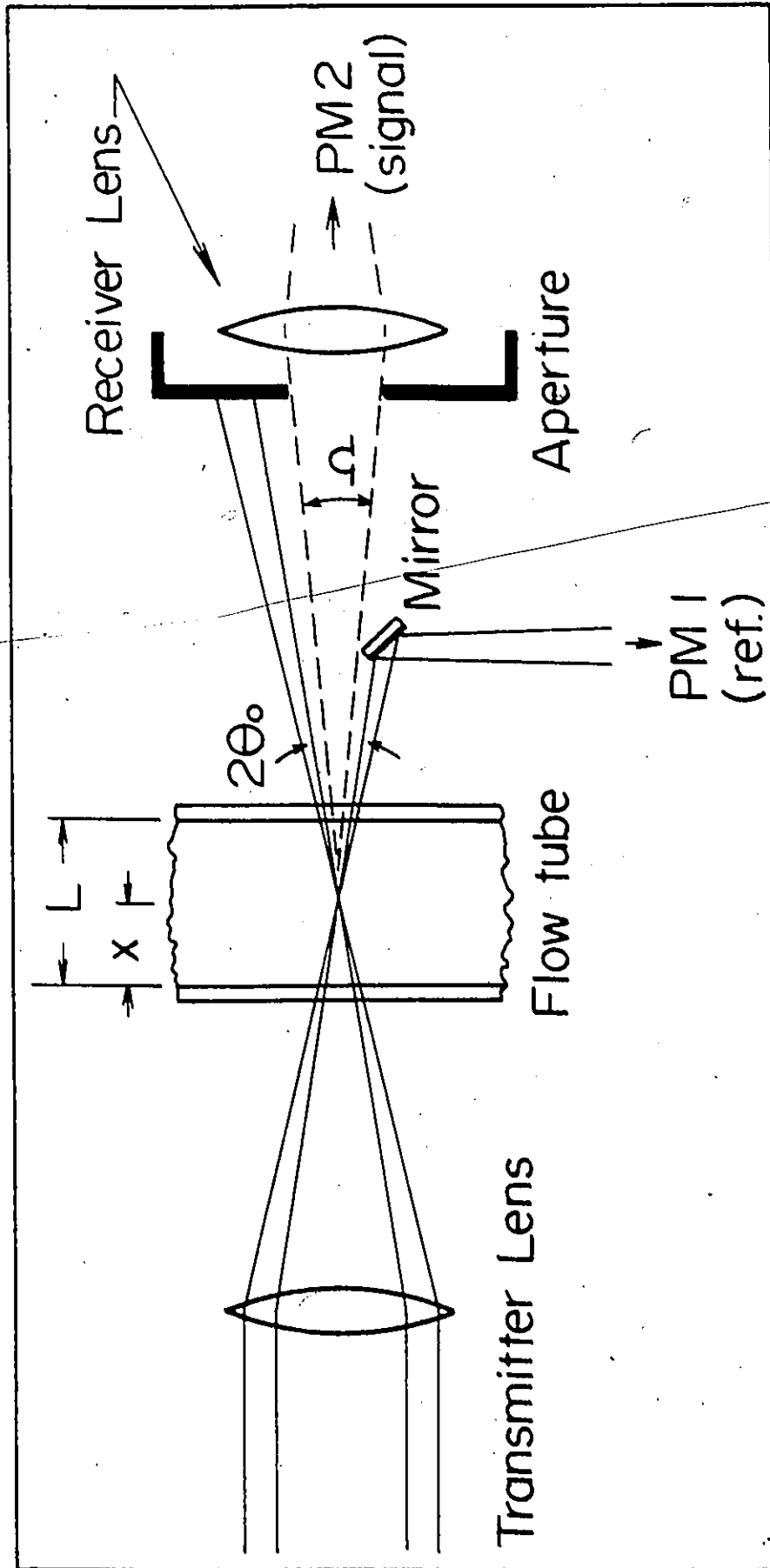


Fig. 6.1: Optical parameters for the flow tube.

$$\beta(\theta) = \frac{\lambda^2}{8\pi^2} \int \frac{dn}{d\alpha} [i_1(\theta, \alpha, m) + i_2(\theta, \alpha, m)] d\alpha \quad (6.5)$$

where $\alpha = 2\pi r/\lambda$ is the ratio of the particle circumference to the wavelength in the medium, m is the index of refraction of the particle relative to the surrounding medium, and $\frac{dn}{d\alpha}$ is the particle number density having radii between α and $\alpha + d\alpha$. Function $i_1(\theta, \alpha, m)$ is the scattering function per particle for light polarized perpendicular to the plane of scattering, while $i_2(\theta, \alpha, m)$ is the corresponding function for light polarized parallel to the plane of scattering. Note that the plane of scattering is defined by the direction of the incident beam and the direction of observation. Let $i(\theta, \alpha, m) = \frac{1}{2}[i_1(\theta, \alpha, m) + i_2(\theta, \alpha, m)]$. Then substitution of Eq. (6.5) into Eq. (6.4) yields

$$P'_S(\theta) = \frac{\lambda^2}{4\pi^2} I(x)V \int_{\Omega} \int_{\alpha} \frac{dn}{d\alpha} i(\theta, \alpha, m) d\alpha d\Omega \quad (6.6)$$

Considerable simplification results if it is assumed that the particles have a uniform size (i.e., $\alpha = \alpha_0$) and that the scattering function $i(\theta, \alpha, m)$ is relatively independent of θ (i.e., a small solid angle). Thus for $\theta = \theta_0$,

$$P'_S(\theta_0) = (\lambda^2/4\pi^2) I(x)V n i(\theta_0, \alpha_0, m) \Omega \quad (6.7)$$

In the above derivation it is assumed that no attenuation of $I(x)$ occurs in the scattering medium. If particle absorption is neglected, as is done in this work, then scattering of the incident beam results in an attenuated beam at the probe volume. This is given, to a

good approximation, by

$$I(x) = I_0 e^{-\sigma n x \sec \theta_0} \quad (6.8)$$

where I_0 is the intensity at x in the absence of scattering and σ the mean scattering cross-section of the particles. There is also secondary scattering of the scattered radiation. Therefore $P'_s(\theta_0)$ will decay exponentially in the distance $(L-x)$ shown in Fig. 6.1. Hence the actual power at the receiver is $P_s(\theta_0) = P'_s(\theta_0) e^{-\sigma n(L-x)}$, or

$$P_s(\theta_0) = (\lambda^2/4\pi^2) I_0 V n i(\theta_0, \alpha_0, m) n e^{-\sigma n L - \sigma n x (\sec \theta_0 - 1)} \quad (6.9)$$

If θ_0 is small, which holds for most practical systems, then Eq. (6.9) is essentially independent of x , and therefore of the location of the probe volume. Using this assumption, and combining Equations (6.2) and (6.9), results in

$$\text{SNR} \propto P_0 V n i(\theta_0, \alpha_0, m) n e^{-\sigma n L} \quad (6.10)$$

where P_0 has been substituted for I_0 . Here P_0 is the incident beam power. It is clear from Eq. (6.10) that the SNR is proportional to n for small n , but deteriorates at large n values. By differentiation of Eq. (6.10) the optimum SNR is achieved when

$$n = n_0 = 1/\sigma L \quad (6.11)$$

Moreover, the optimum condition can be established for a given experiment

by measurement of the transmitted direct beam power, P_t . For small θ_0 , $P_t(L) = P_0 e^{-\alpha nL}$. Substitution of Eq. (6.11) results in

$$P_t(L) = e^{-1} P_0 = 0.37 P_0 \quad (6.12)$$

Thus the optimum number density will occur when the transmitted beam power is reduced to 1/e of the value in the absence of particles.

Equation (6.10) indicates that the SNR is proportional to α . However this only holds for small values of α because of the coherence requirements for the detection of the scattered radiation, as given in the next section.

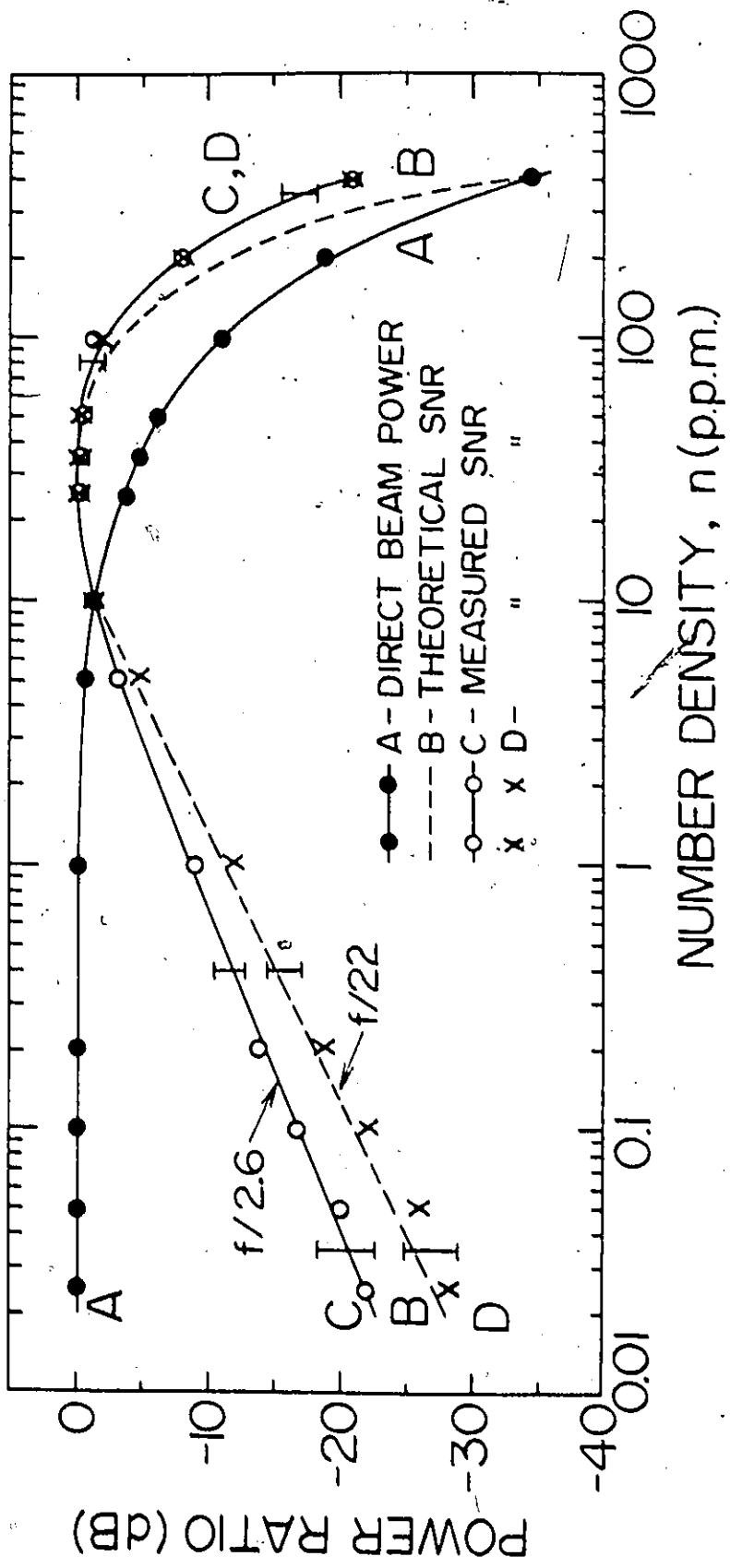
6.2 Effects of Aperture Size and Number Density on SNR

The experimental arrangement for the DLDV SNR measurements is identical to that described in section 3.5, except for the additional photomultiplier (PM1) as shown in Fig. 6.1. Typical spectra for a moderate particle concentration (25 wppm) are shown in Figures 3.10 and 3.11. Similar data were obtained for other particle concentrations. Note that for all DLDV measurements, the pinhole diameter was 35 μm , the IF bandwidth was 0.3 kHz, the scan-width was 0.5 kHz/cm, the scan time was 2 s/cm, and the centre frequency was 10 kHz ($v = 1.6 \text{ cm/s}$). Reliable SNR results can only be obtained from a well-defined signal which is free from excessive stray light and background scattering. Figure 3.11 illustrates that these conditions exist for our data.

Values for the number of particles in the probe volume are presented in Table 5.1 for the particles employed.

Experimental data for 0.62 μm polystyrene particles is presented in Fig. 6.2 for a flow tube with $L = 1$ cm and velocity $v = 1.6$ cm/s. Curve A represents the relative transmitted power P_t as measured by PM1. Curve B is the relative theoretical SNR for a small receiving aperture and is calculated from Eq. (6.10). For this curve, the scattering cross-section σ was calculated from Mie theory [56]. All other parameters, except n , are constant. For Curve B, the maximum SNR was assumed identical to the maximum experimental SNR obtained. Curves C and D are the experimental SNR's for receiving apertures of $f/2.6$ and $f/22$, respectively. The former was limited by the lens dimensions. In the case of the latter, the aperture satisfying the coherent condition, $A\Omega' \leq \lambda^2$, was chosen, where A is the area of the receiver aperture and Ω' the solid angle seen by the detector. The coherent condition ensures effective heterodyning for fields scattered from different particles in the probe volume. Little is gained by increasing Ω at large number densities because heterodyning between fields scattered from different particles becomes dominant. However, heterodyning of fields scattered from the same particle will benefit from an increased Ω , provided that the detection system can distinguish individual particles. These qualitative statements on the effect of detector aperture explain, in part, the differences in the initial slopes of curves C and D in Fig. 6.2. Note that the maximum SNR for both experimental curves is identical (31 ± 1 dB) and occurs at or near the $1/e$ point (-4.3 dB) of curve A, in agreement with the value $n_0 = 34$ wppm calculated from Eq. (6.11). Differences between experiment and theory at the highest number densities probably result from increased Doppler signal due to

Fig. 6.2: DLDV SNR measurements employing 0.62 μm polystyrene particles. Flow tube width $L = 1$ cm. Curve A is the relative transmitted power of the direct beam. Curve B is the relative theoretical SNR. Curves C and D are the experimental SNR's for receiving apertures of $f/2.6$ and $f/22$, respectively. In both cases, the maximum SNR was 31 dB. Some typical error bars are shown.



multiple scattering. The smallest n value measured corresponds to approximately 0.02 particles in the probe volume.

Measurements were repeated using identical experimental parameters except for the use of a different flow tube, for which $L = 0.2$ cm, and for a decrease in the Reynolds number to maintain $v = 1.6$ cm/s. This makes possible a careful check on the reliability of the previous data. Results are presented in Fig. 6.3. All comments in the previous paragraph apply except that the calculated $n_0 = 172$ wppm, the maximum SNR is 36 dB, and that the smallest n employed corresponds to approximately 0.08 particles in the probe volume. Clearly the main effect of decreasing L is to shift the maximum SNR to a correspondingly larger n . Furthermore the maximum SNR should be proportional to n_0 . The increase of 5dB obtained experimentally when L was changed from 1 cm to 0.2 cm agrees, to within experimental error, with a predicted increase of 7dB.

It was of interest to check if the general behaviour of the SNR, as a function of n , was changed when a range of particle sizes was present in the flow region. Simple considerations would indicate that Eq. (6.10), derived on the basis of uniform particle size, might also be applicable in this case, particularly for small values of n . Briefly, each interval of particle size, $\Delta\alpha$, would have an SNR proportional to n . Consequently, the resultant should be proportional to n . For these measurements we employed homogenized milk as the seeding in the flow tube with $L = 1$ cm and $v = 1.6$ cm/s. All other physical parameters were identical to the two previous cases. Results are presented in Fig. 6.4. Note that in this case n represents the solid content of milk, calculated on the assumption that milk contains 12.5%

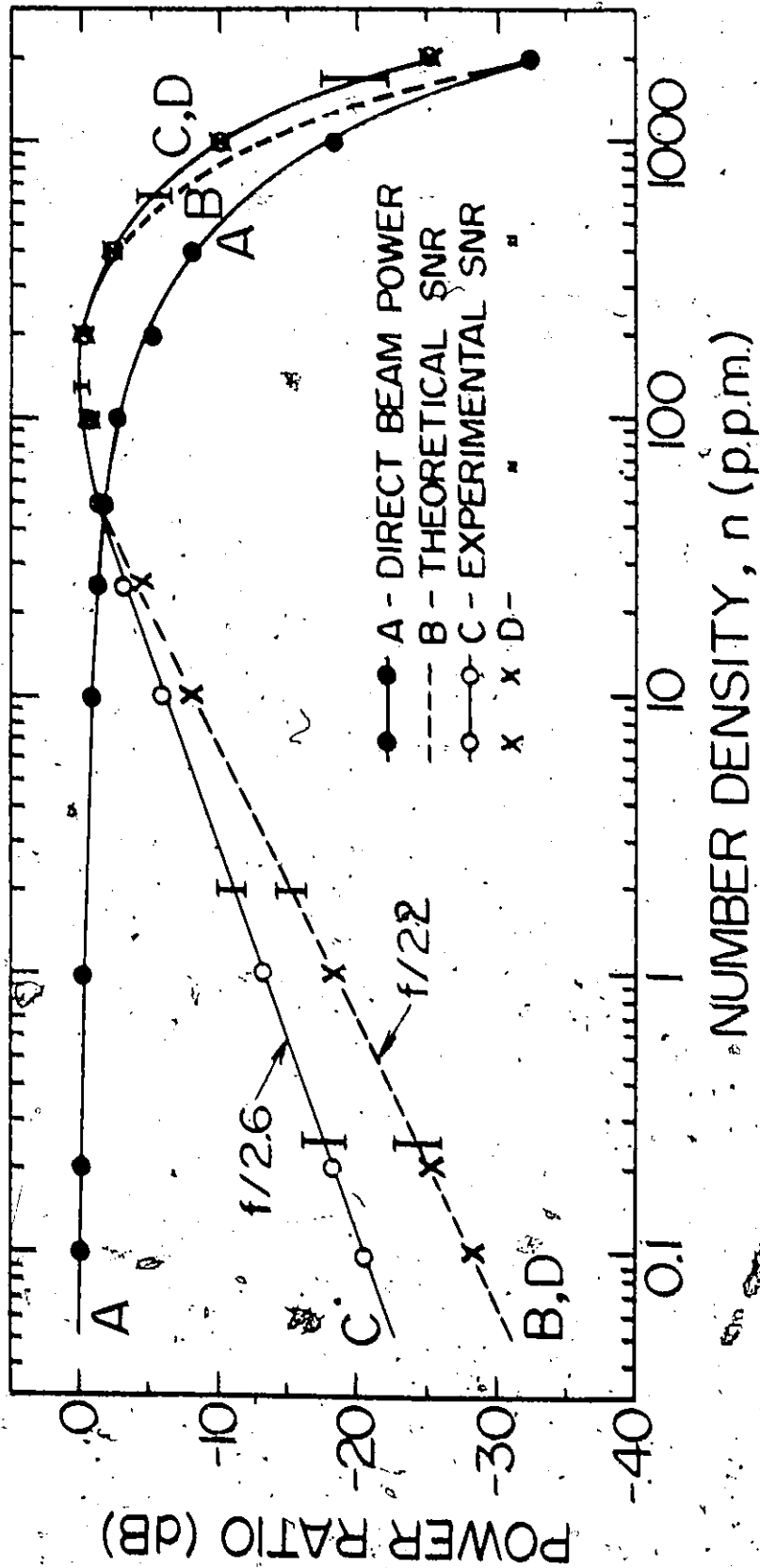
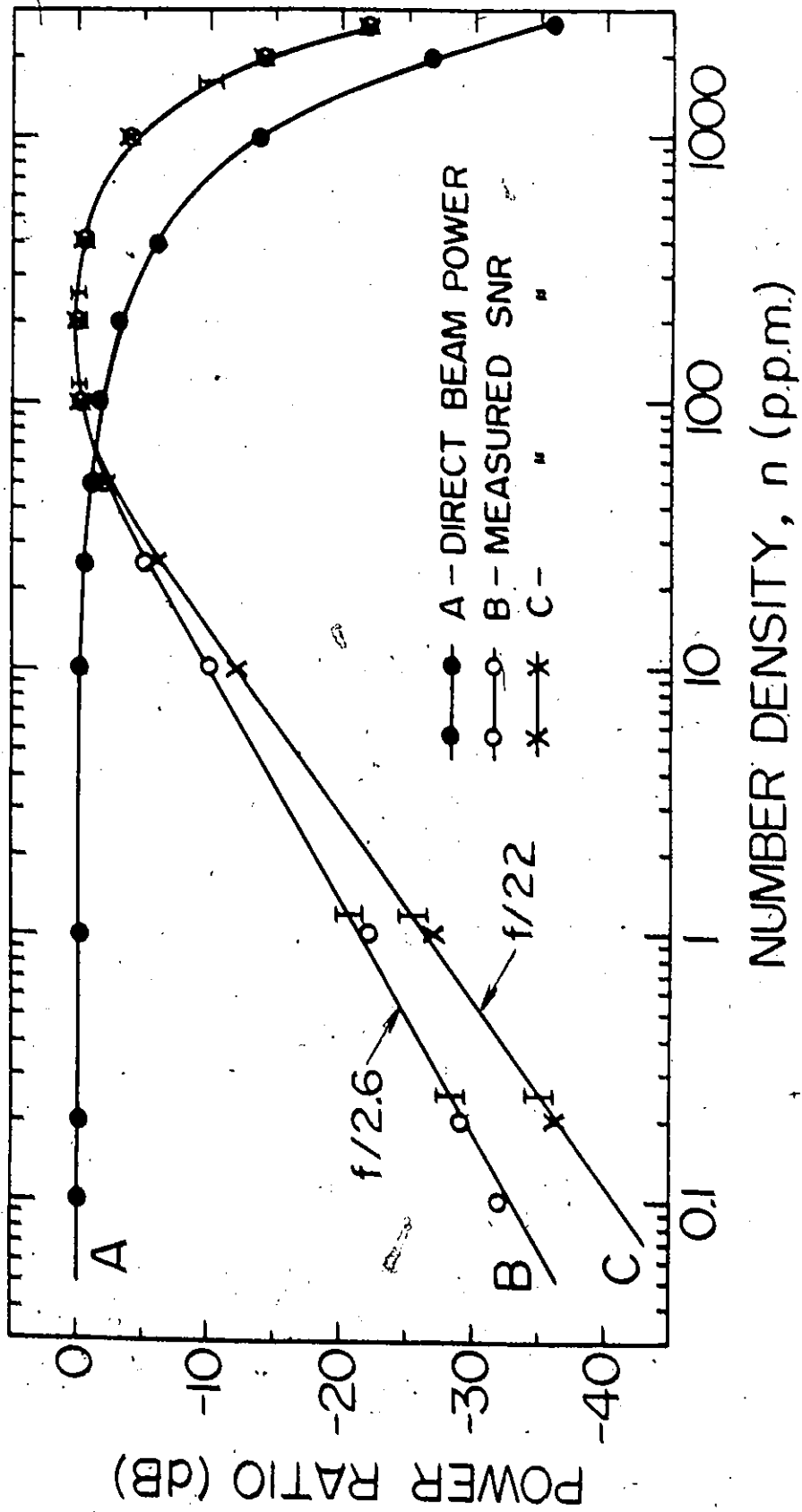


Fig. 6.3. DLDV SNR measurements employing 0.62 μ polystyrene particles. Here the flow tube width

$l = 0.2$ cm. The maximum SNR for both C and D was 35 dB. All other caption data in Fig.

6.2 apply.

Fig. 6.4: DLDV SNR measurements employing homogenized milk. Flow tube width $L = 1$ cm. Number density n represents the solid content of homogenized fluid milk by weight. Curve A is the transmitted power of the direct beam. Curves B and C are the relative experimental SNR's for receiving apertures of $f/2.6$ and $f/22$, respectively. The maximum SNR for both B and C was 35dB. Some typical error bars are shown.



solids, by weight. The maximum SNR occurs at a value of n approximately six times larger than $n = 34$ in Fig. 6.2. This suggests that the scattering originates primarily from particles somewhat larger than $0.62 \mu\text{m}$. Comparing data for $f/22$ apertures, the initial SNR's in Figures 6.2 and 6.3 are both, to a close approximation, proportional to n , as expected from Eq. (6.10). In Fig. 6.4, however, the initial SNR is, to a close approximation, proportional to the $\sqrt{2}$ power of n . This is an interesting deviation from the expected behaviour and illustrates the importance of particle size distribution when comparing experimental and theoretical SNR's. The root causes for these deviations are not fully understood; further investigations are required.

As discussed in section 2.3, in this thesis coherent detection refers to the signal resulting from heterodyning of Doppler shifted components in the scattered radiation. Such measurements require coherent sources (lasers). Incoherent detection refers to the observation of the intensity modulation caused by particles crossing fringes in the flow region. In this case, both coherent and incoherent sources can be employed.

Here we only consider the case where the particles in the flow region are of uniform size. All our results indicate that the behaviour of the SNR is well described by Eq. (6.10) provided that α is kept small enough to satisfy the coherent condition. Thus the SNR is proportional to number density n . This is in agreement with the conclusions of Lading [58]. At large solid angles it is expected that the SNR will be independent of number density n [58]. Our results tend to confirm this, as can be seen from the decrease in slope in Figures 6.2, 6.3 and

6.4 when the aperture is increased.

A surprising result concerns how little the SNR increases with aperture at low n values. With reference to Fig. 6.2, the lowest measured value of $n = 0.025$ corresponds to about 0.02 particles in the probe volume. It might be expected that in this case the system can be treated as a fringe system. Consequently, the increase in SNR should be, to a first approximation, proportional to the aperture because we are clearly in the region of incoherent scattering. The expected theoretical increase is 18dB (15dB if measured dc power ratio is employed) but the observed increase is 6dB. Considerable care was taken in these measurements to ensure that the beams intersected at the focal point of the transmitting lens. We must conclude, therefore, that the observed signal still results from coherent scattering. Either our experimental techniques are at fault, which we think unlikely, or also the coherent scattering signal power is much greater than the incoherent scattering signal power. Resolution of these alternatives will require considerable further research.

6.3 Angular Scattering Function

It had been suggested [59] that the angular volume scattering functions for coherent and incoherent light are not the same in a given aerosol medium, and that the total extinction coefficient likewise differs. It was also suggested [59] that the Mie theory does not account for such a phenomenon. More recently, however, other experimental studies [60, 61] have produced contradicting results. It is now generally believed [60, 61] that the scattering data from the two light sources (coherent

and incoherent) agree to within experimental error, and moreover, the results agree with the Mie theory.

The following derivation is based on the assumption that the Mie theory can be applied to the scattering of a coherent light source. Furthermore, the effect of the fringe pattern in the probe volume is ignored. The main effect of the latter is possibly to reduce the effective number of scattering particles by a factor of two (due to the assumption that dark fringes do not scatter light). This factor is absorbed in the proportionality constant of the following derivation. Inconclusive discussions about the possibility of scattering from dark fringes are found in references [62, 63].

Figure 6.5 depicts the geometry for light scattering measurements. Note that

$$\theta_1 = \theta - \theta_0 \quad (6.13)$$

and

$$\theta_2 = \theta + \theta_0 \quad (6.14)$$

where θ is the detection angle measured from the bisector of the two intersecting beams, and θ_0 is the beam crossing half-angle. The light collected by the receiver lens is the sum of the two powers scattered from beam 1 and beam 2, i.e.,

$$P'(\theta) = P_1(\theta_1) + P_2(\theta_2) \quad (6.15)$$

where, for identical particle size $P_1(\theta_1)$ and $P_2(\theta_2)$ are given by

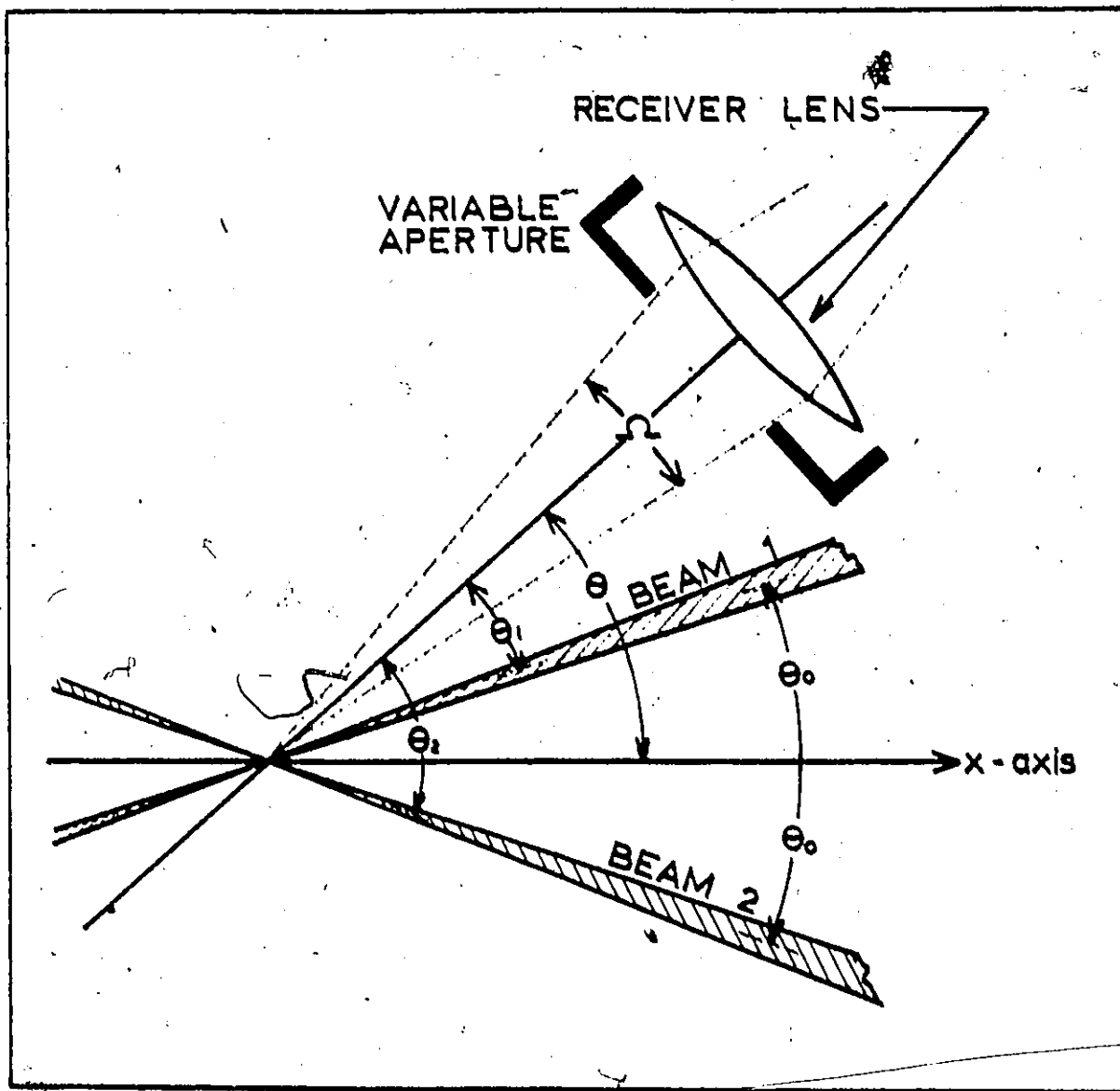


Fig. 6.5: The geometry for light scattering measurements.

$$P_1(\theta_1) = \frac{\lambda^2}{4\pi^2} n I_0 V e^{-\sigma n x \sec \theta_0 e^{-\sigma n (L-x) \sec \theta_1}} \int_{\Omega} i(\theta_1, \alpha, m) d\Omega \quad (6.16)$$

$$P_2(\theta_2) = \frac{\lambda^2}{4\pi^2} n I_0 V e^{-\sigma n x \sec \theta_0 e^{-\sigma n (L-x) \sec \theta_2}} \int_{\Omega} i(\theta_2, \alpha, m) d\Omega \quad (6.17)$$

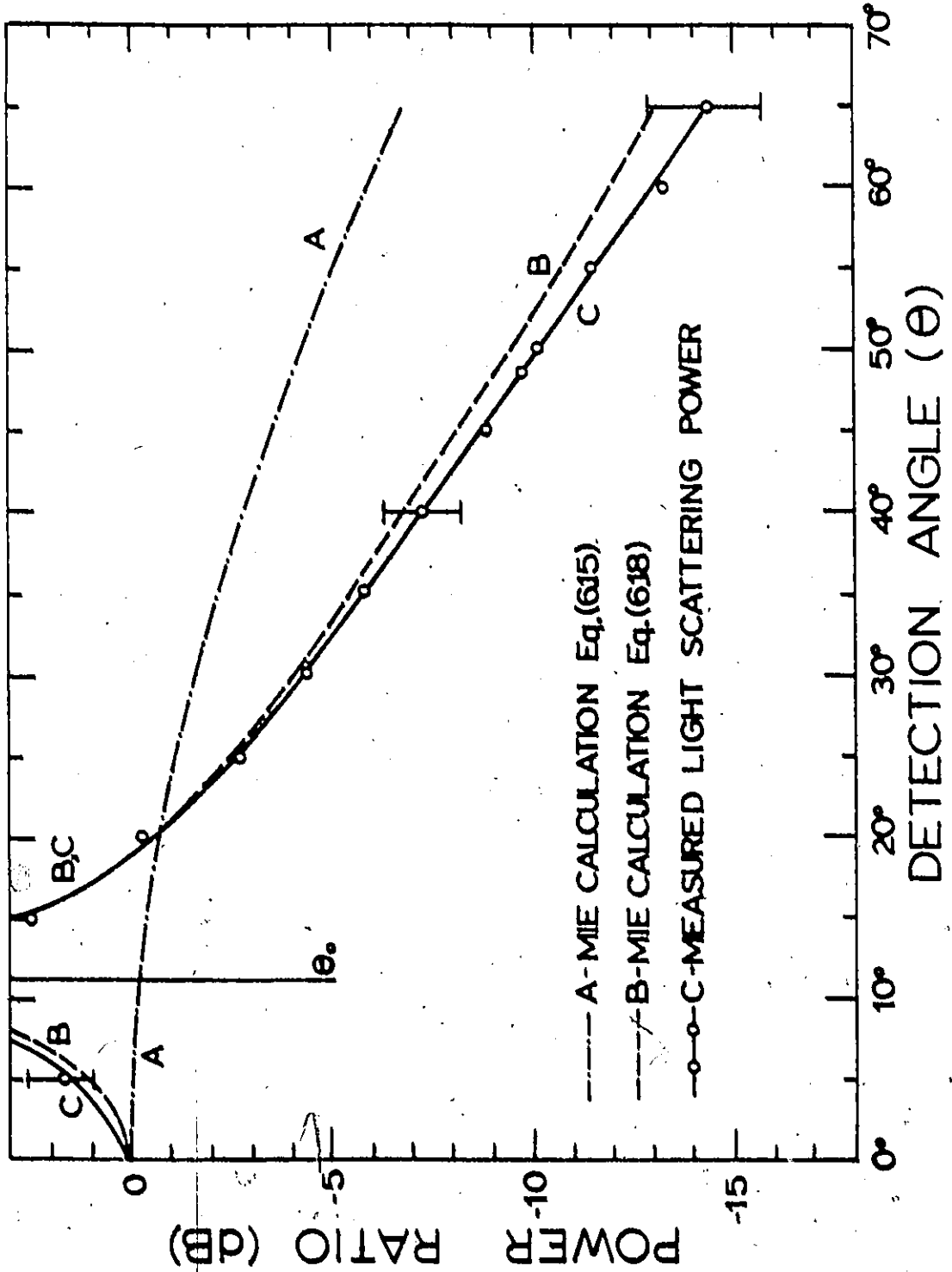
The above equations are obtained from Eq. (6.6) and from application of the attenuation factors, as discussed in section 6.1. In light scattering measurements which involve a change of detection angle, a scattering volume correction factor is normally applied to account for the change in the probe volume [59, 60]. In our case, the volume correction factors for beam 1 and beam 2 are $\csc \theta_1$ and $\csc \theta_2$, respectively. Thus from Eq. (6.15) the detected light power is

$$P(\theta) = P_1(\theta_1) \csc \theta_1 + P_2(\theta_2) \csc \theta_2 \quad (6.18)$$

where $P'(\theta)$ has been changed to $P(\theta)$.

Results of light scattering measurements employing the DLDV system are represented by curve C in Fig. 6.6. For this data the flow velocity was reduced to zero. Identical results were obtained with finite flow velocities, provided that a time average of the intensity was recorded. Curve C is shown for a particle concentration of 25 wppm and a receiver aperture of $f/22$. Nearly identical results (relative) were obtained employing a receiver aperture of $f/2.6$ and also for a particle concentration of 0.2 wppm at both apertures. This is expected because the small size of the particles (0.481 μm polystyrene spheres)

Fig. 6.6: DLDV angular scattering function measurements employing 0.481 μm polystyrene spheres ($\alpha = 3.18$, $m = 1.20$). Curves A and B are the relative scattered power calculated from Equations (6.15) and (6.18), respectively. The theoretical data has been corrected for reflection and refraction at the fluid-tube-air boundary. Curve C is the relative experimental light scattering power for a concentration of 25 wppm and a receiver aperture of $f/22$. θ_0 is the beam crossing half angle. Some typical error bars are shown.



avoids rapid changes in scattered intensity as a function of angle. Although the relative scattered power as a function of angle is similar for both sets of measurements, the absolute powers are different. Employing the same aperture size, the measured scattered powers for the 25 wppm particle concentration are about 20dB larger than the corresponding values for the 0.2 wppm, which is close to theoretical expectation. At a fixed concentration, the measured scattered powers for the f/2.6 aperture are, on the average, 15dB larger than the corresponding values for the f/22 aperture. This, however, is 3dB less than expected from theory (18dB). The loss is probably due to some enlargement of the image size on increasing the aperture (due to lens aberrations), together with the use of a fixed pinhole size (35 μm). Curves A and B (Fig. 6.6) represent the relative scattered powers calculated from Equations (6.15) and (6.18), respectively. Note that the detection angle (θ) has been corrected for refraction (using Snell's law) before being employed in the Mie calculation. Note also that the solid angle (Ω) of the f/22 aperture has an angular field of view of about 1 degree in air. For the f/2.6 aperture the corresponding angular field of view is about 8 degrees. These values were also corrected for refraction in order to provide an effective solid angle in the fluid. These corrected values, which were different for different observation angles were employed in the Mie calculation. Finally, a correction was made for the loss due to Fresnel reflection from the fluid-tube-air interfaces. It can be seen that the agreement between curves B and C is much better than that between curves A and C. This illustrates the importance of the volume correction factors applied to Eq. (6.18)

Considering all the above factors, it is reasonable to conclude

that the light scattering measurements agree with the Mie theory to within experimental error. Moreover, the assumption that the fringe pattern can be neglected in the Mie calculation appears to be a valid one.

6.4 Effect of Detection Angle on SNR

The SNR equation (6.1) was derived under the assumption that the heterodyned wavefronts were perfectly aligned, and that the noise was solely from the shot noise resulting from these two wavefronts. In practice, light scattered from outside the beam-crossover region is also detected because of the finite depth-of-field of the receiver lens. Hence the scattering volume correction factor should also be applied to the SNR equation. Two conditions, however, should be distinguished in the application of the volume correction factor. First, if the receiver aperture satisfies the coherent condition (i.e., light scattered from outside the probe volume will contribute to heterodyne signal), the volume correction factor should be applied to both the ac and dc components of the photomultiplier output. The SNR is thus given by

$$\text{SNR}(0) = \frac{P_1(\theta_1) \text{csc} \theta_1 P_2(\theta_2) \text{csc} \theta_2}{P_1(\theta_1) \text{csc} \theta_1 + P_2(\theta_2) \text{csc} \theta_2} \quad (6.19)$$

where θ_1 and θ_2 are defined in equations (6.13) and (6.14), respectively. Secondly, if the receiver aperture does not satisfy the coherent condition, then light scattered from outside the probe volume will not contribute significantly to the heterodyne signal. A homodyne signal can only be obtained from the fixed beam-crossover region. Consequently, no

volume correction is required for the ac component. The dc component, however, still requires volume correction regardless of the aperture size. Based on this simplified assumption, the SNR is given by

$$\text{SNR}(0) \approx \frac{P_1(\theta_1)P_2(\theta_2)}{P_1(\theta_1)\text{csc}\theta_1 + P_2(\theta_2)\text{csc}\theta_2} \quad (6.20)$$

Note that this equation is only an approximation. Because in practice, a certain amount of heterodyned signal (between different particles) would have entered the detector. This will be further discussed later.

Experiments have been carried out to test the validity of the above equations. The DLDV system employed for the measurements (and for all other similar measurements) is identical to that described in section 3.5. Experimental results taken with a receiver aperture satisfying the coherent condition are shown in Figures 6.7 and 6.8. Figure 6.7 represents data of a fluid flow seeded with 0.2 wppm of 0.481 μm diameter polystyrene spheres (corresponding to $N \approx 0.3$ particles in the probe volume). An f/22 receiver aperture, which satisfies the coherent condition for any number density, was employed. Curve A is the relative theoretical SNR calculated using Eq. (6.19). Excellent agreement is found between the theory and the experiment.

Figure 6.8 represents data obtained from a similar fluid flow seeded with higher number density (25 wppm, $N \approx 41$). In this case, two receiver apertures, f/22 and f/2.6 were employed. Because of the higher number density, heterodyne detection (between different particles) is dominant even for the f/2.6 aperture (this phenomenon has been discussed in section 6.2). Curve A is the relative theoretical SNR for the f/2.6

Fig. 6.7: DLDV SNR(θ) measurements employing a small receiver aperture ($f/22$). The flow was seeded with 0.481 μm diameter polystyrene spheres at a number density $n = 0.2$ wppm ($N = 0.3$). Curve A is the relative theoretical SNR calculated using Eq. (6.19). The theoretical data has been corrected for reflection and refraction at the fluid-tube-air boundary. The discontinuity at θ_0 results from letting either $P_1(\theta_1)$ or $P_2(\theta_2)$ be zero. At either of these positions, the direct beams are blocked by the light cups. The maximum obtainable SNR was 13dB. Some typical error bars are shown.

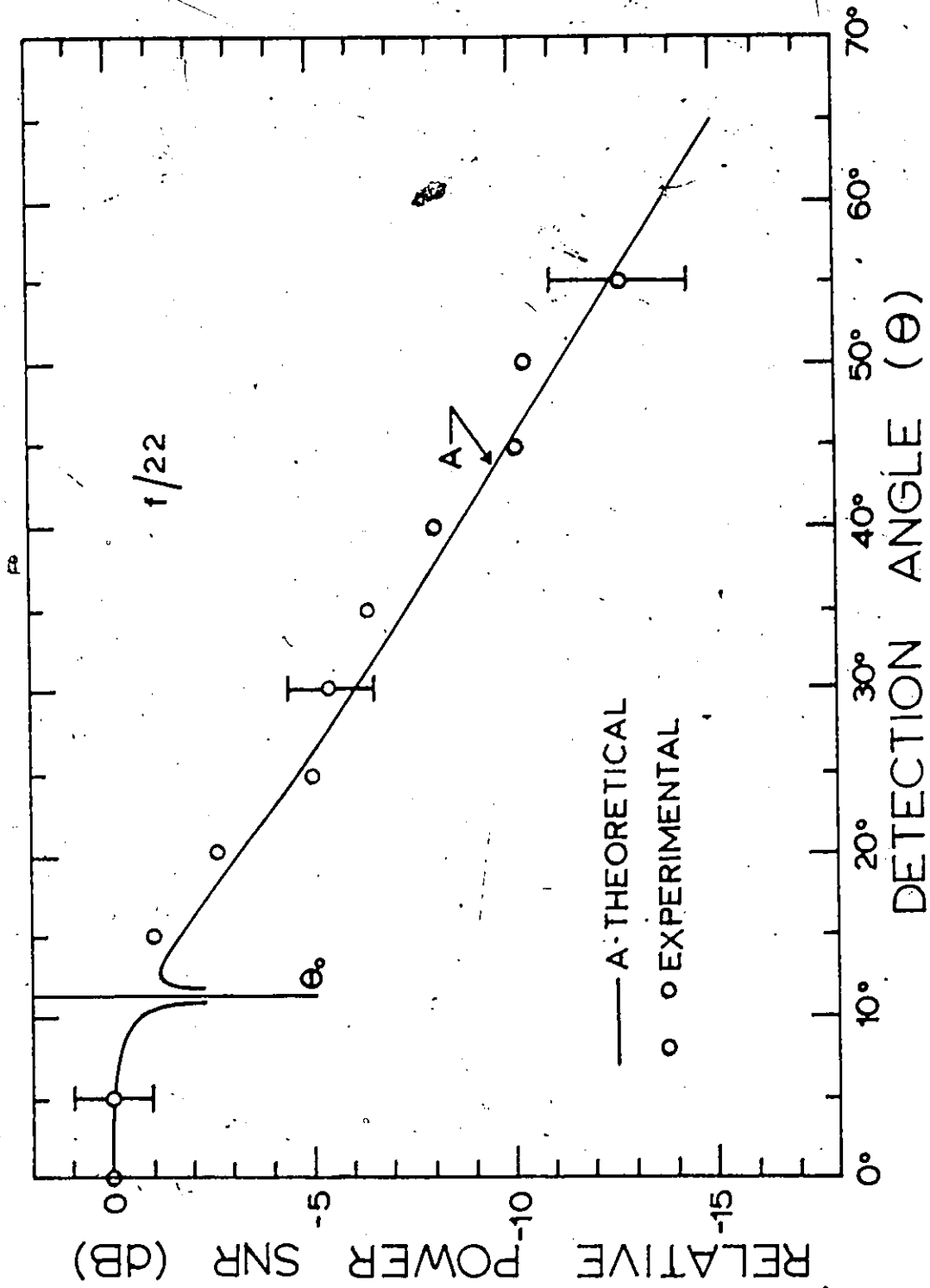
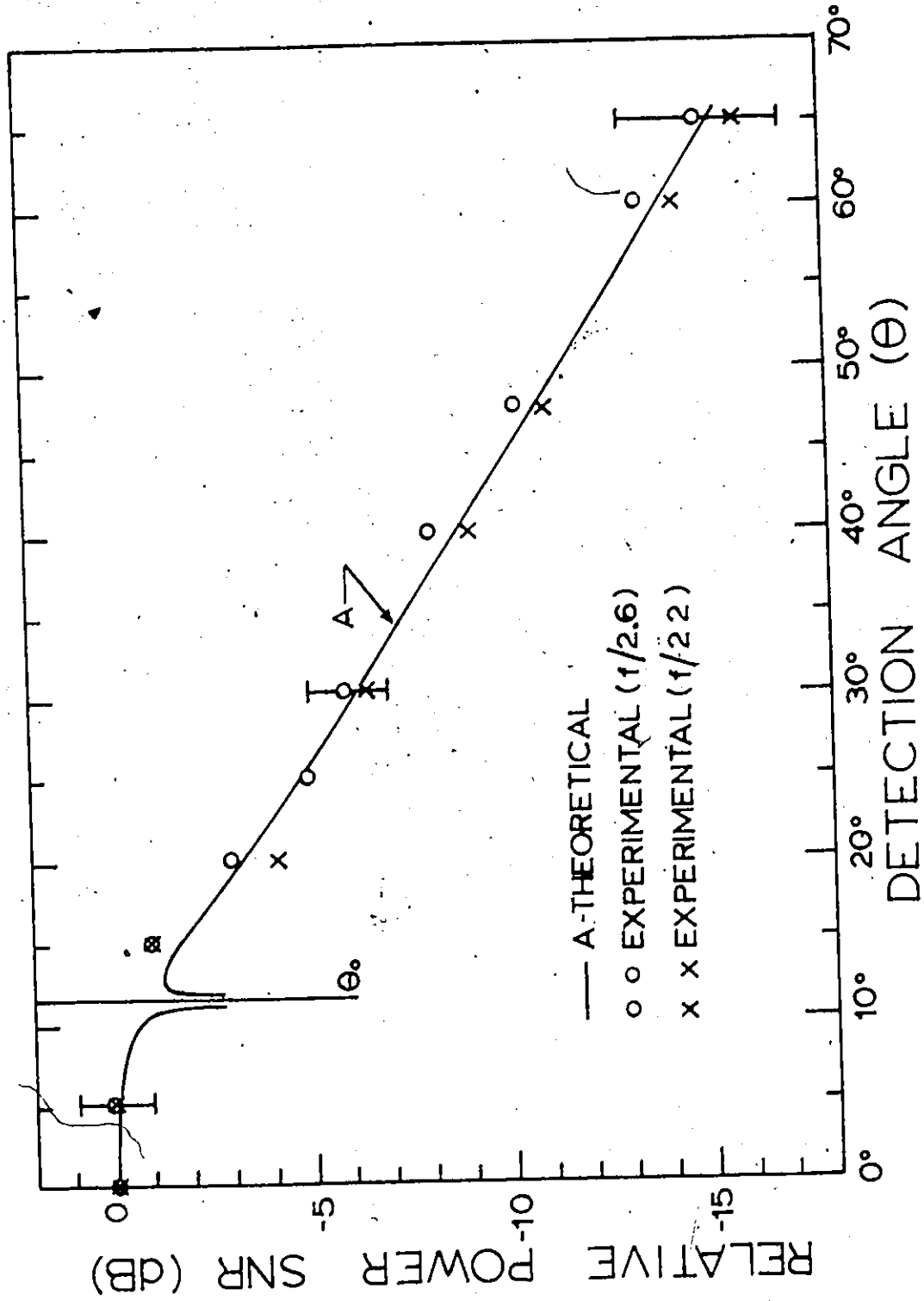


Fig: 6.8: DLDV SNR(θ) measurements employing a higher number density than in Fig. 6.7 (0.481 μm diameter polystyrene spheres, $n = 25$ wppm, $N \approx 41$). Curve A is the relative theoretical SNR for the $f/2.6$ and $f/22$ apertures calculated using Eq. (6.19). The theoretical data has been corrected for reflection and refraction at the fluid-tube-air boundary. The maximum obtainable SNR's are 31dB for both apertures. Some typical error bars are shown.

Fig. 6-8



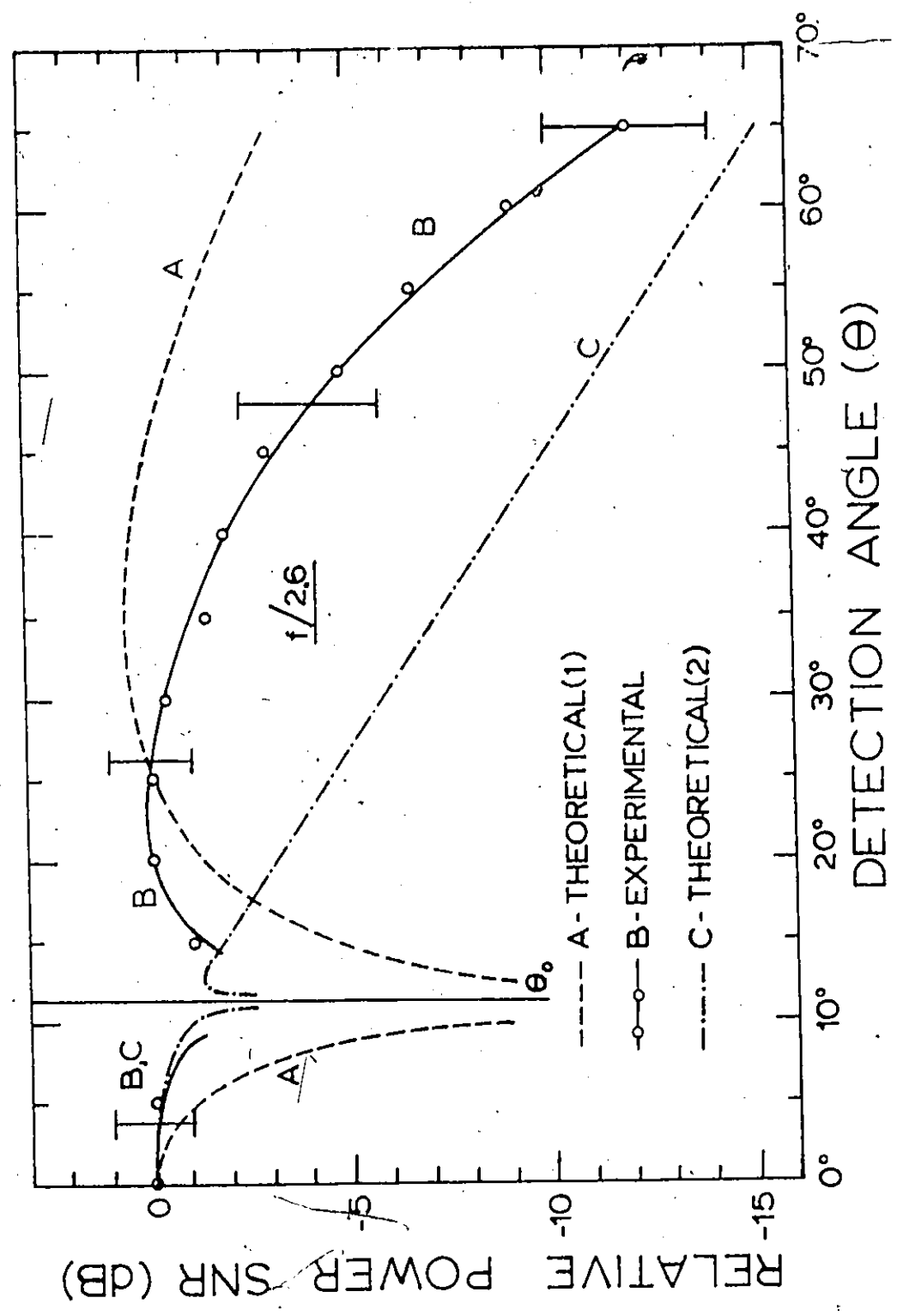
and $f/22$ apertures calculated using Eq. (6.19) (The difference between the corresponding calculation for the two apertures is negligible because of the small size of the particles). It can be seen that the experimental data for the two apertures are almost identical and are in excellent agreement with the theory. This result again shows that at high number density, the performance of a DLDV is not affected by the size of the receiver aperture.

Results of measurements employing a receiver aperture which does not satisfy the coherent condition are shown in Fig. 6.9. The experimental parameters are identical to that employed for Fig. 6.7 except that a larger receiver aperture ($f/2.6$) was used. Curve A is the relative theoretical SNR calculated using Eq. (6.20). This equation is used because homodyne detection is believed to be dominant here ($N \approx 0.3$). Curve B is the relative experimental SNR. It can be seen that there is some agreement between curves A and B at small θ . At large θ ($\geq 45^\circ$) the deviation becomes large. This discrepancy is believed to arise from heterodyning between different particles (within and outside the probe volume) which was not accounted for in Eq. (6.20). For comparison purposes, the theoretical curve given by Eq. (6.19) is also plotted (curve C) in Fig. 6.9. The measured data are generally within the limits established by the two theoretical curves. Thus it is reasonable to conclude that heterodyne detection is still somewhat strong even at a very low number density ($N \approx 0.3$). A similar conclusion was made in section 6.2.

From the above observations it can be seen that a correction factor is required to account for heterodyne detection at very low

Fig. 6.9: DLDV SNR(θ) measurements employing a large receiver aperture ($f/2.6$). The flow was seeded with $0.481 \mu\text{m}$ diameter polystyrene spheres at a number density $n = 0.2$ wppm ($\Pi = 0.3$). Curves A and C are the relative theoretical SNR's calculated from equations (6.20) and (6.19), respectively. The theoretical data has been corrected for reflection and refraction at the fluid-tube-air boundary. Curve B is the relative experimental SNR. The maximum obtainable SNR was 18dB. Some typical error bars are shown.

Fig. 9-3



number densities. At large number densities, however, such a correction factor becomes less important. This can be seen from the experimental results presented in Fig. 6.8, as well as those in section 6.2. It can also be seen that the correction factor is not only a function of the receiver aperture size and of the number density, as was generally believed [18, 58], but it is also a function of detection angle. Determination of such a function, however, requires further research.

6.5 Effects of Light Intensity and Velocity on SNR

From equations (6.1) and (6.10):

$$\text{SNR} = \frac{nA}{2hfB} P_0 V n l(\theta_0, \alpha_0, m) n e^{-\sigma n L} \quad (6.21)$$

It is common practice to limit the noise bandwidth, B , to the Doppler bandwidth, Δf_D , as given by

$$B = \Delta f_D = \frac{v}{D} \quad (6.22)$$

where D is the width of the probe volume which the particles have crossed. This value of B provides greatest signal at near optimum SNR. By substituting Eq. (6.22) into Eq. (6.21) one obtains

$$\text{SNR} = \frac{nDA}{2hfV} P_0 V n l(\theta_0, \alpha_0, m) n e^{-\sigma n L} \quad (6.23)$$

Thus, for a given system, the SNR is directly proportional to the beam power, P_0 , and inversely proportional to the particle velocity, v .

Experiments employing a 10dB neutral density filter inserted in

front of the laser source confirmed that the SNR was also decreased by 10dB.

The effect of velocity on SNR is shown in Table 6.1. The DLDV system employed for the measurements was identical to that described in section 3.5. The fluid flow was seeded with 25 wppm of 0.481 μm polystyrene spheres. It can be seen that the SNR is inversely proportional to the velocity provided the IF bandwidth (instrumental bandwidth) was set approximately equal to the Doppler bandwidth. When the IF bandwidths were decreased to less than the Doppler width, only a small improvement in SNR was observed. This only applied to laminar flow; no improvement was observed in the case of turbulent flow. Some results for laminar flow are listed in Table 6.2. This, and other data, confirm that in most applications, the IF bandwidth should be set equal to or less than the Doppler width in order to achieve optimum SNR.

The inverse relationship between the velocity and the SNR has been observed over a wide range of particle concentration. Thus, to achieve high SNR at very high velocities, relatively high power sources are required.

6.6 Summary

In this chapter, the SNR equation of the DLDV has been extended to include Mie scattering theory. The derivation is simplified by the assumption that the heterodyne wavefronts are perfectly aligned. Comparison of theory with carefully controlled experiments indicates that the assumption is valid for most applications provided that certain corrections are made to satisfy practical operating conditions. These

Table 6.1: Effect of Particle Velocity on DLDV SNR Measurements

Doppler Frequency* (kHz)	IF Bandwidth (kHz)	SNR (dB)
6	0.3	24 ± 1
20	1.0	19 ± 1
60	3.0	14 ± 1
200 [†]	10.0	9 ± 2

* A velocity $v = 1.6$ cm/s ($Re = 75$) corresponds to a Doppler frequency of $f_D = 10$ kHz.

[†] At this Doppler frequency, the flow ($Re \approx 1500$) is in the transition region between the laminar and turbulent flow.

Table 6.2: Effect of IF Bandwidth on DLDV SNR Measurements*

Doppler Frequency (kHz)	SNR (IF Bandwidth = 0.3 kHz) (dB)	SNR (IF Bandwidth = 1 kHz) (dB)
6	24 ± 1	20 ± 1
20	20 ± 1	19 ± 1
60	16 ± 1	16 ± 1
200	9 ± 2	9 ± 2

*The experimental parameters are identical to those in Table 6.1.

corrections include a volume correction factor and a coherence factor.

The SNR equation has been applied to the investigation of the effects of aperture size, number density, detection angle, and particle velocity. In general, the theory agrees with experiments, provided that the coherent condition is satisfied. When the receiver aperture does not satisfy the coherent condition, deviation from the theory is expected. Deviation may be minimized by the use of a coherence factor which relaxes the condition of wavefront alignment. Such a factor is observed to be a function of receiver aperture size, particle number density, and detection angle. The derivation of the functional form of an appropriate factor, however, requires considerable further effort.

The most important conclusion in this chapter is that the DLDV, even at very low particle number density, operates predominantly in the coherent mode. This conclusion is contrary to common belief.

Two important properties result from the coherent mode detection inherent in the DLDV. At very low number densities, the SNR increases with Ω (receiver aperture size) only in the limit of small Ω . At high number densities, the SNR is virtually independent of the receiver aperture size.

CHAPTER 7

SNR INVESTIGATIONS OF A WFIV

Several parameters which affect the performance of a WFIV are described. A derivation of the SNR is given which is based on amplitude modulation of radiation, and on Mie scattering theory. There is excellent agreement between theory and experiment.

The properties of incoherent detection are described. The results indicate that the WFIV and the DLDV (discussed in Chapter 6) possess different SNR characteristics as a function of particle number density and aperture size. There are, however, several basic similarities in the behaviour of the two techniques. The behaviour of the SNR as a function of light intensity, and of flow velocity, is identical for both the WFIV and DLDV. Experimental results are not presented here; results of Chapter 6 can be applied directly.

7.1 Derivation of the SNR (Incoherent Detection)

Derivations are simplified considerably for the case of white light because all scattering is completely incoherent. We consider first the scattering of a single particle crossing white light fringes. It is assumed that only the fundamental frequency component of the ac signal is observed and that this is proportional to

$$\cos(\omega t + \phi) \quad , \quad (7.1)$$

where ω is the angular frequency and ϕ the phase.

For a single particle the scattered radiant power at the receiving aperture, of solid angle Ω , can be represented by

$$P_s = I(x) \int_{\Omega} [1 + M \cos(\omega t + \phi)] i(\theta, \alpha, m) d\Omega \quad (7.2)$$

where $I(x)$ is the average intensity at the particle location x , θ is the angle relative to the forward scattering position, $i(\theta, \alpha, m)$ the scattering function per particle, and $\alpha = 2\pi r/\lambda$ as in section 6.1. Parameter M is related to the shape and visibility of the fringe pattern. Clearly, the first term in the square brackets in (7.2) relates to the dc component, the second term to the ac component. The dc and ac components of the scattered radiation can be considered separately.

The resultant photocathode current is given by

$$I_s = I_{dc} + I_{ac} = (ne/hf)P_s \quad (7.3)$$

where η is the quantum efficiency, e the electron charge, h Planck's constant, and f the mean frequency of the light. Note that the approximation results from the use of a mean frequency. Combining (7.2) and (7.3) yields

$$I_{dc} = (ne/hf)I(x) \int_{\Omega} i(\theta, \alpha, m) d\Omega \quad (7.4)$$

and

$$I_{ac} = (ne/hf)I(x) \int_{\Omega} [M \cos(\omega t + \phi)] i(\theta, \alpha, m) d\Omega \quad (7.5)$$

In what follows it is assumed that the signal component of the detection system output is always proportional to I_{ac} . Furthermore it is assumed that the detection time is sufficiently long for reliable observation of I_{ac} .

The shot noise current is related to (7.4) by

$$\langle I_N^2 \rangle = 2eI_{dc}B, \quad (7.6)$$

where B is the instrumental bandwidth. For a system of particles

$$I_{DC} = V \int I_{dc} \frac{dn}{d\alpha} d\alpha, \quad (7.7)$$

where I_{DC} indicates the total dc current, V the probe volume, and $dn/d\alpha$ the number density of particles between α and $\alpha + d\alpha$.

Next we consider the case where there are at least several particles simultaneously in the probe volume. Because the ac signals scattered from the particles are completely random in phase,

$$\langle I_{AC}^2 \rangle = V \int \langle I_{ac}^2 \rangle \frac{dn}{d\alpha} d\alpha, \quad (7.8)$$

where I_{AC} is the total signal current.

As usual, the power SNR is given by

$$SNR = \frac{\langle I_{AC}^2 \rangle}{\langle I_N^2 \rangle}. \quad (7.9)$$

Here it is assumed that the only significant noise contribution is that

which is due to shot noise. Substitution of (7.4) and (7.5) in (7.7) and (7.8), and carrying out the appropriate time averages, results in

$$\text{SNR} = \frac{nM^2}{2hfB} I(x) \frac{\int_{\alpha} \left[\int_{\Omega} i(\theta, \alpha, m) d\Omega \right]^2 \frac{dn}{d\alpha} d\alpha}{\int_{\alpha} \int_{\Omega} i(\theta, \alpha, m) d\Omega \frac{dn}{d\alpha} d\alpha} \quad (7.10)$$

If all particles are identical ($\alpha = \alpha_0$), then Eq.(7.10) reduces to

$$\text{SNR} = \frac{nM^2}{2hfB} I(x) \int_{\Omega} i(\theta, \alpha_0, m) d\Omega \quad (7.11)$$

We now introduce the concept of beam attenuation, as was done in section 6.1, i.e.,

$$I(x) = I_0 e^{-\sigma n x} e^{-\sigma n (L-x) \sec \theta} \quad (7.12)$$

where the last factor is included to account for the attenuation of the scattered radiation, and where I_0 is $I(x)$ in the absence of attenuation. Substitution of Eq. (7.12) and $I_0 = P_0/a$, where P_0 is the incident beam power and a the area at x , into (7.11) gives

$$\text{SNR} = \frac{nM^2 P_0}{2hfBa} \int_{\Omega} i(\theta, \alpha_0, m) e^{-\sigma n x} e^{-\sigma n (L-x) \sec \theta} d\Omega \quad (7.13)$$

In most experimental arrangements Ω and θ are relatively small and $i(\theta, \alpha_0, m)$ does not change drastically with θ about $\theta = \theta_0$. Thus

$$\text{SNR} = \frac{nM^2 P_0}{2hfBa} i(\theta_0, \alpha_0, m) e^{-\sigma n L} \quad (7.14)$$

which can be put in the form

$$\text{SNR} \propto P_0 i(\theta_0, \alpha_0, m) e^{-\sigma n L} \quad (7.15)$$

Equation (7.15) indicates that the SNR is independent of n , for $\sigma n L \ll 1$, i.e., when there is negligible beam attenuation.

We now consider the case where, on average, there is less than one particle in the probe volume at any given time. In this case, signals from each particle are observed independently. Therefore

$$\langle I_{AC} \rangle = V \int_{\alpha} \langle I_{ac} \rangle \frac{dn}{d\alpha} d\alpha \quad (7.16)$$

For a total of nV identical particles ($\alpha = \alpha_0$)

$$\langle I_{AC} \rangle = nV \langle I_{ac} \rangle \quad (7.17)$$

Making the same assumptions as before, and noting the attenuation can be neglected, results in

$$\text{SNR} \approx \frac{nM^2 P_0 nV}{2hfBa} i(\theta_0, \alpha_0, m) \Omega \quad (7.18)$$

or

$$\text{SNR} \propto nP_0 i(\theta_0, \alpha_0, m) \Omega \quad (7.19)$$

Therefore, for less than 1 particle in the probe volume ($nV \ll 1$), the SNR is proportional to the average fractional number of particles in the probe volume.

7.2 Effect of Aperture Size on SNR

The optical arrangement for the WFIV was similar to that employed in Chapter 4. A 500 W, 35 mm slide projector was used to illuminate a small area of a Ronchi grating (200 lpi). This grating was focused into the flow region by a 135 mm lens. A total of 25 fringes was employed, spaced 40 μm , to provide a total lateral fringe width of 0.1 cm. These had a measured visibility of 0.8 at the focal plane. The longitudinal extent of the probe volume was about 0.1 cm, measured from planes where the visibility was reduced to half of the peak value. The same receiver lens (35 mm camera lens, $f = 50$ mm) was used as for the DLDV. For the present study, its axis was located 30° from the axis of the direct beam in the forward scattering position. An additional change was an increase in the pinhole diameter to 200 μm (to fully contain the lateral extent of the fringe image) and the removal of the filter. The effective probe volume (V) in the flow region was about $1.25 \times 10^{-4} \text{ cm}^3$.

All measurements employed a Hewlett-Packard 3580 A spectrum analyzer operating at a centre frequency of 400 Hz ($v = 1.6$ cm/s). With this instrument, the bandwidth was kept at 30 Hz, together with a fixed scan-width of 50 Hz/cm. A typical frequency spectrum for the WFIV is shown in Fig. 7.1.

Reliable results can only be obtained from a well defined signal which is free from excessive stray light and background scattering. Figure 7.1 illustrates that these conditions exist for our data.

It was shown in the last section that when there was more than one particle in the probe volume, then the SNR is given by Eq. (7.15),

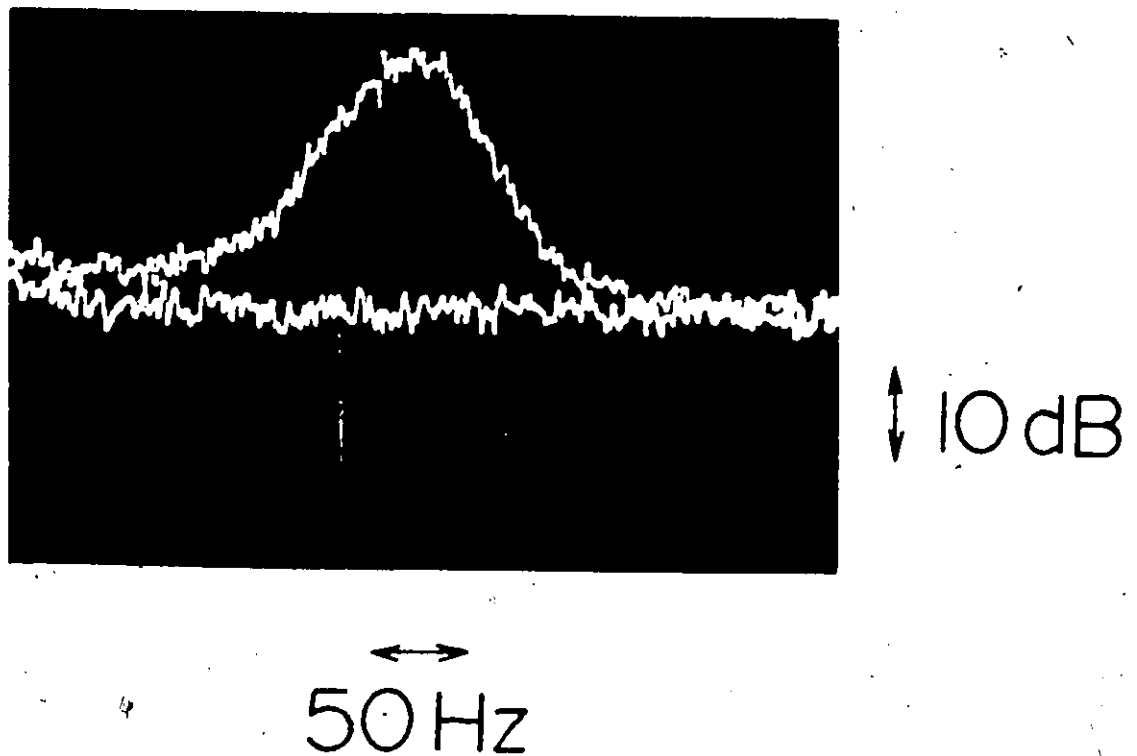


Fig. 7.1: Typical WFIV spectrum. Measurement on 5.7 μm styrene divinylbenzene particles at a number density $n = 100$ wppm. The instrumental bandwidth is 30 Hz at a centre frequency of 400 Hz.

i.e.,

$$\text{SNR} = P_0 i(\theta_0, \alpha_0, m) e^{-\sigma n L} \Omega$$

Results of experiments to confirm that the SNR is indeed directly proportional to Ω for all Ω are presented in Fig. 7.2. The relative power SNR is plotted as a function of the collecting lens f-number. Possible differences between true and engraved f-number, and the finite size of the pinhole (200 μm) could be sources of error. Therefore both the scattered light power and the SNR were measured. The former provided a reference for the actual amount of light being collected, which is directly proportional to the aperture area. The form of the curve in Fig. 7.2 indicates that some lens defects were present. However, from the correspondence between power and SNR data points, we can conclude that the SNR of the WFIV does vary directly with Ω , as expected. This is in contrast to the DLDV, for which proportionality occurs only in the limit of small Ω and at low number density.

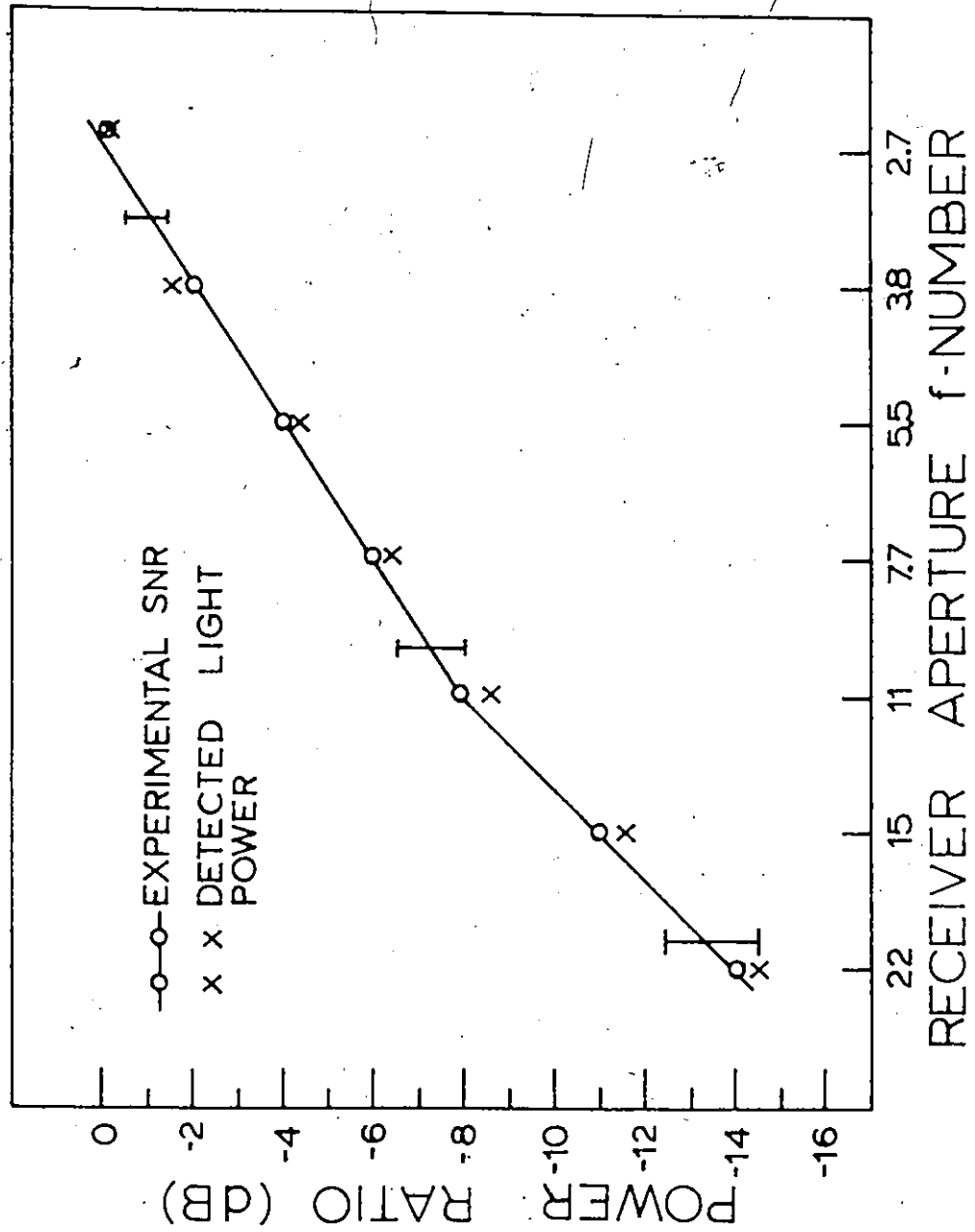
7.3 Effect of Number Density on SNR

It was shown [Eq. (7.15)] that in a WFIV for which there are at least a few identical particles in the probe volume, the SNR is given by

$$\text{SNR} \propto P_0 i(\theta_0, \alpha_0, m) e^{-\sigma n L} \Omega \quad (7.20)$$

Note that, apart from the exponential decay term, the power SNR is independent of the number density n . This should be compared to the

Fig. 7.2: SNR as a function of receiver aperture. 5.7 μm diameter styrene divinylbenzene particles were employed at a number density of $n = 50$ wppm. The f-numbers were corrected for lens-to-image distance (the engraved values ranged from $f/1.9$ to $f/16$). Some typical error bars are shown.



DLDV, where the power SNR given by Eq. (6.10) is proportional to n .

It is also shown [Eq. (7.19)] that, for less than one particle in the probe volume,

$$\text{SNR} \propto n P_0 i(\theta_0, \alpha_0, m) \Omega \quad (7.21)$$

In this case the power SNR is proportional to n .

WFIV data is presented in Fig. 7.3. The experimental conditions were those outlined in section 7.1. Two different particles were employed - 5.7 μm styrene divinylbenzene and 0.62 μm polystyrene. Curves C and C' are the respective relative experimental SNR's. Curves A, A', and B, B', are the corresponding relative transmitted intensities and theoretical SNR's, respectively. Consider the small particles first (Curves A', B', C'). To within the experimental error the three curves are identical, giving excellent agreement between theory and experiment. In particular the SNR is shown to be independent of n when beam attenuation at high n values is taken into account. The smallest n value used corresponds to approximately 20 particles in the probe volume. Measurements using a significantly lower number of particles in the probe volume were not possible because of residual particles in the fluid. A considerable reduction of the probe volume would require a much superior imaging lens than was available to us. An alternative approach is to employ larger particles, as done here, because the scattering increases with size. This can be used to overcome the effect of residual scattering. The smallest n value employed for the 5.7 μm particles corresponds to the 0.025 particles in the probe volume.

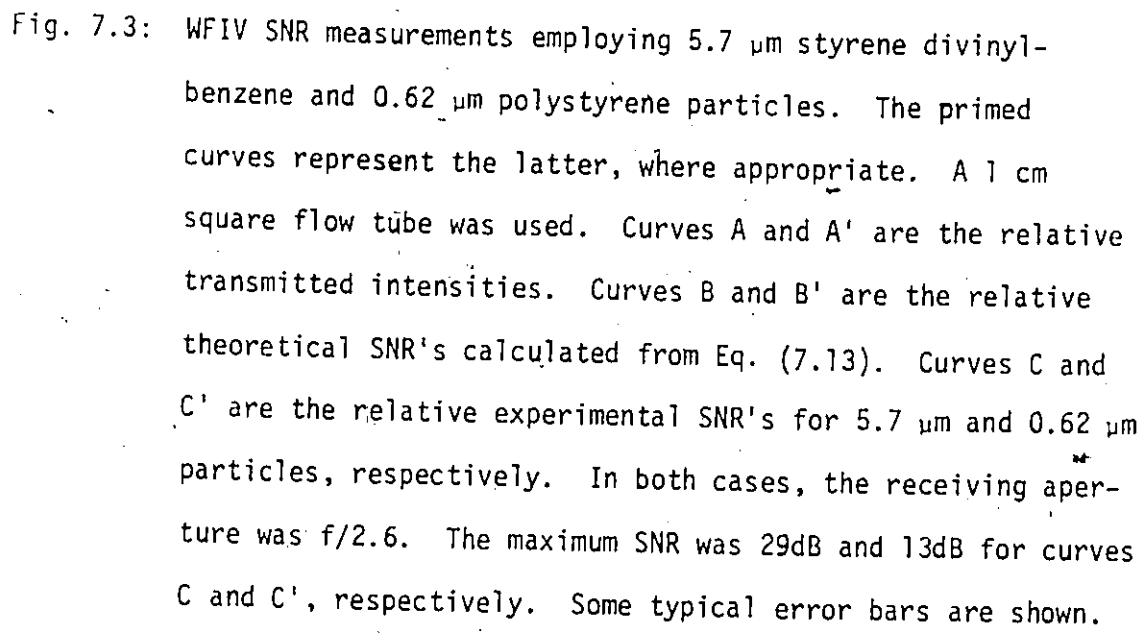
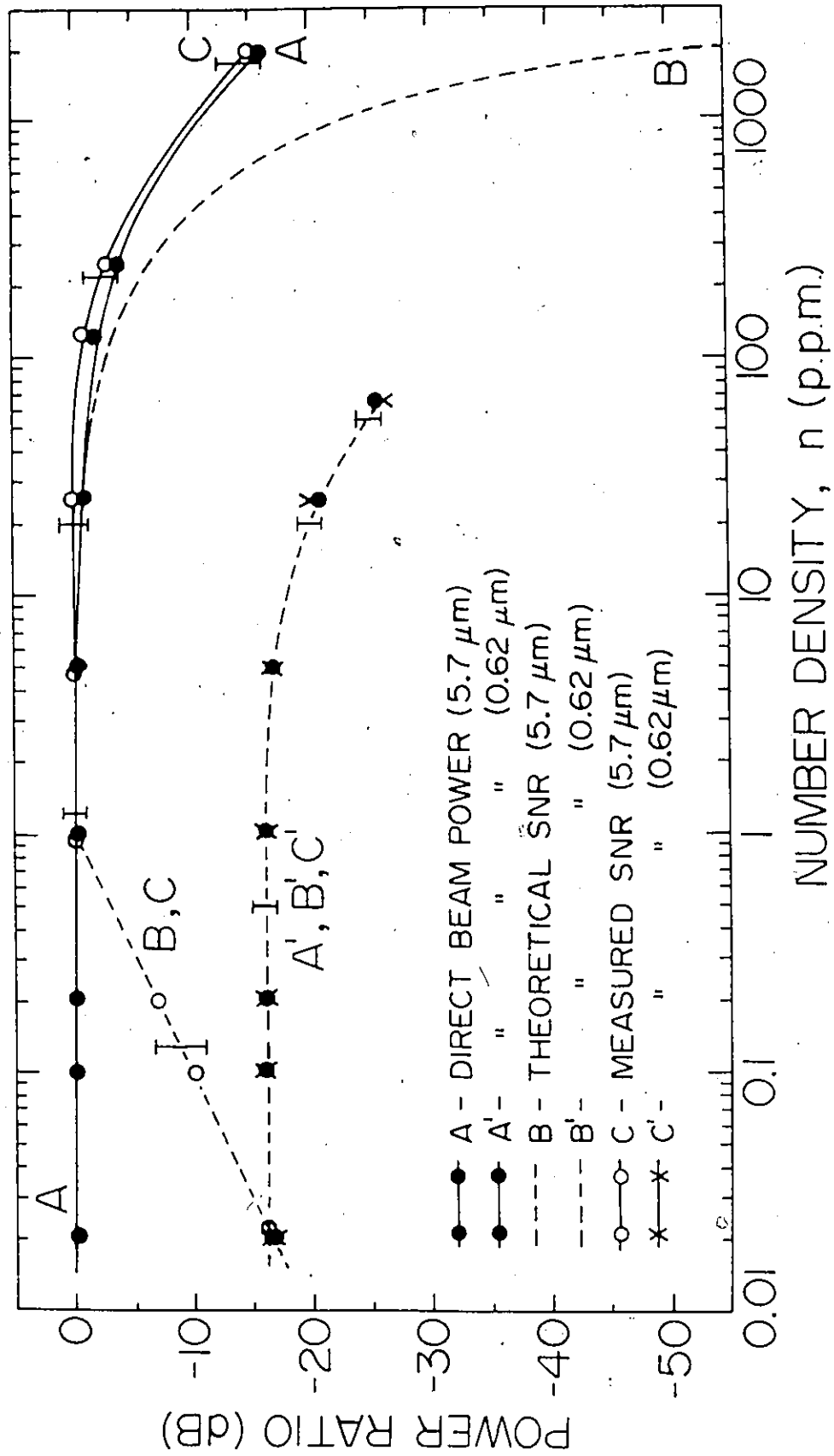


Fig. 7.3: WFIV SNR measurements employing 5.7 μm styrene divinylbenzene and 0.62 μm polystyrene particles. The primed curves represent the latter, where appropriate. A 1 cm square flow tube was used. Curves A and A' are the relative transmitted intensities. Curves B and B' are the relative theoretical SNR's calculated from Eq. (7.13). Curves C and C' are the relative experimental SNR's for 5.7 μm and 0.62 μm particles, respectively. In both cases, the receiving aperture was $f/2.6$. The maximum SNR was 29dB and 13dB for curves C and C', respectively. Some typical error bars are shown.



Results for the larger particles are given by Curves A, B and C. The maximum SNR observed was 29dB compared with 13dB for 0.62 μm particles. There is excellent agreement between theory (as given by Eq. (7.20) and experiment for n in the range 1 to 100. At higher n values both attenuation and SNR are considerably better than expected from Eq. (7.20). This may result either from lack of a reliable value for σ , or from multiple scattering. However, the SNR curve (C) is in excellent agreement with the attenuation curve (A). We may therefore conclude that the SNR for $n > 1$ is independent of n when beam attenuation is considered.

The region below $n = 1$ is of particular interest. It should be noted that $n = 1$ corresponds to approximately 1 particle in the probe volume. For values of n below 1 the SNR is proportional to n . This agrees with the theoretical prediction of Eq. (7.21).

It is clear that incoherent scattering is most efficient at low particle concentrations. We are fully in agreement with the conclusions of Drain [18] that there is little to be gained in going beyond 1 to 2 particles in the probe volume of a fringe system. Our results indicate that the maximum SNR is achieved at about one particle in the probe volume. In addition, the SNR remains constant when the number of particles is increased. Our results also indicate that the SNR is proportional to the number of particles for numbers less than one.

Note that the above results are quite different from those presented in section 6.2, in which the SNR of the DLDV is directly proportional to n (when beam attenuation is considered), irrespective of the total number of particles in the probe volume.

7.4 Effect of Detection Angle on SNR

In this section, the angular scattering function of the WFIV is described first. Next the effect of detection angle on SNR is considered.

Combining equations (7.4) and (7.12), and the volume correction factor, $1/\sin\theta$, results in the following expression for the scattered light power of a WFIV:

$$P(\theta) = \frac{neP_0 V_n}{hf a \sin\theta} \int_{\Omega} i(\theta, \alpha_0, m) d\Omega e^{-\sigma n x} e^{-\sigma n (L-x) \sec\theta} \quad (7.22)$$

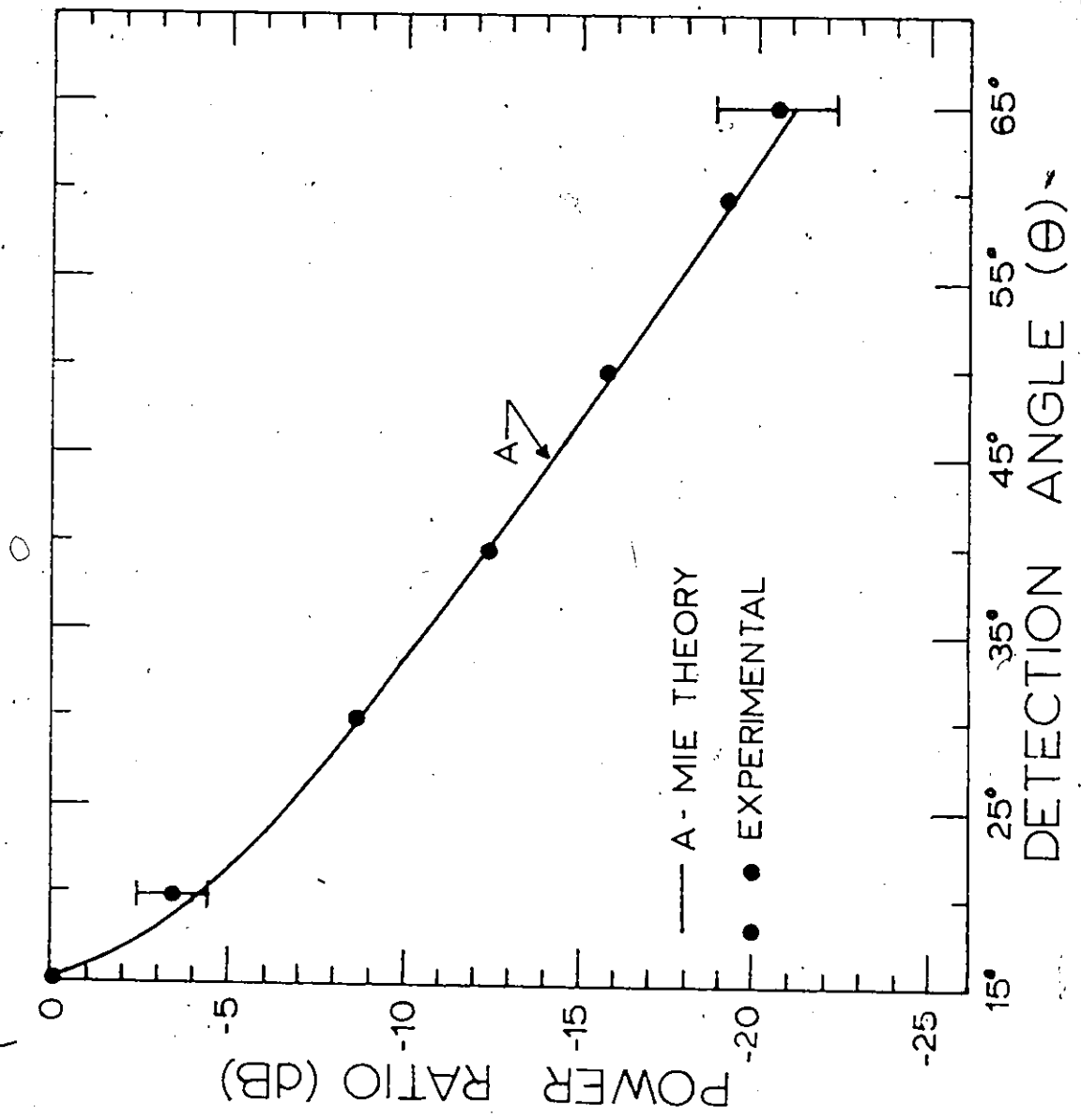
Note that the detection angle θ is measured from the direction of the direct light beam.

Experimental results are presented in Fig. 7.4 for a receiver aperture of $f/2.6$. The experimental arrangement is identical to that described in section 7.2. $5.7 \mu\text{m}$ diameter styrene divinylbenzene particles were employed at a number density of $n = 100 \text{ wppm}$ ($N = 125$). Curve A is the relative angular scattering power calculated using Eq. (7.22). It can be seen that there is excellent agreement between theory and experiment. Note also that a wavelength $\lambda = 0.45 \mu\text{m}$ was used for the calculations because this was the region of maximum photo-multiplier sensitivity. Furthermore, a wide aperture was employed. This minimizes the colour effect in the angular scattering function.

We now consider the effect of detection angle on the SNR of the WFIV. The SNR equation (7.13) can be employed if the volume correction factor is included. Then the SNR equation is given by

Fig. 7.4: WFIV angular scattering function. 5.7 μm diameter styrene divinylbenzene particles were employed at a number density of $n = 100$ wppm ($N = 125$). Curve A is the relative theoretical angular scattering function calculated using Eq. (7.22). The theoretical data has been corrected for reflection and refraction at the fluid-tube-air boundary. Some typical error bars are shown.

Fig. 7-4



8

$$\text{SNR}(\theta) = \frac{n P_0 M^2 \sin^2 \theta}{2 h f B a} \int_{\Omega} i(\theta, \alpha_0, m) e^{-\sigma n x} e^{-\sigma n (L-x) \sec \theta} d\Omega \quad (7.23)$$

Experimental results concerning detection angle are shown in Fig. 7.5. The experimental parameters are identical to those described for Fig. 7.4. Curve A is the relative experimental SNR. Curve B is the relative theoretical SNR calculated using Eq. (7.23). Note that for our condition, the turbidity, σn , is small ($\sigma n = 0.5$). Consequently the effect of the exponential factors is negligible compared to the effect of the intensity function, $i(\theta, \alpha_0, m)$. It can be seen that good agreement exists between theory and experiment. Similar results were obtained from fluid flow measurements employing the same particle size at a lower particle concentration ($n = 1$ wppm).

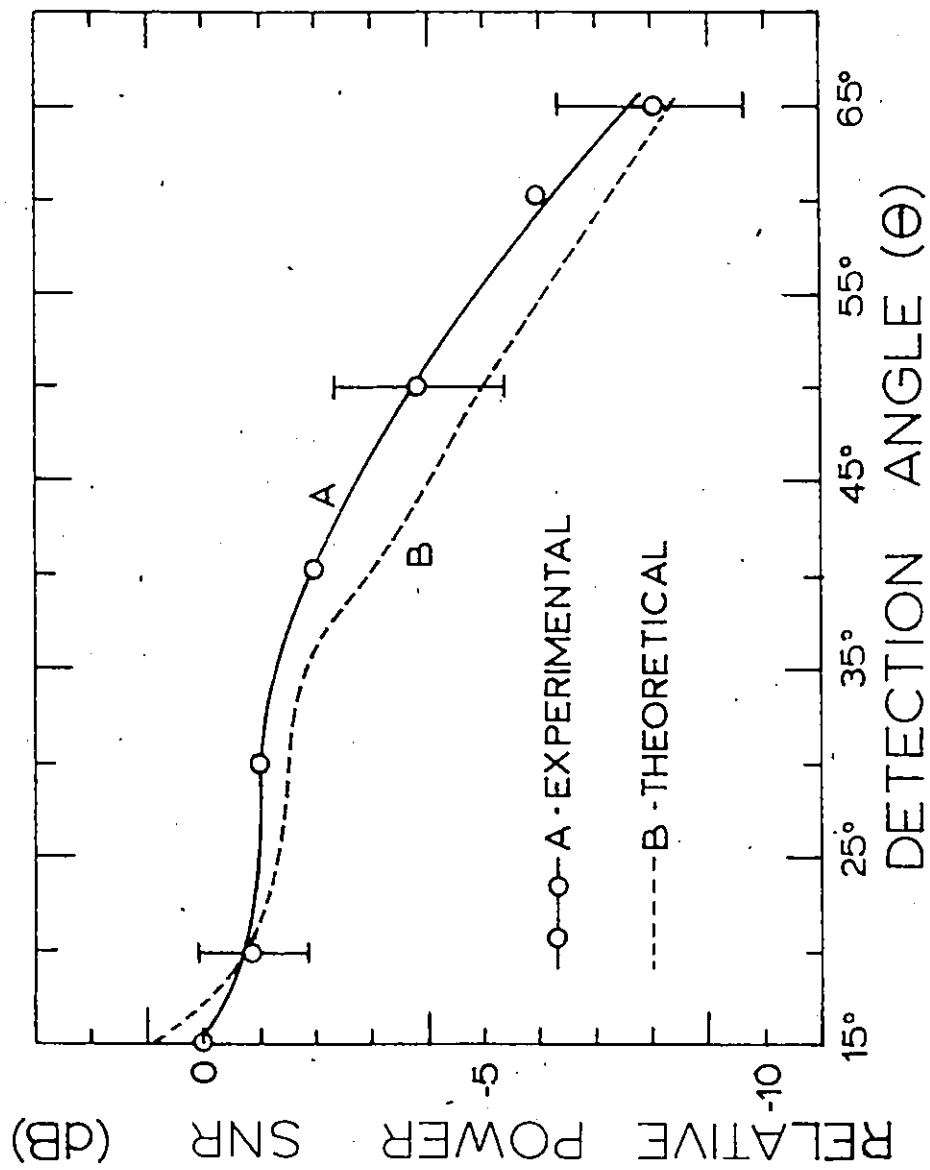
7.5 Summary

In this chapter the basic properties of incoherent detection (fringe crossing) are described. A SNR equation is derived to describe the effects of receiver aperture size, particle number density, and detection angle. There is excellent agreement between the theory and experimental measurements.

It is shown that the SNR of a fringe crossing system is directly proportional to the receiver aperture size. Furthermore, the SNR is independent of particle number density provided that the total number of particles in the probe volume, N , is larger than one. For $N \leq 1$, the SNR is directly proportional to the number density.

The above properties of incoherent scattering have been

Fig. 7.5: WFIV SNR(θ) measurements employing an $f/2.6$ receiver aperture. Curve A is the relative experimental SNR. Curve B is the relative theoretical SNR. The theoretical data has been corrected for reflection and refraction at the fluid-tube-air boundary. The maximum obtainable SNR is 28dB. All other caption data in Fig. 7.4 apply.



predicted by other workers. However, the first experimental confirmation of the theory, results from this work.

The above SNR behaviour is quite different from that of a DLDV. As shown in Chapter 6, the DLDV SNR is neither directly proportional to the receiver aperture size nor independent of the particle number density, even for $N \gg 1$. These significant differences provide further proof that the DLDV operates primarily in the coherent mode, and not in the incoherent mode, as was once commonly believed [20, 21].

CHAPTER 8

FOURIER IMAGE VELOCIMETER

This chapter introduces another new technique for velocity measurements. We refer to this new technique as the Fourier image velocimeter (FIV). The basic operating principle of the FIV is similar to that of WFIV, except that the real fringes are formed by Fourier images. Whereas the WFIV can employ an incandescent light source, the FIV must employ a coherent light source (e.g., a laser).

Included in this chapter are the theory of Fourier images, their characteristics, and their application to velocity measurements.

8.1 History of Fourier Images

Fourier images result from Fresnel diffraction of periodic objects. Under ideal conditions, the Fourier image is accurately similar to the object. They were first observed by Talbot in 1836 [64], but were not explained. In 1881, Rayleigh [65] gave a theoretical deduction for the distance between successive Fourier image orders. In 1956, Fourier images were rediscovered by Cowley and Moodie [26], who also named the phenomena "Fourier image". In addition to the Fourier images, there also exist intermediate images between orders. These diffraction patterns reflect the periodic nature of the object but have a functional form that depends on the distance from the object. This will be discussed later in this chapter.

Fourier images have been used to explain some aspects of insect vision [66, 67]. The insect eye is regarded as an array of small lenses on a curved surface. It is found that certain diffraction images occur in the vicinity of the photoreceptor elements of the insect eye. These diffraction images have been identified as intermediate images located between the original lens array and the first Fourier image [67].

An important application of Fourier images is in the repair of errors in periodic objects [27]. In some aspects of integrated circuit technology (e.g. in the fabrication of targets for silicon vidicons) the periodic object should be perfect. However, a defective periodic object (one or two-dimensional) can be restored if one of its higher order Fourier images is employed.

More recently, Fourier images have been employed for the measurement of particle flow velocities [25]. This work is discussed in detail in the following sections.

8.2 Theory of Fourier Images

A number of authors have discussed the theoretical background of Fourier images [26, 65, 68, 69, 70]. A derivation of the origin of Fourier images is given below which is based on Fourier optics [71]. Basically, the problem consists of obtaining the conditions under which self-imaging can be achieved.

As mentioned previously, Fourier images are a result of Fresnel diffraction. Figure 8.1 illustrates the diffraction geometry. Consider

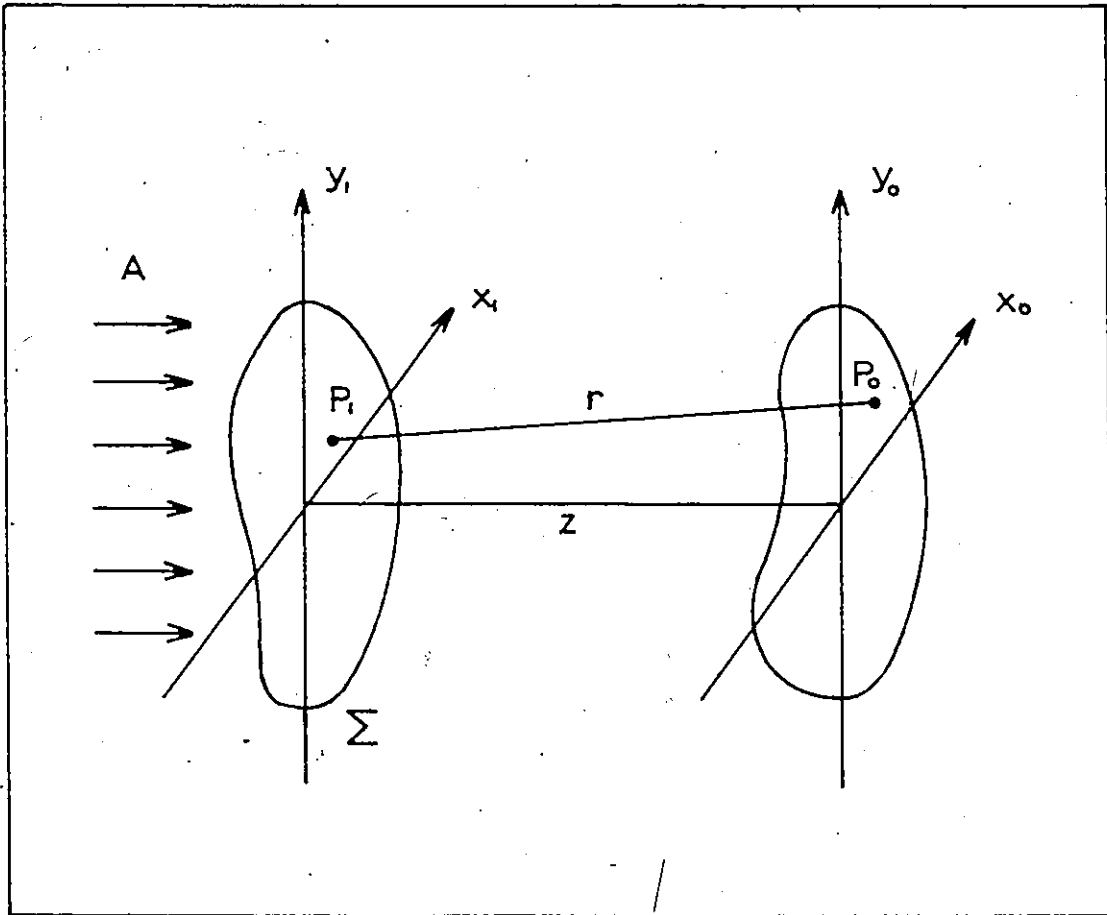


Fig. 8.1: Diffraction geometry. The optical object is illuminated by a plane monochromatic wave.

that the planar object is lying on the rectangular coordinate system (x_1, y_1) and that the observation is made on a plane in the coordinate system (x_0, y_0) . The planes are parallel and separated by a distance z . The field amplitude at a point (x_0, y_0) , for an object (or aperture) illuminated by a monochromatic plane wave, is [71]

$$U(x_0, y_0) = \frac{1}{i\lambda} \iint_{\Sigma} \frac{\exp(ikr)}{r} \cos(\vec{n}, \vec{r}) U(x_1, y_1) dx_1 dy_1 \quad (8.1)$$

where $U(x_1, y_1)$ is the distribution of the field immediately behind the planar object and $\cos(\vec{n}, \vec{r})$ is the obliquity factor. The integral is taken over the aperture Σ . Assuming that the Fresnel approximation is valid, then Eq. (8.1) can be rewritten as the Fresnel formula [71]

$$U(x_0, y_0) = \frac{\exp(ikz)}{i\lambda z} \iint_{-\infty}^{\infty} U(x_1, y_1) \exp\left\{\frac{ikz}{2z} [(x_0 - x_1)^2 + (y_0 - y_1)^2]\right\} dx_1 dy_1 \quad (8.2)$$

Now assume that an optical object, with transmission factor $t(x_1, y_1)$, is illuminated by a plane wave. The field immediately after the object can be represented by

$$U(x_1, y_1) = At(x_1, y_1) \quad (8.3)$$

where A depends on the type of illumination. For a monochromatic plane wave, A is a constant. Substitution into Eq. (8.2) results in a field at point $P_0(x_0, y_0)$ given by

$$U(P_0) = \frac{A \exp(ikz)}{i\lambda z} \iint_{\Sigma} t(x_1, y_1) \exp\left\{\frac{ik}{2z}[(x_0 - x_1)^2 + (y_0 - y_1)^2]\right\} dx_1 dy_1 \quad (8.4)$$

Using the convolution notation Eq. (8.4) can be rewritten as,

$$U(P_0) = \frac{\exp(ikz)}{i\lambda z} At(x_1, y_1) \otimes S(x_1, y_1) \quad (8.5)$$

where

$$S(x_1, y_1) = \exp\left\{\frac{ik}{2z}(x_1^2 + y_1^2)\right\} \quad (8.6)$$

The condition for which the planar object is reproduced can be found from the Fourier transform of Eq. (8.5), i.e.,

$$\begin{aligned} F[U(P_0)] &= \frac{\exp(ikz)}{i\lambda z} AF[t(x_1, y_1)] \cdot F[S(x_1, y_1)] \\ &= \frac{\exp(ikz)}{i\lambda z} AT(\mu, \nu) i\lambda z \exp[-i\pi\lambda z(\mu^2 + \nu^2)] \\ &= \exp(ikz) AT(\mu, \nu) \exp[-i\pi\lambda z(\mu^2 + \nu^2)] \quad (8.7) \end{aligned}$$

where $T(\mu, \nu)$ is the Fourier transform of the transmission factor $t(x_1, y_1)$, and where $F[S(x_1, y_1)]$ has been carried out using Eq. (8.6). The field reproduces the object when

$$F[U(P_0)] = AT(\mu, \nu) \quad (8.8)$$

Consequently

$$T(\mu, \nu) = \exp(ikz) T(\mu, \nu) \exp[-i\pi\lambda z(\mu^2 + \nu^2)] \quad (8.9)$$

One solution is

$$T(u, v) = a_{+1} \delta(u - u_0, v) + a_{-1} \delta(u + u_0, v) \quad , \quad (8.10)$$

where δ is the delta function. The Fourier transform of Eq. (8.10) is

$$t(x_1, y_1) = a_{+1} \exp(2i\pi u_0 x_1) + a_{-1} \exp(-2i\pi u_0 x_1) \quad , \quad (8.11)$$

which is independent of y_1 . This corresponds to a sinusoidal grating object of spacing $d = 1/\mu_0$. Values of z for the location of the Fourier image are determined by substituting Eq. (8.10) into Eq. (8.9), and then by performing the Fourier transform on the resultant equation. This yields

$$\text{L.H.S.} = a_{+1} \exp(2i\pi u_0 x_1) + a_{-1} \exp(-2i\pi u_0 x_1) \quad (8.12)$$

$$\text{R.H.S.} = \int_{-\infty}^{+\infty} \exp(ikz) \{a_{+1} \delta(u - u_0, v) + a_{-1} \delta(u + u_0, v)\} \times$$

$$\exp[-i\pi\lambda z(u^2 + v^2)] \exp(2i\pi u x_1) \exp(2i\pi v y_1) du dv$$

$$= \exp(ikz) \exp(-i\pi\lambda z u_0^2) \{a_{+1} \exp(2i\pi u_0 x_1)$$

$$+ a_{-1} \exp(-2i\pi u_0 x_1)\} \quad (8.13)$$

Equality of equations (8.12) and (8.13) requires

$$\exp(ikz) \exp(-i\pi\lambda z u_0^2) = 1 \quad (8.14)$$

Since we are only concerned with intensity, Eq. (8.14) is multiplied by its complex conjugate. Therefore, it can be seen that the solution given by Eq. (8.10) is independent of z . This indicates that an image of a sinusoidal grating exists for all values of z . Note that Eq. (8.11) can not be a pure amplitude grating because $t(x_1, y_1)$ is real and positive only when a_{+1} and a_{-1} are complex.

Another solution for Eq. (8.9) is

$$T(\mu, \nu) = \sum_{p=-\infty}^{+\infty} a_p \delta(\mu - p\mu_0, \nu) \quad (8.15)$$

where p is an integer. The Fourier transform of $T(\mu, \nu)$ is

$$t(x_1, y_1) = \sum_{p=-\infty}^{+\infty} a_p \exp(2i\pi p\mu_0 x_1) \quad (8.16)$$

Values of z are determined following the same procedure used previously. Substitution of Eq. (8.16) into Eq. (8.9), carrying out the Fourier transform, and then multiplying the resultant equation by its complex conjugate, results in

$$\begin{aligned} \text{L.H.S.} &= \sum_{p=-\infty}^{+\infty} a_p \exp(2i\pi p\mu_0 x_1) \cdot \sum_{p'=-\infty}^{+\infty} a_{p'}^* \exp(-2i\pi p'\mu_0 x_1) \\ &= \sum_{p=-\infty}^{+\infty} \sum_{p'=-\infty}^{+\infty} a_p a_{p'}^* \exp[2i\pi\mu_0 x_1 (p-p')] \end{aligned} \quad (8.17)$$

$$\begin{aligned}
\text{R.H.S.} &= \exp(ikz) \sum_{p=-\infty}^{+\infty} a_p \exp(2i\pi\mu_0 x_1) \exp(-i\pi\lambda z p^2 \mu_0^2) \times \\
&\quad \exp(-ikz) \sum_{p'=-\infty}^{+\infty} a_{p'}^* \exp(-2i\pi p' \mu_0 x_1) \exp(i\pi\lambda z p'^2 \mu_0^2) \\
&= \sum_{p=-\infty}^{+\infty} \sum_{p'=-\infty}^{+\infty} a_p a_{p'}^* \exp[2i\pi\mu_0 x_1 (p-p')] \{ \exp[-i\pi\lambda z \mu_0^2 (p^2 - p'^2)] \} . \quad (8.18)
\end{aligned}$$

The condition L.H.S. = R.H.S. requires

$$\sum_{p=-\infty}^{+\infty} \sum_{p'=-\infty}^{+\infty} a_p a_{p'}^* \exp[2i\pi\mu_0 x_1 (p-p')] \{ \exp[-i\pi\lambda z \mu_0^2 (p^2 - p'^2)] - 1 \} = 0 . \quad (8.19)$$

Equation (8.19) is satisfied if

$$\exp[-i\pi\lambda z \mu_0^2 (p^2 - p'^2)] = 1 , \quad (8.20)$$

for all values of $(p^2 - p'^2)$.

Let

$$m = p^2 - p'^2 . \quad (8.21)$$

Then Eq. (8.20) becomes

$$[\exp(-i\pi\lambda z \mu_0^2)]^m = 1 . \quad (8.22)$$

The only solution of Eq. (8.22) valid for all integer values of m is

$$\pi \lambda z \mu_0^2 = 2n\pi, \quad (8.23)$$

where n is an integer, including zero. This gives

$$z = \frac{2n}{\lambda \mu_0^2} = \frac{2nd^2}{\lambda}, \quad (8.24)$$

where $d = 1/\mu_0$ is the periodicity of the grating.

If a Ronchi grating is used, as in our experiments, then alternate values of p (and therefore p') are missing. Consequently, m is always even. Therefore it can be seen from Eq. (8.22) that

$$z = \frac{nd^2}{\lambda}. \quad (8.25)$$

Note however, that an amplitude phase change of π (relative to the object) occurs for all odd n . This can be seen by inspection of Eq. (8.18), after substitution of Eq. (8.25).

In summary, we have shown that self-imaging occurs in the two cases which we have considered: (i) For a sinusoidal grating, there is an image at every value of z ; (ii) For a periodic grating, there are images at discrete values of z . Similar results can be obtained if the object is illuminated by a spherical coherent wave. However, the distance of the point source from the object plane must be taken into account [26].

In the ideal case (grating of large extent) the intensity distribution of the Fourier image exactly reproduces the intensity distribution of the object. This allows calculation of the position

of the Fourier images, as done above. Although not done here, the position where harmonic components of the grating are reproduced can also be calculated from consideration of Eq. (8.22).

The intensity distribution of the intermediate images can be most readily calculated with the aid of Fresnel integrals.

8.3 Computation of Fresnel Integrals

Here we are only interested in a one-dimensional periodic grating (e.g., a Ronchi grating). Therefore Eq. (8.4) can be rewritten as

$$U(P_0) = \frac{A \exp(ikz)}{i\lambda z} \int_{\Sigma} T(x) \exp\left\{\frac{ik}{2z}(x_1 - x_0)^2\right\} dx_1 \quad (8.26)$$

The integral given by Eq. (8.26) can be simplified by letting

$$\eta = \sqrt{\frac{k}{\pi z}} (x_1 - x_0) \quad (8.27)$$

For the case of a Ronchi grating, Eq. (8.26) can now be put in the form

$$U(P_0) = \frac{A \exp(ikz)}{i\lambda z} \sqrt{\frac{\pi z}{k}} \sum_n \int_{\eta_1}^{\eta_2} \exp\left(\frac{i\pi \eta^2}{2}\right) d\eta \quad (8.28)$$

where the limits of the integral are determined by the relative position of each transmission slit, and the summation, \sum_n , sums over all illuminated slits.

The integral can be evaluated in terms of tabulated functions

known as Fresnel integrals. These are defined by

$$\left. \begin{aligned} C(\alpha) &= \int_0^\alpha \cos \frac{\pi t^2}{2} dt \\ \text{and} \\ S(\alpha) &= \int_0^\alpha \sin \frac{\pi t^2}{2} dt \end{aligned} \right\} \quad (8.29)$$

The Fresnel integrals are also readily available from a computer sub-routine program. Note that

$$\int_{n_1}^{n_2} \exp\left(\frac{i\pi n^2}{2}\right) dn = \int_0^{n_2} \exp\left(\frac{i\pi n^2}{2}\right) dn - \int_0^{n_1} \exp\left(\frac{i\pi n^2}{2}\right) dn \quad (8.30)$$

Hence

$$U(P_0) = A \frac{\exp(ikz)}{i\sqrt{2\lambda z}} \sum_n \{ [C(n_2) - C(n_1)] + j[S(n_2) - S(n_1)] \} \quad (8.31)$$

Finally, the corresponding intensity distribution is given by

$$\begin{aligned} I(P_0) &= U(P_0)U^*(P_0) \\ &= \frac{A^2}{2\lambda z} \left\{ \left[\sum_n [u(n_2) - u(n_1)] + j[S(n_2) - S(n_1)] \right]^2 \right\} \\ &= \frac{A^2}{2\lambda z} \left\{ \left[\sum_n [u(n_2) - u(n_1)] \right]^2 + \left[\sum_n [S(n_2) - S(n_1)] \right]^2 \right\} \quad (8.32) \end{aligned}$$

In the above, the obliquity factor has been neglected because it simplifies derivation and contributes only a small error to the final result.

A further simplification results from neglecting the Gaussian intensity profile of the laser source used in the experiments. However, both of these factors have been included in the computer algorithm used to calculate intensity distribution. Comparison of these distributions with measurements are provided in section 8.5.

8.4 Photographic and Microphotometry Techniques for Diffraction Pattern Measurements

The experimental arrangement employed for recording the diffraction patterns is shown in Fig. 8.2: A He-Ne laser beam (6328 \AA) is passed through a beam expander, which consists of a pinhole ($20 \text{ }\mu\text{m}$) and two lenses. The ratio of the focal lengths (≈ 10) determines the enlarging factor of the beam expander. The final collimated beam diameter is about 2 cm ($1/e^2$ intensity). A 35 mm single-lens reflex camera, with lens removed, is mounted with the film plane perpendicular to the collimated beam. The camera viewer allows accurate positioning of the film plane with the Fourier images. Successive distances between Fourier images can therefore be accurately determined.

Kodak type SO-410 film was employed. This film is sensitive to the laser radiation and in addition has excellent resolution. Thirty-six exposure rolls were employed to ensure that all the necessary data for particular experiments could be recorded on a single roll of film.

The exposure, E , is defined by $E = It$, where I is the light intensity and t the exposure time. For constant I , which is true in our case, E varies with t . For satisfactory tone reproduction, proper exposure time must be found. The purpose is to avoid under exposure

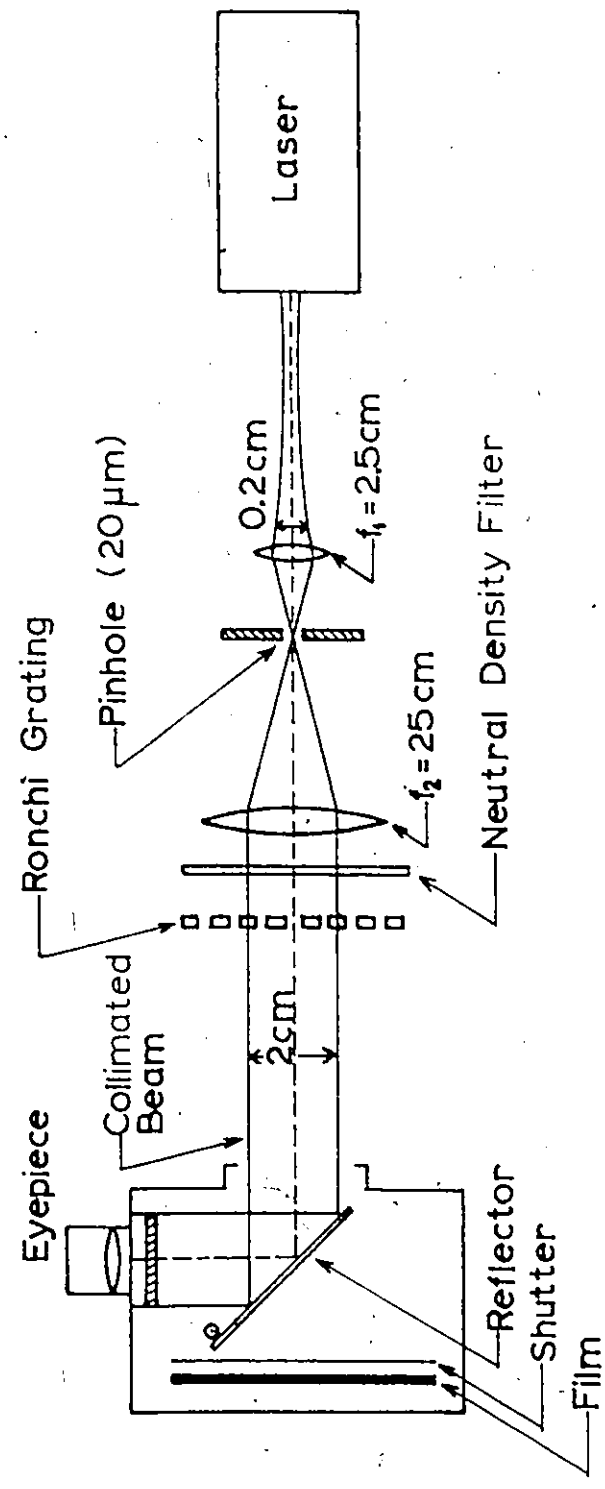


Fig. 8.2: Exoerimental arrangement for photographing diffraction patterns.

(working in the fog density) or over exposure (working in the saturated density). Proper exposure is found by taking a series of photographs employing different times (time-scale exposures). The measured value of density, D , plotted against the logarithm of exposure, $\log E$, results in the H and D curve [73]. Normally, a portion of the curve is a straight line. The exposure is chosen so that the total range of $\log E$ employed is within the linear portion of the curve.

Two parameters associated with the H and D curve are "speed" and "contrast". Speed is associated with the position of the curve on the $\log E$ axis. It is defined by the reciprocal of an E_0 , which is the minimum exposure to produce a specified density above the fog density. Contrast, which can be specified by γ , is related to the slope of the straight line portion of the H and D curve. For a given material and set of exposure conditions, the value of gamma varies with processing, and especially with time of development. Thus gamma is sometimes called "development contrast".

The H and D curve can be evaluated with the aid of a microphotometer (or microdensitometer). The major components of such a device are shown in Fig. 8.3. A stabilized tungsten lamp operating at a colour temperature of about 3000°K is generally used as a light source. The infrared and ultraviolet radiations are usually filtered out. For black and white materials, as in our case, a broad band white light spectrum is satisfactory. For colour materials, it is necessary to employ appropriate filters.

The microscope system, similar to a standard microscope,

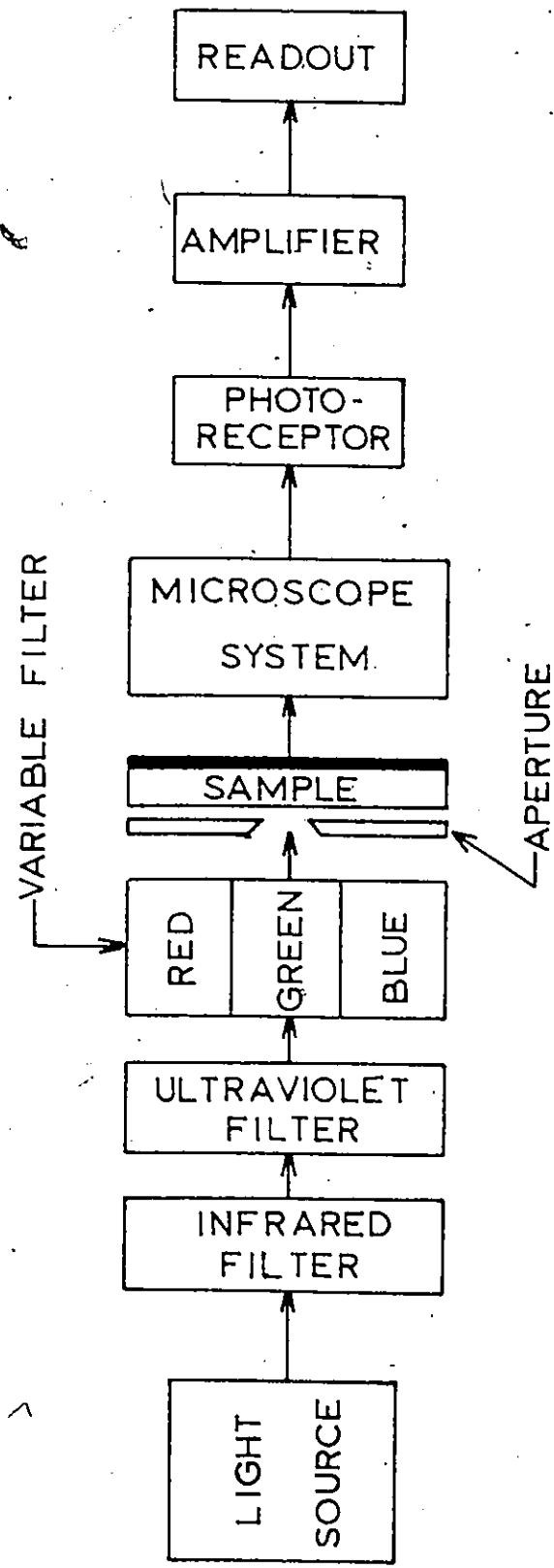


Fig. 8.3: Basic components of a microphotometer.

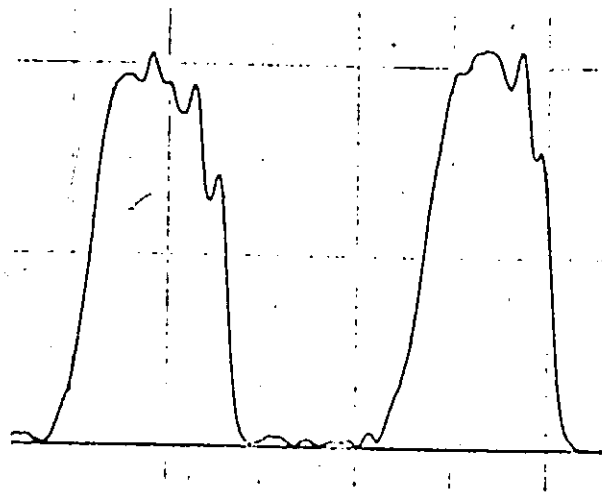
focuses the image of a portion of the sample onto a plane, in which is located a variable slit. This slit can be made as small as a few microns and limits the radiation incident on the detector. Scanning is achieved by linear translation of the sample by means of a low speed drive mechanism.

The amplified detector output can provide a signal which is related either to the density or to the opacity of the sample, depending on the mode selected. In our measurements, the opacity was recorded with the aid of an x-y recorder. The combined speed accuracy of both drives (sample and x-y recorder) was constant to within 0.5%.

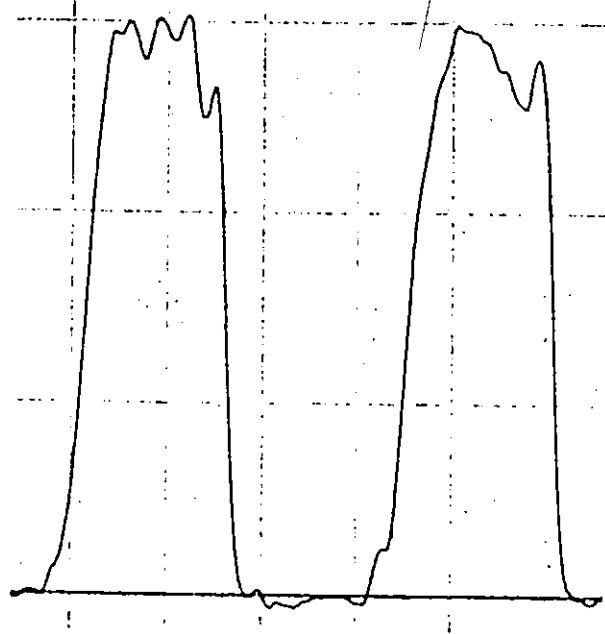
Some of the experimental results in determining the exposure time are shown in Fig. 8.4. These are for the first order Fourier image at $z = 20.4$ cm for a 100 lpi Ronchi grating. Figures 8.4(a), (b), and (c) represent microphotometer tracings of photographs exposed for $1/250$ s, $1/125$ s, and $1/60$ s, respectively. All three exposures are within the straight line portion of the H and D curve. Larger exposure times would result in a loss of detail because of saturation. An exposure time of $1/125$ s was chosen for subsequent observations. This allowed a sufficient safety factor for reliable measurements. Figure 8.4(d) represents a microphotometer tracing of the 100 lpi Ronchi grating. This is shown both for comparison purposes and to illustrate the properties of the grating. The transmission "pip" observed on the edge of each black strip is real and results from the method of grating construction. It is observed on some gratings, but not on others. Note that the "dark" portion appears to be slightly

C.

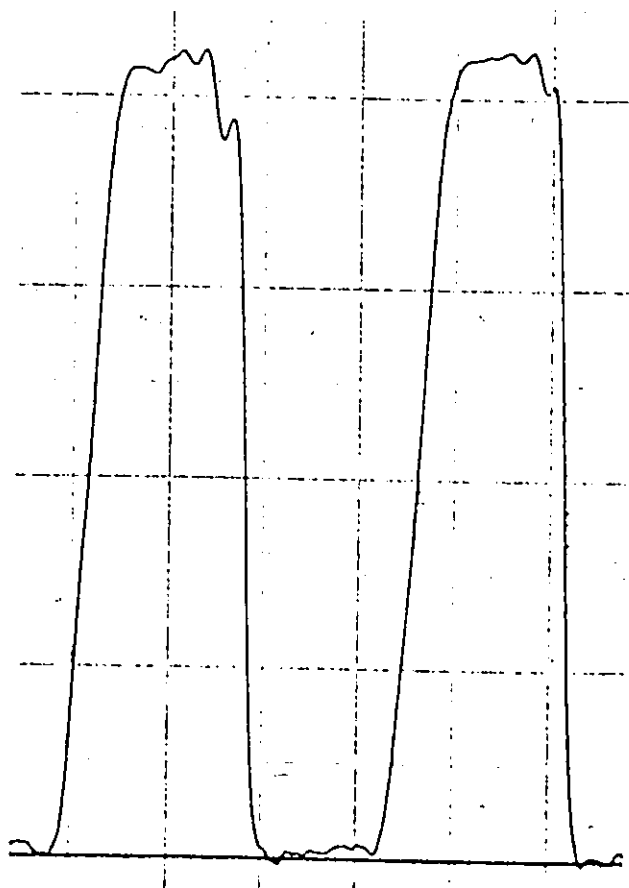
Fig. 8.4: Microphotometer tracings. The first order Fourier image of a Ronchi grating was photographed for $1/250$ s, $1/125$ s, and $1/60$ s in (a), (b), and (c), respectively. (d) was taken directly from a 100 lpi Ronchi grating. The baseline corresponds to maximum transmission of the original photographic negative.



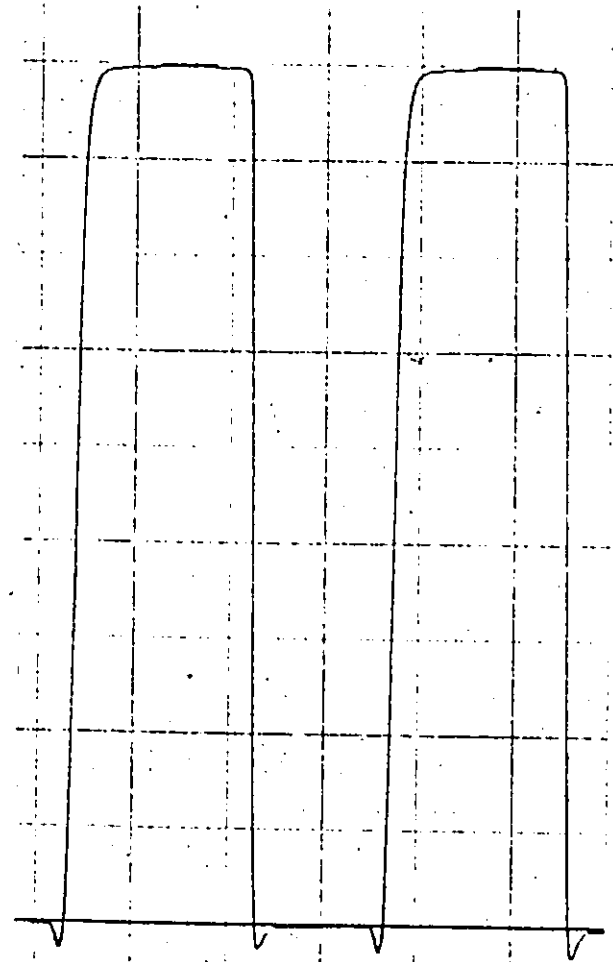
(a)



(b)



(c)



(d)

larger than the "bright" portion. This is due to the finite width of the receptor aperture of the microphotometer. Traveling microscope measurements indicate that both portions are of equal width.

8.5 Diffraction Patterns

Microphotometer tracings of the central portion of the diffraction patterns, together with the corresponding calculated patterns are shown in Fig. 8.5. These are all produced in the region of the first order Fourier image. The object, a Ronchi grating of periodicity $d = 0.0254 \pm 0.0003$ cm, was illuminated by a 2 cm diameter laser beam as indicated in Fig. 8.2. The total number of fringes illuminated was about 75. This number was employed in the evaluation of the Fresnel integral.

Figure 8.5(a) represents the measured first order Fourier image located at $z = 20.4$ cm. This is also the basic distance, $2d^2/\lambda$. The calculated first order Fourier image is represented by a square wave as shown in Fig. 8.5(a'). Note that in the figures, the primes represent calculated patterns. Figures 8.5(b), (c), (d), (e), and (f), represent measured intermediate images located at $z = 21.4$ cm, 23.4 cm, 25.5 cm, 27.4 cm, and 29.4 cm, respectively. The corresponding calculated images are also shown. Note that excellent agreement is found between the calculated and the measured patterns. If the beam is perfectly collimated, and sufficiently large in diameter, then the periodicity of the image has a constant value of d except when z is located in a small region about $d^2/2\lambda$ (one-fourth of the basic distance) in front of or beyond

Fig. 8.5: Microphotometer traces of measured diffraction patterns together with their corresponding calculated patterns. The first Fourier image is located at $z = 20.4$ cm, (a), (b), (c), (d), (e), and (f) correspond to $z = 20.4$ cm, 21.4 cm, 23.4 cm, 25.5 cm, 27.4 cm, and 29.4 cm, respectively. (a'), (b'), (c'), (d'), (e'), and (f') represent the corresponding calculated patterns.

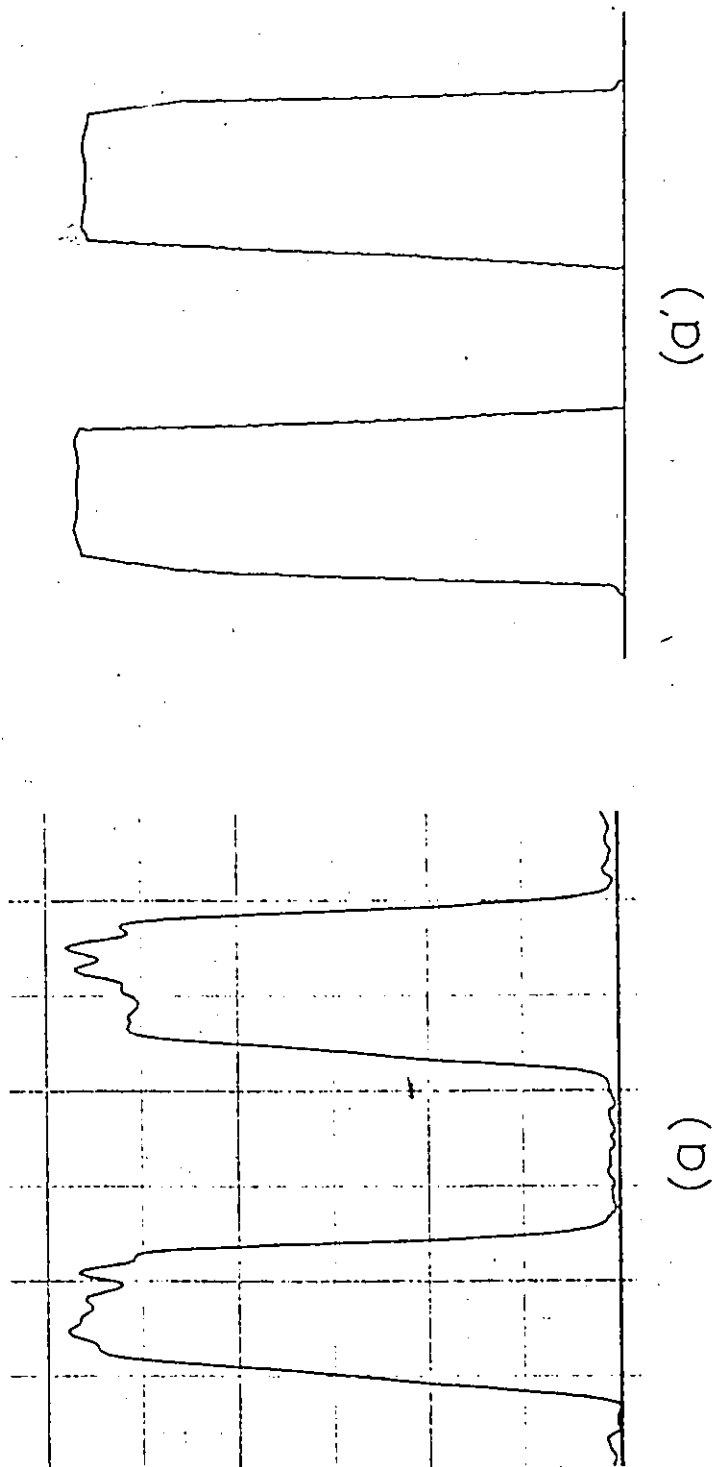
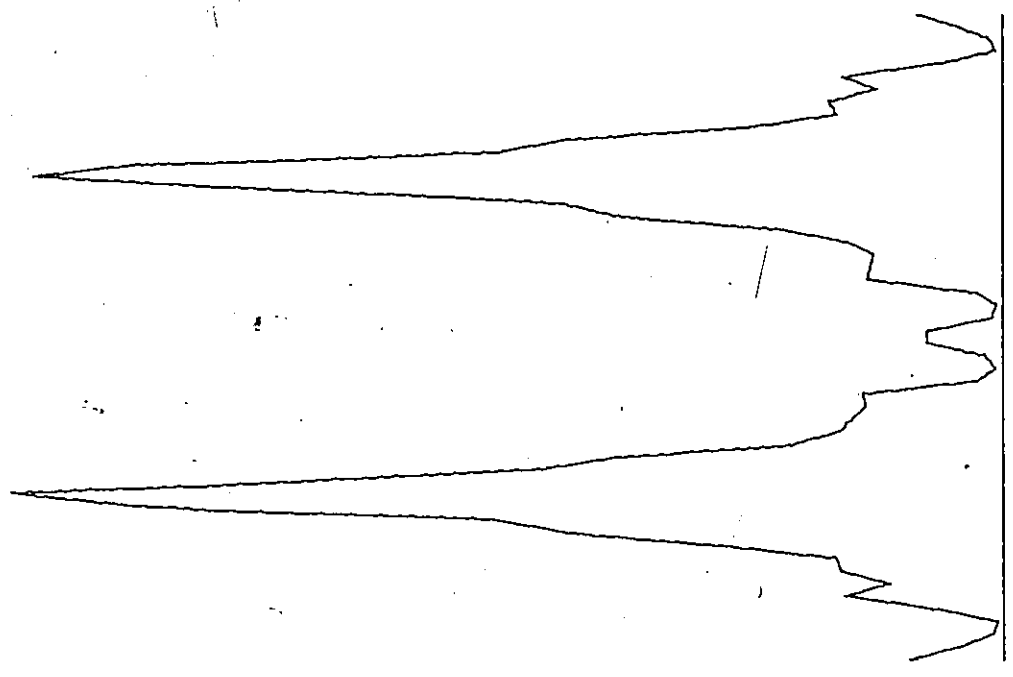
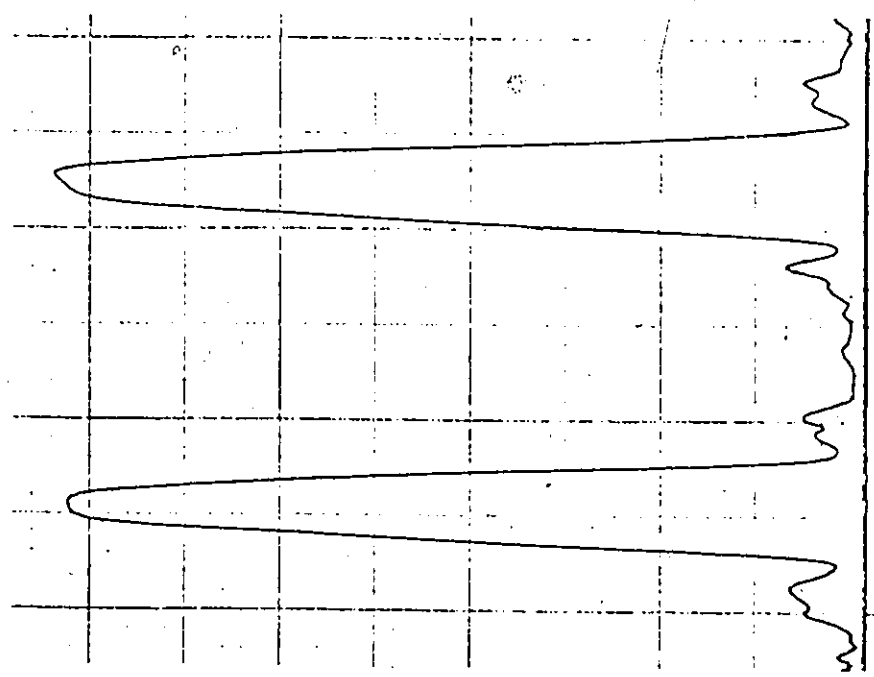


Fig. 2-5.

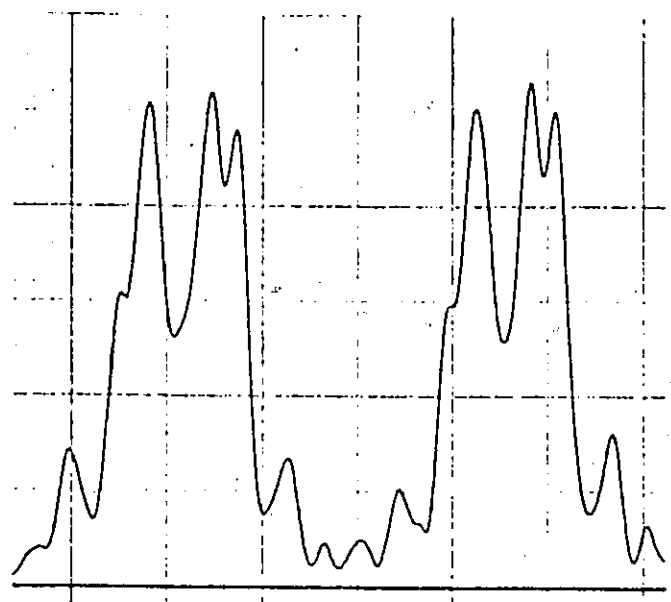


(b')

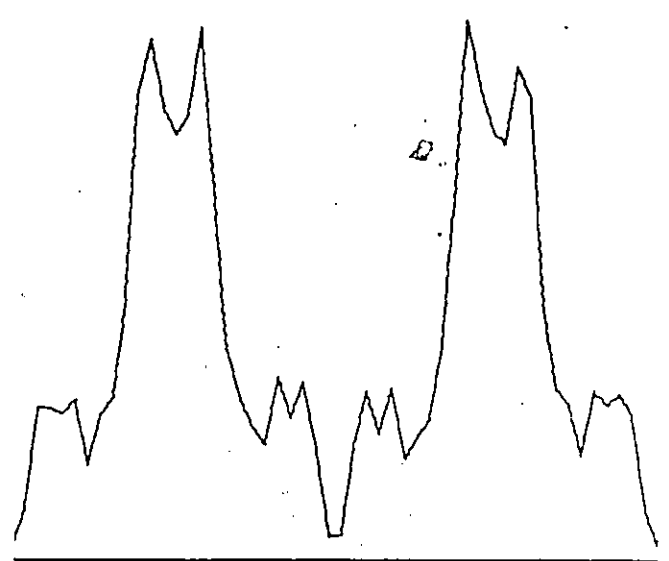


(b)

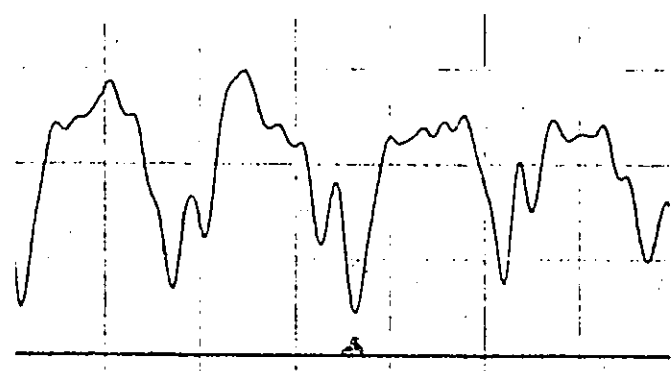
Fig. B-5



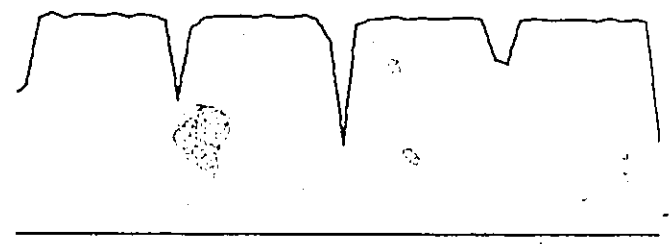
(c)



(c')

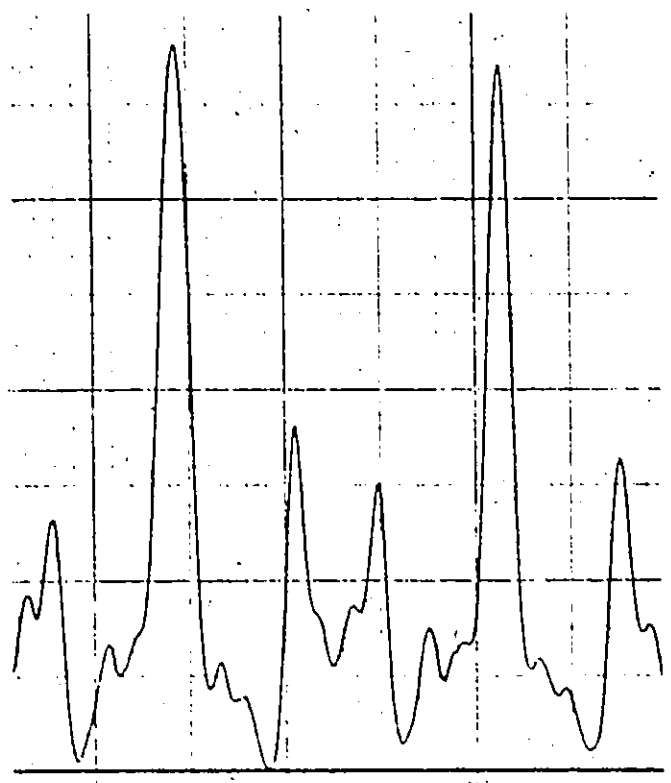


(d)

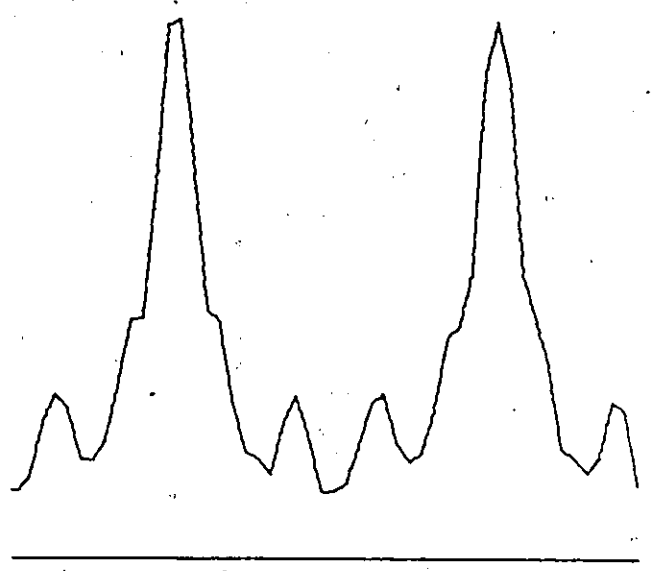


(d')

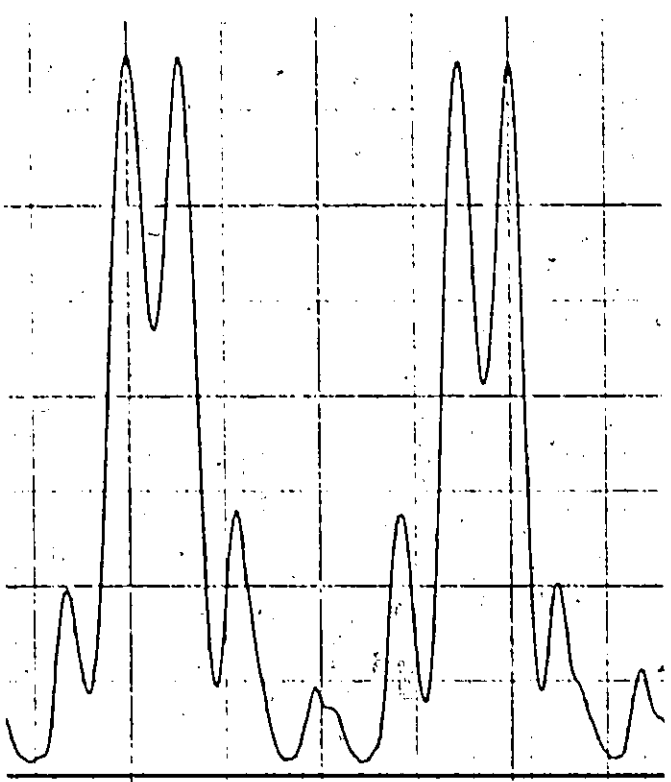
Fig. 8-5



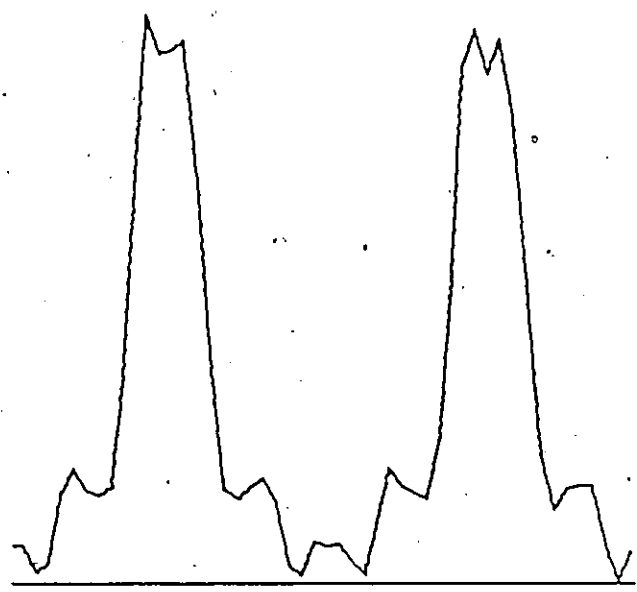
(e)



(e')



(f)



(f')

a Fourier image. Then the periodicity appears to have a value of $d/2$, as shown in Fig. 8.5(d).

In practice we have found that errors in the grating have the greatest effect on images located between the object and the first order Fourier image. The measured variation in the grating periodicity was ± 0.0003 cm for a $d = 0.0254$ cm. Examples of the effect are shown in Figures 8.6 and 8.7.

Figure 8.6(a), (b), (c) and (d) represent measured intermediate images located at $z = 19.4$ cm, 18.4 cm, 17.4 cm, 16.4 cm, respectively. Figure 8.6 (a'), (b'), (c'), and (d') are the corresponding theoretical patterns. The agreement between theory and experiment is not as good as in the case of Fig. 8.5.

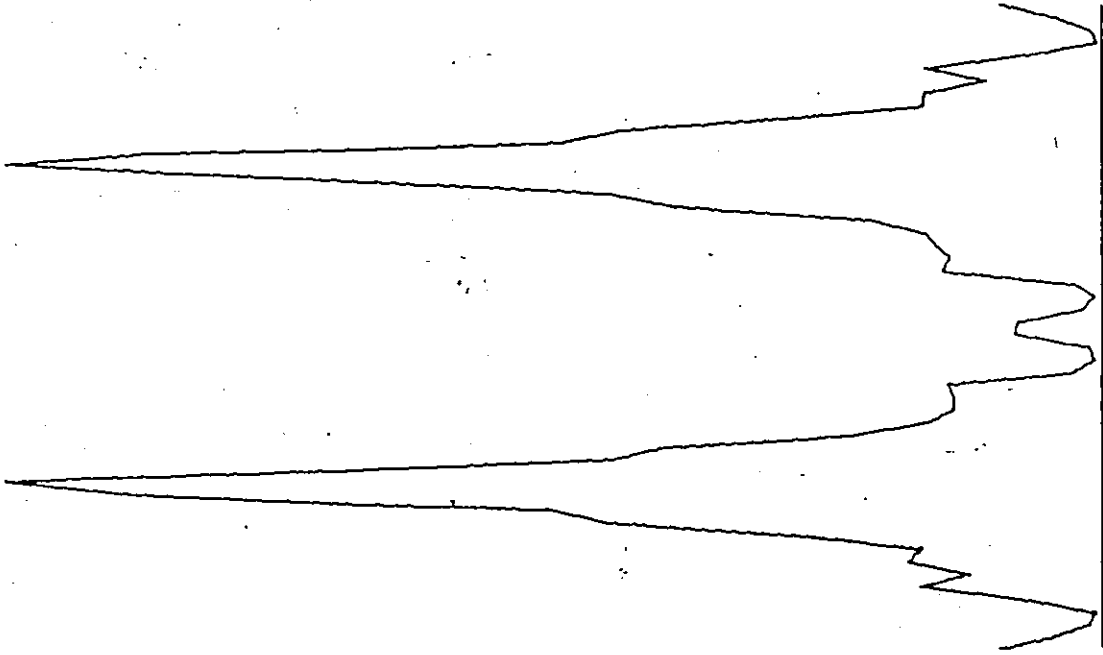
Figure 8.7(a) and (b) represent intermediate images located at $z = 20.5$ cm, and 20.3 cm, respectively. Each is 1 mm away from the plane of the first order Fourier image. It can be seen that the pattern located 1 mm beyond the Fourier image agrees with the theory much better than that located 1 mm before the Fourier image.

Figures 8.5, 8.6, and 8.7 also demonstrate the error repair characteristic of Fourier images [26, 27]. Figure 8.7 indicates that the error repair starts immediately beyond the first order Fourier image.

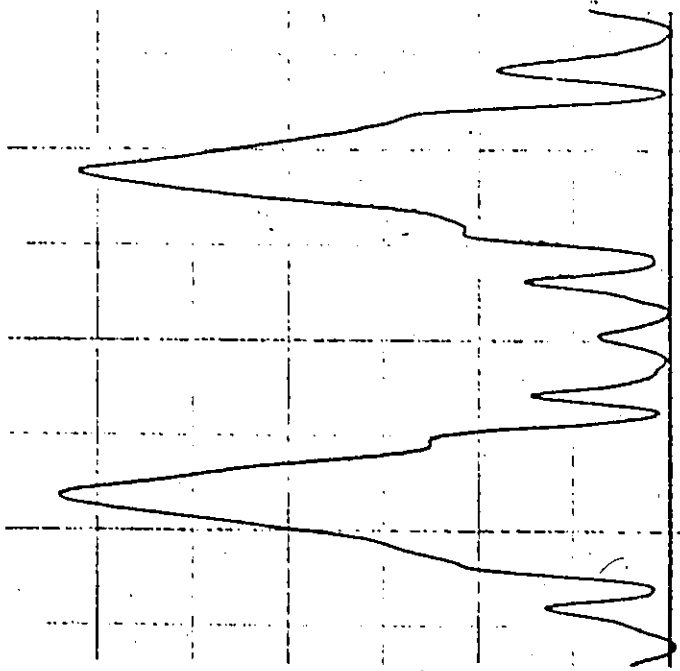
Table 8.1 lists the peak intensities of the measured and calculated diffraction patterns located after the first order Fourier image. Each set is normalized to the Fourier image value. These were taken from the data in Fig. 8.5. It can be seen that excellent agreement exists between corresponding values indicating that the photographic



Fig. 8.6: Microphotometer traces and theoretical curves of the diffraction pattern near the first Fourier image ($z = 20.4$ cm). Experimental results are given by (a), (b), (c), and (d), which correspond to $z = 19.4$ cm, 18.4 cm, 17.4 cm, and 16.4 cm, respectively. The primed figures are the corresponding theoretical curves.

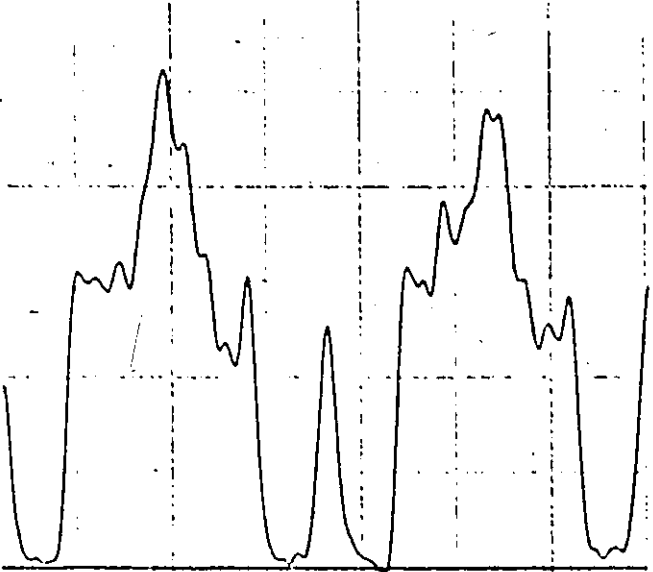


(a)

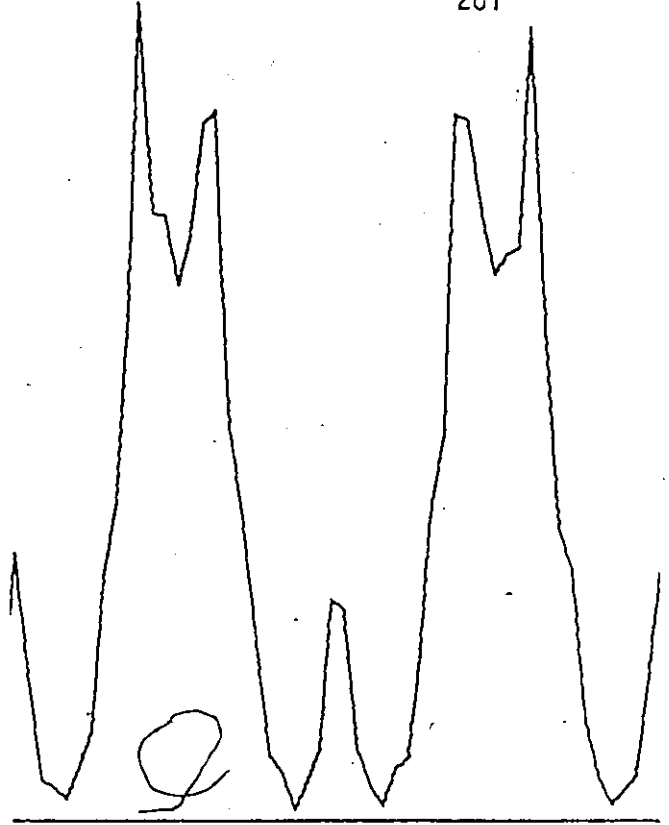


(a)

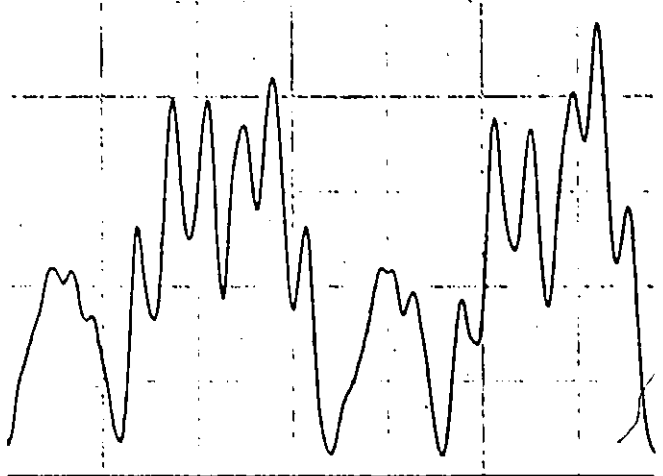
2



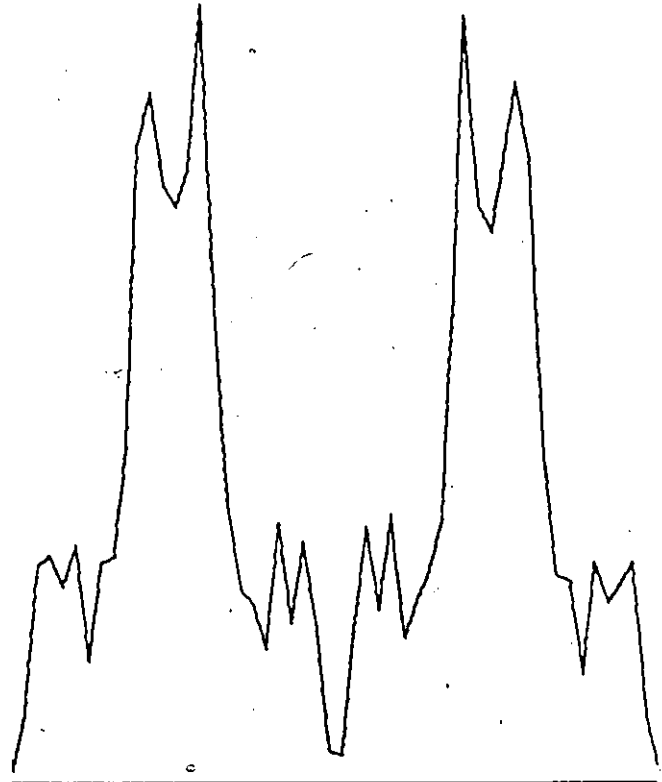
(b)



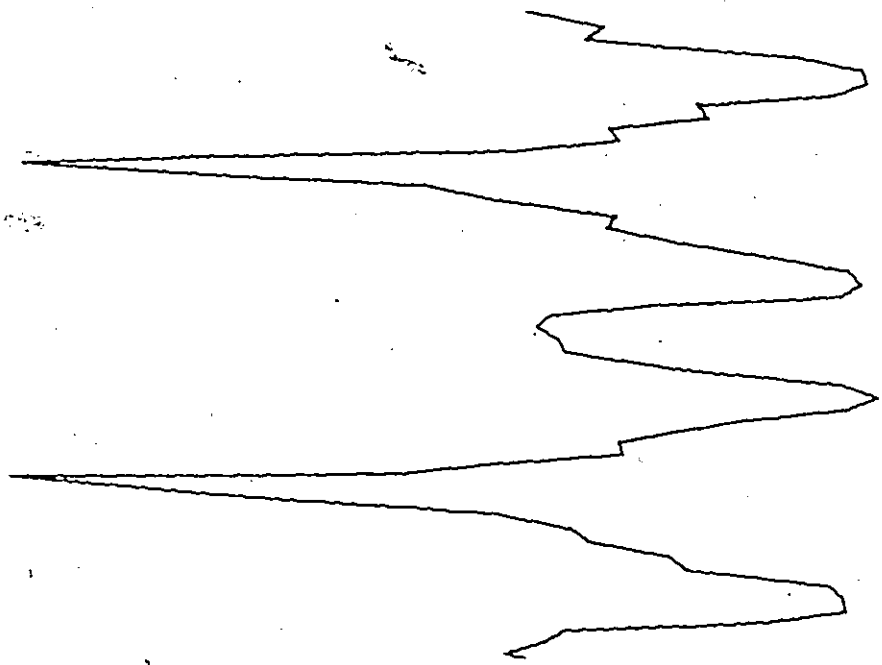
(b')



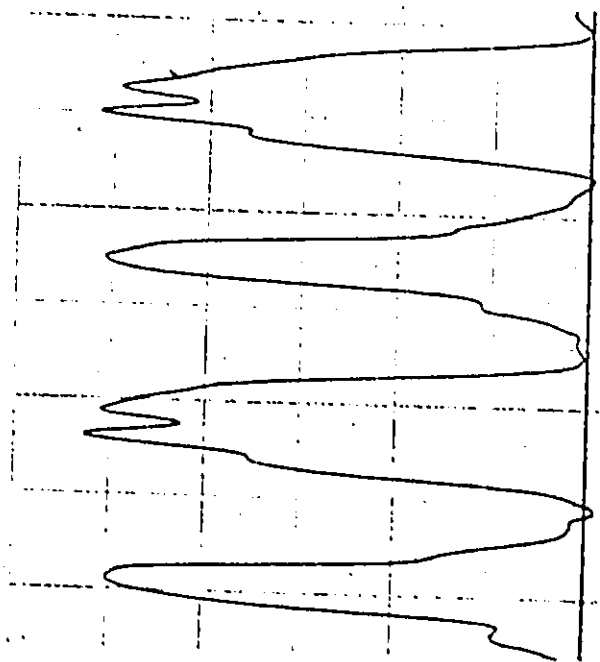
(c)



(c')

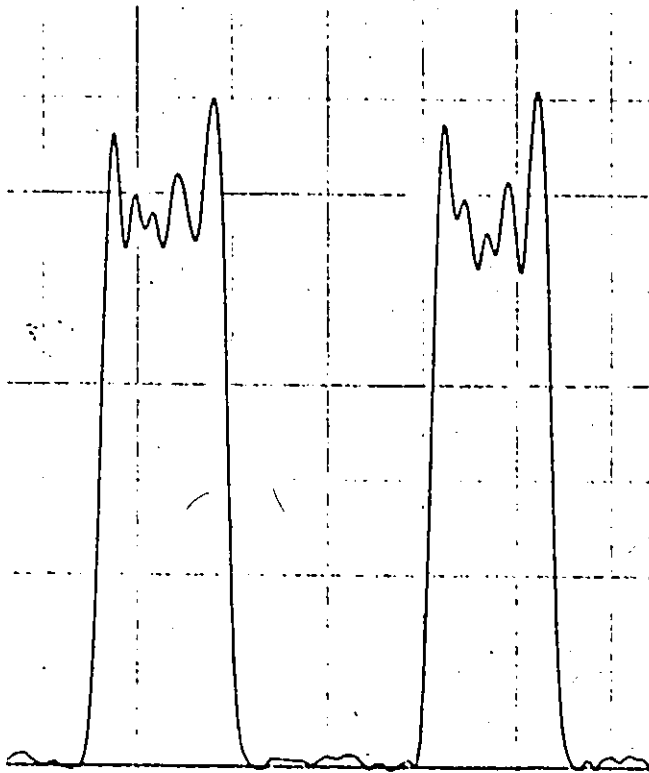


(d')

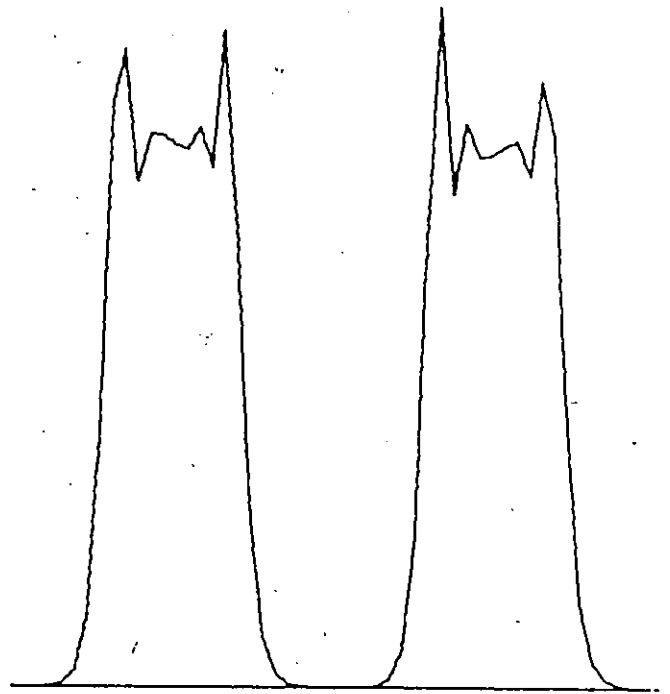


(d)

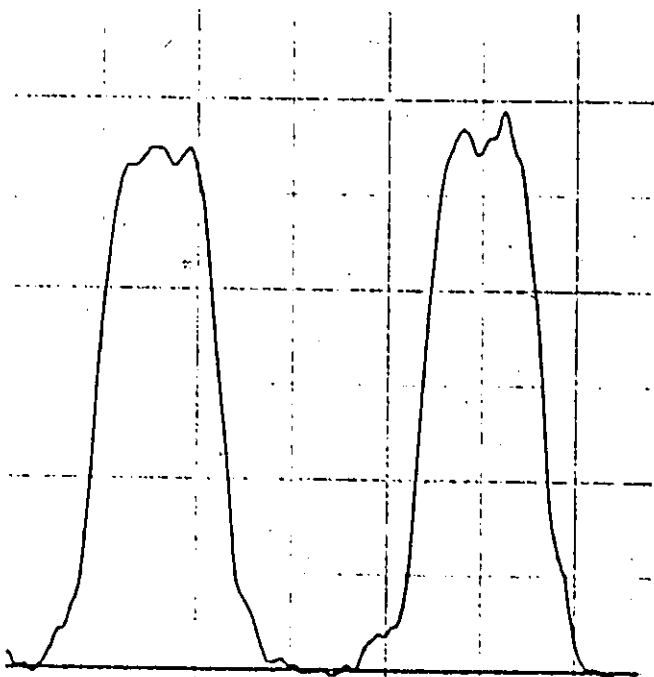
Fig. 8.7: Microphotometer traces and theoretical curves for the diffraction pattern near the first Fourier image ($z = 20.4$ cm). (a) and (b) are the measured patterns and correspond to $z = 20.5$ cm, and 20.3 cm, respectively. (a') and (b') are the corresponding calculated curves.



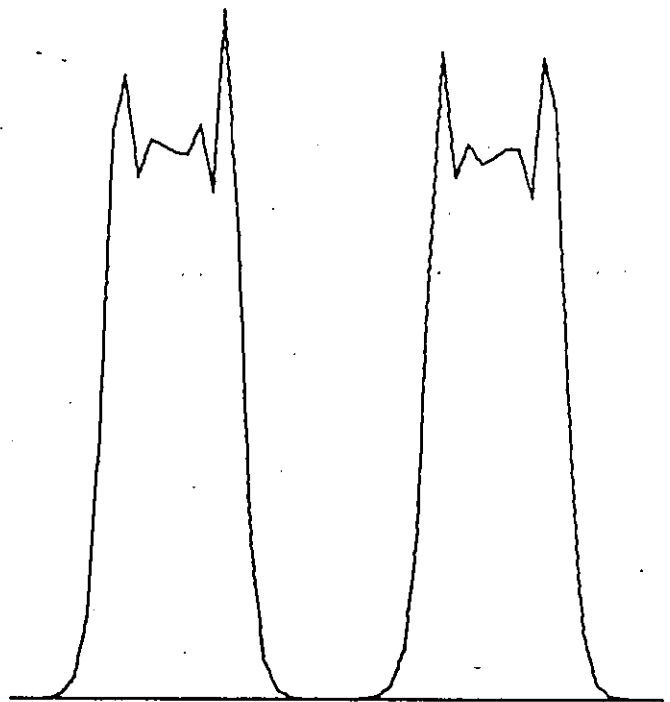
(a)



(a')



(b)



(b')

Table 8.1: Comparison Between Relative Peak Intensities of Measured and Calculated Diffraction Patterns

z	Measured	Calculated
20.4 cm	1.0	1.0
21.4 cm	1.5	1.7
23.4 cm	0.9	0.9
25.5 cm	0.4	0.4
27.4 cm	1.3	1.0
29.4 cm	1.3	1.0

and measurement techniques were satisfactory and that error repair was nearly complete.

Higher order Fourier and intermediate images have also been calculated. Some results are shown in Fig. 8.8. Figure 8.8(a) is the fifth order Fourier image located at $z = 102$ cm. Figure 8.8(b), (c) and (d) are intermediate images located at $z = 103$ cm, 107.1 cm, and 109 cm, respectively. Note that the functional forms of these higher order images are smoother than those of the first order. This is expected because a gradual transition from Fresnel to Fraunhofer diffraction commences at these distances. The above phenomena were also observed experimentally.

Experiments and calculations were also carried out employing 300 lpi and 1000 lpi Ronchi gratings. The agreement between theory and experiment was comparable to that for the 100 lpi grating. However, due to the much smaller periodicity of these gratings, the useful distance for employing Fourier images was shorter. The transition to Fraunhofer diffraction started at $z \approx 35$ cm, and $z \approx 110$ cm, for the 1000 lpi and 300 lpi gratings, respectively. The corresponding distance for the 100 lpi grating was about 350 cm. This data indicates that the useful working distance is directly proportional to the periodicity.

Note that the functional form of the diffraction patterns depends on the number of grating lines employed in the calculation, particularly for a small number of lines. Fast Fourier transform (FFT) [28] techniques can be used to determine the minimum number of lines required. For a small number of lines, the periodicity of the intermediate images can

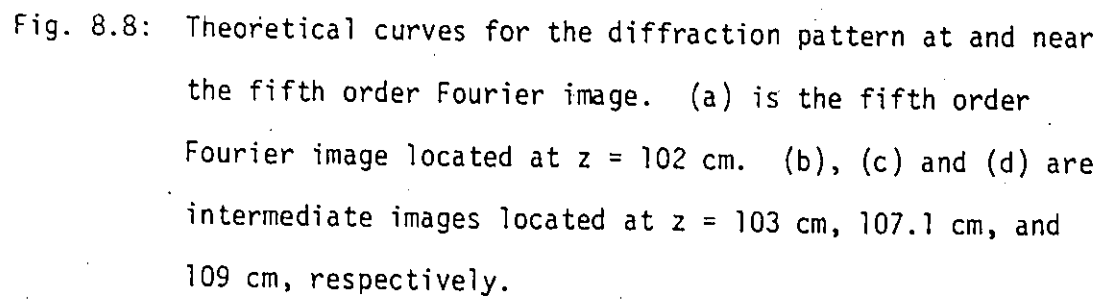
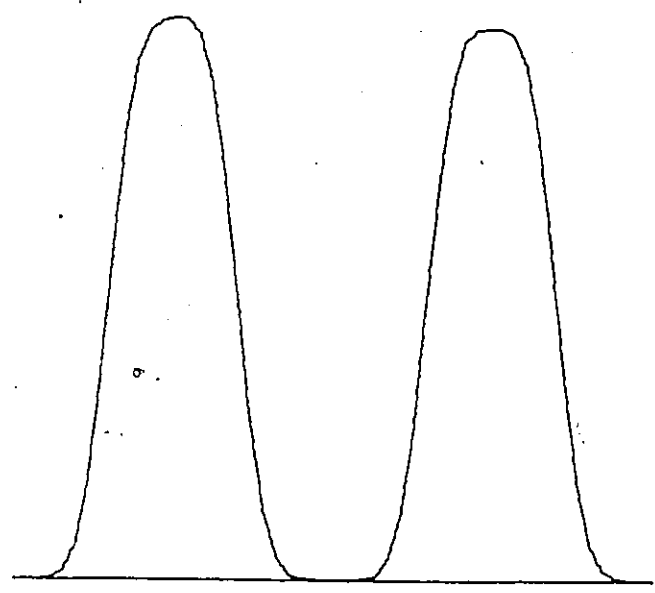
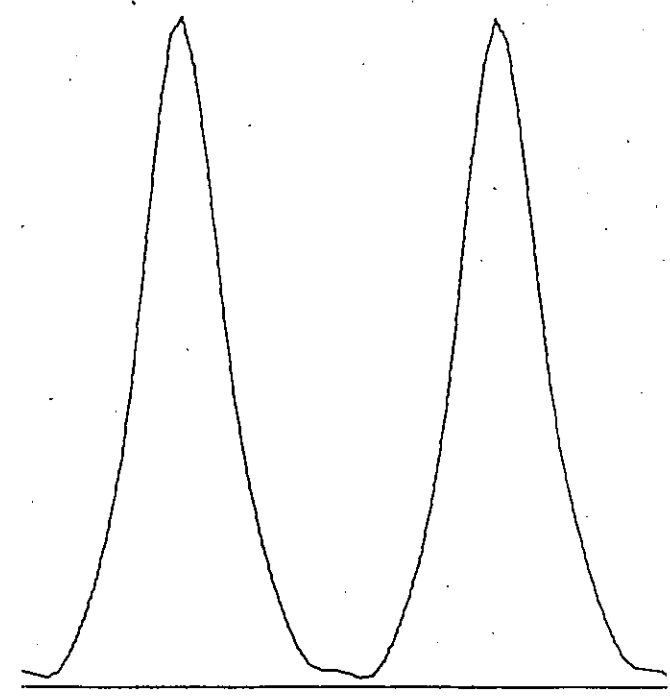


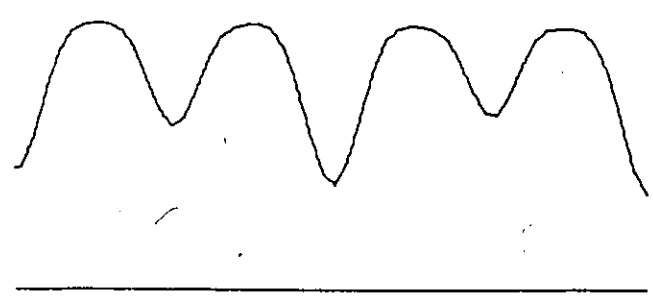
Fig. 8.8: Theoretical curves for the diffraction pattern at and near the fifth order Fourier image. (a) is the fifth order Fourier image located at $z = 102$ cm. (b), (c) and (d) are intermediate images located at $z = 103$ cm, 107.1 cm, and 109 cm, respectively.



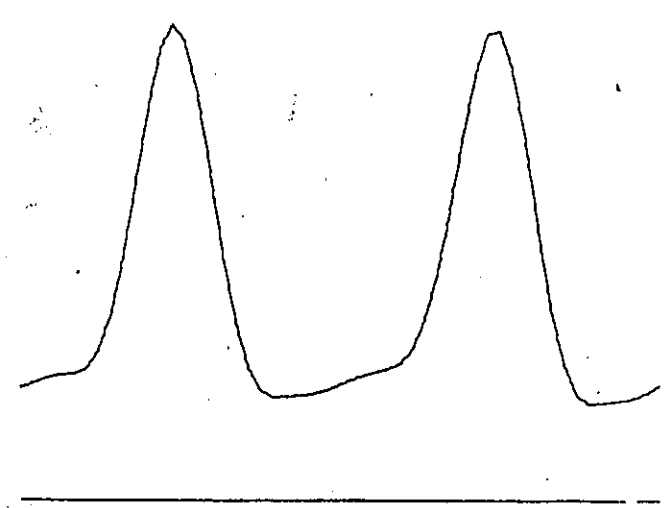
(a)



(b)



(c)



(d)

differ significantly from d . The periodicity of the Fourier images, however, is not affected provided the number of lines is not too small. Examples of such effects will be given in the next section.

8.6 Application of Fourier Images to the Measurement of Velocities

The experimental arrangement for the Fourier image velocimeter (FIV) is shown in Fig. 8.9. The transmitter system (laser source, beam expander, Ronchi grating) is identical to that of Fig. 8.2, except that a different beam expander was used when the beam diameter was changed from 2 cm to 0.7 cm. In addition, the spatial filter was removed for the latter diameter to increase the transmitted beam power ($\approx 20\%$). The reduced beam diameter increases the intensity at the target by nearly ten times. An increased beam power results in a corresponding increase in SNR. Velocity measurements were made employing a rotating disk and also in fluid flow. The receiving system (light collecting lens, field aperture, and PMT) and the signal processing system were similar to those described in Chapter 3.

A total of 75 fringes (2 cm diameter beam) were employed in order to produce accurate fringe patterns in the vicinity of the probe surface or volume. However, the number of fringes detected by the PMT was limited to 25 by the field aperture. The purpose of this was to make direct comparison with measurements employing a 0.7 cm diameter beam (also 25 lines).

The modulation center frequency, f , and the component of velocity v perpendicular to the fringe planes are related by

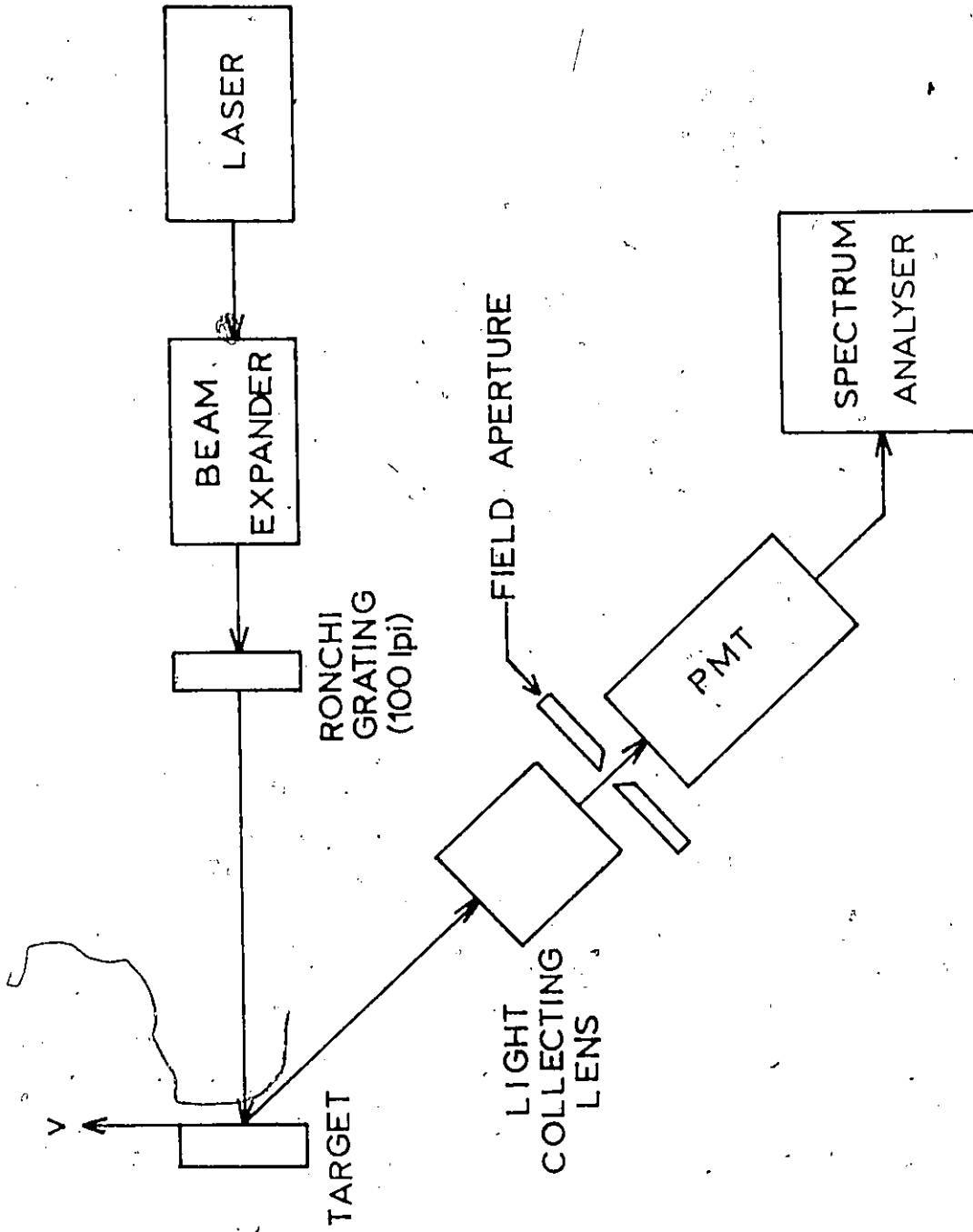


Fig. 8.9: Experimental set-up for the Fourier image velocimeter.

$$v = fd, \quad (8.33)$$

where d is the fringe spacing. Care, however, is required to ensure that the fundamental frequency is used for f in Eq. (8.33). Small particles crossing fringe image intensity distributions similar to those shown in Fig. 8.5 will also produce higher harmonic modulation components in the scattered radiation. This was investigated by detection and spectrum analysis of the scattered radiation from 80μ diameter particles on a rotating disk. For these measurements, the Gaussian incident beam diameter was decreased to 0.7 cm in order to provide higher intensity and a smaller probe area. An example of the harmonic content is shown in Fig. 8.10, which represents data for the suborder image at $z = 21.4$ cm.

Figure 8.11 gives the relative amplitude of the fundamental frequency signal at the first Fourier image and at several neighbouring suborders. These were taken with an incident beam diameter of 2 cm. For Fig. 8.11(a), the diffraction patterns were located, in order of decreasing amplitude, at $z = 20.4, 21.4, 22.4, 23.4, 24.4,$ and 25.5 cm. The latter two amplitudes are nearly zero. For Fig. 8.11(b), the diffraction patterns were located, in order of decreasing amplitude, at $z = 20.4, 19.4, 18.4, 17.4, 16.4,$ and 15.4 cm. It was found that the maximum amplitude occurs close to the Fourier image. Note that the constancy of the center frequency in Fig. 8.11 provides a test of the degree of collimation of the radiation incident on the grating, as well as other conditions to be discussed later. An additional, and improved, test of collimation may be made by comparing the frequencies at several Fourier images. They should be, and have been checked to be, identical.

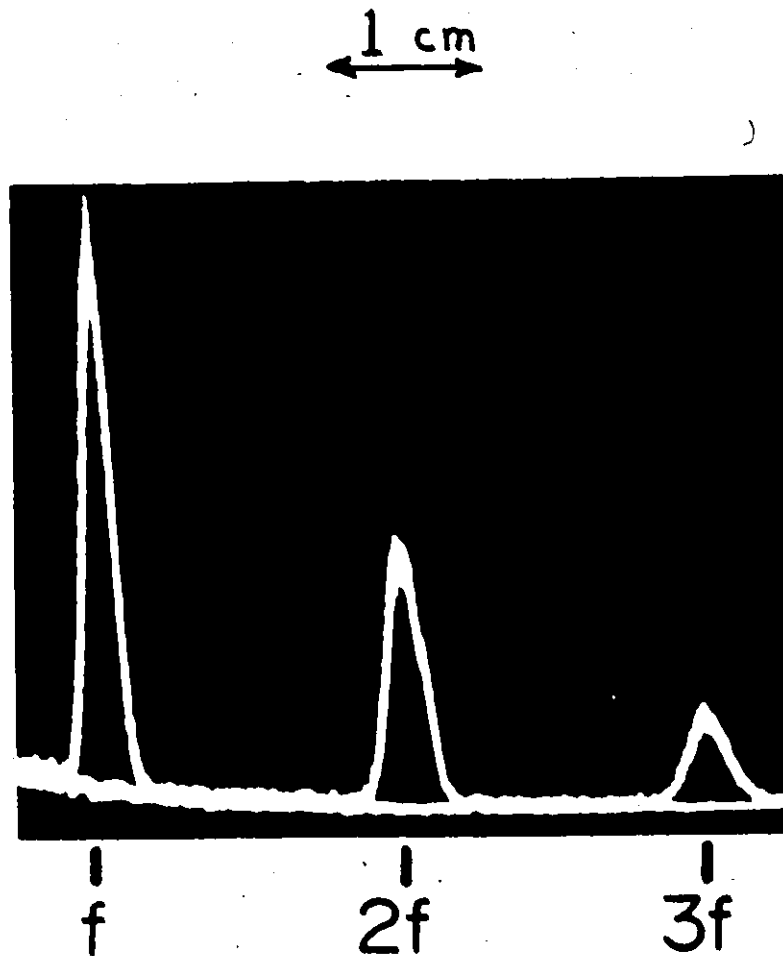
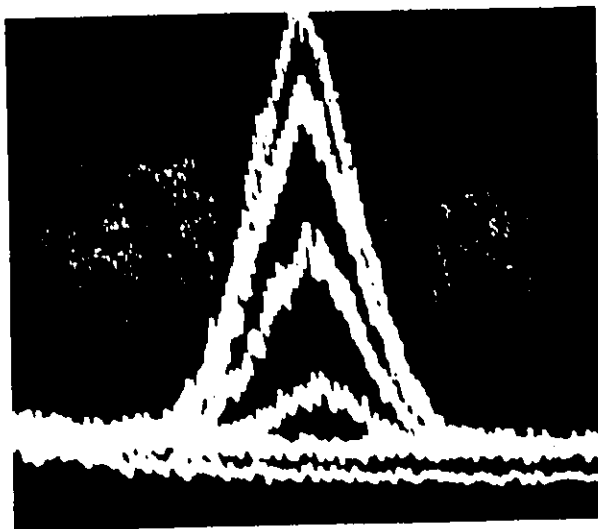


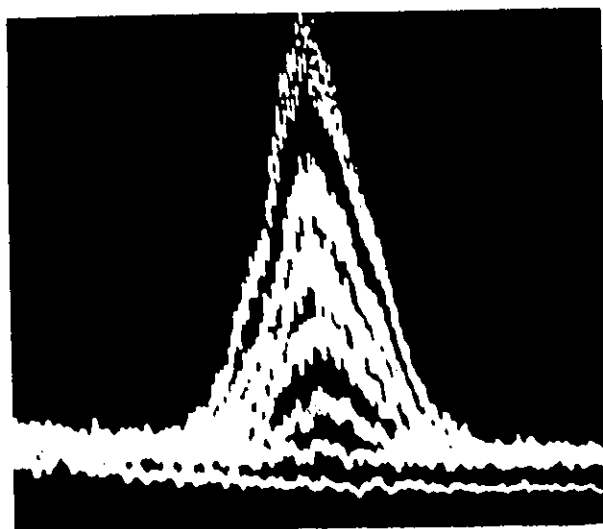
Fig. 8.10: Harmonic content of scattering at $z = 21.4$ cm. A fringe periodicity $d = 0.0254$ cm and a particle velocity $v = 1000$ cm/s results in $f = 39.4$ kHz. The scan width is 20 kHz/cm and the instrumental bandwidth is 1 kHz. The base line represents zero scattered intensity at the detector. A linear vertical scale was employed.

Fig. 8.11: Relative fundamental frequency amplitudes, at and near the first Fourier image, taken with an incident beam diameter of 2 cm. In both photographs, the peak amplitude occurs at the first order Fourier image ($z = 20.4$ cm). The images for (a), in order of decreasing amplitude, were located at $z = 20.4$ cm, 21.4 cm, 22.4 cm, 23.4 cm, 24.4 cm, and 25.4 cm. Note that the latter two amplitudes are essentially zero. Those for (b), in order of decreasing amplitude, were located at $z = 20.4$ cm, 19.4 cm, 18.4 cm, 17.4 cm, 16.4 cm, and 15.4 cm. All parameters given in Fig. 8.10, other than z and scan width (2 kHz/cm), apply.

1 cm
←→



(a)



(b)

It was shown in the last section that there is good agreement between the theoretical and experimental diffraction patterns. We now investigate the variation of signal frequency with image location. Theoretically, the frequency spectra, is in first order, given by the Fourier transform of the diffraction pattern. Numerical calculation for our system has been carried out by the fast Fourier transform (FFT) technique [28]. Figure 8.12(a) and Fig. 8.12(b) represent the Fourier transforms of the diffraction patterns located at z 's identical to those shown in Fig. 8.11(a) and Fig. 8.11(b), respectively. Note that an identical number of fringes are used for both calculation and measurement. Note that the curves in Fig. 8.12 were calculated only at the plotted points because of limitation in the resolution of the FFT technique. The peaks are extrapolated and therefore the peak amplitudes are not necessarily very accurate.

Qualitatively there is good agreement between the theory and experiment. The results indicate that there is, for our beam configuration and experimental arrangement, a constant periodicity. Consequently, accurate velocity measurements can be achieved. Note that the major cause of the differences in the magnitudes of the corresponding signal amplitudes in Figures 8.11 and 8.12 is due to the fact that the Mie scattering characteristic of the 80 μm particles has not been included in the Fourier transform. This should not affect the constancy of the center frequency, which is the main concern of the present investigation.

The FFT algorithm also provides information on the properties of the higher harmonics. The amplitude ratio of the harmonics was calculated.

Fig. 8.12(a): Calculated fundamental frequency amplitudes for an incident beam diameter of 2 cm. The Fourier image and its suborders are calculated from a beam configuration of 2 cm diameter. The Fourier transform, however, is based on the 25 fringes which are located in the centre portion of the incident beam. The images, in order of decreasing amplitude, are located at $z = 20.4$ cm (first order Fourier image), 21.4 cm, 22.4 cm, 23.4 cm, 24.4 cm, and 25.4 cm. Note that the centre frequencies of the suborders are aligned with the centre frequency of the Fourier image.

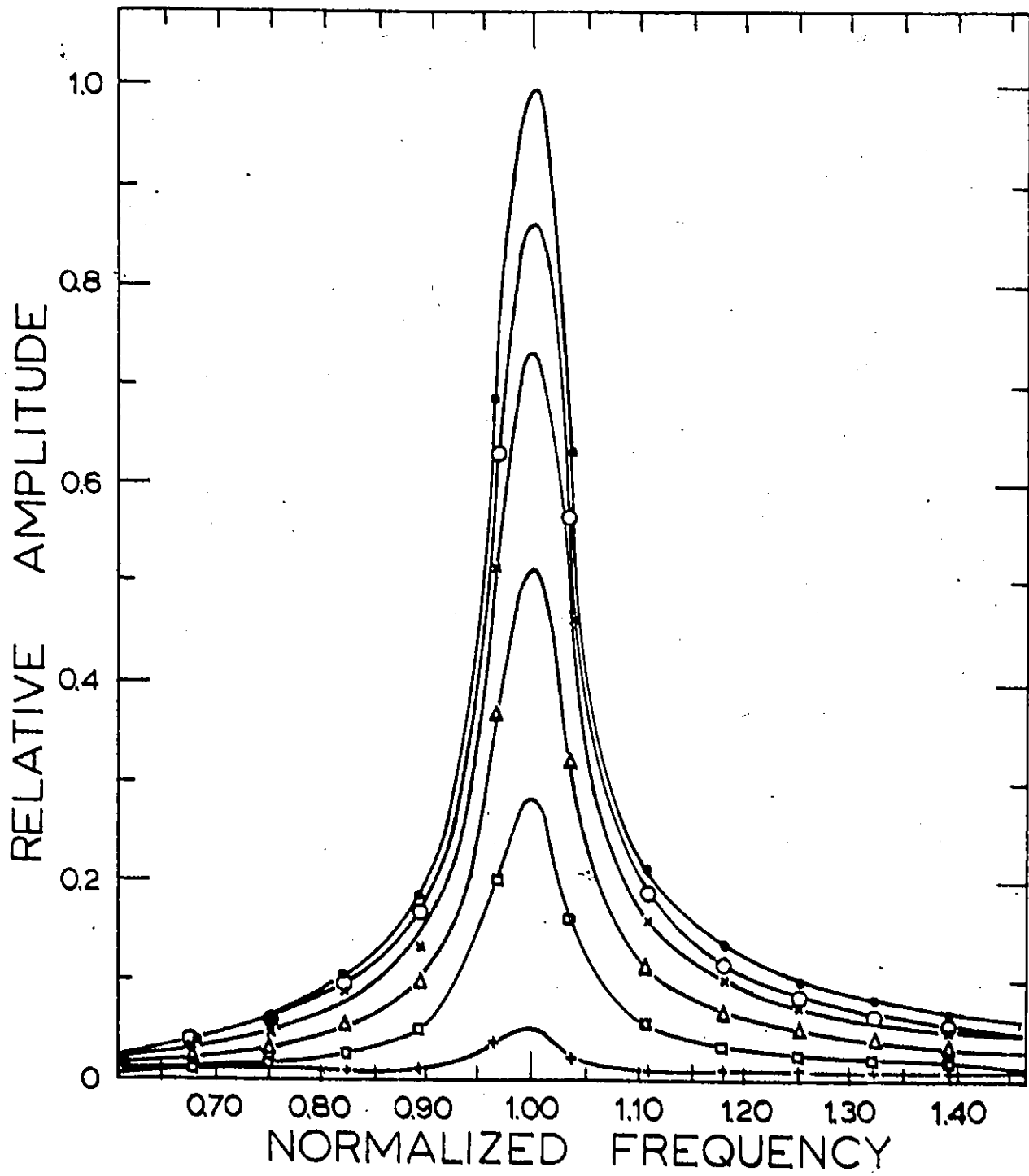
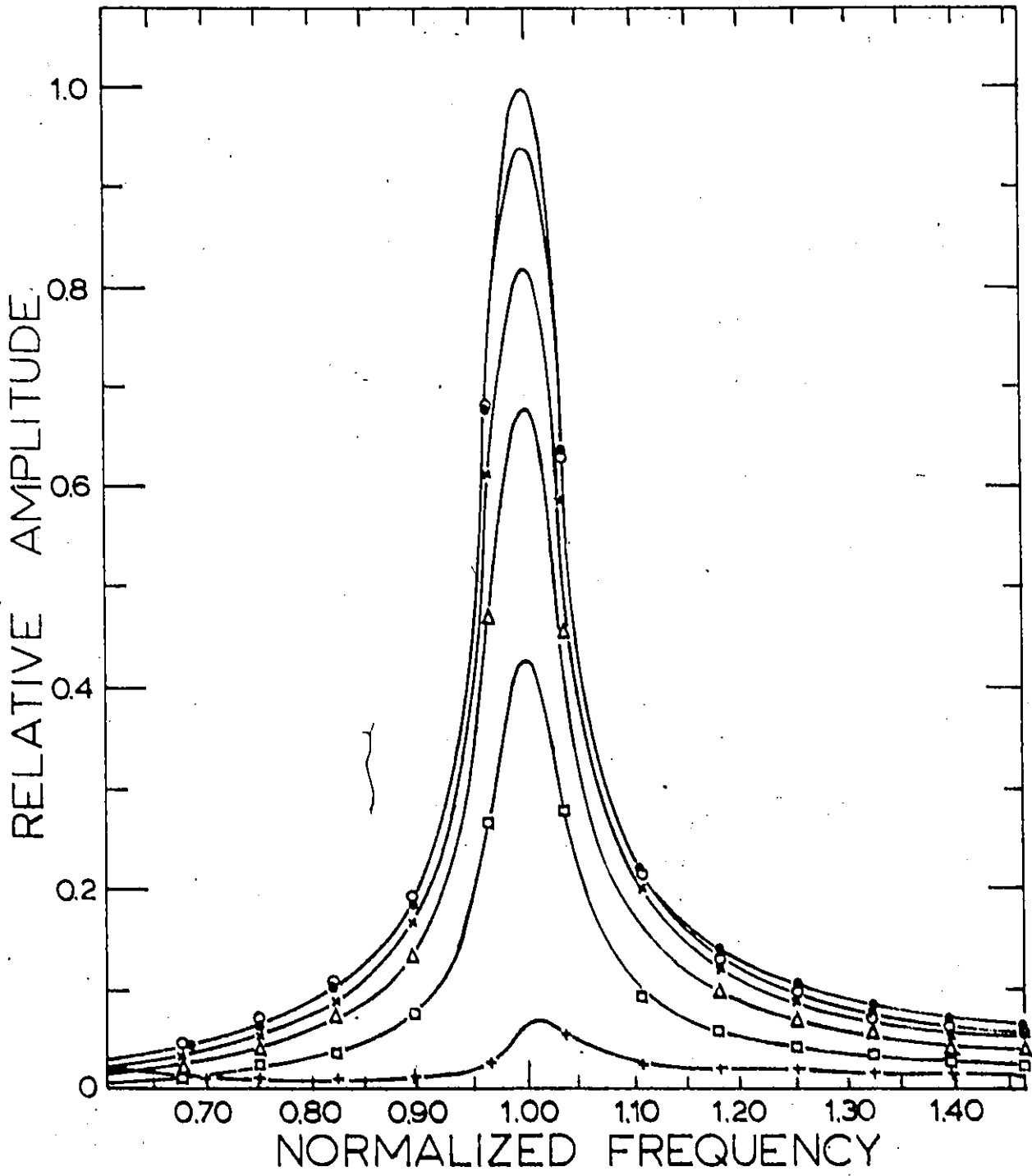


Fig. 8.12(b): Calculated fundamental frequency amplitudes for an incident beam diameter of 2 cm. The number of lines employed, and the technique used is identical to that of Fig. 8.12(a). The images in order of decreasing amplitudes are located at $z = 20.4$ cm, 19.4 cm, 18.4 cm, 17.4 cm, 16.4 cm, and 15.4 cm. Note that the centre frequencies of the suborders are aligned with the centre frequency of the Fourier image ($z = 20.4$ cm).



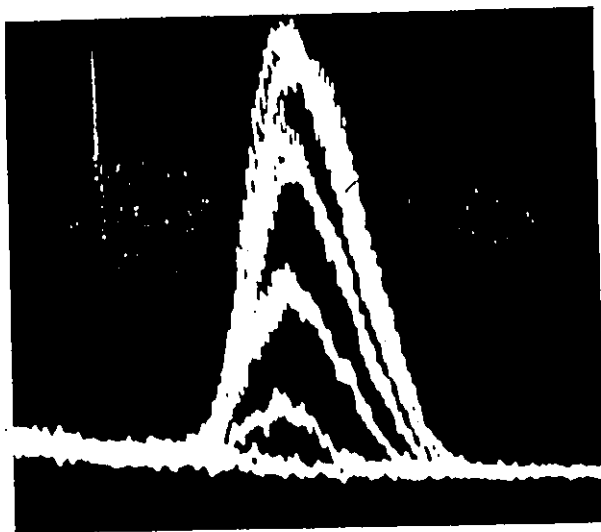
However, the theoretical result did not always agree with the experiment, particularly for the more complicated diffraction patterns. Again this is most likely a consequence of neglecting Mie scattering. It is obvious that the more complex patterns require a greatly modified FFT program. This will not be attempted here.

With smaller incident beam diameters, the maximum fundamental frequency signal amplitude occurs a small distance beyond the Fourier image. This is illustrated in Fig. 8.13 for the case of a beam diameter of 0.7 cm. As before, the Fourier image is located at $z = 20.4$ cm. The maximum signal amplitude, however, occurs at $z = 21.1$ cm. For Fig. 8.13 (a), the images were located, in order of decreasing amplitude, at 21.4, 20.4, 22.4, 23.4, 24.4, and 25.4 cm. The last amplitude is nearly zero. In the case of Fig. 8.13(b), the images were located, in order of decreasing amplitude, at 20.4, 19.4, 18.4, 17.4, 16.4, and 15.4 cm. The latter amplitude is zero. In both figures, the baseline corresponds to zero scattered intensity. It can be seen from consideration of Fig. 8.13 that if the full active fringe region is employed for flow measurements, then the average signal frequency is shifted a little below the Fourier image frequency.

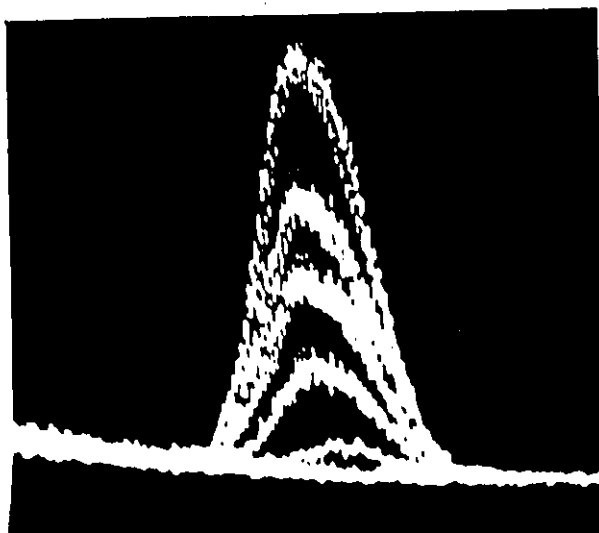
The fundamental frequency amplitudes of the above Fourier image and suborder images, calculated using the FFT program, are presented in Fig. 8.14(a) and Fig. 8.14(b), respectively. There is generally good agreement between theory and experiment. The results indicate that the suborder frequencies are shifted slightly from the Fourier image frequency. Those images before the Fourier image tend to have higher center

Fig. 8.13: Relative fundamental frequency amplitudes at and near the first Fourier image taken with an incident beam diameter of 0.7 cm. The images for (a), in order of decreasing amplitude, were located at $z = 21.4$ cm, 20.4 cm, 22.4 cm, 23.4 cm, 24.4 cm, and 25.4 cm. The last amplitude is nearly zero. Those for (b), in order of decreasing amplitude, were located at $z = 20.4$ cm, 19.4 cm, 18.4 cm, 17.4 cm, 16.4 cm, and 15.4 cm. The latter amplitude is zero. All parameters given in Fig. 8.10, other than z and scan width (2 kHz/cm) apply.

1 cm
↔



(a)



(b)

Fig. 8.14(a): Calculated fundamental frequency amplitudes for an incident beam diameter of 0.7 cm. The number of fringes employed in the calculation is 25. The images, in order of decreasing amplitude, are located at $z = 20.4$ cm, 21.4 cm, 22.4 cm, 23.4 cm, 24.4 cm, and 25.4 cm. Note that in Fig. 8.13(a), the peak amplitude occurs at $z = 21.4$ cm. The centre frequencies of the suborders are slightly down shifted.

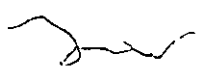


Fig. B-14(a)

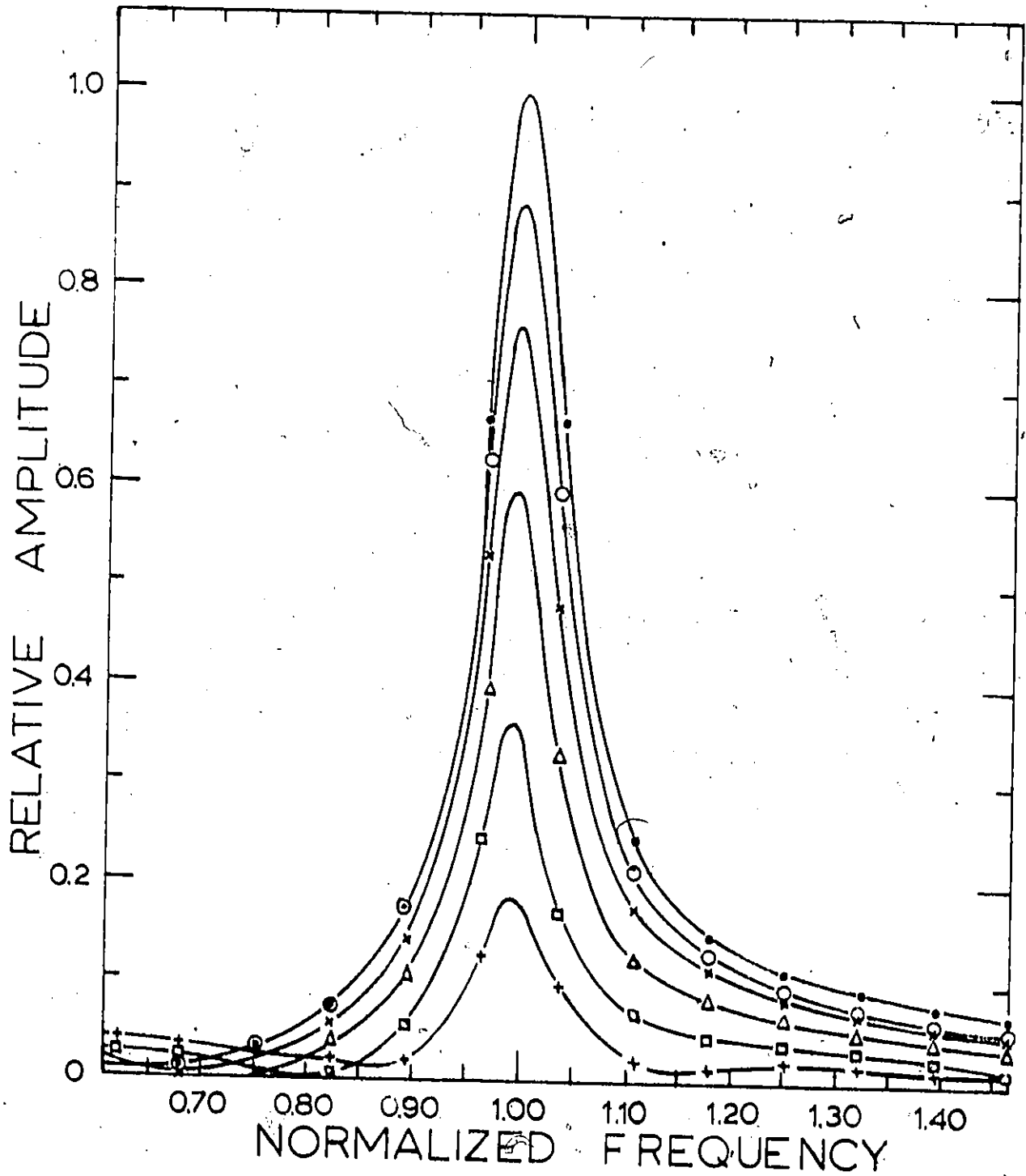


Fig. 8.14(b): Calculated fundamental frequency amplitudes for an incident beam diameter of 0.7 cm. The number of fringes employed in the calculation is 25. The images, in order of decreasing amplitude, are located at $z = 20.4$ cm, 19.4 cm, 18.4 cm, 17.4 cm, 16.4 cm, and 15.4 cm. Note that the centre frequencies of the suborders are slightly up shifted.

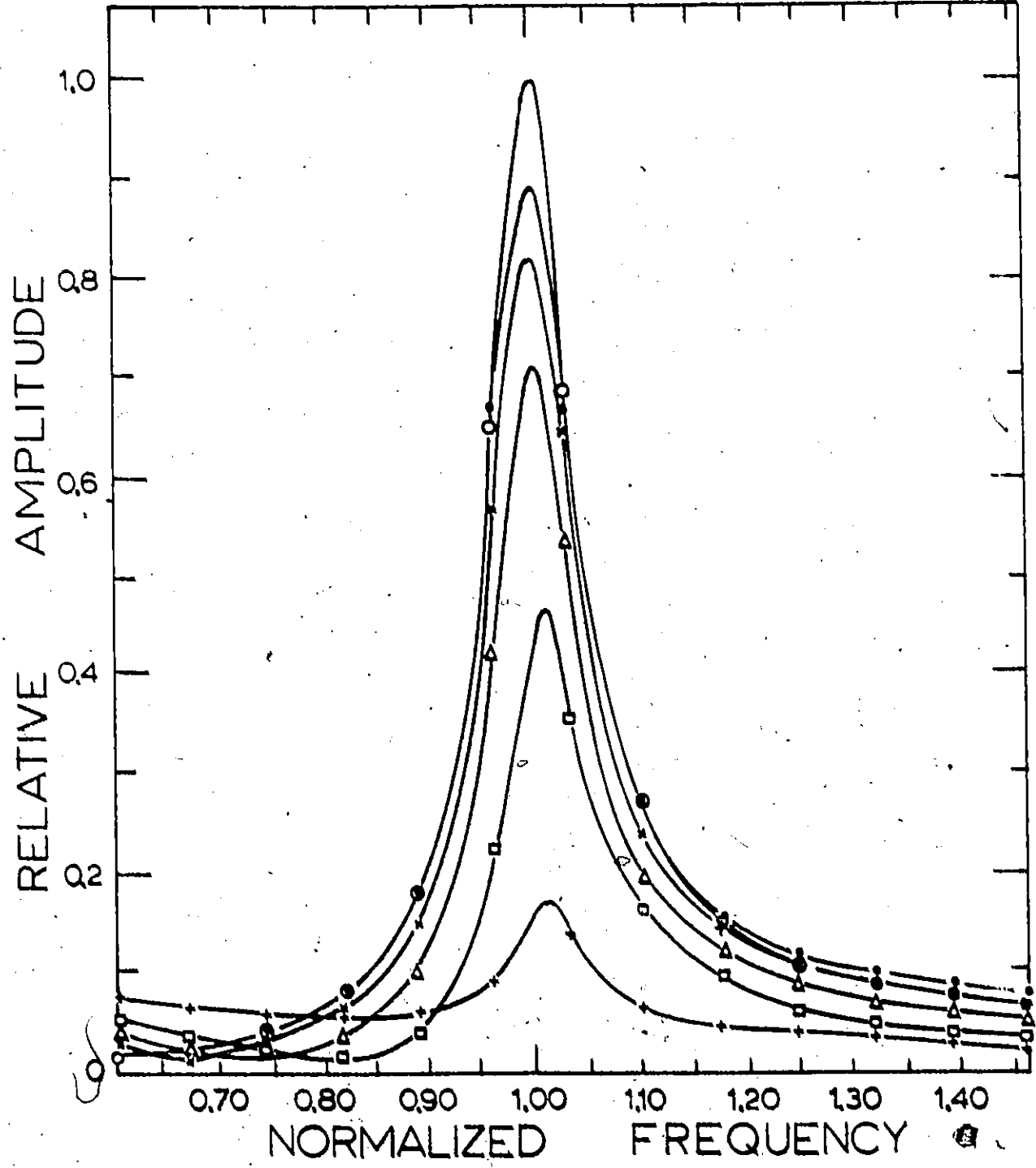


Fig. 2-1-50

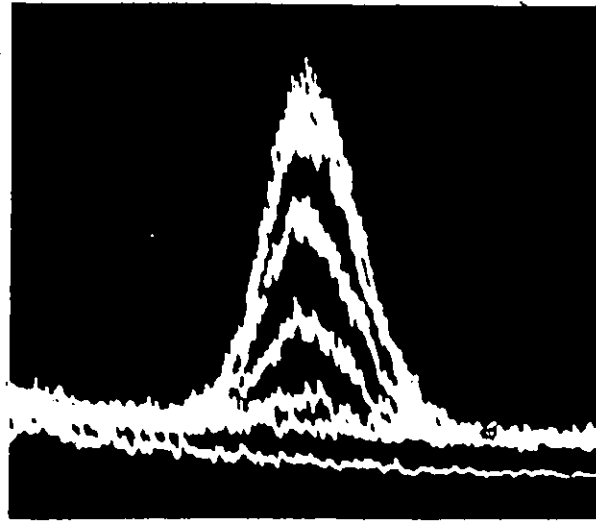
frequencies, while those beyond the Fourier image have lower center frequencies. The experimental deviation appears greater than the calculated one. For $z = 24.4$ cm (and 16.4 cm), where the deviation is maximum, the difference is about 5%. The corresponding theoretical figure is less than 2%. The frequency shifts in the present case result from the small number of grating lines employed, as mentioned in the last section. Thus for small beam diameter (i.e., with a reasonable number of active grating rulings) the periodicity at the suborders can differ significantly from d . The periodicity of the Fourier images, however, is not affected.

Under normal conditions, the linewidth of the signal frequency is inversely proportional to the number of fringes traversed by the scattering center, as has been discussed in much detail in Chapter 5. This is also true for the Fourier image velocimeter. For the Fourier image and its suborders shown in Fig. 8.11, the average linewidth is about 3.4 kHz (fullwidth at half peak amplitude). This is in excellent agreement with the width ($\approx 9\%$ of the center frequency) measured from the calculated frequency spectra shown in Fig. 8.12.

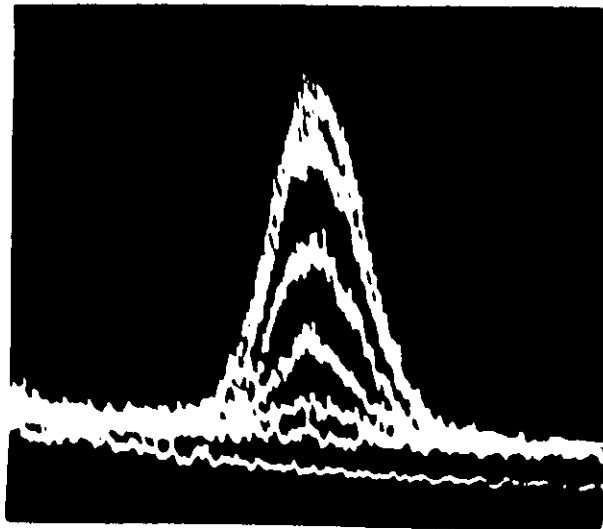
Higher order Fourier images are also suitable for velocity measurements. The largest usable order depends on both the fringe spacing d and on the incident beam diameter. Excellent results were obtained experimentally to beyond $n = 5$ ($z = 102$ cm) for $d = 0.0254$ cm and a beam diameter of 0.7 cm. Larger n values could be used with a 2 cm beam diameter. Figure 8.15 gives the relative amplitude of the fundamental frequency signal at and near the fifth Fourier image for an

Fig. 8.15: Relative fundamental frequency amplitudes, at and near the fifth Fourier image, taken with an incident beam diameter of 2 cm. The images for (a), in order of decreasing amplitude, were located at $z = 102$ cm (fifth Fourier image), 103 cm, 104 cm, 105 cm, 106 cm, and 107 cm. The first two amplitudes are almost equal, and the last amplitude is approximately zero. Those for (b), in order of decreasing amplitude, were located at $z = 102$ cm, 101 cm, 100 cm, 99 cm, 98 cm, and 97 cm. The last amplitude is nearly zero. All parameters given in Fig. 8.10, other than z and scan width (2 kHz/cm), apply.

1 cm



(a)



(b)

incident beam diameter of 2 cm. Note that the peak amplitude and the SNR are only slightly lower than those of the first order Fourier image shown in Fig. 8.11. Also note that the suborder peak amplitudes are almost identical for both Figures 8.15(a) and 8.15(b).

Figures 8.11 and 8.13, and similar data, indicate that the fundamental frequency component has significant amplitude in an extended region about each of the Fourier images. This region is about 20% of the basic distance, $2d^2/\lambda$, for the data presented in Figures 8.11 and 8.13, and is located approximately symmetrically about the maximum amplitude position. This unusually large probe volume (longitudinally and laterally) should allow employment of the FIV to measure velocities of very rough surfaces. This can not be done with a DLDV or WFIV.

The effect of number density on the SNR has not been studied for the case of the FIV. It is believed the results will be very similar to those for the WFIV. The detection is solely incoherent because of the existence of a real fringe pattern and also because of single beam operation. Low heterodyne frequencies (close to dc) may arise from scattering centers moving with different velocities. However, these low frequency signals do not provide "absolute" velocity information. Therefore, the problem of distinguishing coherent and incoherent detection, as in the case of the DLDV, does not exist here.

Experimental investigations, similar to those described above and elsewhere (e.g., Chapter 5), have been carried out using a range of particle sizes, both on rotating disks and in fluid flow. For the latter, particle diameters ranging from 0.6 μm (latex) to 360 μm (polystyrene)

have been used. Various grating spacings (300 lpi and 1000 lpi) were also tried. It was found that the Fourier image method for particle velocity measurement is comparable in most respects to the fringe image method. The major difference is that the Fourier image technique is not capable of producing highly localized fringes. This may, however, be an advantage, in some applications, such as the measurement of particle velocity on rough surfaces.

8.7 Summary

This chapter presents the theoretical and experimental investigations of the FIV. Briefly, it is found that under appropriate conditions the Fourier image and its nearby diffraction pattern can be employed for accurate velocity measurements. Excellent agreement is found between theory and experiment on the functional form of the diffraction pattern. The interesting phenomenon of the Fourier image error repairs [27] is also observed. Microphotometer tracings show that the repair starts after the first Fourier image, and proceeds along the beam. Many other properties of the FIV, such as the periodicity of the diffraction patterns at different locations, were studied with the aid of the FFT technique. The FIV technique is evaluated by measurements of particle velocities on a rotating disk. Good agreement exists between theory and experiment.

CHAPTER 9

CONCLUSION

Most of the previous chapters end with a summary describing the observations and the conclusions of that particular chapter. This final chapter is concerned with providing a summary of the important conclusions and with giving a brief account of the overall significance of the research.

The following discussion focuses on two main areas. These are the basic operating principles, and the optimization, of optical velocimeters.

Two terminologies are often used in this work: coherent and incoherent. As stated in the introduction, our use of the term incoherent scattering implies particles crossing a fringe system (white light or laser). This results in an amplitude modulation of the scattered radiation. Coherent scattering refers to a Doppler shift in the frequency of the scattered radiation which is detected by homodyning and/or heterodyning at a photocathode. For fixed system parameters, incoherent and coherent scattering have identical detector output frequencies.

There has been much discussion as to whether the DLDV operates in the coherent or in the incoherent mode [17, 18, 19, 36]. Some workers [20, 21] tend to interpret the DLDV as a fringe crossing system (incoherent mode) rather than as a Doppler shift system (coherent mode).

Several theoretical models have been proposed [76, 77, 78] which have not been adequately verified with experimental results. This is due, in part, to the difficulty of carrying out reliable experiments.

We have employed two different methods to establish the operating mode of the DLDV. One method follows the standard technique of proposing a theoretical model for the DLDV, and then to compare it with experimental results. The other method is by deduction from measurements on the WFIV.

In the first approach, a SNR equation is derived on the basis of optical heterodyning and Mie scattering theory. The SNR is used as a criterion because it is the most important factor in determining the sensitivity of optical velocimeters. A set of experiments was carried out which includes the effects of receiver aperture size, particle number density, detection angle, light intensity, and velocity, on SNR. It is found that there exists, in general, good agreement between theory and experiment. Since the SNR equation is based on optical heterodyning, therefore it is reasonable to conclude that the DLDV operates predominantly in the coherent mode. Results of the above investigations are presented in Chapter 6.

In the second approach, we compare the performance of the DLDV with that of a WFIV, which can only operate in the incoherent mode (fringe crossing). Thus the WFIV allows us to investigate incoherent scattering completely independent of coherent scattering. This is not generally possible using a laser source. It was found that the two systems (DLDV and WFIV) exhibit a very different SNR behaviour as a

function of receiver aperture size and of particle number density. Consequently, it is inferred that the DLDV does not operate in the incoherent mode. The work on the WFIV is presented in Chapter 7.

It should be noted that at very low particle number density ($N = 0.02$) the SNR of the DLDV tends to increase with the receiver aperture size (section 6.2). It might be expected that in this case the system can be treated as a fringe system. However, an aperture change from $f/22$ to $f/2.6$ increases the SNR by only 6dB, as can be seen from Fig. 6.2. For a fringe system, the theoretical increase should be about 18dB (15dB when various system losses are considered). In the WFIV, the corresponding increase is measured to be 14dB (section 7.2). This is in excellent agreement with the theory when system losses are considered. Therefore the assumption that the DLDV is a fringe crossing system is not a valid one even at very low number density.

In the derivation of the SNR of the DLDV, it is assumed that the wavefronts are perfectly aligned (i.e., the antenna theorem is satisfied). When this condition is not satisfied, the SNR equation can not fully describe the measurements. A correction factor, which is generally referred to as a coherence factor [18], is required to account for the deviation. It is observed experimentally (Chapter 6) that the coherence factor is not only a function of receiver aperture size and particle number density, as is generally believed [18, 58], but is also a function of detection angle. Derivation of an appropriate factor requires further effort. Our conclusion concerning the coherent property of the DLDV system, however, is independent of the form of the coherence factor.

Light copy

The SNR of optical velocimeter can always be increased by increasing source power. However, the practical problem is to obtain optimum SNR with a fixed light power and under certain experimental constraints. The best technique and operating parameters depends on particular circumstances. Some general rules for optimizing the parameters for best SNR are given below.

Measurements employing a DLDV:

- (i) It is found experimentally that the SNR increases with decreasing probe volume resulting from focusing of the incident beams. This is most likely because the coherent condition is better satisfied.
- (ii) A pinhole should be placed at the image plane of the receiver lens to limit the detected light to that scattered from the probe volume. This enhances the SNR and improves the spectral quality. Furthermore, a filter should be employed to pass only the wavelength region of the laser source.
- (iii) When the particle number density is very low, the maximum practicable receiver aperture can be used. The increased SNR, however, will not be directly proportional to the aperture size.
- (iv) Very little is gained by employing a large receiver aperture when the particle number density is very high. The SNR at large aperture is identical to that employing a receiver aperture which satisfies the coherent condition.

- (v) The SNR increases with increasing particle number density until the attenuation of the illuminating and scattered beams becomes the dominant factor. The SNR peaks at a number density which reduces the direct beam intensity by a factor of $1/e$.
- (vi) The highest SNR is detected in the forward direction along the bisector of the two crossing beams. If the number density is very low, then the SNR is relatively insensitive to the detection angle as long as it remains in the direction of the forward scattering lobe.

Measurements employing a WFIV:

- (i) A careful choice of optical components is important. The intensity of illumination in the probe volume should be made as high as possible by employing a proper condenser arrangement. Good image quality requires an imaging lens relatively free of chromatic aberrations and image distortion. The minimum probe volume is determined by the achievable fringe visibility.
- (ii) Apertures should be employed to limit detection to light scattered from the probe volume. This will reduce detection of background light and result in enhanced SNR and better spectral quality.
- (iii) The optimum SNR is obtained when the total number of particles (N) in the probe volume is about one. When N is less than one, the SNR is directly proportional to N .

Little is gained by increasing N beyond one.

- (iv) The optimum detection angle is in the forward scattering lobe of the illuminating beam. Little is gained by making observations closer than about 15° from the direct beam.

A compact WFIV employing a microscope objective as the imaging lens has been applied to the measurement of laminar water flow in a square duct. Under our experimental conditions, the sensitivity and accuracy of the WFIV are comparable to those of the DLDV. Results of these investigations are presented in Chapter 5.

The third optical velocimeter studied in this work is the FIV, which has a large longitudinal fringe extent. This is in contrast to the DLDV and WFIV, where the fringes are highly localized. Theoretical and experimental studies indicate that the FIV can be used to measure the velocity of particles or surface irregularities on rough surfaces. This can not be done easily with a DLDV or a WFIV. The basic properties of, and the requirements for, an FIV are summarized below.

- (i) The intensity of the collimated beam should be as high as possible, subject to the diameter requirements given below.
- (ii) The grating periodicity and beam diameter are inter-related. The minimum beam diameter is determined by the working distance within which the Fresnel diffraction is dominant. For a given beam diameter, the optical path length at which Fraunhofer diffraction becomes dominant is approximately proportional to the periodicity of the grating.

(11) The periodicity of the Fourier image and its suborders can differ from that of the object grating if the illuminating beam is not properly collimated, or if the beam is collimated but does not contain a sufficient number of grating lines. In the latter case, the periodicity of the suborders can differ significantly from that of the object. The periodicity of the Fourier images, however, is not affected provided that the number of active grating lines is not too small.

APPENDIX A

ANGULAR MIE SCATTERING

The results of Mie scattering theory are presented here. The algorithms for computing the intensity functions in this work are based on these results. The subroutines were supplied by IBM [57].

Most problems in theoretical optics involve the solution of Maxwell's equation. This approach should be used when a full, formal solution is required [56]. Mie [74] solved the case for an incident monochromatic plane wave falling upon a homogeneous, isotropic sphere of radius r . The surrounding medium was assumed transparent, homogeneous, and isotropic. The incident wave induces forced oscillations of free and bound charges which are synchronous with the applied field. This induces secondary electric and magnetic fields, each of which consists of two parts, one inside the sphere, the other outside the sphere.

If the incident radiation is unpolarized and its intensity is I_0 , then the intensity of the radiation scattered in the direction θ and at a distance d from the particle can be put in the form [56]

$$I(\theta, m) = (I_0 \lambda^2 / 8\pi^2 d^2) \{I_1(\theta, \alpha, m) + I_2(\theta, \alpha, m)\}, \quad (A.1)$$

where $\alpha = 2\pi r/\lambda$ is the ratio of the particle circumference to the wavelength in the medium, m is the index of refraction of the particle

relative to the surrounding medium, and θ is the scattering angle, taken with respect to the forward direction of the incident beam. The quantities I_1 and I_2 are called intensity functions. I_1 is proportional to the intensity whose electric oscillations are perpendicular to the plane of scattering; I_2 is proportional to the intensity whose electric oscillations are in the plane of scattering. Equation (A.1) indicates that the scattered radiation from a single particle is always polarized even if the radiation is unpolarized. The intensity functions are given by [56]

$$I_1 = |S_1|^2 = \left| \sum_{n=1}^{\infty} \frac{(2n+1)}{n(n+1)} \{a_n(\alpha, m)\tau_n(\cos\theta) + b_n(\alpha, m)\pi_n(\cos\theta)\} \right|^2, \quad (\text{A.2})$$

and

$$I_2 = |S_2|^2 = \left| \sum_{n=1}^{\infty} \frac{(2n+1)}{n(n+1)} \{a_n(\alpha, m)\tau_n'(\cos\theta) + b_n(\alpha, m)\pi_n'(\cos\theta)\} \right|^2, \quad (\text{A.3})$$

where a_n and b_n are given by

$$a_n(\alpha, m) = \frac{\psi_n'(m\alpha)\psi_n(\alpha) - m\psi_n(m\alpha)\psi_n'(\alpha)}{\psi_n'(m\alpha)\epsilon_n(\alpha) - m\psi_n(m\alpha)\epsilon_n'(\alpha)}, \quad (\text{A.4})$$

and

$$b_n(\alpha, m) = \frac{m\psi_n'(m\alpha)\psi_n(\alpha) - \psi_n(m\alpha)\psi_n'(\alpha)}{m\psi_n'(m\alpha)\epsilon_n(\alpha) - \psi_n(m\alpha)\epsilon_n'(\alpha)}. \quad (\text{A.5})$$

$\psi_n'(z)$ and $\epsilon_n'(\alpha)$ are the derivatives of $\psi_n(z)$ and $\epsilon_n(\alpha)$ with respect to

z and α , respectively ($z = m\alpha$).

$$\psi_n(z) = zJ_n(z) \quad , \quad (\text{A.6})$$

$$c_n(\alpha) = \alpha[J_n(\alpha) - iY_n(\alpha)] \quad , \quad (\text{A.7})$$

$$\psi'_n(z) = zJ_{n-1}(z) - nJ_n(z) \quad , \quad (\text{A.8})$$

and

$$c'_n(\alpha) = \alpha[J_{n-1}(\alpha) - iY_{n-1}(\alpha)] - n[J_n(\alpha) - iY_n(\alpha)] \quad (\text{A.9})$$

J_n and Y_n are the spherical Bessel functions of the first and second kind, respectively.

The phase functions π_n and τ_n in Equations (A.2) and (A.3) can be expressed in terms of the Legendre polynomials as follows:

$$\pi_n(\cos\theta) = \frac{dP_n(\cos\theta)}{d(\cos\theta)} \quad , \quad (\text{A.10})$$

and

$$\tau_n(\cos\theta) = \cos\theta \pi_n(\cos\theta) - (1 - \cos^2\theta) \frac{d\pi_n(\cos\theta)}{d(\cos\theta)} \quad (\text{A.11})$$

A physical picture for the mechanism of the scattering process can be explained as follows. From Equations (A.2) and (A.3), it is seen that the scattered wave is composed of various partial waves, and the amplitudes of these partial waves depend on a_n and b_n . These Mie coefficients (a_n and b_n) can be interpreted physically as the n th electrical

partial wave and the n th magnetic partial wave, respectively. The values of a_n and b_n depend on the material (index of refraction m) and the size of the particle (α). The partial wave can be considered as coming from an electric or magnetic multipole field. Hence, the first partial wave comes from a dipole, the second from a quadrupole, and so on. The results show that the Mie coefficient a_{n+1} of the $(n+1)$ th electrical partial wave is of the same order of magnitude as b_n of the n th magnetic partial wave. The coefficients π_n and τ_n denote that the angular functions depend only on the scattering angle θ , and are completely independent of m and α .

Parameters other than the intensity functions can also be obtained from a_n and b_n . One of these is the efficiency factor for extinction, Q_e , which is the ratio of the total amount of energy removed from the incident beam to the geometric cross-section (πr^2) of the particle. This is given by [56]

$$Q_e(\alpha, m) = \frac{2}{\alpha^2} \sum_{n=1}^{\infty} (2n+1) [R_e(a_n) + R_e(b_n)] \quad (\text{A.12})$$

The efficiency factor for scattering, Q_s , is given by [56]

$$Q_s(\alpha, m) = \frac{2}{\alpha^2} \sum_{n=1}^{\infty} (2n+1) [|a_n|^2 + |b_n|^2] \quad (\text{A.13})$$

If there is no absorption, i.e., the imaginary part of the index of refraction is zero, then $Q_e = Q_s$. Otherwise, Q_a , the efficiency factor for absorption is given by

$$Q_d = Q_e + Q_s \quad (\text{A.14})$$

Note that the total scattering cross-section, σ , is given by

$$\sigma = \pi r^2 Q_s \quad (\text{A.15})$$

Note also that the Rayleigh formula can be obtained from the Mie expressions if both α and m are sufficiently small. The Rayleigh equation is given by [75]

$$I = \frac{8\pi^4 r^6}{d^2 \lambda^4} \left| \frac{m^2 - 1}{m^2 + 2} \right|^2 (1 + \cos^2 \theta) \quad (\text{A.16})$$

The range of validity of the Rayleigh equation is that the particle radius should not exceed about one-twentieth of the wavelength.

For reference purposes, the Mie scattering functions for three diameters of transparent spheres, calculated at a wavelength $\lambda = 6328 \text{ \AA}$ and $m = 1.20$, are listed in Table A1.

The efficiency factor for scattering, Q_s , and the total scattering cross-section, σ , for the three spheres are listed in Table A2.

Table A.1: Mie Scattering Functions for Three Diameters of Transparent Spheres. The Diameters are 0.481 μm , 0.62 μm , and 5.7 μm . The Calculations Employ $\lambda = 6328 \text{ \AA}$ and $m = 1.20$.

Angle θ°	Scattering Function, $i(0, \alpha, m)$		
	$\alpha = 3.183$ (0.481 μm)	$\alpha = 4.103$ (0.62 μm)	$\alpha = 37.723$ (5.7 μm)
1	2.000000	1.000000	1.000000
2	1.999999	0.999999	0.999999
3	1.999997	0.999997	0.999997
4	1.999994	0.999994	0.999994
5	1.999990	0.999990	0.999990
6	1.999985	0.999985	0.999985
7	1.999979	0.999979	0.999979
8	1.999972	0.999972	0.999972
9	1.999964	0.999964	0.999964
10	1.999955	0.999955	0.999955
11	1.999945	0.999945	0.999945
12	1.999934	0.999934	0.999934
13	1.999922	0.999922	0.999922
14	1.999909	0.999909	0.999909
15	1.999895	0.999895	0.999895
16	1.999880	0.999880	0.999880
17	1.999864	0.999864	0.999864
18	1.999847	0.999847	0.999847
19	1.999829	0.999829	0.999829
20	1.999810	0.999810	0.999810
21	1.999790	0.999790	0.999790
22	1.999769	0.999769	0.999769
23	1.999747	0.999747	0.999747
24	1.999724	0.999724	0.999724
25	1.999700	0.999700	0.999700
26	1.999675	0.999675	0.999675
27	1.999649	0.999649	0.999649
28	1.999622	0.999622	0.999622
29	1.999594	0.999594	0.999594
30	1.999565	0.999565	0.999565
31	1.999535	0.999535	0.999535
32	1.999504	0.999504	0.999504
33	1.999472	0.999472	0.999472
34	1.999439	0.999439	0.999439
35	1.999405	0.999405	0.999405
36	1.999370	0.999370	0.999370
37	1.999334	0.999334	0.999334
38	1.999297	0.999297	0.999297
39	1.999259	0.999259	0.999259
40	1.999220	0.999220	0.999220
41	1.999180	0.999180	0.999180
42	1.999139	0.999139	0.999139
43	1.999097	0.999097	0.999097
44	1.999054	0.999054	0.999054
45	1.999010	0.999010	0.999010
46	1.998965	0.998965	0.998965
47	1.998919	0.998919	0.998919
48	1.998872	0.998872	0.998872
49	1.998824	0.998824	0.998824
50	1.998775	0.998775	0.998775
51	1.998725	0.998725	0.998725
52	1.998674	0.998674	0.998674
53	1.998622	0.998622	0.998622
54	1.998569	0.998569	0.998569
55	1.998515	0.998515	0.998515
56	1.998460	0.998460	0.998460
57	1.998404	0.998404	0.998404
58	1.998347	0.998347	0.998347
59	1.998289	0.998289	0.998289
60	1.998230	0.998230	0.998230
61	1.998170	0.998170	0.998170
62	1.998109	0.998109	0.998109
63	1.998047	0.998047	0.998047
64	1.997984	0.997984	0.997984
65	1.997920	0.997920	0.997920
66	1.997855	0.997855	0.997855
67	1.997789	0.997789	0.997789
68	1.997722	0.997722	0.997722
69	1.997654	0.997654	0.997654
70	1.997585	0.997585	0.997585
71	1.997515	0.997515	0.997515
72	1.997444	0.997444	0.997444
73	1.997372	0.997372	0.997372
74	1.997299	0.997299	0.997299
75	1.997225	0.997225	0.997225
76	1.997150	0.997150	0.997150
77	1.997074	0.997074	0.997074
78	1.997000	0.997000	0.997000
79	1.996924	0.996924	0.996924
80	1.996847	0.996847	0.996847
81	1.996769	0.996769	0.996769
82	1.996690	0.996690	0.996690
83	1.996610	0.996610	0.996610
84	1.996529	0.996529	0.996529
85	1.996447	0.996447	0.996447
86	1.996364	0.996364	0.996364
87	1.996280	0.996280	0.996280
88	1.996195	0.996195	0.996195
89	1.996109	0.996109	0.996109
90	1.996022	0.996022	0.996022
91	1.995934	0.995934	0.995934
92	1.995845	0.995845	0.995845
93	1.995755	0.995755	0.995755
94	1.995664	0.995664	0.995664
95	1.995572	0.995572	0.995572
96	1.995479	0.995479	0.995479
97	1.995385	0.995385	0.995385
98	1.995290	0.995290	0.995290
99	1.995194	0.995194	0.995194
100	1.995097	0.995097	0.995097

(cont.)

Table A.1 (Cont.)

60			
61			
62			
63			
64			
65			
66			
67			
68			
69			
70			
71			
72			
73			
74			
75			
76			
77			
78			
79			
80			
81			
82			
83			
84			
85			
86			
87			
88			
89			
90			

Table A.2: The Efficiency Factor for Scattering, Q_s , and the Total Scattering Cross-Section, σ , for Three Transparent Spheres.

Sphere Diameter	Q_s	σ
0.481 μm	0.741	$1.346 \times 10^{-9} \text{ cm}^2$
0.62 μm	1.242	$3.749 \times 10^{-9} \text{ cm}^2$
5.7 μm	2.046	$5.221 \times 10^{-7} \text{ cm}^2$

REFERENCES

- [1] Y. Yeh and H.Z. Cummins, Appl. Phys. Lett. 4, 176 (1964).
- [2] R.J. Goldstein and W.F. Hagen, Phys. Fluids 10, 1349 (1967).
- [3] E.R. Pike, D.A. Jackson, P.J. Bourke, and D.I. Page, J. Phys. E1, 727 (1968).
- [4] R.M. Huffaker, C.E. Fuller, and T.R. Lawrence, S.A.E. Conference Detroit (1969).
- [5] R.D. Lewis, J.W. Foreman, Jr., H.J. Watson, and J.R. Thornton, Phys. Fluids 11, 433 (1968).
- [6] E.B. Denison and W.H. Stevenson, Rev. Sci. Instrum. 41, 1475 (1970).
- [7] R.M. Huffaker, A.V. Jelalian, and J.A.L. Thomson, Proc. IEEE 58, 322 (1970).
- [8] R.E. Anderson, C.E. Edlund, and B.W. Vanzant, J. Appl. Phys. 42, 2741 (1971).
- [9] P.J. Bourke and C.G. Brown, Optics and Laser Technology, p.23, (Feb: 1971).
- [10] T.R. Lawrence, D.J. Wilson, C.E. Craven, I.P. Jones, R.M. Huffaker, and J.A.L. Thomson, Rev. Sci. Instrum. 43, 512 (1972).
- [11] F. Durst, A. Mellng, and J.H. Whitelaw, Combustion and Flame 18, 197 (1972).
- [12] R.J. Taylor and H. House, Opto-Electron. 4, 343 (1972).
- [13] P.L. Eggins, D.A. Jackson, and D.M. Paul, Opto-Electron. 5, 91 (1973).
- [14] H.J. Pfeifer and H.D. Vom Stein, Opto-Electron. 5, 53 (1973).
- [15] W.M. Farmer, Appl. Opt. 11, 2603 (1972).
- [16] R.M. Fristrom, A.R. Jones, M.J.R. Schwar, and F.J. Weinberg, Faraday Symposia of the Chemical Society, No.7, 183 (1973).

- [17] M.R. Rudd, J. Phys. E2, 55 (1969).
- [18] L.E. Drain, J. Phys. D5, 481 (1972).
- [19] C.M. Miller, Opto-Electron. 4, 367 (1972).
- [20] W.M. Farmer and D.B. Brayton, Appl. Opt. 10, 2319 (1971).
- [21] A.J. Hughes and E.R. Pike, Appl. Opt. 12, 597 (1973).
- [22] C.M. Penney, Appl. Phys. Lett. 16, 167 (1970).
- [23] H.D. Vom Stein and H.J. Pfeifer, Metrologia 5, 59 (1969).
- [24] M. Gaster, J. Fluid Mech. 20 (part 2), 183 (1964).
- [25] J.H.C. Chan and E.A. Ballik, Appl. Opt. 13, 234 (1974).
- [26] J.M. Cowley and A.F. Moodie, Proc. Phys. Soc. (London) B70, 486,497,505 (1957).
- [27] H. Dammam, G. Groh, and M. Kock, Appl. Opt. 10, 1454 (1971).
- [28] J.W. Cooley and J.W. Tukey, Math. Comput. 19, 297 (1965).
- [29] R.J. Goldstein and D.K. Kreid, J. Appl. Mech. 34, Series E, 813 (1967).
- [30] L.D. Landau and E.M. Lifshitz, The Classical Theory of Fields, (Addison-Wesley, 1959).
- [31] M. Ross, Laser Receivers, (John Wiley and Sons, N.Y., 1967).
- [32] G. Pietri and J. Nussli, Philips Technical Review 29, 267 (1968).
- [33] J.W. Foreman, Jr., Appl. Opt. 6, 821 (1967).
- [34] A.L. Bloom, Appl. Opt. 5, 1500 (1966).
- [35] O.E. Delange, IEEE Spectrum 5, 77 (Oct. 1968).
- [36] L. Lading and S. Hanson, private communication.
- [37] M. Born and E. Wolf, Principles of Optics, (Pergamon, N.Y., 1965).
- [38] A.E. Siegman, Appl. Opt. 5, 1588 (1966).

- [39] M.K. Mazumder and D.L. Wankum, *Appl. Opt.* 9, 633 (1970).
- [40] F. Dürst and J.H. Whitelaw, *Proc. R. Soc.* A324, 157 (1971).
- [41] H. Kogelnik, *Bell System Tech. J.* 44, 455 (1965).
- [42] S. Hanson, *J. Phys.* D6, 164 (1973).
- [43] D.B. Brayton, and W.H. Goethert, *ISA Transactions* 10, 40 (1971).
- [44] E.M.I. Photomultiplier Tubes (Brochure), (Whittaker Corp., Plainview, N.Y.).
- [45] RCA Phototubes and Photocells, Technical Manual PT-60, (Radio Corp. of Am., Lancaster, Pennsylvania, 1963).
- [46] A. Cox, Optics, (Focal Press, London, 1961).
- [47] G.B. Parrent, Jr., and B.J. Thompson, Physical Optics Notebook, (Society of Photo-Optical Instrumentation Engineers, Redondo Beach, Calif., 1969).
- [48] R.J. Goldstein, R.J. Adrian, and D.K. Kreid, *Ind. and Eng. Chem. Fundam.* 8, 498 (1969).
- [49] W.T. Snyder and W.H. Goethert, AEDC-TR-69-186.
- [50] J.S. Chung and W.P. Graebel, *Phys. Fluids* 15, 546 (1972).
- [51] L.S. Han, *J. Appl. Mech.* 27, 403 (1960).
- [52] H. Rouse, Advanced Mechanics of Fluids, (Wiley, N.Y., 1959).
- [53] R.V. Edwards, J.C. Angus, M.J. French, and J.W. Dunning, Jr., *J. Appl. Phys.* 42, 837 (1971).
- [54] R.V. Edwards, J.C. Angus, and J.W. Dunning, Jr., *J. Appl. Phys.* 44, 1694 (1973).
- [55] L. Lading, *Appl. Opt.* 10, 1943 (1971).
- [56] H.C. Van de Hulst, Light Scattering by Small Particles, (Wiley N.Y., 1957).

- [57] J.S. Dave, "Subroutines for Computing the Parameters of the Electromagnetic Radiation Scattered by a Sphere", (Rep. 320-3237, IBM Scientific Center, Palo Alto, California, 1968).
- [58] L. Lading, *Opto-Electron.* 5, 175 (1973).
- [59] W. Carrier and L.J. Nugent, *Appl. Opt.* 4, 1457 (1965).
- [60] G.C. Sherman, F.S. Harris, Jr., and F.L. Morse, Jr., *Appl. Opt.* 7, 423 (1968).
- [61] E. Reisman, G. Cumming, and C. Bartky, *Appl. Opt.* 6, 1969 (1967).
- [62] J.C. Owens, *Appl. Opt.* 11, 2977 (1972).
- [63] W.M. Farmer and D.B. Brayton, *Appl. Opt.* 11, 2979 (1972).
- [64] F. Talbot, *Phil. Mag.* 9, 401 (1836).
- [65] Lord Rayleigh, *Phil. Mag.* 11, 196 (1880).
- [66] E.T. Burtt and W.T. Catton, *Proc. R. Soc.* B157, 53 (1962).
- [67] G.L. Rogers, *Proc. R. Soc.* B157, 83 (1962).
- [68] J.T. Winthrop and C.R. Worthington, *J. Opt. Soc. Am.* 55, 373 (1965).
- [69] E.A. Hiedemann and M.A. Breazeale, *J. Opt. Soc. Am.* 49, 372 (1959).
- [70] G.L. Rogers, Handbook of Gas Laser Experiments, (Iliffe, London, 1970).
- [71] J.W. Goodman, Introduction to Fourier Optics, (McGraw-Hill, N.Y., 1968).
- [72] C.E.K. Mees and T.H. James, The Theory of the Photographic Process, (MacMillan, N.Y., 1966).
- [73] F. Hurter and V.C. Drifffield, *J. Soc. Chem. Ind. (London)* 9, 455 (1890).

[74] G. Mie, Ann. Physik. 25, 377 (1908).

[75] M. Kerker, The Scattering of Light and Other Electromagnetic Radiation, (Academic Press, N.Y., 1969).

[76] C.P. Wang, Appl. Phys. Lett. 18, 522 (1971).

[77] H. Mishina, T. Asakura, Opto-Electron. 4, 399 (1972).

[78] I. Lading, Opto-Electron. 4, 385 (1972).